# UNIVERSITY OF SOUTHAMPTON

FACULTY OF ENGINEERING AND THE ENVIRONMENT

ELETROMECHANICAL ENGINEERING

# An Investigation of Boundary-driven Streaming in Acoustofluidic Systems for Particle and Cell Manipulation

by

**Junjun Lei**

Thesis for the degree of Doctor of Philosophy

October 2015

UNIVERSITY OF SOUTHAMPTON

# ABSTRACT

FACULTY OF ENGINEERING AND THE ENVIRONMENT

ELECTROMECHANICAL ENGINEERING

Thesis for the degree of Doctor of Philosophy

# AN INVESTIGATION OF BOUNDARY-DRIVEN STREAMING IN ACOUSTOFLUIDIC SYSTEMS FOR PARTICLE AND CELL MANIPULATION

Junjun Lei

Acoustic streaming is a nonlinear effect and is a steady current driven by the absorption of acoustic oscillations in a fluid, forced by the action of Reynolds stresses. In most bulk acoustofluidic particle and cell manipulation devices working at MHz frequencies, acoustic streaming flows are mainly dominated by the boundary-driven streaming, which is generated from the acoustic energy attenuation due to the presence of the viscous boundary layer. Another important streaming pattern, Eckart streaming, generally requires acoustic absorption over longer distances than those found in such devices. This thesis develops two numerical methods which have been proposed for the modelling of both two-dimensional (2D) and three-dimensional (3D) boundary-driven streaming fields in acoustofluidic systems, allowing the interpretation of experimental observations that cannot be explained by existing theories and the prediction of boundary-driven streaming flows in acoustofluidic systems for suppressing or enhancing the streaming effects.

Classical boundary-driven streaming, “Rayleigh-Schlichting streaming”, is well-known and describes the eight streaming vortex pairs (with circulations perpendicular to the transducer radiating surface) within each wavelength of a one-dimensional standing wave field in 2D rectangular channels. 2D simulations from the Reynolds stress method have allowed us to understand the driving mechanism of this streaming pattern in depth in this thesis, which shows that it is the distinct rotationality of the Reynolds stress force (RSF) within and immediately outside the viscous boundary layer that drives the inner and outer streaming vortex pairs and limits the inner streaming vortex in the viscous boundary layer region with a size of $\sim\delta_v$ (viscous boundary layer thickness). This method has then been applied to investigate the effects of surface profile on the boundary-driven streaming fields in 2D rectangular channels, and it is shown that the rotationality of the RSF in the viscous boundary layer region can be dramatically modified by curved surfaces forming wall shape-dependent patterns rather than the resonance-dependent pattern found from the classical boundary-driven streaming. The outer streaming fields in devices with profiled surfaces have been found to be similar to those in devices with flat surfaces. The driving mechanism, however, is different to that of the classical Rayleigh streaming.

The limiting velocity method, which solves the outer streaming fields from limiting velocity boundary conditions, has allowed the demonstration of the 3D nature of acoustic streaming flows from 3D modelling of both fluid channels and full configurations of acoustofluidic systems. Using this method, the formation mechanisms of various boundary-driven streaming patterns that cannot be explained by existing theories have been illustrated for the first time in this thesis. “Transducer plane streaming” (streaming vortices with circulations parallel to the transducer radiating surface) observed in planar acoustofluidic manipulation devices has been found to be closely related to the active sound intensity field, which is known to be rotational in acoustic fields. From the analysis of the limiting velocity field in a 3D cavity mode, a new boundary-driven streaming pattern, referred to here as “modal Rayleigh-like streaming”, has been proposed and experimentally verified in a layered acoustofluidic particle manipulation device. Moreover, it has been found that a change on the dimension of the fluid channel cross-sections can alter the limiting velocity field from one pattern to another due to the rotational and irrotational characteristics of respectively the active and reactive sound intensity fields, resulting in different streaming patterns, which provides a basis for predicting the boundary-driven streaming patterns in layered acoustofluidic devices for particle and cell manipulation.

# Table of Contents

# List of Tables

# List of Figures

# DECLARATION OF AUTHORSHIP

I, Junjun Lei, declare that this thesis and the work presented in it are my own and have been generated by me as the result of my own original research.

[Title of thesis] An investigation of boundary-driven streaming in acoustofluidic systems for particle and cell manipulation

I confirm that:

1. This work was done wholly or mainly while in candidature for a research degree at this University;
2. Where any part of this thesis has previously been submitted for a degree or any other qualification at this University or any other institution, this has been clearly stated;
3. Where I have consulted the published work of others, this is always clearly attributed;
4. Where I have quoted from the work of others, the source is always given. With the exception of such quotations, this thesis is entirely my own work;
5. I have acknowledged all main sources of help;
6. Where the thesis is based on work done by myself jointly with others, I have made clear exactly what was done by others and what I have contributed myself;
7. Parts of this work have been published as [see details in Appendices]:

[1] **Junjun Lei**, Peter Glynne-Jones and Martyn Hill, Acoustic streaming in the transducer plane in ultrasonic particle manipulation devices, *Lab Chip*, 2013, **13**(11): p. 2133-43.
[2] **Junjun Lei**, Martyn Hill and Peter Glynne-Jones, Numerical simulation of 3D boundary-driven acoustic streaming in microfluidic devices, *Lab Chip*, 2014, **14**(3): p. 532-41.
[3] Dyan N Ankrett, Dario Carugo, **Junjun Lei**, Peter Glynne-Jones, Paul A Townsend, Xunli Zhang and Martyn Hill, The effect of ultrasound-related stimuli on cell viability in microfluidic channels, Journal of nanobiotechnology, 11(1), 20.

[4] **Junjun Lei**, Peter Glynne-Jones and Martyn Hill, Modal Rayleigh-like streaming in layered acoustofluidic manipulation devices, *Physics of Fluids* (Under review).

Signed:........................................................................................................

Date: ..........................................................................................................

# Acknowledgements

First of all, I would like to express my deepest gratitude to Professor Martyn Hill and Dr Peter Glynne-Jones for providing me with the opportunity to pursue my doctoral study. Peter, who is always open to discussions, has provided me invaluable advices on COMSOL modelling and experiments especially at the initial stage of my doctoral study. Martyn, in addition to the enthusiastic guidance and full support on my research, has put great energy on the management of the progress of my doctoral study. I am also thankful for their time on proofreading this thesis.

I would like to acknowledge the China Scholarship Council (CSC) and the EPSRC for their financial support.

I would like to thank my thesis advisory committee members: Dr Nick Harris and Dr Itzíar González for their participation, time and valuable comments.

My appreciation goes to all the people in the Electro-mechanical group, especially those from the ultrasound standing wave group. I appreciate my senior colleges Puja Mishra and Roy Green for their useful discussions on the COMSOL modelling and µPIV. I acknowledge Dario Carugo and Dyan Ankrett for collaborations on sonoporation and their knowledge sharing on bioengineering.

I am grateful to Chamaporn Chianrabutra, Puja Mishra and many others, whom I share a big office with, for their help with a lot of small things.

A big thank you goes to Yu Zhang and many other close friends around the country for their continual moral support throughout my doctoral study.

I would like to express my special gratitude to my parents for their love, patience, understanding and encouragement during my stay in the UK. Without this most important source of motivation I would have never imagined myself being at this stage in my life.

Finally, thank you God, without whom nothing would be possible.

# Nomenclature

| | |
|---|---|
| $\boldsymbol{F_{ac}}$ | Acoustic radiation force |
| $\boldsymbol{F_d}$ | Acoustic streaming induced drag force |
| $\boldsymbol{F}$ | Reynolds stress force |
| $F_x, F_y, F_z$ | $x$-, $y$- and $z$- components of $\boldsymbol{F}$ |
| $\rho, p, \boldsymbol{u}$ | Fluid density, pressure and velocity |
| $\rho_0, p_0$ | Steady density and pressure (absence of sound) |
| $\rho_1, p_1$ | First-order density and pressure |
| $\boldsymbol{u_1}$ | Acoustic velocity |
| $\boldsymbol{u_2}$ | Acoustic streaming velocity |
| $u_1, v_1, w_1$ | $x$-, $y$- and $z$- components of $\boldsymbol{u_1}$ |
| $u_2, v_2, w_2$ | $x$-, $y$- and $z$- components of $\boldsymbol{u_2}$ |
| $u_L$ | $x$-component limiting velocity |
| $v_L$ | $y$-component limiting velocity |
| $\lambda$ | Acoustic wavelength |
| $f$ | Driving frequency |
| $k$ | Wave number |
| $\omega$ | Angular frequency |
| $c$ | Sound speed |
| $Re$ | Reynolds number |
| $\mu$ | Dynamic viscosity of fluid |
| $\mu_b$ | Bulk viscosity of fluid |
| $\nu$ | Kinematic viscosity of fluid |
| $\delta_v$ | Viscous boundary layer thickness |

# List of Abbreviations

| | |
|---|---|
| 1D | One-dimensional |
| 2D | Two-dimensional |
| 3D | Three-dimensional |
| ARF | Acoustic radiation force |
| ASF | Acoustic streaming induced drag force |
| CFD | Computational fluid dynamics |
| LOC | Lab-on-a-chip |
| LDV | Laser Doppler velocimetry |
| LDA | Laser Doppler anemometry |
| LV | Limiting velocity |
| LVM | Limiting velocity method |
| PIV | Particle image velocimetry |
| PZT | Piezoelectric transducer |
| μPIV | Micro particle image velocimetry |
| Re | Reynolds number |
| RSF | Reynolds stress force |

# Chapter 1. Introduction

## 1.1. Background and Motivation

### 1.1.1. Particle and Cell Manipulation

Over the last decade with the rapid advancement of lab-on-a-chip (LOC) systems, miniaturization is being increasingly applied to biology studies and diagnostic instruments for biological and chemical analysis processes[1-8]. Compared to conventional techniques, it has various of advantages, including the reduction in sample and reagent use, high sensitivity and spatial resolution, short processing time, increased portability and low device cost[9].

Among the many functions required in LOC devices, particle manipulation, including separation of particles in complex fluids and arranging cells and microparticles into desired patterns, is important and is critical for various applications, including industrial processing[10], environmental assessment[11], clinical diagnosis[12, 13], and biochemical analysis[7, 14]. Numerous methods, most notably electrical[15-20], magnetic[21-23], optical[24-26], and acoustic methods[27-29], have been explored by researchers for particle manipulation. Manipulation can normally be classified into two types: one uses forces on the particles, depending on their size, electric property, magnetism or optical polarizability, to separate different cells from each other; and the other is arranging all particles and cells into desired patterns for counting or detecting. As a good example, arranging micro-particles and cells into desired patterns is a necessary step for accurately counting and detecting particles in micro flow cytometers[30-32]. However, these two types of manipulation can sometimes happen simultaneously in an acoustofluidic device, e.g. for separating size-dependent particles.

In terms of electric methods, forces used for particle manipulation can be classified into electrophoresis and dielectrophoresis. The former arises from the interaction of a cell's charge and an electric field and is proportional to the net charge of the object and the applied electric field, whereas the later arises from a cell's polarizability and is the product of the particle's dipole moment and the spatial gradient of the electric field.

With regard to magnetic methods, they can be used to sort and separate magnetically labelled particles. Sample cells are first incubated with magnetic beads for “magnetic labelling” and then a magnetic field gradient is used to isolate the magnetic beads, which in turn picks out the cells. According to Thiel et al.[33], up to $10^{11}$ cells can be processed in 30 minutes. And it was shown that the magnetic particles do not influence viability or function of the labelled cells [33, 34].

These two approaches (electric and magnetic methods) can achieve high throughput and be miniaturized easily but have limited flexibility in controlling single particles and pre-labelling of magnetic materials[35].

For optical methods, light is used to manipulate and separate particles depending on their optical polarizability. Similar to DEP, a phenomenon in which a force is exerted on a dielectric particle, the operating principle of optical methods is using an optically induced dielectrophoresis force on particles to manipulate or separate particles depending on their sizes. The optics-based patterning and manipulating techniques can have high precision, achieve high throughput, and low power consumption. However, compared to other manipulation techniques, they are difficult to miniaturize as they commonly require bulky, complicated optical setups[36].

The acoustic method for particle manipulation, based on acoustic standing waves or travelling waves, has gained increased attention and is considered to be an ideal particle manipulation method for LOC devices as it is non-invasive, requires no pre-treatment of the particles and can be used to manipulate any type of particle regardless of their optical or charge properties[37]. Among the existing techniques, the acoustic method is considered to have better cell-patterning techniques that simultaneously meet specifications for miniaturization, versatility, throughput, speed and power consumption[36].

### 1.1.2. Acoustofluidic Manipulation

As the main topic of this thesis investigates boundary-driven streaming fields in acoustofluidic systems and their effects on particle and cell manipulation, in the following, a brief introduction on the principle of acoustofluidic manipulation is discussed.

When talking about acoustofluidic manipulation, two terms, acoustofluidics and acoustophoresis, can be frequently encountered. Acoustofluidics, from its constitution, means fluidic systems with ultrasound technologies. Acoustophoresis means migration with sound, i.e., "phoresis" - migration and "acousto" - sound waves are the cause of the movement, which is a noncontact and label-free mode of manipulating particle and cell populations.

Most bulk acoustofluidic particle manipulation devices are based on ultrasonic standing waves, which are generated either by the use of two opposing sound sources such as loudspeakers[38] or more commonly by a single ultrasonic transducer with a solid layer working as a sound reflector in the propagation of sound waves. As early as the 19th century, acoustic standing waves were already characterised by Kundt[39] with his famous tube experiments. Ultrasound is sound with a frequency greater than the upper limit of human hearing, which is approximately 20 kHz in young, healthy adults. Ultrasonic particle manipulation devices in LOC systems typically work at frequencies from 0.1 to 10 MHz [40].

A typical bulk acoustofluidic manipulation device is made up of four layers, the transducer layer, carrier layer, fluid channel and the reflector layer. Particles in the fluid channel of acoustofluidic system suffer from two main forces: the acoustic radiation force (ARF) and acoustic streaming induced drag force (ASF). The ARF on the particles within a standing wave field, the main mechanism of particle manipulation, has been described extensively by King[41], Yosioka and Kawasima[42], Gorkov[43], Nyborg[44], Doinikov[45] and Bruus[46] et al. In addition, particles within standing wave field experience other forces, such as secondary radiation forces (when the distance between the particles is extremely small, e.g. $< 10$ μm[47]), buoyancy forces and gravitational forces. The movement of particles is a balance of all these forces.

### 1.1.3. Motivation for this Research

The main mechanism of acoustofluidic particle manipulation is based on the ARF on the particles, which generally concentrates the particles to the pressure nodal plane. However, it has been observed in experiments that some particles, generally those with diameters smaller than ~1 µm, are driven away from the desired particle concentration positions by acoustic streaming flows. The marginal particle size of streaming-dominated motion was found to be related to the actuation frequency, the acoustic contrast factor and the kinematic viscosity of the fluid [48]. Streaming patterns like this will, obviously, disturb the process of particle manipulation predicted by the ARF such that acoustic streaming field is generally treated as a disturbance in acoustofluidic particle and cell manipulation systems.

Moreover, even with plenty of experimental observations, the computational results and analytical solutions predicting streaming fields within ultrasonic standing wave fields for particle manipulation are relatively scarce. Most previous simulations of acoustic streaming in bulk acoustofluidic particle manipulation devices shown in the literature focus on the classical Rayleigh-Schlichting streaming[49, 50] based on 2D simplified models. However, acoustic streaming patterns, in reality, are 3D problems. In addition, researchers from many groups have also demonstrated boundary-driven streaming vortices in standing wave fields that cannot be explained by previous theories, which cannot be predicted using 2D simplified models, but have been frequently observed in acoustofluidic manipulation systems. In order to understand the driving mechanisms of unknown streaming patterns, computationally efficient method are required to predict the 3D streaming flows in acoustofluidic manipulation devices.

Therefore, it is necessary to numerically investigate the 3D streaming problems that have not been discussed in the literature due to the high computer-demand of current numerical methods. This is important because of the wide applications of acoustofluidic particle manipulation and its growing importance for experimental procedures and theoretical studies. Numerical investigation of acoustic streaming from its origin, Reynolds stress, is also useful to understand and control this phenomenon.

In addition to the influence on ultrasonic particle manipulation, acoustic streaming has found potential applications in other fields. As noted by Riley[51], streaming is a phenomenon that occurs more widely than its origin suggests and it can be found in many circumstances. One of the most important applications is in heat transfer enhancement [52, 53]. Besides, streaming also has other applications for example in non-contact surface cleaning[54-57], micro-mixing[58, 59], biosensors[60], transport enhancement[61, 62], clinical study[63, 64], micro-fluidic devices[65], thermoacoustic engines and refrigerators[66-68].

Understanding the driving mechanisms of the streaming patterns within a standing wave field is important in order to precisely control it for the enhancement or suppression of acoustic streaming in various applications, which is the main task of this thesis.

### 1.1.4. Objectives of this Research

This thesis aims to fully describe and analyse the 3D boundary-driven streaming fields within layered bulk acoustofluidic manipulation devices, including classical boundary-driven streaming in rectangular chambers and transducer plane streaming with circulations parallel to the transducer radiating surface, using numerical models and experimental validations. Several problems related to this will be investigated in this thesis:

- Explore computationally efficient methods for the simulation of 3D boundary-driven streaming fields in acoustofluidic systems;
- Validate the numerical methods from the simulation of classical boundary-driven streaming patterns in 2D rectangular chambers;
- Undertake a thorough investigation of the four-quadrant transducer plane streaming that has frequently been observed in thin-layered acoustofluidic particle manipulation devices from experimental measurements and numerical simulations;
- Propose explanations for the transducer plane streaming;
- Conduct a thorough investigation of 3D boundary-driven acoustic streaming patterns to understand the unusual phenomena observed in acoustofluidic particle manipulation systems;
- Establish the conditions under which each of the 3D boundary-driven streaming patterns occurs in an acoustofluidic device in order to predict the boundary-driven streaming fields;
- Explore the feasibility of techniques to control boundary-driven streaming.

In the following Section *1.1.4*, a detailed review of previous investigations of acoustic streaming, emphasising boundary-driven acoustic streaming, including theoretical analyses, experimental measurements and numerical simulations, is conducted.

## 1.2. Literature Review

### 1.2.1. Concept of Acoustic Streaming

Sound waves propagating through a fluid are often associated with some steady (non-zero time-averaged) and circulatory fluid motions, known as acoustic streaming. It is a nonlinear effect, driven by the absorption of high amplitude acoustic oscillations, which can be observed both near sound emitters and in acoustic wave fields confined by solid boundaries. Acoustic streaming formed in the former case is due to the interaction of acoustic waves with the medium alone while the latter one is on account of the interaction of sound waves with solid boundaries, which gives rise to first order rotational motion in the vicinity of the boundary.

Acoustic streaming can be defined from its generating mechanisms. Firstly, from its origin, it is a steady current in a fluid driven by the absorption of high amplitude acoustic oscillations and forced by the action of Reynolds stress[69], defined as the mean value of the acoustic momentum flux. Then, from its velocity composition, it is a generic term used to refer to the second order steady velocity that is induced by and superimposed on the dominating first order acoustic velocity, so it is a nonlinear effect and cannot be analysed by linear acoustics.

A comprehensive review of several classes of acoustic streaming, which is classified based on the different mechanisms by which it is generated, was done by Boluriaan and Morris[70] and recently by Valverde[71]. At present, several types of acoustic streaming are known and have been rather thoroughly investigated. It can be classified in several ways. Based on the mechanism by which streaming is generated, acoustic streaming can be classified to boundary-driven streaming (including inner streaming and outer streaming), jet driven streaming, Gedeon streaming and Eckart streaming.

Boundary-driven streaming consists of two types of streaming: outer streaming (also known as Rayleigh streaming[49]) and inner streaming (also known as Schlichting streaming[50]). The reason for the term of “boundary-driven streaming” is that this type of flow motion is driven by viscous stresses on the boundaries either when a sound wave reaches a boundary or when a boundary is vibrating in a still medium. A schematic presentation of 2D classical boundary-driven streaming is shown in *Figure 1.1*.

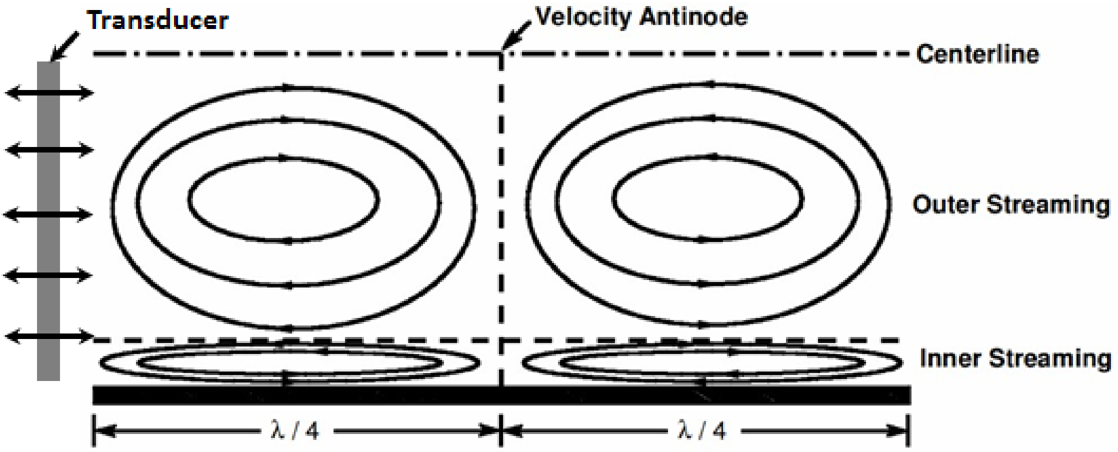

Figure 1.1 Schematic of classical boundary-driven streaming[70] in a one-dimensional (1D) standing wave field, where $\lambda$ is the acoustic wavelength.

Jet driven streaming links with the periodic suction and ejection of a viscous fluid through an orifice or a change in cross section, shown in *Figure 1.2*[70]. This kind of streaming originates from the vortices formed around the orifice or change in cross sectional area. The mechanism of jet driven streaming depends on the fact that a fluid behaves differently during the suction and ejection periods. As shown in *Figure 1.2*, in the suction period, the flow in the orifice comes effectively from all directions. However, a jet is generated that induces a mean flow in a certain direction during ejection. Finally, “traveling wave streaming” occurs in the presence of a progressive wave, which exhibits certain unique features.

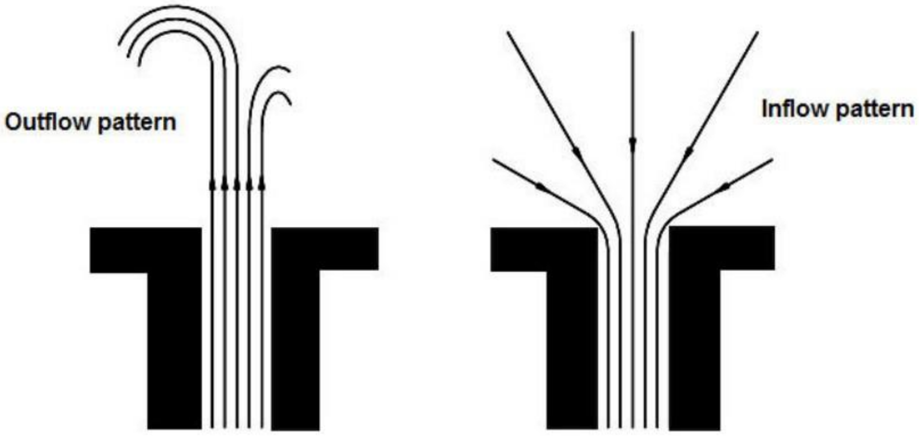

Figure 1.2 Jet-driven streaming: outflow and inflow patterns at the transition between a small tube and open space[70]

Gedeon streaming is associated with travelling waves, and is named after Gedeon for his contribution to analysing acoustic streaming in Stirling and pulse tube thermoacoustic refrigerators for the first time. Therefore, travelling wave streaming in Stirling thermoacoustic engines and refrigerators is usually referred to as Gedeon streaming.

Eckart streaming[72] is generated by the dissipation of acoustic energy in the fluid. Unlike boundary-driven streaming, which is caused by the interaction of the acoustic field at the fluid and solid boundaries, Eckart streaming is driven by the absorption of high amplitude acoustic oscillation during propagation. The induced flow of Eckart streaming is predominant in high frequency range and the streaming velocities become greater at higher frequencies because of higher absorption. Since the radiation pressure gradient due to the absorption of the acoustic wave during propagation is the driving force of the flow, wave reflections are avoided in Eckart streaming experiments. Under this condition, an acoustic absorber is commonly used in an experimental setup, shown in ***Figure 1.3*** (a).

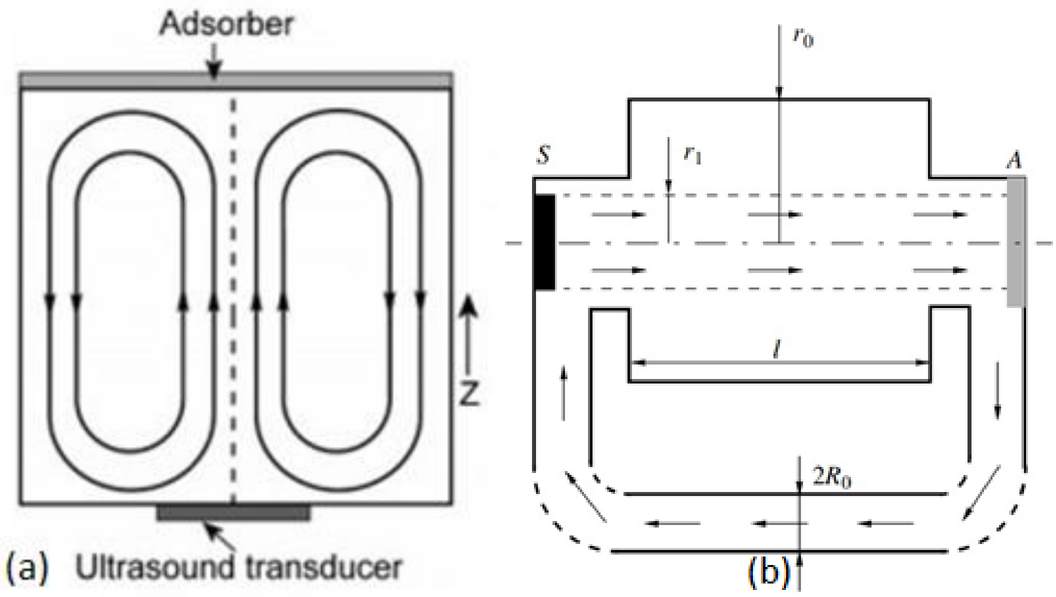

Figure 1.3 Eckart streaming: (a) Schematic of container-scale Eckart streaming [60]; (b) Schematic diagram of an acoustic pump. The source S generates an ultrasonic beam of radius $r_1$ which passes through the Eckart cell (its radius is $r_0$ and its length is $l$) and is absorbed by the layer A. A tube of radius $R_0$ and length $L$ is connected to the cell[73].

Another way to classify acoustic streaming is based on the magnitude of the streaming velocity. Using this approach, it can be divided into slow streaming and fast streaming. Slow streaming is when the streaming velocity is considerably smaller than the magnitude of the acoustic velocity. Fast streaming is when the acoustic velocity and the streaming velocity are the same order of magnitude. Streaming can also be categorized as ‘slow’ or ‘fast’ by the acoustic Reynolds number (Re). The case Re<<1 corresponds to the slow streaming[38] while the case Re>>1 is referred to fast streaming or nonlinear streaming. Most types of acoustic streaming observed in acoustofluidic systems are slow with the exception of jet driven streaming, which is considered as fast streaming.

In the following sections, the relevant literature on the three most widely studied types of acoustic streaming, namely streaming outside the boundary layer, streaming inside the boundary layer and Eckart streaming, including their histories, analytical solutions, experimental studies and numerical simulations, are reviewed.

### 1.2.2. Early Observations of Acoustic Streaming

It is widely accepted that the phenomenon of acoustic streaming was first observed by Faraday[74] in 1831, when he was considering the phenomenon of air currents generated over an oscillating plate. In that experiment, Faraday found the fine particles lying on a vibrating plate were collected at the regions of maximum vibration of the plate. He explained that air currents, which are commonly referred to as acoustic streaming later, are established in the air lying upon the surface of the plate, which ascend from the vibration antinode of the plate and descend at the nodes when a plate is made to vibrate, shown in ***Figure 1.4*** (a). In fact, a few years earlier, a similar phenomenon had been noticed by Savarat. In 1876, Dvorak (summarised in [75]) observed similar air currents when he did an experiment in a Kundt’s tube, which was first analysed and solved by Rayleigh[49] a few years later. Later in 1878, in another experiment, Sedley Taylor[76] added “sonorous vibrations on liquid films” and observed that aerial vortices were reacting laterally upon the film.

### 1.2.3. Analytical Solutions for Acoustic Streaming

The streaming problem was first solved by Rayleigh[49] in 1883 with an analytical solution, which he later reiterated in his book "the theory of sound"[75]. In that paper, the three problems discussed in the section above were considered and solved. He started his analysis from the equations of motion in two dimensions, which will be illustrated in detail in ***Chapter 2***. With the first approximation of neglecting the second order in the velocities, he obtained the equations for the linear acoustic velocity. Then, he noted that it is impossible to gain the acoustic streaming velocity if the acoustic equations are solved based only on the first approximation as acoustic streaming is a second order effect. By considering the second order velocity component, he obtained the fluid velocity equation for the steady motion of periodic vortices, which, between two parallel plates, rise from the bottom over the velocity nodes and fall back over the velocity antinodes. In the second problem, Rayleigh illustrated that the fluid must be treated as compressible as the motion in the Kundt's tube is supposed to be approximately in one dimension. As in the former problem, in his analysis, the terms of second order velocities were omitted first but considered to generate the streaming velocity equations. It is interesting to note that the direction of the mean flow over the oscillating plate (shown in ***Figure 1.4*** (a)) is opposite to that in the second problem conducted in a Kundt's tube, shown in ***Figure 1.4*** (b). Another remarkable fact Rayleigh found is that the maximum value of the streaming velocity is independent of value of the coefficient of viscosity even though it arises due to the fluid viscosity. Rayleigh's method has become the dominant tool for the study of acoustic streaming since then.

Rayleigh's solution only describes the fluid motion outside the boundary layer, so it is commonly referred to as outer streaming as well as Rayleigh streaming. In fact, inside the boundary layer, there also exist streaming vortices, whose directions are opposite to the outer streaming, Rayleigh streaming vortices. A study of the streaming field inside the boundary layer, or inner streaming, was first developed by Schlichting[50] in 1932, who considered an incompressible oscillatory flow over a flat plate. Hence, inner streaming can also be referred as Schlichting streaming. He also estimated the thickness of the inner streaming vortices which is about 1.9 $\delta_v$, where $\delta_v$ is the thickness of the viscous boundary layer, defines as

$$\delta_v = \sqrt{\frac{2\nu}{\omega}}, \tag{1.1}$$

where $\nu$ is the kinematic viscosity of the fluid and $\omega$ is the angular frequency. However, the vortex outside the boundary layer is not examined in his analysis.

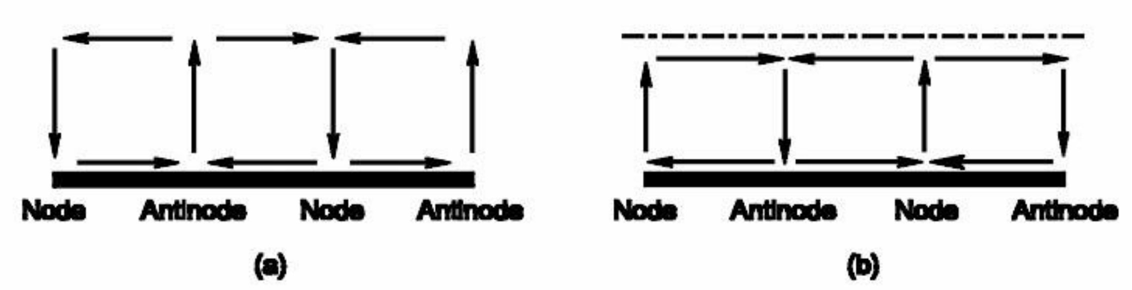

Figure 1.4 Rayleigh streaming patterns: (a) mean flow over a vibrating plate; (b) mean flow in a Kundt's tube[70]. Node and Antinode show the velocity node and antinode, respectively.

Rayleigh and Schlichting analysed the boundary-driven streaming within a standing wave field, confined between two parallel plates. After that, a series of modifications and subsequent development of their solutions were proposed, most notably by Eckart[72], Westervelt[77], Nyborg[78] and Hamilton[79].

Eckart[72] first developed a solution for solving the problem of streaming flows caused by a beam of sound (e.g. the quartz wind) in 1947. His analysis considers a long tube of radius $r_0$, whose walls are rigid, and whose ends are closed by some material that permits an axial sound beam to enter and leave the tube without reflection, similar to ***Figure 1.3*** (a). Eckart showed that by solving the hydrodynamic equations with the inclusion of viscous forces, found to be both generating and resisting forces of streaming field, the vortex motion would ultimately reach a steady state. He also illustrated that the streaming velocity depended on the bulk viscosity for the reason that the resisting forces depended only on the shear viscosity while the generating forces depended also on the bulk viscosity. He suggested that the bulk viscosity can be determined from the measurement of the magnitude of the streaming velocities as he found that the streaming velocities generated by a beam of sound is proportional to the value b, defined as

$$b = (4/3) + (\mu_b/\mu), \tag{1.2}$$

where $\mu_b$ and $\mu$ are the bulk and shear viscosities.

Eckart's theoretical work on the streaming caused by an acoustic field was re-examined by Markham[80] in 1952. The first modification is that he focused his attention on the mass flow of the fluid instead of on the particle velocity as he found that one can reach the incorrect conclusion that there is no streaming even in a viscous fluid if Eckart's solution is applied to the mass flow instead of to the particle velocity. Then, he concluded that the magnitude of the streaming does not depend solely on the bulk and shear viscosities, but on the coefficient of sound absorption. This conclusion was confirmed by later analytical solutions obtained by Nyborg[78] and Westervelt[77].

Nyborg[81] reviewed the theories for calculating steady streaming associated with sound fields and compared the methods and approximations of various authors. He worked out two illustrative problems, both for rectilinear flow due to irrotational sound fields. The first deals with a single attenuated plane wave travelling down a tube and the second deals with a pair of crossed plane waves, which give rise to a quite different kind of streaming. He found that the streaming velocities depend critically upon the attenuation constant, which may be caused by heat conduction, scattering, thermal effects, etc. He reached a conclusion, from these results, that streaming measurements cannot be used to distinguish between absorption mechanisms. Moreover, as illustrated by Nyborg, previous theoretical approaches to acoustic streaming at that stage were based on successive approximations to solutions of nonlinear hydrodynamical equations and accurate solutions exist only for cases where boundaries are planes, cylinders, or spheres and where the specified velocity distributions on these boundaries are very simple. In 1958, Nyborg[78] developed an approximate solution for sonically-induced steady flow near a fluid-solid interface, which is valid for the flow near any portion of surface based on the assumption that the irrotational oscillatory velocity distribution of the flow in the vicinity of the surface is known. In his analysis, the streaming pattern in and slightly beyond the viscous boundary layer for an object with an arbitrary shape but with a smooth surface in an arbitrary wave can, in principle, be calculated.

Starting from the Navier-Stokes equations, Westervelt[77] obtained a general equation for the production of time independent vortices in 1952. This approach, unlike the previous theoretical solutions obtained by Rayleigh and Schlichting (based on the assumption of solenoidal first order motion) and Eckart (restricted to cases in which the first order motion is irrotational), is free from the irrotational and solenoidal restrictions on the first order velocity. The developed theory is in agreement with the results obtained by Eckart and subsequently modified by Markham when it is applied to Eckart's problem. However, when it is applied to a two-dimensional (2D) standing wave problem, the streaming velocity in the boundary layer is found to differ from the results obtained by Rayleigh. In the region outside the boundary layer, the streaming flow matches well with that obtained by Rayleigh.

The apparent discrepancies between the observations with regard to the direction of acoustic streaming near obstacles was re-examined by Andres and Ingard[82, 83] in 1953. It is pointed out that the direction of acoustic streaming is dependent on the acoustic Re, which is defined as

$$Re = U_0 a/\nu, \tag{1.3}$$

where $U_0$ is the particle velocity in the incident sound wave, $a$ is the radius of the cylinder, and $\nu$ is the kinematic viscosity. Acoustic streaming at high acoustic Re was firstly investigated and the distortion of the streaming flow patterns as a function of sound intensity was discussed[82]. The results obtained were found to be in agreement with the experiment results from Andrade[84] and Schlichting[50]. The corresponding problem for low acoustic Re was considered later, and it was shown that the flow pattern obtained around a cylinder in a sound field is opposite to the one corresponding to high Re, which validates the experiment observations of Carrière[85]. However, as pointed by Wang[86], both Schlichting and Andres and Ingard used the planar boundary layer equations, which will be in error because the curvature of the body will affect the second order solutions.

The steady flow around a sphere was first studied by Lane[87] in 1955 by following the method of analysis of streaming flows near an oscillating cylinder. Lane found that the characteristic parameters are quite similar to what had been found for the cylinder. He also implemented an experiment to verify the theory by comparing the observed boundary-layer thickness with that found from the theory, which showed good agreement. However, as illustrated by Lee and Wang[88], the inner flow obtained from Lane's method in the limit of small boundary layer thickness, without the velocity transform, does not agree with what one would obtain using Schlichting's method and Lane's equations do not even seem to be self-consistent. They believe that Lane's analysis contains some mathematical errors although his approach is in principle correct.

Wang[89] re-examined the analytical solutions on the streaming field near an oscillating cylinder or sphere and presented an approximation method to analyse the flow field induced by an oscillating sphere in 1965. He found that all the previous solutions were limited to a region very near the body. Large errors will be introduced if these solutions were extended away from the body because of bad convergence. In addition, Wang pointed out that the expansion in the single parameter $(1/ReS)^{1/2}$, where and $S$ is Strouhal number, was not sufficient to describe the flow near the body because he found that, unlike the first order solutions, which contain only the combined parameter $(r-1)\sqrt{ReS}$ ($r$ is the distance to the centre of the sphere), the second order solutions contain not only $\sqrt{ReS}$ but also combined parameters like $1/S$, $1/\sqrt{ReS}$ and $(r-1)\sqrt{Re/S}$. Wang illustrated that both the "inner" and "outer" flow fields need to be determined simultaneously. The outer solutions satisfy the boundary conditions at infinity and the inner solutions, solved in a stretched coordinate, satisfy the boundary conditions on the body. However, Lee and Wang[90] found that Wang's solution failed the test of its validity when it was substituted to the vorticity equations although the inner flow agrees with that from Schlichting's method[50].

Stuart[91] considered a double boundary layer model and unsteady laminar boundary layers on solid bodies with a fluctuating external flow of small amplitude. He applied his analysis to the streaming associated with a long oscillating cylinder in an infinite medium and explained that associated with any outer streaming, there are streaming vortices within the boundary layer, which is consistent with the experiment results obtained by Schlichting[50] and the concept of boundary-layer streaming people have today.

Most previous classical theoretical studies on acoustic streaming mentioned above, such as those solved by Rayleigh[49], Schlichting[50], Eckart[72], were based on a series of approximations, like assuming incompressible fluid, neglecting thermal effects, neglecting the effects of fluid inertia, etc. The effects of the heat conduction on the outer streaming including the effect of variable tube wall temperature were first considered by Rott[92] in 1974. The calculations were carried out in the limiting case when the boundary layer is thin compared to the tube radius. In the case of a zero temperature gradient, the axial streaming velocity obtained by Rott can be given by

$$\overline{u_{2,Rott}} = (1+\alpha)\overline{u_{2,Rayleigh}}, \tag{1.4}$$

where the constant $\alpha$ represents a correction to the magnitude of the streaming velocity. A typical value for $\alpha$ in air at standard conditions is $\alpha = 0.03$, which predicts an axial acoustic streaming velocity that is 3% larger than the axial streaming velocity obtained from Rayleigh's method.

In 1988, Lee and Wang[88] modified Nyborg's theory[78] on acoustic streaming near a solid boundary, where some curvilinear effects were ignored, and applied it to study the acoustic streaming pattern near a small sphere due to two orthogonal standing waves, which have the same frequency but are out of phase. They followed the corrected approach and found the nature of flow inside and immediately outside the viscous boundary layer around a small sphere. Later in 1990, Lee and Wang[90] studied the effect of compressibility on the streaming pattern. In that work, they concentrated on the more visualizable streaming outside the boundary layer, which can be relevant to heat and mass transfers. They concluded that compressibility can affect the inner but not the outer streaming flow for the flow between parallel plates, but that for two or three-dimensional (3D) objects, such as a cylinder or a sphere, the compressibility also affects the outer streaming pattern. They used the limiting velocity (LV) at the edge of the inner streaming layer as a slip boundary condition to solve for the large outer streaming. As a test for their formulation, both the streaming patterns due to a standing wave grazing two parallel plates and around a sphere or cylinder were calculated.

A similar investigation with regard to the effect of compressibility on acoustic streaming was studied by Qi[93] in 1993. A plane travelling wave near a rigid boundary was considered. His work solved a long existent inconsistency: while the compressibility is a necessary condition for the propagation of acoustic wave, previous analysis of acoustic streaming were limited to incompressible fluid. It is shown that the inclusion of compressibility leads to a larger streaming velocity outside the boundary layer. The effect was found to be significant in gases, but not in liquids.

All the above-cited studies assume the streaming to be very slow, which is slow enough to leave the first-order variables unperturbed. Vainshtein[94] analysed Rayleigh streaming in a fluid confined between two parallel walls, shown in *Figure 1.5*, with a standing wave in the transverse direction at high streaming Re by solving the full Navier-Stokes equations in order to investigate the effects of streaming upon in the shear flow in the longitudinal direction. The results show that acoustic streaming can markedly enhance the mean wall shear stress at the walls. The effects of fluid inertia on acoustic streaming was then analytically studied by Menguy and Gilbert[95] in 2000. The streaming field in an acoustic standing wave generated by a sinusoidal standing wave inside a cylindrical waveguide was considered. A comparison of slow and nonlinear (determined by the Re) acoustic streaming was presented, which showed that the nonlinear effect of fluid inertia will noticeably distort the streaming patterns.

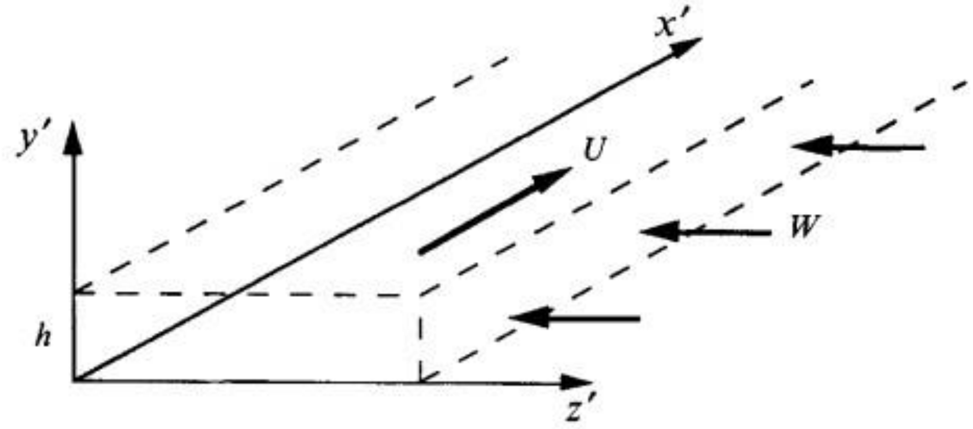

Figure 1.5 A Schematic presentation of the problem presented by Vainshtein[94], where $h$ is the distance between the walls, $U$ is the velocity of the upper wall, $W$ is the velocity of the imposed standing sound wave.

Waxler[96] included heat conduction in a study of streaming in a gas between closely spaced parallel plates. Coupled equations for the time-averaged pressure gradient, velocity, and temperature were obtained and solved. Bailliet et al.[97] later derived an analytical solution for acoustic streaming in steady-state thermoacoustic devices, both in the parallel plate and in the cylindrical tube geometries, in the case of zero second-order time-averaged mass flux across the resonator section, which included the temperature dependence of the viscosity in addition to heat conduction. In both Waxler and Bailliet et al.'s cases, the mean temperature was assumed to vary along the channel walls to account for such variations within the stacks of thermoacoustic engines.

Hamilton et al.[79] derived an analytical solution for the acoustic streaming generated by a standing wave confined by parallel plates in 2003. Both the outer, Rayleigh streaming vortices and the inner, boundary layer vortices were accurately described. The solution was compared with those earlier analytical solutions, such as those derived by Rayleigh [49], Westervelt[77], and Nyborg[78], which are restricted to wide channels, and showed good agreement for wide channels. Hamilton illustrated that, as channel width is reduced, the inner vortices increase in size relative to the Rayleigh vortices and for channel widths less than about 10 times the boundary layer thickness, the Rayleigh vortices disappear and only the inner vortices exist. Later, they extended their analysis to a gas in which heat conduction and dependence of the viscosity on temperature were taken into account[98]. They found that the results for cylindrical tubes and for 2D channels were qualitatively the same. In channels that are very wide or of the same order in comparison with the viscous penetration depth, the thermal effect is comparable but small. In channels having intermediate widths, 10–20 times the viscous penetration depth, however, the effect of heat conduction can be substantial.

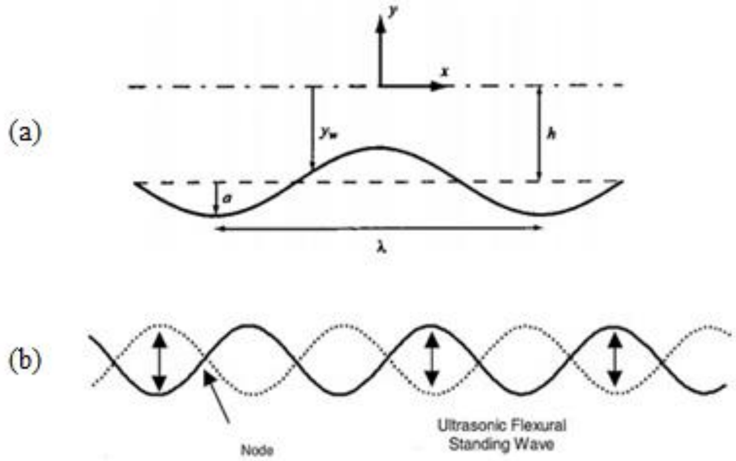

Figure 1.6 The problem presented by Carlsson et al.[99] (a) Sketch of the vibrating wall of a 2D infinitely long channel; (b) the standing wave field generated.

The steady acoustic streaming field generated in a standing wave field in a viscous Newtonian fluid confined in a 2D infinitely long channel was analytically investigated by Carlsson et al.[99] by solving time-dependent first-order and time-averaged second-order equations. The acoustic field is generated by the transverse vibration of its bottom wall, which formed a standing wave within the channel, shown in ***Figure 1.6***. The influence of two dimensionless parameters $H = hk$ and $\alpha^2 = \omega/\nu k^2$, where $h$ is the channel half width, $k$ is the wave number, $\omega$ is the angular frequency and $\nu$ is the kinematic viscosity, on the steady streaming patterns was investigated. It was found that for small values of $\alpha^2$ and $H$ the flow is dominated by viscous effects and a single layer covers the full domain of the channel half-width. However, the inertial effects become increasingly important and eventually two streaming layers show up with the increased value of $\alpha^2$. As the magnitude of $H$ is increased, the importance of the opposite wall is reduced and three distinct regions were found for large values of $H$: if $\alpha^2$ is small viscous diffusion produces two layers of vortices; an increase in $\alpha^2$ rapidly destroys the inner streaming layer reproducing the solution found at small values of both $\alpha^2$ and $H$; a further increase of $\alpha^2$ eventually leads to the formation of three cell layers. A plot which reveals the influence of the value of $\alpha^2$ and H on the streaming patterns in the channel is shown in ***Figure 1.7***.

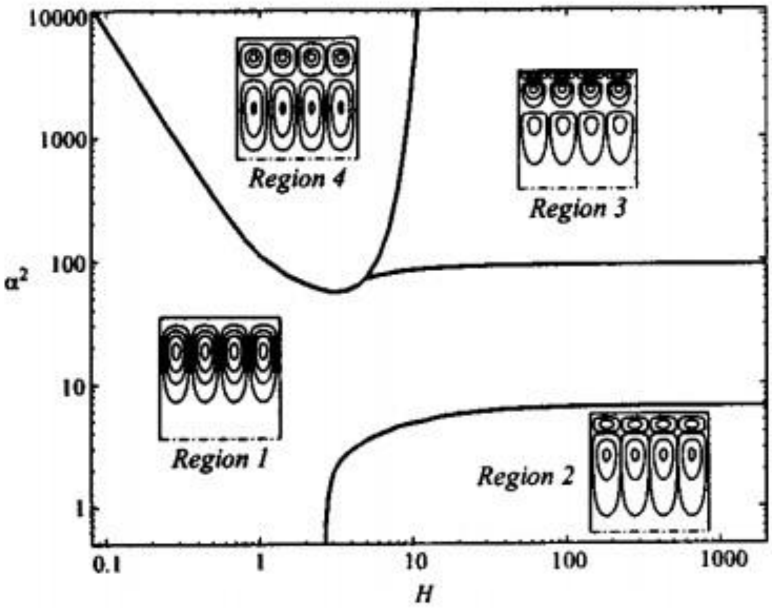

Figure 1.7 Streaming patterns at different values of $\alpha^2$ and $H$, reproduced from Carlsson et al.[99].

Rednikov and Sadhal[100] revisited the inner acoustic streaming for a motionless boundary in 2011. As originally realized by Nyborg[78], the problem of the inner acoustic streaming can be analysed in general terms and the inner streaming can be determined by a given distribution of the acoustic amplitude along the boundary. Rednikov and Sadhal obtained new compact and easy-to-use expressions for inner acoustic streaming by working in terms of surface vectors. The first one was the expression of slip velocity at the boundary, which is often considered to be the sole driving force for the outer streaming. Another important development was that non-adiabatic effects, whose contribution into the streaming, in the Stokes layer were taken into account, was often ignored in the previous analysis. A few examples were provided to indicate the application of newly derived general inner-streaming expressions. Further reviews of acoustic streaming can be found in references [69, 101-107].

### 1.2.4. Experimental Investigations on Acoustic Streaming

Carriere[85] experimentally investigated the streaming patterns around a cylinder in 1929. A steady circulatory streaming, the direction of which, was found in each quadrant around the cylinder, was towards the cylinder along the axis of oscillation.

A detailed experimental investigation of acoustic streaming in a gas-filled tube excited by a standing wave and vortex motion around cylinders and spheres was conducted by Andrade[84] in 1931, shown in ***Figure 1.8***. He used smoke particles as tracing points to visualise the behaviour of flow in the tube as they follow closely the motion of air in which they are suspended. In the tube experiment, he found that the gas moved from antinode to node along the wall and returned up the centre, which verified the air circulations predicted by Rayleigh's theoretical work[4]. The circulation around a cylinder or sphere observed was similar to those identified by Carrier, but flowing in the opposite direction.

Based on Eckart's theory of acoustical streaming, Liebermann[108] conducted a set of experiments to explore the streaming field in the vicinity of sound source, shown in ***Figure 1.9*** (a). He also obtained the value of the bulk viscosity for a variety of organic liquids and for water from these experiments and found that the non-periodic motion of the fluid near a sound source is dependent on the shear viscosity and the bulk viscosity.

The acoustic streaming field around small orifices was experimentally studied by Ingard and Labate[109] in 1950 by the use of smoke particles. They found that there existed four definite regions of flow as the particle velocity in the orifice is increased. Acoustic impedance, the nonlinear properties of which, was determined under each observed condition, were due to the interaction between the sound field and the circulation effect.

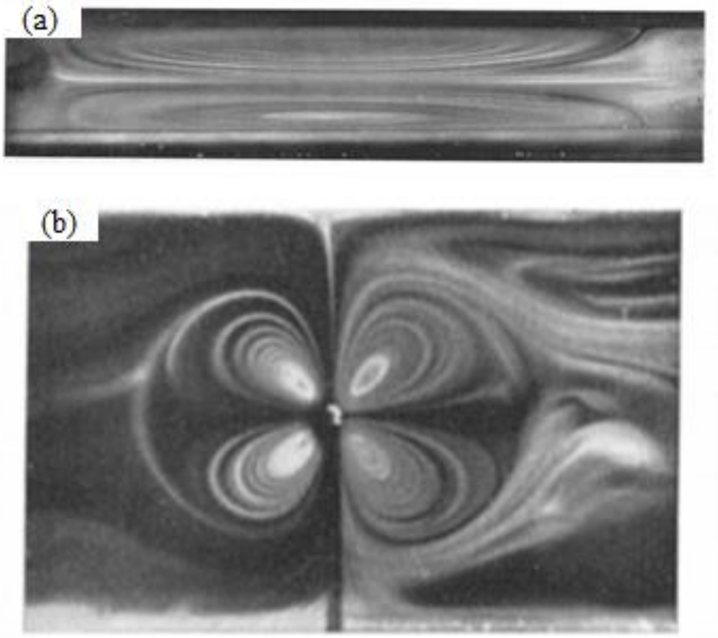

Figure 1.8 Acoustic streaming patterns: (a) a node to antinode action of circulation in a Kundt's tube; (b) vortex motion around a cylinder or a sphere.[84]

An investigation of the movements of air in the neighbourhood of oscillating cylinders, by means of smoke particles, was made by West[110] in 1951. This experiment was similar to Andrade's work[84]. However, the circulations observed by West were in an opposite direction to those observed by Andrade. Later, Westervelt[77] concluded that the streaming direction was observed to change direction when the amplitude of the vibration was approximately equal to the diameter of the oscillating cylinder.

Holtsmark et al.[111] studied the streaming flow near a circular cylinder in a Kundt tube by the use of smoke particles in 1954. His result mainly concentrated at the streaming patterns within the boundary layer, which was compared to the results obtained by Schlichting. The streaming structures in and outside the boundary layer around a cylinder was later visualized by Raney et al.[112] in 1954, which a mixture of water and glycerine was used and confirmed the predictions that for small oscillation amplitudes the streaming patterns will be the same whether the cylinder oscillates in a quiescent fluid or is fixed in an oscillating fluid.

Trinh and Robey[113] experimentally studied the streaming flows associated with ultrasonic levitators, in which, composed of an ultrasonic driver, a fluid layer and a reflector, shown in *Figure 1.9* (b), a standing wave was generated between the driver-reflector gap. Their experimental results also confirmed different characteristics of streaming flows at different sound pressure levels. As with other experiments, the streaming flow was visualised by the use of smoke particles.

It can be seen that most of the measurements of acoustic streaming introduced above were conducted by the use of smoke particles to make the streaming vortices visible. In the last decades, attention has focused on boundary layer streaming and numerous techniques have been developed by researchers to measure and characterise acoustic streaming flow field, most notably Laser Doppler Velocimetry (LDV) and particle image velocimetry (PIV). However, as illustrated by Moreau et al.[38], only a couple of groups have succeeded in obtaining quantitative measurements of streaming ahead of their experimental investigation.

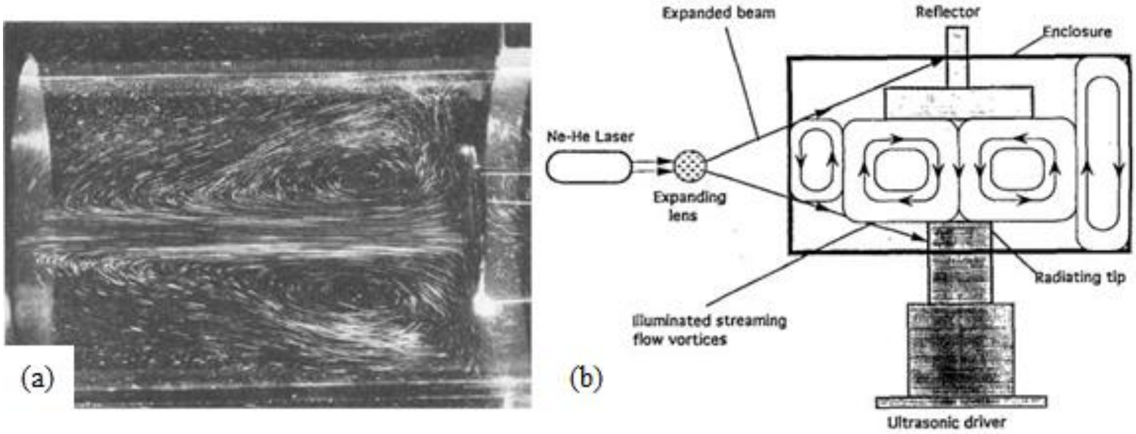

Figure 1.9 Acoustic streaming patterns: (a) acoustic streaming near a sound source (Eckart streaming)[84]; (b) Schematic of the experimental apparatus and streaming pattern in ultrasonic levitator[113].

Laser Doppler velocimetry (LDV), also known as Laser Doppler Anemometry (LDA), is the technique of using Doppler shift in a laser beam to measure the fluid velocities. It is a point-measurement technique, which means that it is able to measure the three-components of a fluid’s velocity at one spatial location. Particle image velocimetry (PIV) is an optical method of flow visualization. The basic principle of this technique is that tracer particles suspended in the flow are illuminated by a light sheet. The position of these particles at different time intervals are recorded and from measuring the particle displacement the fluid motion can be determined.

As early as 1995, Hartley[114] used Doppler signal processing to measure streaming velocity using blood and water in order to characterise the acoustic streaming field generated by pulsed ultrasonic beams. He found the streaming velocities at different diagnostic power levels and concluded that streaming was measurable in pulsed ultrasonic beams.

Mitome et al.[115] used a LDV to measure the acoustic streaming field generated by 5.05 MHz ultrasound in water in 1996 in order to clarify the establishment process of the streaming. They found that, at low frequencies, the streaming velocity would increase and reach a steady value when the ultrasound was switched on. The streaming velocities, at high frequencies, however, would show irregular behaviour in the establishment process.

Nowicki et al.[116] derived an approximate solution for the streaming velocity generated by flat and weakly focused transducers in 1998, which was verified with experiments. The streaming velocity was measured along the ultrasonic beam using a 32 MHz pulsed Doppler unit and visualised using the PIV method.

Thompson and Atchley[117] conducted acoustic and streaming velocities measurements in an air-filled cylindrical standing wave resonator by the use of LDA in 2005. The axial component of streaming velocities was measured along the resonator axis. Later on, following this experimental method, Thompson and Atchley[118] investigated the influence of a temperature gradient and fluid inertia on acoustic streaming in an air-filled cylindrical standing wave resonator. The same with the former experiment, the axial component of Lagrangian streaming velocity was measured along the resonator axis. They found that the axial temperature gradient has significant influence on the axial component of the streaming velocity field. With the increase of the magnitude of the temperature gradient, the magnitude of the streaming velocities decrease and increasingly distorted shapes of streaming cells were observed.

Kumer et al.[119] used both LDV and PIV to measure and visualize the acoustic streaming patterns and velocities in sonochemical reactors. The measured streaming velocities from the two optical techniques were compared to the theoretical calculations, which shows that the theoretical and measured velocities are almost identical at low dissipated power but at higher power dissipation levels, the measured velocity is much higher than the theoretical velocity. This experimental work, as suggested by the authors, should be useful in establishing sound design strategies for sonochemical reactors.

Moreau et al.[38] measured the axial velocities of inner and outer streaming vortices in a standing waveguide with loudspeakers at each end in 2007. Both the slow and the fast streaming, characterized by acoustic Re, were studied. For small Re, their experimental results matched well with the slow streaming theory.

The acoustic streaming field in a travelling wave, closed-loop resonator was measured by Desjouy et al.[120] using the LDV method in 2008. It was shown that measurement was quite difficult to manage because of its strong sensitivity to the environment parameters and further work, as illustrated by the authors, was needed to characterize more deeply the streaming patterns in such a device. Later, Desjouy et al.[121] further examined their former work of measuring the acoustic streaming field in a closed-loop traveling wave resonator in 2009. An analytical model of the acoustic field and a theoretical estimate of the acoustic streaming are presented. The measured cross-section average acoustic streaming velocities, performed using laser Doppler velocimetry, was in good agreement with the value predicted by the theoretical model. The experimental results obtained also show that the profile of acoustic streaming may be influenced by the curvature of the resonator.

To my knowledge, the measurement of acoustic streaming field using the PIV techniques was first conducted by Sharp et al.[122] in 1989. The streaming generated by a 1D mono-frequency acoustic standing wave in a resonator was investigated.

Arroyo and Greated[123] used a new technique, called stereoscopic PIV, which combines the particle image velocimetry with the stereoscopy, to study the Rayleigh streaming in a rectangular chamber. Using this method, three components of the velocity field in a plane can be measured simultaneously, which offers possibilities for the investigation of 3D flows. However, they only measured the streaming velocity field in a region within 2 cm around the velocity node.

A method by which the flow velocity and acoustic particle velocity can be measured simultaneously over an area was outlined by Hann and Greated[124] in 1997. They used PIV techniques to measure acoustic and streaming velocities in a standing wave tube with a monotonic sound field of sufficient strength. Some limitations of this technique were also discussed by the authors.

Chouvellon et al.[125] used PIV techniques to examine the influence of certain parameters such as the electric power, the water height and the fluid viscosity on the velocity field of a sonochemical reactor in 2000. Their experimental results show that the velocity increases in a nonlinear way with the increase of electric power, decreases in a regular way when the water height increases, and increases with the fluid viscosity until it reaches a threshold.

Campbell et al.[126] did a review of LDA and PIV on measurement of sound and acoustic streaming in 2000. A velocity map of PIV image on acoustic streaming was presented in that review.

Frenkel et al.[127] used PIV to investigate the ultrasound-induced acoustic streaming in a system to enhance the uptake of the substances from the aquatic medium into the skin of fish in 2001. Four distinct streaming flow patterns around the modelled fish were observed from their PIV measurements.

Loh et al.[128] used PIV techniques to experimentally investigate the acoustic streaming field induced by a cylindrical ultrasonic vibrator in open boundaries between the vibrating surface and air. Both the streaming patterns and the velocity field were presented. Clear symmetric steady rotational flow was observed in the gap between the ultrasonic vibrator and the glass plate.

Nabavi et al. [129-133] conducted a series of experiments to measure the acoustic streaming velocities using PIV techniques. Nabavi et al.[129] developed a novel approach using the synchronized PIV technique to simultaneously measure 2D acoustic and streaming velocity fields at any location along the standing wave resonator in 2007. Before this investigation, as illustrated by the authors, only one experiment conducted by Thompson et al.[117], which has been discussed above, simultaneously measured the acoustic and streaming velocities at different locations along a resonator.

However, LDA that Thompson et al. used in their experiments is a point-measurement technique, which means that it measures velocity at one spatial location at a time and is unable to simultaneously map the flow in a 2D region. An experiment was conducted by Nabavi et al. [132] in 2008 in order to investigate the formation process of acoustic streaming in a rectangular enclosure. The streaming velocity fields generated by a standing wave in an air-filled resonator were measured by the use of PIV. The results showed that the formation of acoustic streaming depends on the driven frequency and vibrational displacement of the acoustic driver. Later, the influence of transverse temperature gradient on the acoustic streaming velocity fields in a standing wave resonator was experimentally investigated by Nabavi et al.[130, 131]. The same to the previous experiments, the synchronized PIV technique was used to measure the streaming velocity fields. They found that the symmetric streaming vortices about the channel's centreline were deformed by the temperature difference between the top and bottom walls and the amplitude of streaming velocity increases as the temperature difference increases. The formation of regular and irregular acoustic streaming patterns induced by a standing wave generated in an air-filled rectangular chamber was experimentally investigated by Nabavi et al.[133] using synchronized PIV technique in 2009. The experiment minimized the effects of temperature gradient on acoustic streaming by putting the resonator inside a larger water tank to maintain isothermal boundary conditions at the channel walls. The results showed that the formation of regular and irregular streaming patterns was determined by the streaming Re. For $Re < 50$, regular streaming patterns were established and then deform to irregular and complex shapes when $Re$ exceeds 50.

Rabenjafimanantsoa et al.[134] described a method for determining the streaming effect in a Non-Newtonian viscous fluid medium, water-Polyanionic Cellulose solution in 2009. PIV techniques were used for visualization and quantification of the acoustic streaming field. They found that the maximum velocity along the transducer beam is in the axial position and the magnitude of the streaming velocity depends on the applied transducer voltage and viscosity.

The acoustic streaming field and heating generated by a high intensity acoustic horn in a thermo-viscous fluid was experimentally investigated by Layman et al.

[135] using synchronized PIV and infrared thermography in 2011. The streaming flow fields in the plane perpendicular to the surface of an acoustic horn were measured by a synchronized PIV system both in degassed water and in a glycerine-water mixture. The correlation between flow and temperature fields without cavitation was explored, which, as illustrated by the author, should be helpful for reactor design optimization.

The synchronized technique of PIV and infrared thermography was further studied by Sou et al.[136] to explore the subsurface coherent structures from acoustic streaming in a rectangular tank with an acoustic horn mounted horizontally at the side wall. The formation and propagation of a vortex pair along the acoustic horn axis was observed using the PIV method.

Barnkob et al. [48] measured the acoustophoretic motion of microparticles over a wide range of sizes in a microchannel with PIV, where the acoustic radiation- and acoustic streaming-dominated motions were demonstrated. The ratio between the acoustic radiation- and streaming-induced particle velocities were analysed analytically and validated experimentally, and was found to be proportional to the actuation frequency, the acoustic contrast factor, the square of the particle size and inversely proportional to the kinematic viscosity.

Reyt et al. [137] measured the acoustic streaming patterns in a cylindrical waveguide for high streaming Re with a combination of PIV and LDV. The standing wave field was generated by two loudspeakers with one at each end of the tube. The measured acoustic streaming field compared well with the classical theories for small Re but significant deviations were found for high Re. It was found that, with the increase of streaming Re, the outer streaming cells were distorted towards the acoustic velocity nodes until additional counter-rotating vortices were generated near the acoustic velocity antinodes, which was consistent with their experimental and numerical investigations conducted earlier.[138]

Unlike LDA which only provides information about a point in the flow, PIV produces 2D or even 3D vector fields. With the increasing power of computers and widespread use of CCD cameras, digital PIV has increasingly been used and to the point today it totally dominates. Measurements of particle movement in this research were implemented through the PIV method.

### 1.2.5. Numerical Simulations of Boundary-driven Streaming

Numerical simulation of acoustic streaming, compared to its analytical solutions and experimental investigations, is relatively scarce. Developments in computer power and software in the last decade have led to an increasing number of numerical simulations of acoustic streaming and acoustophoretic motion of microparticles within acoustofluidic systems, which can provide predictions of ultrasonic particle manipulation in microfluidic systems that agree reasonably well with experimental observations and thus begin to offer a powerful tool for acoustofluidic system design.

Kawahashi and Arakawa[139] used a similar calculation model to study the acoustic streaming in a standing wave in an air-filled closed duct by applying a fourth-order spatial difference method in 1996. The standing wave field in a 2D duct closed at one end is induced by air oscillation, which is driven by finite-amplitude oscillation of a piston at the other end, shown in *Figure 1.10*. Velocity distribution in the oscillatory boundary layer and the steady streaming structures were calculated for various amplitudes of oscillation. The results showed that the structure of calculated acoustic streaming changes with the amplitude of oscillation. When the amplitude of oscillation increases, the circulatory streaming predicted theoretically occurs and develops and is then distorted to a complex structure. The existence of a double boundary layer streaming structure in the vicinity of the duct wall was also presented.

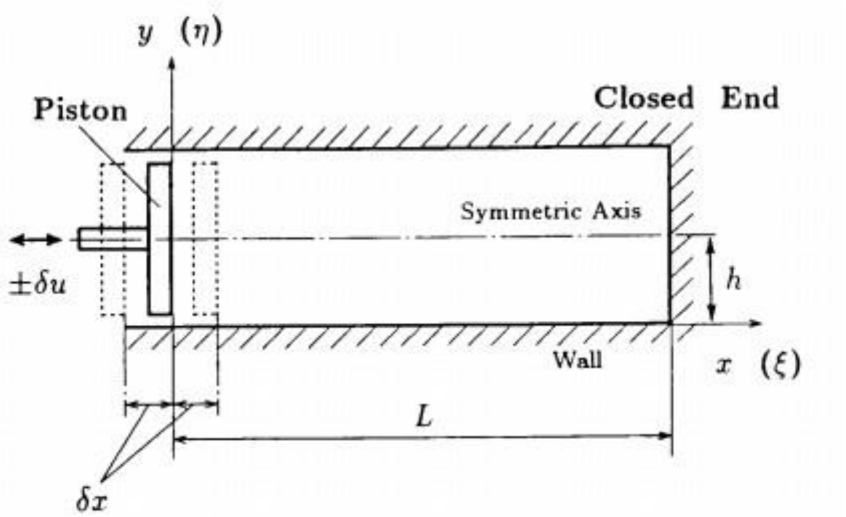

Figure 1.10 Schematic of the calculation model presented by Kawahashi and Arakawa[139].

Stansell and Greated[140] numerically investigated the acoustic streaming field generated by a standing wave between two parallel plates using a lattice gas approach in 1997. Both the inner streaming and outer streaming were modelled and compared with Rayleigh's analytical solution, which shows fairly good agreement except the velocity distribution in the boundary layer. The evident discrepancy between the model results and Rayleigh's analytical solution is acceptable as the theory makes the approximation that the boundary layer thickness is much smaller than the channel height and Rayleigh's solution counts only the streaming patterns outside the boundary layer.

A numerical model, shown in ***Figure 1.11***, similar to Kawahashi and Arakawa's, was considered by Yano[141] in 1999. The turbulent acoustic streaming excited by gas oscillation with periodic shock waves in a 2D rectangular closed tube was studied. The 2D Navier-Stokes equations were directly solved without introducing further assumptions. It was found that shock waves are formed and the resonant gas oscillation attains a quasi-steady state when the acoustic Mach number $M \ll 1$. The magnitude of the resulting acoustic streaming velocity is found in the same order with $M$ as well as the piston velocity at the sound source.

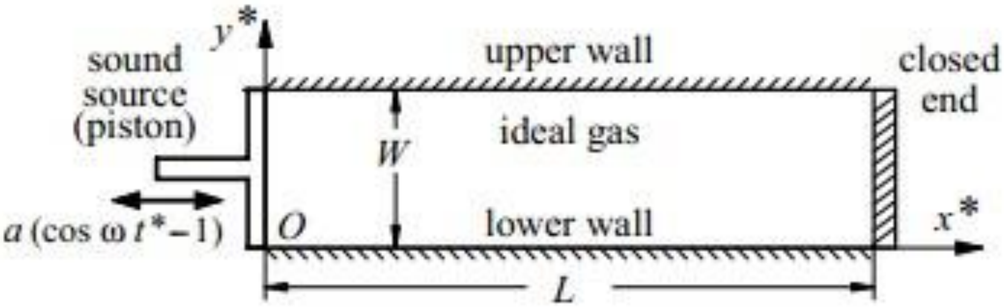

Figure 1.11 Schematic of the calculation model presented by Yano[141].

Haydock and Yeomans[142] used a Lattice Boltzmann model to model the acoustic streaming produced by the interaction of an acoustic wave with a boundary in 2001. Both the streaming patterns around a cylinder and between two plates of finite length were presented and compared to the analytical solutions. It was shown that the modelled streaming velocities both inside and outside the boundary layer compares well with the theoretical results in large chambers but are significantly lower than that predicted by the theory when the channel width is close to a wavelength. Later, Haydock and Yeomans[143] proved that lattice Boltzmann simulations can also be used to model attenuation-driven acoustic streaming. In that work, the streaming field around a porous material in an attenuating acoustic field was modelled. These simulations, as pointed out by the authors, can be useful in understanding the acoustic enhancement of rate limiting processes such as diffusion, heat transfer, sonochemical reactions or mixing.

Rednikov and Riley[144] provided numerical and analytical solutions for the streaming flows on suspended particles within acoustic levitators, which had already been observed by Trinh and Robey[113] in their experiments. The results showed that the numerical and analytical simulations and the observed flow patterns are entirely consistent in both isothermal and nonisothermal situations.

Aktas and Farouk[145] numerically investigated the acoustic streaming in the standing wave field induced in a compressible gas-filled 2D rectangular enclosure. The standing wave field in the enclosure is generated due to the harmonic oscillation of the left wall, shown in ***Figure 1.12***. They directly solved the compressible Navier-Stokes equations using a control-volume-based finite-volume method based on the flux-corrected transport algorithm. Both the inner and outer acoustic streaming patterns were simulated and compared to the analytical solutions. The effects of the sound field intensity on the streaming structures are also numerically investigated in his study. They found that the streaming patterns (regular or irregular) were determined by the wall vibration amplitude and the width of the channel. Later on, the effects of a transvers temperature gradient on the formation of regular and irregular streaming patterns in the same device (***Figure 1.12***) was numerically investigated by Aktas and Ozgumus.[146] The vertical walls of the chamber were considered adiabatic whereas the horizontal walls were heated differentially or symmetrically to obtain the temperature gradient. As before, the full Navier-Stokes equations were solved using a flux-corrected transport scheme. It was shown that acoustic streaming velocities and patterns in such a device were strongly influenced by the transverse temperature gradient. The regular (symmetric) streaming patterns were distorted by temperature difference between the top and bottom walls, which was consistent with Navabi et al.[131]'s experimental results. They also found that the streaming velocities significantly increased with the increase of temperature and the heat transfer from the bottom wall, which, is enhanced by the acoustic streaming flows, is maximized at regions where the streaming velocities move towards the wall.

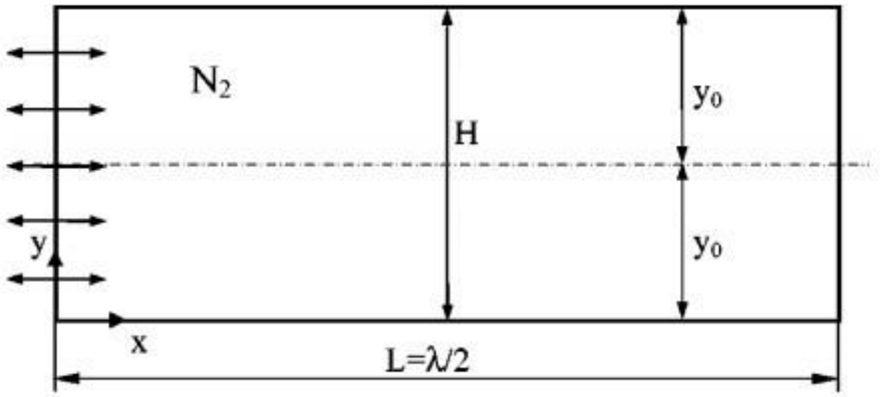

Figure 1.12 Schematic of the calculation model 3[145]

Sastrapradja and Sparrow[147] numerically simulated the classical Rayleigh streaming field in a cylindrical tube in 2006. The governing equations used are the vorticity equation, Poisson's equation, and an equation that relates the stream function with the velocity. The numerical results were compared with the analytical solutions, which agreed fairly well. It is shown that this method requires shorter computing time compared to previous simulations and it can be done on a single computer. The authors also suggested that this method is a valid method to be used as a tool in thermoacoustic design.

Recently, several investigations focusing on numerical simulation of nonlinear acoustic streaming patterns in standing wave fields have been presented. Feng et al.[148] studied the acoustic streaming motion in a compressible air-filled 2D cylindrical resonator using the gas-kinetic scheme. The standing wave was generated by the oscillation of a piston at one end of the cylinder. Five cases with different excitation amplitudes ranging from linear to nonlinear regions were considered and numerically investigated. It was found that the simulated streaming pattern compares well with classical theories when the driving amplitude is small, but shock waves are formed and irregular streaming structures are generated while the driving amplitude increases to a certain value. Moreover, the critical streaming Re for the transition to turbulence was numerical found at about 280 for their case, which is close to the previous experimental findings. However, only the outer streaming field was presented. Daru et al.[149] modelled the nonlinear acoustic streaming fields in closed 2D channels for high intensity standing waves using high order finite differential schemes. Both the streaming inside and outside the acoustic boundary layer were characterised. It was found that, with the increase of acoustic Re, streaming cells can be significantly distorted with the centres of streaming cells pushed toward the end-walls (acoustic velocity node). The numerical simulations, which demonstrate the transition from regular acoustic streaming patterns to irregular patterns, were shown to be in agreement with previous experiments. Later on, Reyt et al.[138] modelled the nonlinear Rayleigh streaming in a cylindrical acoustic standing waveguide with Re ranging from 1 to 30 considered. The compressible Navier-Stokes equations were solved from the high resolution finite difference schemes. It was found that, same to the previous findings, the streaming cell centres were pushed to the acoustic velocity nodes as the Re increases. Moreover, it was also shown that additional outer cells were formed for Re larger than about 30, which can also be observed from Daru et al.'s research[149].

## 1.3. Outline of This Thesis and Novel Contributions

The remaining chapters of this thesis are organized as follows.

In ***Chapter 2***, the fundamental equations for the acoustic streaming theory are introduced. Two numerical methods are proposed for the simulation of 2D and 3D boundary-driven streaming fields in acoustofluidic systems.

In ***Chapter 3***, classical boundary-driven streaming patterns in 1D standing wave fields in 2D rectangular chambers are numerically studied using two numerical methods. The formation mechanism of classical boundary-driven streaming is proposed.

In ***Chapter 4***, “four-quadrant transducer plane streaming” in layered acoustofluidic particle manipulation devices with circulations parallel to the transducer radiating surface is thoroughly studied using both numerical and experimental methods. The driving mechanism of this new boundary-driven streaming pattern is proposed.

In ***Chapter 5***, 3D boundary-driven streaming fields in acoustofluidic systems are thoroughly investigated from simulations of full configurations of acoustofluidic manipulation devices. The 3D nature of Rayleigh streaming in rectangular channels is presented and the driving mechanism of an unusual transducer plane streaming pattern due to 2D standing waves is proposed.

In ***Chapter 6***, 3D boundary-driven streaming patterns in layered acoustofluidic manipulation devices with various cross-sections on the fluid channels are numerically studied and experimentally validated. A new boundary-driven streaming pattern, “modal Rayleigh-like streaming”, is proposed.

In ***Chapter 7***, the effects of surface profile on the acoustic and boundary-driven streaming fields are numerically investigated. A new boundary-driven streaming pattern is proposed.

Conclusions and future work are summarised in ***Chapter 8***.

# Chapter 2. Underlying Equations and Numerical Methods for Boundary-driven Streaming in Acoustofluidic Systems

## 2.1. Introduction

Acoustic streaming is a nonlinear effect and a steady, time-averaged flow current driven by the absorption of high amplitude acoustic oscillations in a fluid. Various acoustic streaming patterns have been analysed in acoustofluidic devices due to different mechanisms of energy attenuation, most notably Eckart streaming[72] and boundary-driven streaming. The former is generated due to the energy dissipation in the bulk of a fluid while the latter is formed from the decay of acoustic energy due to the presence of the viscous boundary layer[106]. It is the dissipation of acoustic energy which creates gradients in momentum flux that force acoustic streaming motions. This gradient of momentum flux is usually known as the Reynolds stress force (RSF)[69].

Generally speaking, these two acoustic streaming patterns co-exist in a single fluid channel and which one dominates is dependent on the dimension of the fluid channel (compared to the acoustic wavelength). In most bulk acoustofluidic manipulation devices working in standing wave fields of interest, the acoustic streaming fields are generally dominated by boundary-driven streaming as the Eckart type streaming generally needs longer distances to allow acoustic attenuation in the bulk of the fluid. This thesis investigates boundary-driven streaming patterns in acoustofluidic systems in order to understand the driving mechanisms of the unusual acoustic streaming patterns observed in acoustofluidic manipulation devices, thus providing effective advice for the design of acoustofluidic manipulation devices on utilising or suppressing the acoustic streaming effects.

In this chapter, two numerical methods are introduced for the simulation of boundary-driven streaming in acoustofluidic systems. Fluid dynamic equations, including the continuity and momentum equations for both compressible and incompressible fluid, are firstly presented in Section *2.2*, followed by the two numerical methods. A brief conclusion is drawn in Section *2.3*.

## 2.2. Acoustic Streaming Models

In this thesis, bold and normal-emphasis fonts are used to represent the vector and scalar quantities, respectively.

Before describing the two numerical methods, the fundamental governing equations of acoustic streaming theory are introduced. Here, a homogeneous isotropic fluid is assumed, in which the continuity and momentum equations for the fluid motion are

$$\frac{\partial \rho}{\partial t} + \nabla \cdot (\rho \boldsymbol{u}) = 0, \tag{2.1a}$$

$$\rho\left(\frac{\partial \boldsymbol{u}}{\partial t} + \boldsymbol{u} \cdot \nabla \boldsymbol{u}\right) = -\nabla p + \mu \nabla^2 \boldsymbol{u} + \left(\mu_b + \frac{1}{3}\mu\right) \nabla\nabla \cdot \boldsymbol{u}, \tag{2.1b}$$

where $\rho$ is the fluid density, $t$ is time, $\boldsymbol{u}$ is the fluid velocity, $p$ is the pressure, and $\mu$ and $\mu_b$ are respectively the dynamic and bulk viscosity coefficients of the fluid. It is worth considering the meaning of each term in Equation *(2.1b)*. The left-hand-side represents the inertia force per unit volume on the fluid and the two terms in the bracket are the unsteady acceleration and convective acceleration of a fluid particle, respectively. The right-hand-side indicates the divergence of stress, including the pressure gradient and the viscosity force. Other forces, such as the gravity force, are not shown as they are generally negligible compared to the forces presented.

The two numerical methods introduced in this chapter are based on the perturbation theory, which assumes that the second-order acoustic streaming is superposed on the first-order acoustic velocity field. Following this theory, the fluid density, pressure, and velocity can respectively be expressed as:

$$\rho = \rho_0 + \rho_1 + \rho_2 + \cdots, \tag{2.2a}$$

$$p = p_0 + p_1 + p_2 + \cdots, \tag{2.2b}$$

$$\boldsymbol{u} = \boldsymbol{u_1} + \boldsymbol{u_2} + \cdots, \tag{2.2c}$$

where the subscripts 0, 1 and 2 represent the static (absence of sound), first-order and second-order quantities, respectively.

Substituting Equations *(2.2)* into Equations *(2.1)* and considering the equations to the first-order, Equations *(2.1)* for solving the first-order acoustic velocity take the form,

$$\frac{\partial \rho_1}{\partial t} + \rho_0 \nabla \cdot \boldsymbol{u_1} = 0, \tag{2.3a}$$

$$\rho_0 \frac{\partial \boldsymbol{u_1}}{\partial t} = -\nabla p_1 + \mu \nabla^2 \boldsymbol{u_1} + \left(\mu_b + \frac{1}{3}\mu\right) \nabla\nabla \cdot \boldsymbol{u_1}. \tag{2.3b}$$

Repeating the above procedure, considering the equations to the second-order and taking the time average of Equations *(2.1)* using Equations *(2.2)*, the continuity and momentum equations for solving the second-order time-averaged acoustic streaming velocity can be turned into

$$\frac{\partial \overline{\rho_2}}{\partial t} + \nabla \cdot \overline{\rho_1 \boldsymbol{u_1}} + \rho_0 \nabla \cdot \boldsymbol{u_2} = 0, \tag{2.4a}$$

$$\rho_0 \overline{\boldsymbol{u_1} \nabla \cdot \boldsymbol{u_1} + \boldsymbol{u_1} \cdot \nabla \boldsymbol{u_1}} = -\nabla p_2 + \mu \nabla^2 \boldsymbol{u_2} + \left(\mu_b + \frac{1}{3}\mu\right) \nabla\nabla \cdot \boldsymbol{u_2}. \tag{2.4b}$$

Here, the upper bar means a time-averaged value. In these equations and hereafter, $p_2$ and $\boldsymbol{u_2}$ are used to represent the time-averaged second-order pressure and velocity, $\overline{p_2}$ and $\overline{\boldsymbol{u_2}}$, respectively. Specifically, the streaming problem in most practical bulk acoustofluidic manipulation devices can be approximated as incompressible as liquid (e.g. water) is usually utilised as a fluid medium. Moreover, the inertial force on the fluid is generally negligible compared to the viscosity force in such systems, which results in the creeping motion. With these approximations, Equation *(2.4)* can be written as

$$\nabla \cdot \boldsymbol{u_2} = 0, \tag{2.5a}$$

$$\nabla p_2 = \mu \nabla^2 \boldsymbol{u_2} + \boldsymbol{F}, \tag{2.5b}$$

where $\boldsymbol{F} = -\rho_0 \overline{\boldsymbol{u_1} \nabla \cdot \boldsymbol{u_1} + \boldsymbol{u_1} \cdot \nabla \boldsymbol{u_1}}$ is the Reynolds stress force.

### 2.2.1. The Reynolds Stress Method (RSM)

Acoustic streaming is a steady current or motion in a fluid driven by the absorption of high amplitude acoustic oscillations and forced by the action of Reynolds stress. As can be seen from Equation *(2.5b)*, in most practical bulk acoustofluidic manipulation devices, there are two main force terms in the momentum equation, $\nabla p_2$ and $\boldsymbol{F}$, respectively. However, as the pressure gradients are irrotational, $\nabla \times \nabla p_2 \equiv 0$, taking the curl of Equation *(2.5b)*, the following equation is established

$$\mu \nabla^2 (\nabla \times \boldsymbol{u_2}) = -\nabla \times \boldsymbol{F}. \tag{2.6}$$

It can be seen that the acoustic streaming velocity, $\boldsymbol{u_2}$, can be solved as long as the distribution of rotational RSF field is known. In order words, in both 2D and 3D models, it can be established whether acoustic streaming vortices can be generated in a plane from the rotationality of the RSF field in that plane.

The first method presented here solves the boundary-driven acoustic streaming directly from its driving force, the RSF, so is referred to as the RSM. In 3D Cartesian coordinates $(x, y, z)$, the three components of the RSF vector $\boldsymbol{F}$, ($F_x$, $F_y$, $F_z$), can be expressed as[69]

$$F_x = -\rho_0 \left( \frac{d\overline{u_1^2}}{dx} + \frac{d\overline{u_1 v_1}}{dy} + \frac{d\overline{u_1 w_1}}{dz} \right), \tag{2.7a}$$

$$F_y = -\rho_0 \left( \frac{d\overline{u_1 v_1}}{dx} + \frac{d\overline{v_1^2}}{dy} + \frac{d\overline{v_1 w_1}}{dz} \right), \tag{2.7b}$$

$$F_z = -\rho_0 \left( \frac{d\overline{u_1 w_1}}{dx} + \frac{d\overline{v_1 w_1}}{dy} + \frac{d\overline{w_1^2}}{dz} \right), \tag{2.7c}$$

where $u_1$, $v_1$ and $w_1$ are the three components of acoustic velocity vector $\boldsymbol{u_1}$ along coordinates $x$, $y$ and $z$, respectively.

Firstly, let us demonstrate mathematically why the RSF in a non-viscous fluid cannot generate acoustic streaming vortices from the rotationality of $\boldsymbol{F}$,

$$\nabla \times \boldsymbol{F} = \left( \frac{dF_z}{dy} - \frac{dF_y}{dz} \right) \boldsymbol{i} + \left( \frac{dF_x}{dz} - \frac{dF_z}{dx} \right) \boldsymbol{j} + \left( \frac{dF_y}{dx} - \frac{dF_x}{dy} \right) \boldsymbol{k}, \tag{2.8}$$

where $\boldsymbol{i}$, $\boldsymbol{j}$ and $\boldsymbol{k}$ are the unit vectors along coordinates $x$, $y$ and $z$, respectively. To start with, the $x$-component of Equation *(2.8)* can be expanded to

$$\begin{aligned}\frac{dF_z}{dy}-\frac{dF_y}{dz}=-\frac{\rho_0}{2}\Bigg[&\left(2w_1\frac{d^2w_1}{dydz}+2\frac{dw_1}{dy}\frac{dw_1}{dz}+2\frac{du_1}{dy}\frac{dw_1}{dx}+u_1\frac{d^2w_1}{dxdy}\right.\\&\left.+w_1\frac{d^2u_1}{dxdy}+2\frac{dv_1}{dy}\frac{dw_1}{dy}+v_1\frac{d^2w_1}{dy^2}+w_1\frac{d^2v_1}{dy^2}\right)\\&-\left(2\frac{dv_1}{dz}\frac{dv_1}{dy}+2v_1\frac{d^2v_1}{dydz}+2\frac{du_1}{dz}\frac{dv_1}{dx}+u_1\frac{d^2v_1}{dxdz}\right.\\&\left.+v_1\frac{d^2u_1}{dxdz}+2\frac{dv_1}{dz}\frac{dw_1}{dz}+v_1\frac{d^2w_1}{dz^2}+w_1\frac{d^2v_1}{dz^2}\right)\Bigg].\end{aligned} \tag{2.9}$$

In a lossless fluid, the acoustic field is irrotational, such that

$$\nabla\times\boldsymbol{u_1}=\left(\frac{dw_1}{dy}-\frac{dv_1}{dz}\right)\boldsymbol{i}+\left(\frac{du_1}{dz}-\frac{dw_1}{dx}\right)\boldsymbol{j}+\left(\frac{dv_1}{dx}-\frac{du_1}{dy}\right)\boldsymbol{k}=0. \tag{2.10}$$

Therefore, Equation *(2.9)* can be simplified to

$$\frac{dF_z}{dy}-\frac{dF_y}{dz}=-\frac{\rho_0}{2}(w_1\nabla^2v_1-v_1\nabla^2w_1). \tag{2.11}$$

Moreover, based on the 3D acoustic wave equation,

$$\nabla^2\boldsymbol{u_1}-\frac{1}{c^2}\frac{\partial^2\boldsymbol{u_1}}{\partial t^2}=0, \tag{2.12}$$

where $c$ is the sound speed in the fluid, the following relationships establish

$$\nabla^2v_1=\frac{\omega^2}{c^2}v_1 \text{ and } \nabla^2w_1=\frac{\omega^2}{c^2}w_1. \tag{2.13}$$

Substituting it into Equation *(2.11)*, the equation can be turned into

$$\frac{dF_z}{dy}-\frac{dF_y}{dz}=0. \tag{2.14}$$

Similarly, the other two terms in the right-hand-side of Equation *(2.8)* also respectively equal to zero such that its left hand side has

$$\nabla\times\boldsymbol{F}=\boldsymbol{0}. \tag{2.15}$$

Hence the 3D RSF field is irrotational in a lossless fluid, which cannot generate acoustic streaming vortices.

Therefore, for the main topic of this thesis – boundary-driven streaming, it can be concluded that it is the energy loss within the viscous boundary layer producing rotational RSF terms that generates acoustic streaming vortices in that thin layer (normally referred to as inner streaming). The streaming velocity at the edge of the inner streaming vortices (the LV shown in Section *2.2.2*) in the viscous boundary layer region can then induce large streaming vortices in the bulk of the fluid (referred to as outer streaming). The boundary-driven streaming both inside and outside the viscous boundary layer can be modelled provided that the distribution of RSF within the viscous boundary layer is known.

To conclude, the whole procedure of the RSM for solving the boundary-driven streaming fields in acoustofluidic systems can be split into three steps: 1) the acoustic velocity fields including those within and without the viscous boundary layer region are solved; 2) the RSF field can be calculated from Equations *(2.7)*; 3) the acoustic streaming fields are solved from the momentum Equation *(2.5)* with the RSF working as a body force per unit volume on the fluid.

### 2.2.2. The Limiting Velocity Method (LVM)

The RSM described in the previous section can be used to effectively predict the boundary-driven streaming fields in 2D models but not in 3D models due to that the need for tiny mesh elements in the viscous boundary layer to resolve the acoustic velocity field in that region. Large numbers of mesh elements require computers with a high specification and require a long simulation time. Reducing a 3D model to a series of 2D investigations requires a-priori knowledge of the streaming structure that is not typically available. In reality, acoustic streaming fields have 3D characteristics and it will be shown later in this thesis that in some cases the acoustic streaming fields cannot be simplified to 2D problems. Therefore, alternative ways should be explored to predict the boundary-driven streaming fields in 3D models.

Here, a LVM is introduced. Unlike the RSM, in which nonslip boundary conditions are commonly considered in order to solve the acoustic and streaming fields in the viscous boundary layer region, this method only solves the streaming fields outside the boundary layer by implying a slip velocity on the boundary and ignores the streaming patterns inside the boundary layer which is acceptable as the influence of inner streaming is usually negligible in large chambers ($h \gg \delta_v$), where, as will be shown later, the thickness of the inner streaming vortex is only approximately $\delta_v$. In other words, in most real acoustofluidic manipulation devices, only the acoustic streaming patterns in the bulk of the fluid channel are of interest.

Rayleigh[49] was the first researcher to present the LV equation for 2D models. In that paper, it was demonstrated that the limiting streaming velocity immediately outside the viscous boundary layer can be approximated as a function of the irrotational first-order acoustic velocity field. Nyborg[78] later derived the LV equations for 3D problems. Nyborg's analysis is based on the basic Equations *(2.5)*.

In Nyborg's analyses, the near-boundary streaming was studied by considering the streaming near a given point P in the vicinity of surface S, shown in ***Figure 2.1***. Let $(x_1, x_2, x_3)$ be an orthogonal coordinate system used to define the position of point P. $x_1$ and $x_2$ indicate the projection of point P on the surface S and $x_3$ is the normal distance of P above the surface S. It is more convenient to use another coordinate system $(x, y, z)$ in order to make the results fit the geometry of the surface. The transformation can be expressed as $dx_1 = h_x dx, dx_2 = h_y dy, dx_3 = h_z dz$.

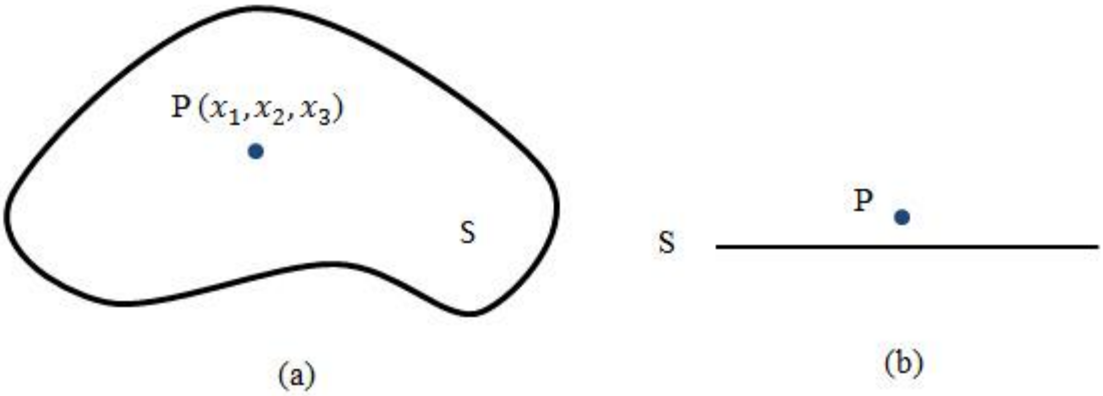

Figure 2.1 Schematic of the problem: (a) top view; (b) side view

The whole process of solving the acoustic streaming fields can be divided into three steps. Firstly, the approximate solution for the first-order acoustic velocity field is obtained (only the real parts):

$$u_1 = u_0[\cos \omega t - e^{-\beta z} \cos(\omega t - \beta z)], \tag{2.16a}$$

$$v_1 = v_0[\cos \omega t - e^{-\beta z} \cos(\omega t - \beta z)], \tag{2.16b}$$

$$w_1 = w_0 \cos \omega t + \frac{\gamma}{\sqrt{2}\beta}\left[\cos(\omega t - \frac{\pi}{4}) - e^{-\beta z} \cos\left(\omega t - \beta z - \frac{\pi}{4}\right)\right], \tag{2.16c}$$

where $u_0$, $v_0$ and $w_0$ are respectively the three components of the irrotational acoustic velocity vector $\boldsymbol{u_0}$ ($\boldsymbol{u_{a0}}$ in [78]), $\beta = 1/\delta_v$, and $\gamma = \partial(h_y u_0)/\partial x + \partial(h_x v_0)/\partial y$. In Nyborg's analyses[78], three steps were used to solve successively the irrotational particle velocity, $\boldsymbol{u_0}$, the velocity due to viscosity, $\boldsymbol{u_b}$ and the wall dependent velocity, $\boldsymbol{u_c}$. The total acoustic velocity vector, $\boldsymbol{u_1}$ was then given by the sum $(\boldsymbol{u_0} + \boldsymbol{u_b} + \boldsymbol{u_c})$, which is an approximate solution of the governing equation for oscillatory flow in a viscous medium and satisfies the prescribed boundary conditions, $\boldsymbol{u_1} = 0$.

Then, inserting acoustic velocity equations above into Equation *(2.5b)*, the force components, $(F_x, F_y)$, can be determined:

$$F_x = -\frac{\rho_0}{2}\left(q_x N_\alpha + u_0\left(\frac{\partial w_{a0}}{\partial z} N_\beta + (\nabla \cdot \boldsymbol{u}_0) N_\gamma - \frac{\partial(h_x h_y)}{\partial z} w_1 N_\delta\right)\right), \tag{2.17a}$$

$$F_y = -\frac{\rho_0}{2}\left(q_y N_\alpha + v_0\left(\frac{\partial w_0}{\partial z} N_\beta + (\nabla \cdot \boldsymbol{u}_0) N_\gamma - \frac{\partial(h_x h_y)}{\partial z} w_1 N_\delta\right)\right), \tag{2.17b}$$

where

$$\begin{gathered} q_x = u_0 \frac{\partial u_0}{\partial x} + v_0 \frac{\partial u_0}{\partial y}, \\ q_y = u_0 \frac{\partial v_0}{\partial x} + v_0 \frac{\partial v_0}{\partial y}, \\ N_\alpha = e^{-2n} - 2e^{-n} \cos n, \\ N_\beta = n e^{-n}(\cos n + \sin n) - e^{-n} \sin n, \\ N_\gamma = e^{-n}(\sin n - \cos n), \\ N_\delta = e^{-n} \sin n, \\ n = \beta z. \end{gathered} \tag{2.18}$$

Finally, the streaming velocities can be solved from Equation *(2.5a)*:

$$u_2 = -\frac{1}{\omega}\left(q_x u_\alpha + u_0\left(\frac{\partial w_0}{\partial z} u_\beta + (\nabla \cdot \boldsymbol{u}_0) u_\gamma - \frac{\partial(h_x h_y)}{\partial z} w_0 u_\delta\right)\right), \tag{2.19a}$$

$$v_2 = -\frac{1}{\omega}\left(q_y u_\alpha + v_0\left(\frac{\partial w_0}{\partial z} u_\beta + (\nabla \cdot \boldsymbol{u}_0) u_\gamma - \frac{\partial(h_x h_y)}{\partial z} w_0 u_\delta\right)\right), \tag{2.19b}$$

where

$$\begin{gathered}u_\alpha = \frac{1}{4}e^{-2n} + e^{-n}\sin n - \frac{1}{4},\\ u_\beta = \frac{1}{2}ne^{-n}(\cos n - \sin n) - e^{-n}\sin n - \frac{1}{2}e^{-n}\cos n + \frac{1}{2},\\ u_\gamma = \frac{1}{2}e^{-n}(\sin n + \cos n) - \frac{1}{2},\\ u_\delta = \frac{1}{2}(e^{-n}\cos n - 1).\end{gathered} \tag{2.20}$$

Letting $n$ be infinite[78], the LV equations can be obtained:

$$u_L = -\frac{1}{4\omega}\left(q_x + 2u_0\left(\nabla\cdot\boldsymbol{u}_0 - \frac{\partial w_0}{\partial z} - \frac{\partial(h_x h_y)}{\partial z}w_0\right)\right), \tag{2.21a}$$

$$v_L = -\frac{1}{4\omega}\left(q_y + 2v_0\left(\nabla\cdot\boldsymbol{u}_0 - \frac{\partial w_0}{\partial z} - \frac{\partial(h_x h_y)}{\partial z}w_0\right)\right). \tag{2.21b}$$

This method was modified by Lee and Wang[88] to a generalized version. Here I simply introduce the corrections they made in that paper, which is explained in more detail in reference[88].

In Nyborg's analysis[78], $h_z$ is equal to 1 and $h_x$ and $h_y$ are approximately equal to 1, which, as illustrated by Lee and Wang[88], is not true. For example, in spherical coordinates, $dx_1 = Rd\theta, dx_2 = R\sin\theta\, d\varphi$, and $dx_3 = dr$ such that $dx = d\theta, dy = d\varphi$, and $dz = dr$, and $h_x = R, h_y = R\sin\theta$, and $h_z = 1$. For a curvilinear coordinate system, as Lee and Wang illustrated, Nyborg neglected the fact that the basis vectors are also space dependent, which resulted in the missing of some terms in the final results. In addition to the terms in Equation *(2.18)*, two more geometry quantities were introduced:

$$\begin{gathered}T_{ijk} = e_i\cdot\frac{\partial e_j}{\partial x_k},\\ H = \frac{\partial(h_x h_y)}{(h_x h_y \partial z)},\end{gathered} \tag{2.22}$$

where each of the characters $i$, $j$, $k$ can be 1, 2 or 3 and $e_i$ is the unit vector associated with the coordinate $x_i$.

The acoustic velocity, which was taken to be real in Nyborg's analysis, was changed to be complex in order to fit the general situation. The second-order driving force $\boldsymbol{F}$ was split into two parts: $\boldsymbol{F_a}$, due purely to the inviscid acoustic motion and $\boldsymbol{F_b}$, considered to be due to the presence of the viscous boundary layer (the part that can generate acoustic streaming).

Considering the curvilinear corrections and the complex acoustic velocities, the terms in Equation *(2.18)* are turned into:

$$\begin{gathered}
n = \beta z, \\
q_x = u_0\left(\frac{\partial u_0^*}{\partial x_1} + v_0^* T_{121}\right) + v_0\left(\frac{\partial u_0^*}{\partial x_2} + v_{a0}^* T_{122}\right), \\
q_y = u_0\left(\frac{\partial v_0^*}{\partial x_1} + u_0^* T_{211}\right) + v_0\left(\frac{\partial v_0^*}{\partial x_2} + v_0^* T_{212}\right), \\
N_\alpha = e^{-2n} - 2e^{-n}\cos n, \\
N_\beta = ne^{-n}(\cos n + \sin n) - e^{-n}\sin n \\
+ i(-ne^{-n}(\sin n - \cos n) - e^{-n}\cos n + e^{-2n}), \\
N_\gamma = e^{-n}(\sin n - \cos n) + i(e^{-n}(\sin n + \cos n) - e^{-2n}), \\
N_\delta = e^{-n}\sin n + i(e^{-n}\cos n - e^{-2n})
\end{gathered} \tag{2.23}$$

Then, the driving force Equations *(2.17)* are solved:

$$F_{bx} = -\frac{\rho_0}{2} Re\left(q_x N_\alpha + u_0^*\left(\frac{\partial w_0}{\partial z} N_\beta + (\nabla \cdot \boldsymbol{u}_0) N_\gamma - H w_0 N_\delta\right)\right), \tag{2.24a}$$

$$F_{by} = -\frac{\rho_0}{2} Re\left(q_y N_\alpha + v_0^*\left(\frac{\partial w_0}{\partial z} N_\beta + (\nabla \cdot \boldsymbol{u}_0) N_\gamma - H w_0 N_\delta\right)\right),$$

where $F_{bx}$ and $F_{by}$ are the $x$ and $y$ components of $\boldsymbol{F_b}$ and $Re(\cdot)$ represents the real part of a complex value. The streaming velocities solved from Equation *(2.5a)* can be given by

$$u_2 = \frac{1}{\omega} Re\left(q_x u_\alpha + u_{a0}^*\left(\frac{\partial w_{a0}}{\partial z} u_\beta + (\nabla \cdot \boldsymbol{u}_{a0}) u_\gamma - H w_{a0} u_\delta\right)\right), \tag{2.25a}$$

$$v_2 = \frac{1}{\omega} Re\left(q_y u_\alpha + v_{a0}^*\left(\frac{\partial w_{a0}}{\partial z} u_\beta + (\nabla \cdot \boldsymbol{u}_{a0}) u_\gamma - H w_{a0} u_\delta\right)\right), \tag{2.25b}$$

Where

$$
\begin{aligned}
u_\alpha &= \frac{1}{4}e^{-2n} + e^{-n}\sin n - \frac{1}{4}, \\
u_\beta &= \frac{1}{2}ne^{-n}(\cos n - \sin n) - e^{-n}\sin n - \frac{1}{2}e^{-n}\cos n + \frac{1}{2} \\
&\quad + i\left(-\frac{1}{2}ne^{-n}(\cos n + \sin n) - e^{-n}\cos n + \frac{1}{2}e^{-n}\sin n \right. \\
&\quad \left. + \frac{1}{4}e^{-2n} + \frac{3}{4}\right), \\
u_\gamma &= \frac{1}{2}e^{-n}(\sin n + \cos n) - \frac{1}{2} + i\left(\frac{1}{2}e^{-n}(\cos n - \sin n) - \frac{1}{4}e^{-2n} - \frac{1}{4}\right), \\
u_\delta &= \frac{1}{2}(e^{-n}\cos n - 1) + i\left(-\frac{1}{2}e^{-n}\sin n - \frac{1}{4}e^{-2n} + \frac{1}{4}\right).
\end{aligned}
\tag{2.26}
$$

Finally, the limiting value of $u_2$ and $v_2$ can be expressed as

$$u_L = -\frac{1}{4\omega}Re\left[q_x + u_0^*\left((2+i)\nabla\cdot\boldsymbol{u_0} - (2+3i)\frac{\partial w_{a0}}{\partial z} - (2-i)Hw_0\right)\right], \tag{2.27a}$$

$$v_L = -\frac{1}{4\omega}Re\left[q_y + v_0^*\left((2+i)\nabla\cdot\boldsymbol{u_0} - (2+3i)\frac{\partial w_0}{\partial z} - (2-i)Hw_0\right)\right]. \tag{2.27b}$$

It is interesting to notice that the resulting streaming field is independent of fluid viscosity as the LV equations do not contain the viscosity coefficient even though viscosity is the initial cause of acoustic streaming fields.

Also of note is the fact that as the limiting velocity equations in a near-boundary region are, to a large extent, independent of boundary conditions far away from the boundary, they can be applied to solve the streaming pattern immediately outside the viscous boundary layer (the outer streaming) near any element of the surface where the local radius of curvature is much greater than $\delta_v$.[78]

## 2.3. Conclusions

In this chapter, the fundamental equations for solving the acoustic streaming fields based on the perturbation theory were described. Based on the fundamental equations, two numerical methods were introduced for the modelling of boundary-driven streaming fields in acoustofluidic manipulation systems.

On the basis of the characteristics of these two methods, their preferred scope of application can be defined. The RSM, which solves the boundary-driven streaming directly from its driving force, can be used to effectively predict the streaming fields both within and without the viscous boundary layer in 2D models. The LVM, which is more computationally efficient, can be applied to model both 2D and 3D outer streaming fields in practical acoustofluidic systems provided that the radius of curvature of the surface is much greater than the thickness of the viscous boundary layer.

In the following chapters, the viability and applicability of these two methods, which, will be firstly justified, will then be applied to solve a variety of problems in the following chapters.

# Chapter 3. Numerical Simulations of 2D Classical Boundary-driven Streaming in Acoustofluidic Systems

## 3.1. Introduction

The main topic of this thesis is the investigation of boundary-driven streaming fields in acoustofluidic systems in order to understand unusual streaming patterns observed in acoustofluidic manipulation devices. In ***Chapter 2***, two numerical methods, the RSM and LVM, have been introduced for the modelling of boundary-driven streaming fields in acoustofluidic manipulation devices. In order to verify their accuracy and applicability, in this chapter, they are applied to 2D rectangular chambers to solve the classical boundary-driven streaming fields, Rayleigh-Schlichting streaming[49, 50]. This is the most common type of acoustic streaming discussed in literature, and the modelled results can be compared to the corresponding analytical solutions (most previous analytical solutions are developed from Rayleigh's analytical solution and solve the Rayleigh-Schlichting streaming fields).

The simulations were performed in the commercial finite element analysis software, COMSOL 4.4[150]. Firstly, the RSM was used to explore the origin of these streaming flows — the net force on the fluid, aiming at investigating how these vortices are generated within acoustic standing wave fields. First-order acoustic pressure and velocity fields, net force distributions, and second-order streaming velocity distributions were presented. The modelled results were compared to Hamilton et al.'s analytical solutions[79] on acoustic streaming velocity fields both inside and outside the viscous boundary layer, which show good agreements. Then, the LVM was used to simulate the outer streaming fields in the bulk of the fluid. It was found that the modelled results show good consistence with Rayleigh's analytical solution[49] on the outer streaming field.

In Sections ***3.2*** and ***3.3***, numerical simulations of classical boundary-driven streaming from two methods are presented. Comparisons on the streaming velocities modelled from these two methods are then given in Section ***3.4*** in order to demonstrate the driving mechanism of classical boundary-driven streaming and the viability and applicability of these two methods. Overall conclusions are drawn in Section 3.5.

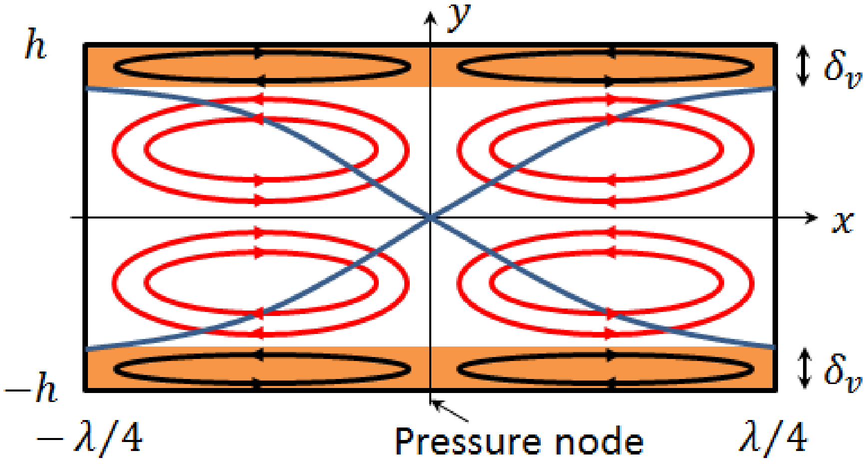

Figure 3.1 schematic presentation of the classical boundary-driven acoustic streaming patterns in a one-dimensional standing wave field, where $\lambda$ is the acoustic wavelength, $\delta_v$ is the thickness of the viscous boundary layer and the curves are the distribution of acoustic pressure magnitudes in the channel.

## 3.2. The Reynolds Stress Method

### 3.2.1. Model

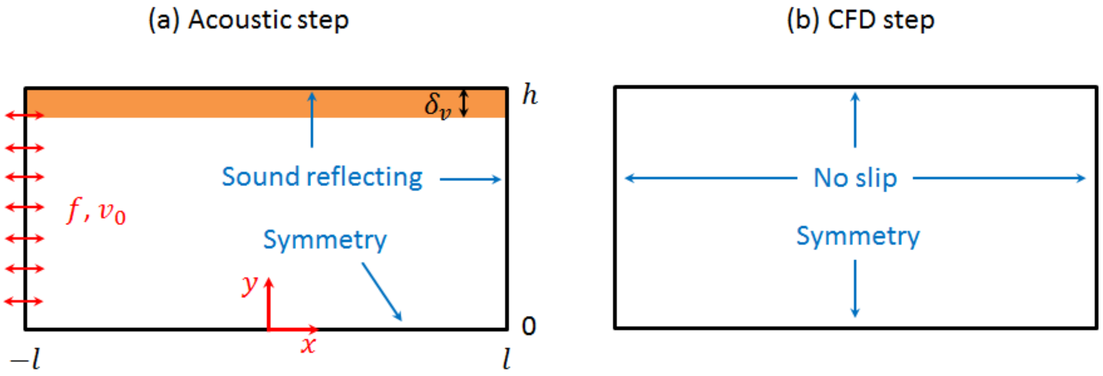

Figure 3.2 Boundary conditions for the two steps of the Reynolds stress method on the modelling of classical boundary-driven acoustic streaming fields in 2D rectangular chambers, where $\delta_v$ is the thickness of the orange viscous boundary layer (not to scale) and $f$ and $v_0$ are respectively the frequency and amplitude of the excitation.

Boundary-driven streaming originates from the dissipation of acoustic energy inside the thin viscous boundary layer, which results in non-zero time-averaged volume forces, namely RSF, on the fluid. In this section, classical boundary-driven streaming fields in 2D rectangular chambers were investigated using the RSM. The standing wave fields in the rectangular chambers were established by a harmonic vibration of the left walls with velocity amplitude of $v_0$ and a frequency of $f = 1$ MHz, shown in ***Figure 3.2*** (a). As the speed of sound in water, $c$, is approximately $1480$ m/s, the acoustic wavelength $\lambda = c/f \approx 1.48$ mm. Here, a series of fluid chambers, summarised in ***Table 3.1***, with chamber heights, $h$, ranging from $\delta_v$ to $250\delta_v$ were considered with chamber length $2l = 0.74$ mm. Therefore, for each case, a half-wavelength standing wave can be established in the $x$-direction of the chamber.

The numerical process is split into two steps, an acoustic step and a computational fluid dynamics (CFD) step. Firstly, the first-order acoustic pressure and velocity fields are solved, from which the RSF can be calculated. Then, the acoustic streaming fields are solved from the RSF which works as a body force per unit volume on the fluid.

Table 3.1 Parameters for 2D classical boundary-driven streaming simulations.

| Quantities | Abbreviation | Value | Unit |
|---|---|---|---|
| Frequency | $f$ | 1 | MHz |
| Density of water | $\rho_0$ | 998 | kg·m$^{-3}$ |
| Dynamic viscosity of water | $\mu$ | 0.893 | mPa·s |
| Bulk viscosity of water | $\mu_k$ | 2.47 | mPa·s |
| Viscous boundary layer | $\delta_v$ | 0.53 | μm |
| Speed of sound in water | $c$ | 1480 | m·s$^{-1}$ |
| Acoustic wavelength | $\lambda$ | 1.48 | mm |
| Channel dimensions | $2w \times h$ | $\lambda/2 \times 0{\sim}250\delta_v$ | mm$^2$ |

As the thickness of the viscous boundary layer is only a very small fraction of the acoustic wavelength, ultra-small mesh elements (size of ~0.01 μm here) should be used inside the viscous boundary layer to resolve the detailed acoustic velocity fields near the boundaries. The mesh conditions in the fluid chamber for the RSM are shown in *Figure 3.3*, where only a small portion of the chamber in the $x$-direction is presented as the aspect ratio of the chambers ($h/l$) considered are very small.

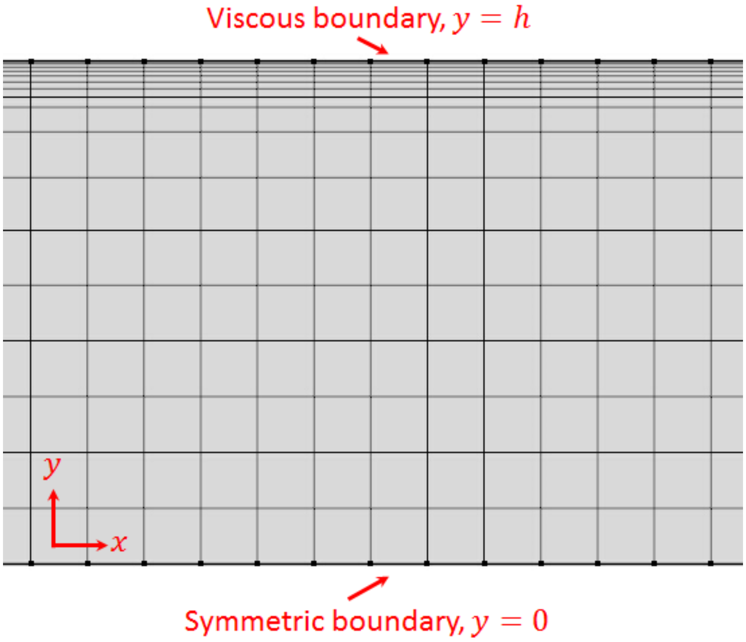

Figure 3.3 A portion of the mesh constitutions in a chamber ($h = 40\delta_v$).

### 3.2.2. Acoustic Pressure and Particle Velocity Fields

Firstly, a COMSOL '*Thermoacoustics, Frequency Domain*' interface was used to model the first-order acoustic pressure and particle velocity fields. The corresponding equations for the acoustic pressure, $p_1$, and the particle velocity, $\boldsymbol{u_1}$, are

$$\nabla^2 p_1 + \frac{\omega^2}{c^2} p_1 = 0, \tag{3.1a}$$

$$i\omega\rho_0 \boldsymbol{u_1} = -\nabla p_1 + \mu\nabla^2 \boldsymbol{u_1} - \left(\frac{2}{3}\mu - \mu_B\right)\nabla(\nabla \cdot \boldsymbol{u_1}), \tag{3.1b}$$

$$i\omega\rho + \rho_0 \nabla \cdot \boldsymbol{u_1} = 0, \tag{3.1c}$$

where $p_1$ is defined at position $r$ using the relation,

$$p_1(r,t) = Re\left[\, p_1(r) e^{i\omega t}\right], \tag{3.2}$$

and makes the assumptions[151] of small acoustic disturbances, an inviscid, Newtonian fluid, and adiabatic processes. The fluid was also assumed at rest so the streaming velocities must be small in comparison to the acoustic velocities. In this step, the boundary conditions were chosen as follows: the left wall was the velocity excitation, the bottom wall was symmetric boundary condition and the remaining walls were sound hard boundary conditions, which are shown in ***Figure 3.2*** (a).

Here, the model where $h = 40\delta_v$ was chosen as an example to show the distributions of dimensionless acoustic fields in the fluid channels. The modelled first-order acoustic pressure and velocity fields were shown in ***Figure 3.4***. It can be seen that a 1D half-wave standing wave was established in the $x$-direction of the chamber with pressure node staying at the centre ($x = 0$) and antinodes at the two ends ($x = \pm l$), ***Figure 3.4*** (a). The half-wave standing wave field can be seen more clearly in ***Figure 3.4*** (c) where the distribution of the acoustic pressure magnitudes along the $x$-direction of the chamber was plotted. ***Figure 3.4*** (b) plots the normalised acoustic velocity magnitudes in the chamber, from which the formation of the boundary layer near the top wall, $y = h$, can be seen. This acoustic boundary layer can be distinguished in more detail from the line plot shown in ***Figure 3.4*** (d), where the vertical distribution of the normalised acoustic velocity magnitudes, $|\boldsymbol{u_1}|/|\boldsymbol{u_1}|_{max}$, is plotted. It can be seen that the magnitude of the $x$-component acoustic velocity increases rapidly from zero at the top boundary, $y = h$, to its maximum value and then decreases a little to a constant value in the bulk of the fluid. The variation of dimensionless $y$-component acoustic velocity, $|v_1|/|v_1|_{max}$, has the same tendency with that of the $x$-component velocity near the top boundary. However, it drops gradually to zero $(y = 0)$ after reaching its peak near the boundary.

(a) $|p_1|/|p_1|_{max}$ (b) $|\boldsymbol{u}_1|/|\boldsymbol{u}_1|_{max}$

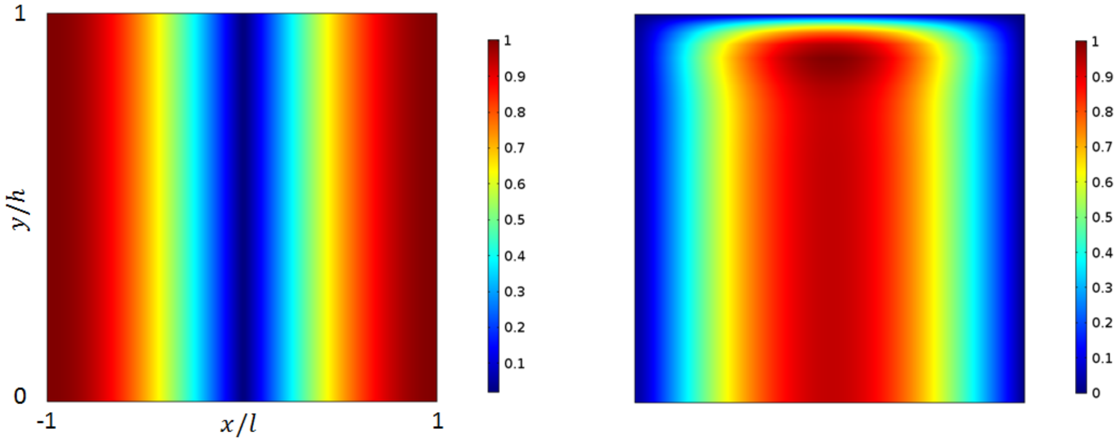

(c) Normalised pressure along $y = h/2$ (d) Normalised acoustic velocity along $x = 0$

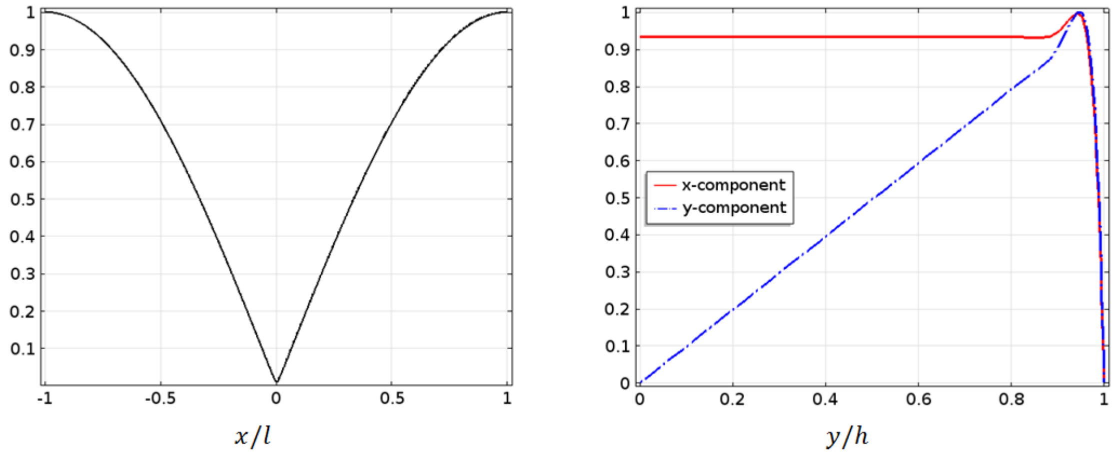

Figure 3.4 Modelled first-order acoustic pressure and velocity fields: (a) normalised magnitude of acoustic pressure; (b) normal magnitude of acoustic velocity for $h = 40\delta_v$; (c) axial distribution of normalised magnitude of acoustic pressure; (d) vertical distribution of normalised distribution of acoustic velocity, where the solid and dash-dot lines show the dimensionless $x$-component and $y$-component acoustic velocities ($|u_1|/|v_1| \approx 660$), respectively.

### 3.2.3. Net Force Fields

The RSF equations for 3D models have been derived in ***Chapter 2***. For the 2D models shown in ***Figure 3.1***, the force equations can be expressed as

$$F_x = -\rho_0\left(\frac{\partial\overline{u_1^2}}{\partial x} + \frac{\partial\overline{u_1 v_1}}{\partial y}\right), \tag{3.3a}$$

$$F_y = -\rho_0\left(\frac{\partial\overline{u_1 v_1}}{\partial x} + \frac{\partial\overline{v_1^2}}{\partial y}\right). \tag{3.3b}$$

Here, the model where $h = 40\delta_v$ was chosen to demonstrate how the net force distribution changes inside the viscous boundary layer and generates the boundary-driven acoustic streaming patterns. The vertical distributions of $F_x$ and $F_y$ along $x = l/2$ were plotted in ***Figure 3.5***. Similar to the distribution of $x$-component acoustic velocity, due to the presence of the viscous boundary layer, the $x$-component RSF grows rapidly from zero to its maximum value, the positon of which is about $1.9\delta_v$ from the boundary.

Then, it can be seen that the $x$-component force, $F_x$, is much larger than the $y$-component force, $F_y$, such that $F_x$ has a bigger contribution on the generation of the inner streaming vortices. In the following, $F_x$ is further analysed in order to clarify how it is influenced by the acoustic velocity fields. To simplify the statement, here a parameter $h_0$ is define as

$$h_0 = h - y, \tag{3.4}$$

to describe the vertical distance to the top boundary ($h = y$).

It can be seen from Equation ***(3.3a)*** that the $x$-component net force $F_x$ is consisted of two partial derivatives, $\partial\overline{\rho u_1^2}/\partial x$ and $\partial\overline{\rho u_1 v_1}/\partial y$. The axial distributions of these two terms on different heights of the chamber are shown in ***Figure 3.6***.

It can be seen that, for $h_0 > 2\delta_v$ (e.g. ***Figure 3.6*** (a)), these two terms have different signs so they work against each other, with a negligible contribution from $\partial\overline{\rho u_1 v_1}/\partial y$. For $h_0 \leq 2\delta_v$ (e.g. ***Figure 3.6*** (b)-(f)), they combine to create $F_x$. The different signs of these two terms and their magnitudes give rise to a change in the contribution of each term in the formation of streaming patterns. These two terms were found to have equal values at positions where $h_0 \approx 0.4\delta_v$.

Therefore, the $y$-differential term, $\partial\overline{\rho u_1 v_1}/\partial y$ has a bigger contribution to $F_x$ at region: $h_0 < 0.4\delta_v$. While for $h_0 > 0.4\delta_v$, the $x$-differential term, $\partial\overline{\rho u_1^2}/\partial x$, has a higher contribution to $F_x$.

The axial distribution of $F_x$ has a sine-wave distribution: zero at $x = 0$ and $x = \pm l$; and maximum values at $x = \pm l/2$, which drives the maximum streaming velocities always at $x = \pm l/2$ with a distance of a few $\delta_v$ to the boundaries (shown below).

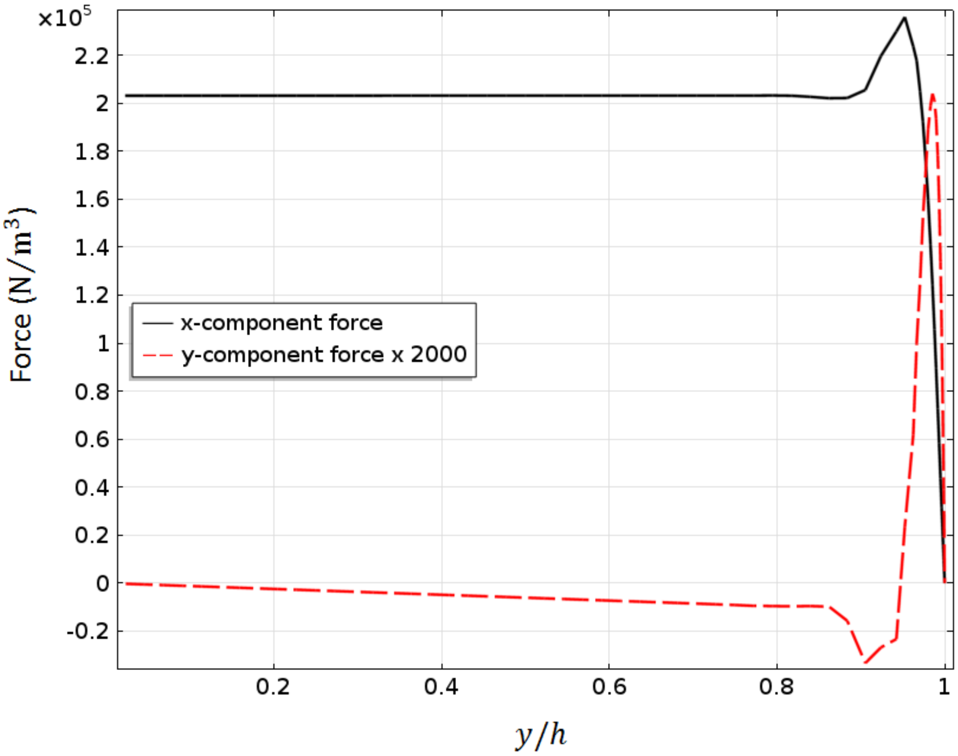

Figure 3.5 Vertical distributions of the Reynolds stress force along $x = l/2$ in Case D ($h = 40\delta_v$), where the solid and dashed lines show the distributions of $x$- and $y$-component forces, $F_x$ and $F_y$, respectively. In order to show the two forces in the same graph, the $y$-component force has been enlarged 2000 times, and the forces presented in the figure are obtained from an excitation of $v_0 = 6.17$ mm/s.

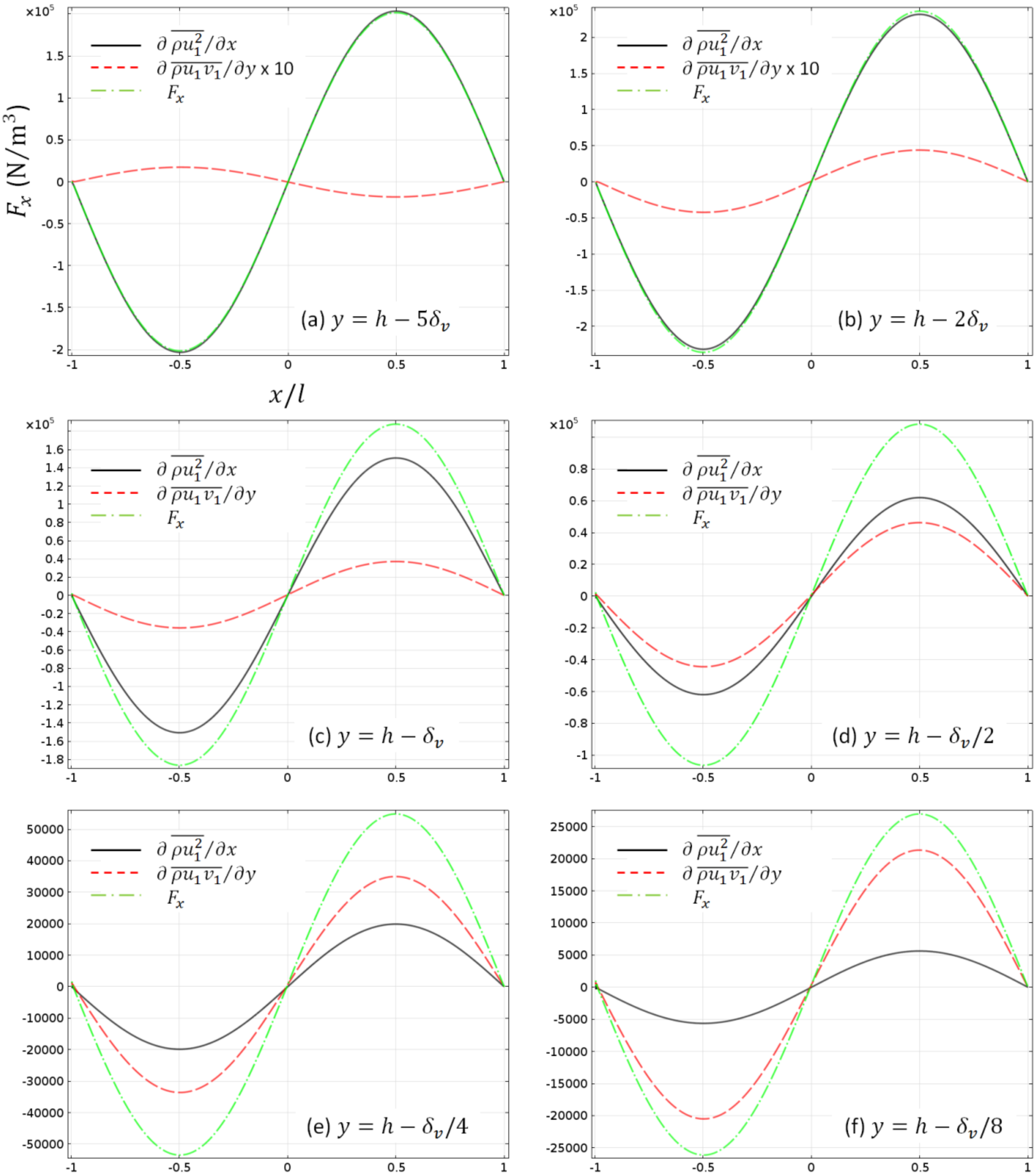

Figure 3.6 Axial distributions of the $x$-component net force, $F_x$, along lines: (a) $y = h - 5\delta_v$; (b) $y = h - 2\delta_v$; (c) $y = h - \delta_v$; (d) $y = h - \delta_v/2$; (e) $y = h - \delta_v/4$; (f) $y = h - \delta_v/8$, where the solid and dashed lines represent two components of $F_x$ (dash-dot lines), $\partial\,\overline{\rho u_1^2}/\partial x$ and $\partial \overline{\rho u_1 v_1}/\partial y$, respectively. The force magnitudes are modelled from oscillation amplitude of $v_0 = 6.17$ mm/s.

### 3.2.4. Acoustic Streaming Fields

To model the second-order streaming velocities, a COMSOL '*Creeping Flow*' interface was used. This is justified as the streaming Re, defined as the ratio of inertia and viscous terms in the Navier-Stokes equations, $Re = \rho \boldsymbol{u_2} \cdot \nabla \boldsymbol{u_2} / (\mu \nabla^2 \boldsymbol{u_2}) \approx 10^{-3}$, is much smaller than one in all the cases considered here. Here, the following equations were solved

$$0 = -\nabla p_2 + \mu \nabla^2 \boldsymbol{u_2} + \boldsymbol{F}, \tag{3.5a}$$

$$\nabla \cdot \boldsymbol{u_2} = 0. \tag{3.5b}$$

With the RSF, $\boldsymbol{F}$, obtained from the acoustic velocity fields, acting as a volume force per unit volume on the fluid, the fluid motion can be obtained within the standing wave in the rectangular chambers.

The modelled acoustic streaming patterns in four modelled chambers are shown in ***Figure 3.7***. It can be seen from ***Figure 3.7*** (d) that in a device where $h = 40\delta_v$ the overall streaming field is predominantly Rayleigh streaming and the size of inner streaming vortices ($y$-extent), $S_{in}$, are only a small portion of that of Rayleigh streaming vortices, $S_{out}$. For increasingly wider channels ($h > 40\delta_v$), the vertical sizes of inner streaming vortices becomes negligible compared to the Rayleigh streaming. As the chamber height becomes narrow (e.g. ***Figure 3.7*** (d)–(a)), the inner streaming vortices grows in size relative to the Rayleigh streaming vortices. And it was found that only inner streaming vortices exist in the whole chamber when $h \leq 5.6\delta_v$ (e.g. ***Figure 3.7*** (a)), which is close to that obtained from Hamilton et al.'s analytical solution[79], which is about $5.7\delta_v$.

The measured $S_{in}$ ($y$-extent) in chambers with $h$ ranging from 0 to 250$\delta_v$ are plotted in ***Figure 3.8***. It can be seen that $S_{in}$ scales linearly with the growth of $h$ in devices where $h \leq 5.6\delta_v$ as only inner vortex was obtained in the entire chambers, which is close to the value found from Hamilton et al.'s analytical solution[79]. As outer streaming vortices are able to form, $S_{in}$ plunges with a further increase of $h$ and soon stabilises at $\sim\delta_v$, which was the value found in devices where $h \gg \delta_v$, shown in ***Figure 3.8***.

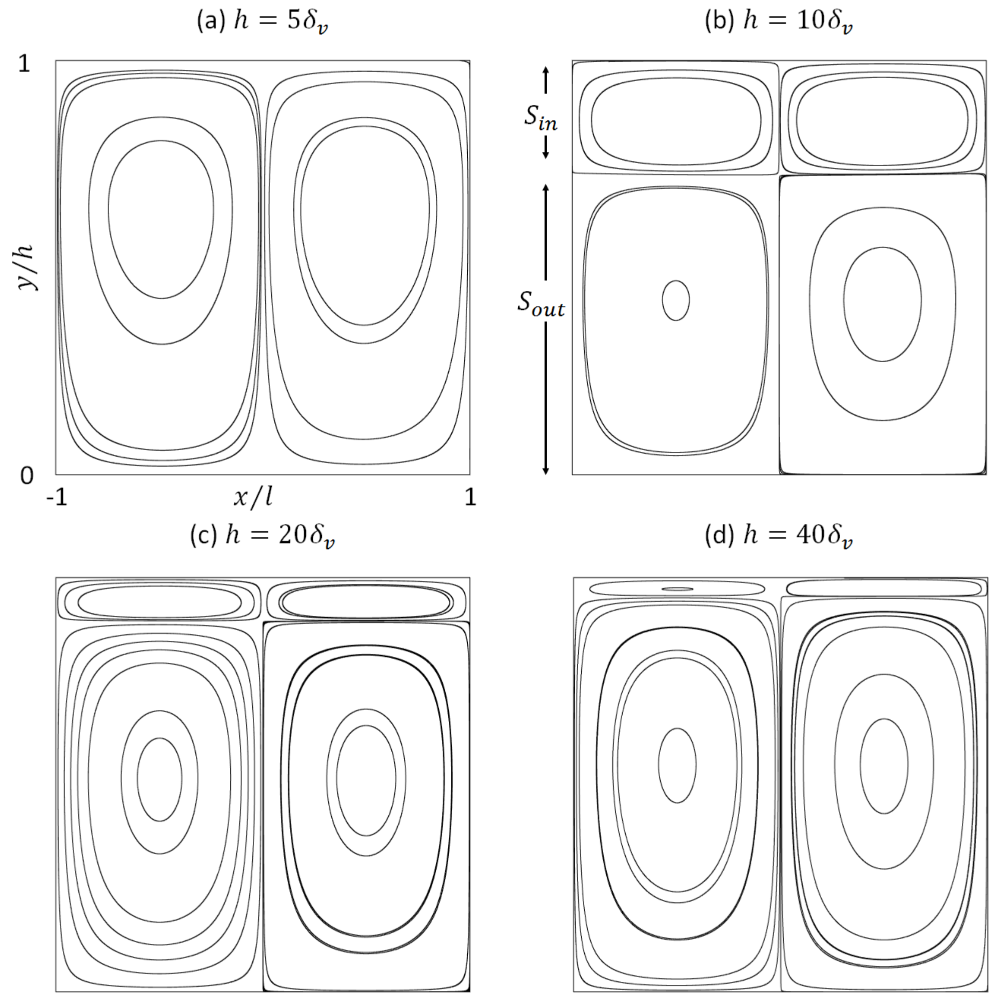

Figure 3.7 Modelled acoustic streaming patterns in four rectangular chambers: (a) $h = 5\delta_v$; (b) $h = 10\delta_v$; (c) $h = 20\delta_v$; (d) $h = 40\delta_v$, where $\delta_v$ is the thickness of the viscous boundary layer and $S_{in}$ and $S_{out}$ are the vertical sizes of the inner and outer streaming vortices, respectively.

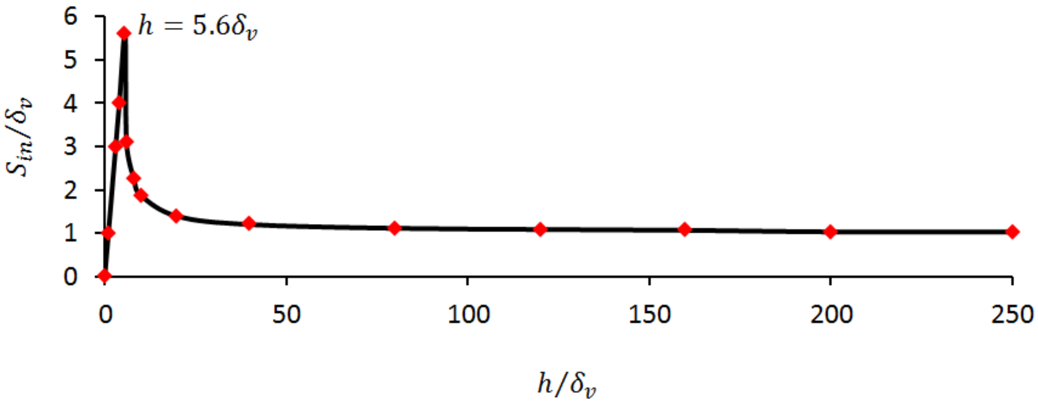

Figure 3.8 The sizes of inner streaming vortices in devices with various heights, $h$, where $\delta_v$ is the thickness of viscous boundary layer and $S_{in}$ represents the vertical sizes of inner streaming vortices.

*Figure 3.9* shows the transverse distributions of the $x$-component acoustic streaming velocities along $x = -l/2$ in four models, where the modelled results (solid lines) are compared to Hamilton et al.[79]'s analytical solution (dashed lines). It can be seen that, in the shown four cases, the modelled results compare well with the results obtained from Hamilton et al.'s solution on the velocity distributions and the difference between them on the velocity magnitudes becomes smaller as $h$ increases. In chambers where the heights are much bigger than the thickness of viscous boundary layer (e.g. *Figure 3.9* (d)), the only difference between the modelled results and that obtained from Hamilton et al.'s solution is the velocity magnitudes inside the viscous boundary layer, which may be attributed to the reason that the streaming velocity field modelled here are assumed to be the second-order velocity, which is different with that derived in Hamilton et al.'s analytical solution, which is the mass transport velocity[79]. By adding the additional term, $\overline{\rho_1 \boldsymbol{u_1}}/\rho_0$, to $\boldsymbol{u_2}$, it is found that the modelled streaming velocities match those obtained from Hamilton et al.'s analytical solution both inside and outside the viscous boundary layer.

From the good comparisons between the models and analytical solutions, it can be seen that the RSM is an effective method for the simulation of 2D boundary-driven streaming fields. However, due to the need in the RSM for tiny mesh elements near the viscous boundaries to resolve the acoustic and streaming fields inside the viscous boundary layer, it can be a very computationally demanding method for modelling boundary-driven streaming fields in real acoustofluidic devices where the dimensions of the fluid channel are usually orders of magnitude larger than $\delta_v$ and usually 3D models are required to demonstrate the 3D nature of acoustic streaming flows.

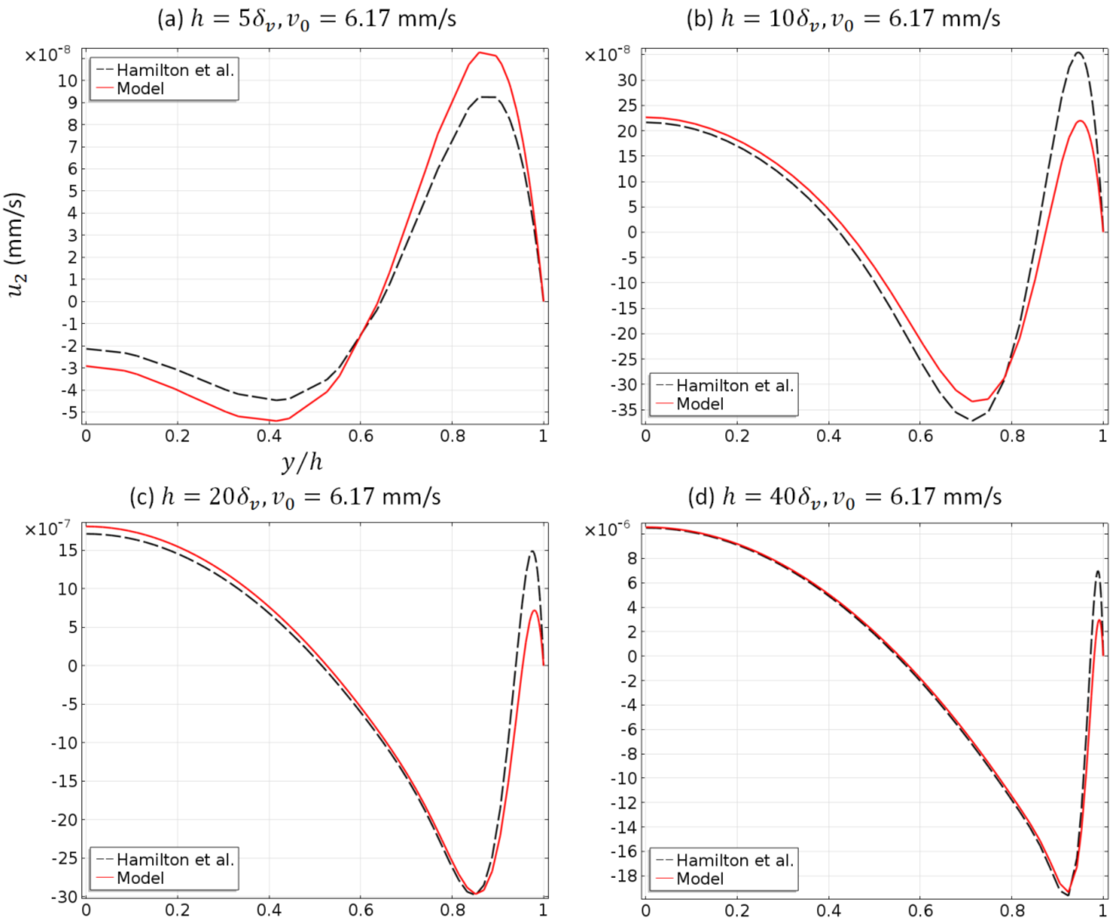

Figure 3.9 Vertical $(y)$ distributions of the dimensionless $x$-component streaming velocity along $x = -l/2$, where the solid and dashed lines are respectively the modelled results and the results obtained from Hamilton et al.'s analytical solution[79]. $\delta_v$ is the thickness of the viscous boundary layer and $v_0$ is the amplitude of oscillation for driving the standing wave fields.

## 3.3. The Limiting Velocity Method

As illustrated, for the boundary-driven streaming, it is the RSF within the viscous boundary layer region that generates acoustic streaming vortices in that thin layer, which further induces the large streaming vortices outside it. Moreover, it has been discussed in *Chapter 2* that the streaming velocity at the extremity of the inner streaming (the LV) can be approximated as a function of the first-order linear acoustic velocity field outside the viscous boundary layer as long as the radius of curvature of the surface is much greater than the viscous boundary layer thickness[78, 88]. Therefore, the acoustic streaming fields outside the viscous boundary layer (the outer streaming) can be predicted from the LV field working as a slip velocity boundary condition provided that the distribution of the first-order irrotational acoustic velocity field outside the viscous boundary layer is known, the LVM. Thus, this approach only predicts the velocity of the streaming field *outside* the viscous boundary layer, and does not calculate the streaming field inside the viscous boundary layer. In typical acoustofluidic devices working in the MHz region this is useful as generally only the main body of the fluid is of interest in devices which are typical orders of magnitude thicker than the thickness of viscous boundary layer. A 2D schematic presentation of the streaming flow over a vibrating surface is shown in *Figure 3.10*.

The LVM is more computationally efficient, compared to the RSM, as the acoustic and streaming fields in the thin viscous boundary layer do not need to be resolved.

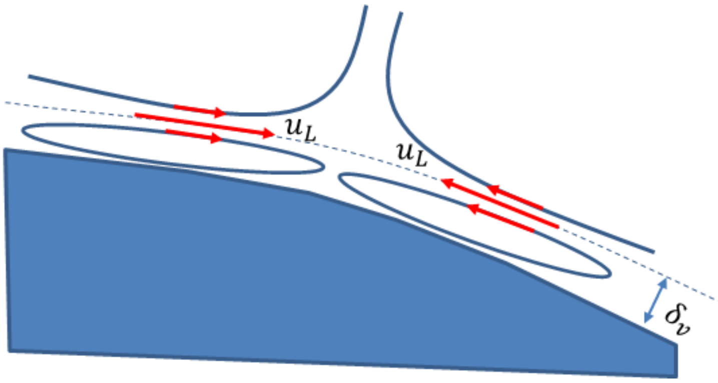

Figure 3.10 A schematic presentation of the streaming fields over a vibrating surface in 2D models, where $u_L$ is the limiting velocity and $\delta_v$ is the thickness of viscous boundary layer.

### 3.3.1. Model

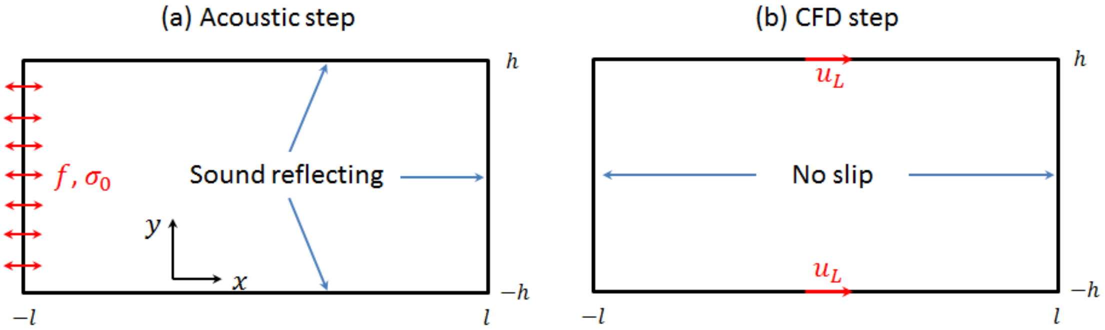

Figure 3.11 Schematic illustration of the limiting velocity method, which solves the outer acoustic streaming field in a rectangular chamber from two steps: (a) the acoustic step, where the left wall of the chamber vibrates with a frequency of $f = 1$ MHz and amplitude of $\sigma_0 = 0.2$ MPa; and (b) the computational fluid dynamics (CFD) step, where $u_L$ is the limiting velocity.

In this section, the classical Rayleigh streaming in a water-filled rectangular chamber, shown in *Figure 3.11*, is investigated using the LVM. The standing wave field in the chamber was induced by a harmonic vibration of its left wall with a frequency of $f = 1$ MHz and amplitude of $\sigma_0 = 0.2$ MPa. An appropriate value for the length of the chamber was selected such that a half-wave standing wave in the $x$-direction of the chamber can be established. Here, the dimensions of the chamber were chosen as: $l \times h = 740 \times 84.8$ μm², where the size of inner streaming vortices is negligible in comparison with the outer streaming vortices. As shown in *Figure 3.11* (a), the origin of coordinates was set at the centre of the chamber.

The modelling process can be split into two steps. Firstly, the first-order acoustic pressure and velocity fields are solved, from which the LV, $u_L$, can be calculated. Then, the acoustic streaming fields are calculated from the LV field which are applied as slip velocity boundary conditions on the top and bottom walls of the rectangular chamber, *Figure 3.11* (b). In this model, a uniform distribution of rectangular mesh elements (the size of which is unimportant) was used as no tiny mesh elements inside the viscous boundary layer are required to resolve the acoustic and streaming fields inside the viscous boundary layer. A portion of the mesh constitution in the $x$-direction of the channel is shown in *Figure 3.12*. Other model parameters have been shown in *Table 3.1*.

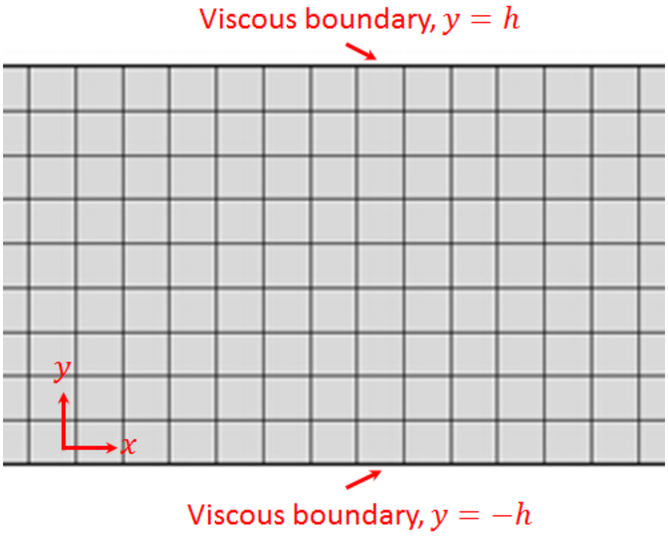

Figure 3.12 Mesh condition for the limiting velocity method

## 3.3.2. First-order Acoustic Fields

The device shown in ***Figure 3.11*** was modelled using the COMSOL '*Pressure Acoustics, Frequency Domain*' interface to obtain the first-order acoustic velocity and pressure fields, which solves the harmonic, linearized acoustic equation shown in Equation ***(3.1a)***. In this interface, the acoustic velocity field was calculated following: $u_1 = i \cdot p_1/\rho_0 c$. The other component $v_1$ is everywhere zero. In this step, the boundary conditions were chosen as follows: the left wall was the normal stress excitation and the remaining walls were sound hard boundary conditions.

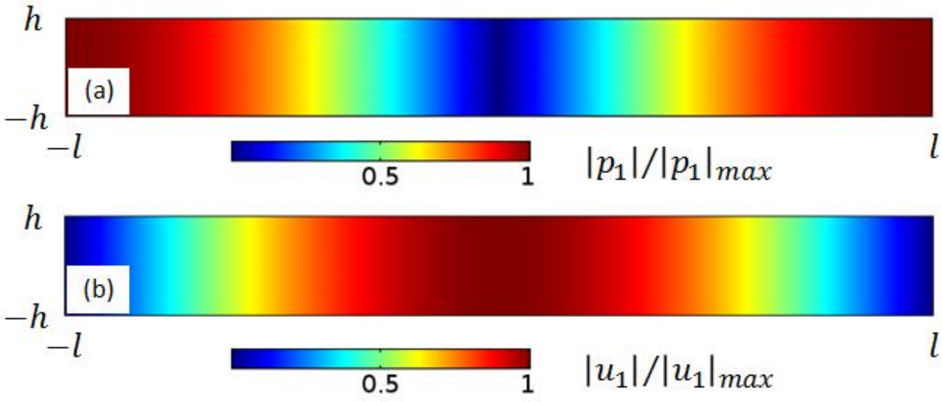

Figure 3.13 Normalised amplitudes of the modelled (a) acoustic pressure field and (b) acoustic velocity field, where $|p_1|_{max}$ and $|v_1|_{max}$ show the maximum magnitudes of pressure and velocity, respectively.

*Figure 3.13* (a) shows the distribution of the normalised magnitude of the modelled first-order acoustic pressure field. It can be seen that a half-wave standing wave is established in the $x$-direction of the chamber with acoustic pressure node staying at the centre ($x = 0$) and two pressure antinode at left and right walls ($x = \pm l$). The normalised acoustic velocity field is shown in *Figure 3.13* (b), from which a uniform distribution of velocity along the height of the chamber can be seen as the acoustic boundary layer is not solved in this interface.

### 3.3.3. Second-Order Acoustic Streaming Field

A COMSOL '*Creeping Flow*' interface is then used to model the second-order acoustic streaming fields. The theory of this physics has been introduced in Section *3.2.4*. Here, the following equations were solved:

$$0 = -\nabla p_2 + \mu \nabla^2 \boldsymbol{u_2}, \tag{3.6a}$$

$$\nabla \cdot \boldsymbol{u_2} = 0. \tag{3.6b}$$

There is no volume force term in the momentum Equation *(3.6a)* as for this case, where a 1D standing wave was established, the RSF in the bulk of the fluid are irrotational so cannot generated streaming vortices (Section *2.2.1*). In this step, the boundary conditions were chosen as follows: as shown in *Figure 3.11* (a), the top and bottom walls were slip velocity boundary conditions and the remaining walls were set as non-slip boundary conditions. For a 2D rectangular chamber presented here, within which a 1D standing wave field was generated in the $x$-direction, the LV, $u_L$, shown in *Figure 3.11* (b), can be calculated from the following equation (derived from Equation *(2.27)*):

$$u_L = -\frac{3}{4\omega} \cdot u_1^* \frac{du_1}{dx}. \tag{3.7}$$

The modelled streaming field within the rectangular chamber is shown in *Figure 3.14*. It can be seen from *Figure 3.14* (a) that four vortices are generated in the $x$-direction within the half-wavelength standing wave field, which is consistent with Rayleigh's analysis. A comparison on the modelled streaming velocities with the Rayleigh's theory[49] is presented in *Figure 3.14* (b) & (c), from which it can be seen the modelled magnitudes of streaming velocities compare well with that calculated from Rayleigh's analytical solution.

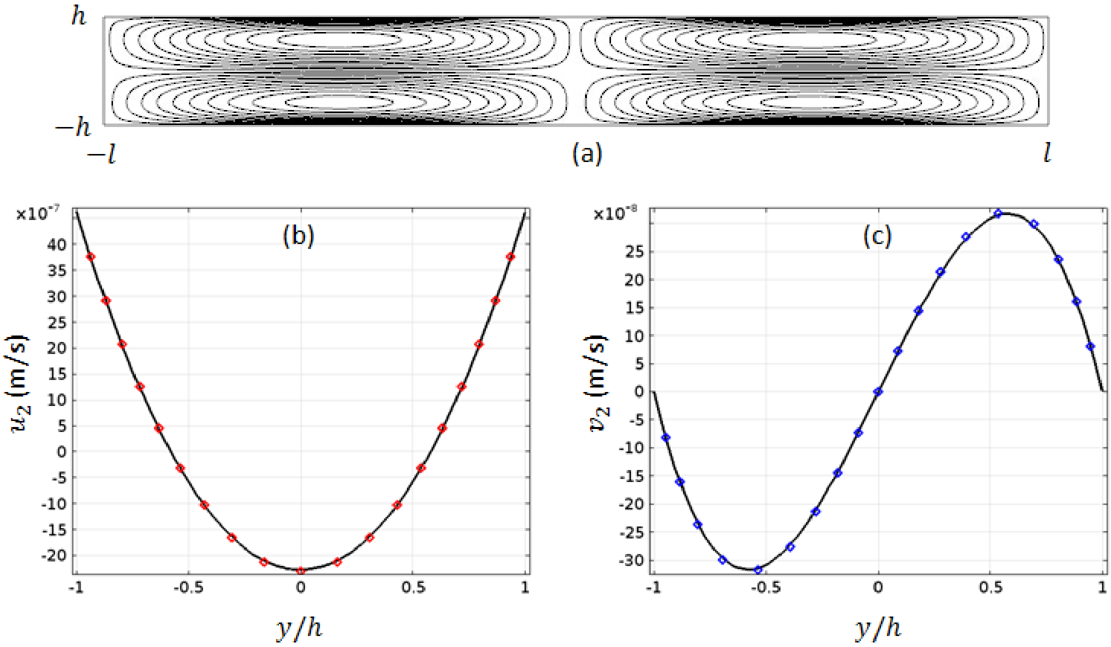

Figure 3.14 (a) Modelled Rayleigh streaming pattern in a 2D rectangular chamber; (b) $u_2$, the $x$-component of streaming velocity along $x = l/2$; (c) $v_2$, the $y$-component of streaming velocity along $x = 0$, where the solid lines and the diamonds show respectively the model results and that obtained from Rayleigh's analytical solution[49]. The magnitude of streaming velocities is obtained from an excitation of $\sigma_0 = 0.2$ MPa.

## 3.4. Discussion and Comparisons

### 3.4.1. Mechanism of Classical Boundary-driven streaming

In Section *3.3*, it has been shown that in devices where $h \gg \delta_v$, the sizes of the inner vortex remain stable at approximately $\delta_v$. Here, it may come up with a question that now that it is the acoustic energy attenuation within the viscous boundary layer that generates streaming vortices, why the inner streaming vortex does not have a container scale (i.e. half height of fluid channel) and there are vortex pairs within and without the boundary layer region? In this part, how the RSF fields vary within and without the boundary layer region is investigated in order to unlock this mystery and demonstrate the formation mechanism of classical boundary-driven streaming patterns in 2D rectangular chambers.

***Figure 3.15*** shows the RSF field in a channel where $h = 40\delta_v$, where all the quantities have been normalised on their magnitudes as only the distributions are of interest. It can be seen from ***Figure 3.15*** (a) that the RSF has a sine-wave distribution along the standing wave ($x$-direction). In the vertical direction ($y$), as shown in ***Figure 3.15*** (b), the force field has a similar distribution with the $x$-component acoustic velocity that, with the increase of $h_0$, the magnitudes shoot up and reach the peak at $h_0 \approx 1.9\delta_v$ and then decrease a little to a constant value in the bulk of chamber. Here, only $F_x$ was shown as it has been shown previously the $y$-component force $F_y$ is thousands of times smaller due to 1D standing wave established in the $x$-direction of the chamber. Moreover, under such a condition, the curl of the RSF can be approximated to

$$\nabla \times \boldsymbol{F} \approx -\frac{\partial F_x}{\partial y}\boldsymbol{k}, \tag{3.8}$$

where $\boldsymbol{k}$ is the unit vector perpendicular to the $xy$ plane. This means that, in these devices where a 1D standing wave was established along the $x$-axis, the $y$-derivative of $F_x$ determines the rotationality of the RSF in the $xy$ plane, resulted in whether the RSF can generated streaming vortices in the $xy$ plane of interest. Based on the distribution of $F_x$ along the channel height, two main gradients can be found in the viscous boundary layer region, as shown with arrows in *Figure 3.15* (b), which in turn determines the rotationality of $\boldsymbol{F}$ in the near boundary region.

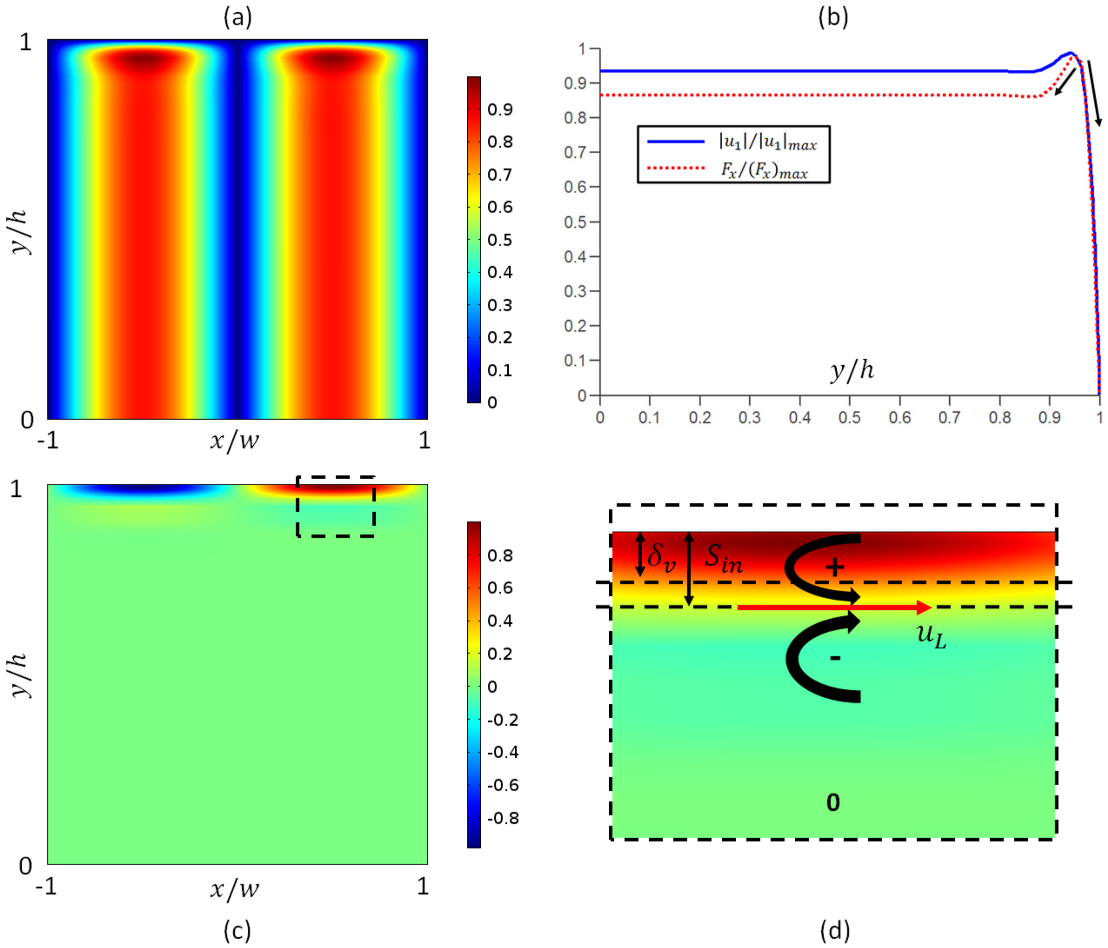

Figure 3.15 The modelled results in a device where $h = 40\delta_v$: (a) the distribution of normalised Reynolds stress force, $\boldsymbol{F}$; (b) the vertical distribution of normalised $|u_1|$ (solid-line) and $F_x$ (dot-line) along $x = w/2$, where $|\cdot|_{max}$ represents the maximum absolute value; (c) the distribution of normalised $\nabla \times \boldsymbol{F}$; and (d) the distribution of $\nabla \times \boldsymbol{F}$ near the top boundary in the dashed box shown in (c), where $\delta_v$ is the thickness of viscous boundary layer, $S_{in} \approx 1.2\delta_v$ shows the size of inner streaming vortex, $u_L$ is the limiting velocity that drives the outer streaming vortex, 0, -, and + represent the magnitudes of $\nabla \times \boldsymbol{F}$ and the curved arrows represent the rotationality of $\boldsymbol{F}$ that drives the streaming vortices in the $xy$ plane.

The distribution of $\nabla \times \boldsymbol{F}$ in the whole chamber is shown in *Figure 3.15* (c) and a magnification of $\nabla \times \boldsymbol{F}$ near the top boundary, the dashed box shown in *Figure 3.15* (c), is presented in *Figure 3.15* (d), where '+' and '-' signs were used to show its magnitudes. It can be seen that it is zero in the bulk of the chamber and non-zero only in the viscous boundary layer region. In the bulk of the fluid chamber, the RSF is irrotational as $F_x$ is a constant value along the channel heights (***Figure 3.15*** (b)), which cannot generate streaming vortices itself. The force field is rotational in regions near the top boundary with different directions in areas inside the boundary layer and that immediately outside it. The distinct rotationality on the force field in the viscous boundary layer region can generate an anticlockwise and clockwise streaming vortex pair themselves, which can result in a balanced streaming velocity at the juncture of these two vortices, shown as $u_L$ in ***Figure 3.15*** (d). This streaming velocity is the LV that drives the inner and outer streaming vortex pairs inside and outside the viscous boundary layer within each $\lambda/4$ of the standing wave in the half chamber, as shown in ***Figure 3.15*** (d) with curved arrows. It is also the different rotationality on the RSF within the viscous boundary layer and that immediately without it that determines the size of inner streaming vortices ($S_{in}$), forcing it in the thin viscous boundary layer region at a size of $\sim\delta_v$.

### 3.4.2. Comparisons of these Two Methods

In the previous sections, the classical boundary-driven streaming fields in 2D rectangular chambers have been simulated from the RSM and the LVM, which were compared to corresponding analytical solutions. Rayleigh's solution[49] and the LVM both ignore the acoustic and streaming fields near the boundaries and only describes the boundary-driven streaming outside the viscous boundary layer. Therefore, in order to clarify the accuracy and the applicability of the LVM on the simulation of boundary-driven acoustic streaming fields, further comparisons on the streaming velocity magnitudes in the bulk of the fluid between the RSM and the LVM in models with channel heights ranging from 6 $\delta_v$ to 200 $\delta_v$ were undertaken. For each case, the percentage of difference (POD) on the modelled streaming velocity magnitude at point ($-l/2$, 0) were calculated by

$$\text{POD\_}u_2 = (u_{2l} - u_{2r})/u_{2l}, \tag{3.9}$$

where $u_{2l}$ and $u_{2r}$ are the streaming velocities obtained from the LVM and the RSM, respectively.

It can be seen from ***Figure 3.16*** that the difference between the streaming velocity magnitudes modelled for these two methods tends to be smaller with the increase of channel heights. Based on these results, it is thus not recommended to use the LVM to model the boundary-driven streaming in devices where the channel heights are below $50\delta_v$, which introduce more than 10% of error on the magnitude in the acoustic streaming velocities. Especially in devices where $h < 5.6\delta_v$, there are only inner streaming vortices in the chambers, the modelled streaming fields will be in different orientation on each single vortex. However, for most real experimental devices, where 1D or 2D standing wave fields are established and where 3D models are often required to solve the acoustic and streaming fields, the LVM can be effectively applied as the channel dimensions are usually several orders of magnitude bigger than the viscous boundary layer thickness and thus only the acoustic streaming fields outside the viscous boundary layer are usually of interest.

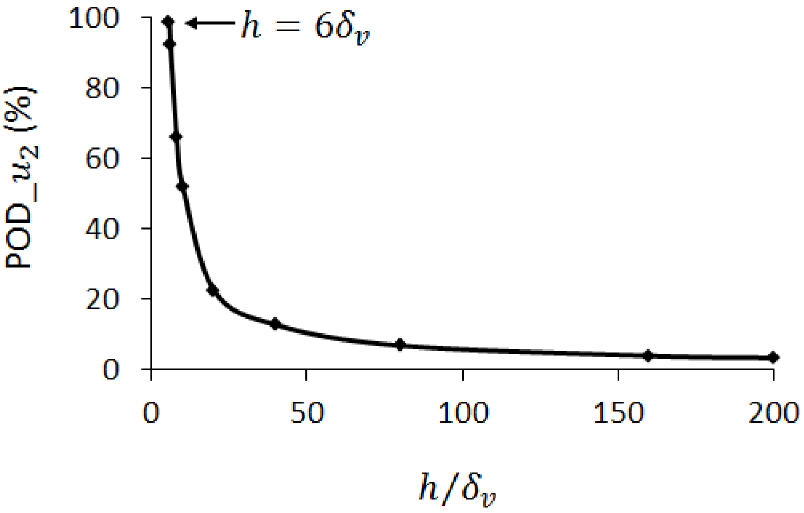

Figure 3.16 Comparisons of the modelled acoustic streaming velocities in the bulk of the fluid from these two methods, the Reynolds stress method (RSM) and the limiting velocity method (LVM), where POD_$u_2$ represents percentage of difference on the $x$-component of acoustic streaming velocity, $u_2$, at point $(-l/2,\ 0)$. POD_$u_2 = (u_{2l} - u_{2r})/u_{2l}$, where $u_{2l}$ and $u_{2r}$ are the streaming velocities obtained from the LVM and the RSM, respectively.

## 3.5. Conclusions

Two methods for the modelling of boundary-driven acoustic streaming patterns were presented and compared in this chapter, which can provide effective advice for researchers in the field of acoustofluidics on choosing appropriate methods to model the acoustic streaming patterns observed in experimental devices and on device designs to optimise their performances.

Firstly, the classical boundary-driven streaming fields, Rayleigh-Schlichting streaming, in 2D rectangular chambers within standing waves, excited from a harmonic oscillation of its left wall, were simulated in a 2D Cartesian coordinate system from its driving force. The distribution of the acoustic field, net forces and acoustic streaming were presented and compared with the classical analytical solutions. It was found that, in terms of the streaming flow structure, as the height of the chamber decreases, the inner streaming vortices increases in size relative to the Rayleigh streaming vortices and only the inner vortices exist when the chamber is sufficiently narrow ($\leq 5.6\delta_v$). The modelled streaming velocity magnitudes were compared to Hamilton et al.'s analytical solution showing that the differences between them become smaller, especially the streaming velocities outside the viscous boundary layer, with the increase of chamber heights. In the chamber where $h = 40\delta_v$, there is almost no difference on the streaming velocities in the bulk of the fluid. In increasingly wider chambers, the only differences on the streaming velocities between the model and theory are that near the viscous boundary, which was analysed to be attributed to the different quantities plotted in these two solutions. Then, the Rayleigh streaming fields outside the viscous boundary layer in 2D rectangular chambers were simulated from the LVM. It was shown that the modelled streaming patterns and velocities show very good consistence with that obtained from classical solutions.

While the RSM has high precision on modelling both acoustic streaming patterns and magnitude of acoustic streaming velocities, the tiny mesh element required to resolve the acoustic and streaming fields within the thin viscous boundary layer suggests it is a computationally demanding method and thus not suitable for 3D models or even 2D models when the channel heights are several orders of magnitude larger than the viscous boundary layer thickness. The other method, the LVM, is more computationally efficient. The error it introduces increases with the decrease of the channel dimensions such that it is not recommended to use this method to model the outer acoustic streaming fields in devices where $h < 50\delta_v$. However, The LVM can be effectively applied to solve both 2D and 3D boundary-driven acoustic streaming fields in most real experimental acoustofluidic particle manipulation devices where the channel dimensions are usually several orders larger than the viscous boundary layer thickness such that only the acoustic streaming fields outside the viscous boundary layer are usually of interest.

The driving mechanism of the classical boundary-driven streaming has been deeply analysed. It was found that it is acoustic attenuation in the viscous boundary layer forming rotational RSF in the viscous boundary layer region which have distinct directions within and immediately without the viscous boundary layer that generates the inner and outer streaming vortices and forces the inner streaming vortex in the thin viscous boundary layer with a size of $\sim\delta_v$ in devices where $h \gg \delta_v$.

# Chapter 4. Acoustic Streaming in the Transducer Plane in Layered Acoustofluidic Systems[*]

## 4.1. Introduction

In most micro-acoustofluidic particle manipulation devices (excepting surface acoustic wave (SAW) devices), the acoustic streaming field is generally dominated by boundary-driven streaming (Eckart streaming requires acoustic absorption over longer distances than those typically found in such devices[69]). Boundary-driven streaming is a result of the interaction between the acoustic oscillations and solid boundaries. Rayleigh[49] was the first to present a theoretical analysis of 2D boundary-driven streaming generated in 1D standing wave fields. With a series of assumptions, he obtained equations for the steady motion of periodic vortices within a standing wave field, comprising four pairs of counter-rotating vortices within each wavelength. His solution only describes the fluid motion outside the viscous boundary layer, so it is commonly referred to as ‘outer streaming’ as well as ‘Rayleigh streaming’. Subsequently, a series of modifications of Rayleigh’s solution have been proposed, most notably by Westervelt[77], Nyborg[81] and Schlichting[50], reviewed by Boluriaan *et al.*[70] and Wiklund *et al.*[153]. Hamilton *et al.*[79] derived an analytical solution for the acoustic streaming generated by a standing wave confined by parallel plates that described the streaming field inside the viscous boundary layer in addition to the outer streaming field.

The literature discussed above generally describe the classical boundary-driven streaming pattern in which the plane of the streaming vortices contains the axis of the standing or travelling waves (in most cases this axis is perpendicular to the transducer). However, experimental observations in planar micro-acoustofluidic resonators have described streaming patterns with vortices flowing parallel to the transducer plane[153, 154]. Similar vortices had previously been described by Spengler *et al.*[155] and later work from

---

[*] A portion of the results presented in this chapter are in ref.152. Lei, J., P. Glynne-Jones, and M. Hill, *Acoustic streaming in the transducer plane in ultrasonic particle manipulation devices.* Lab Chip, 2013. **13**(11): p. 2133-43.

Kuznetsova and Coakley[156] also discusses ‘unexpected wall-independent’ suspension vortices with circulation planes parallel to the transducer radiating surface. They called this streaming pattern an “unexpected vortex” for the reason that this kind of streaming pattern is different from the classical streaming (*e.g.* Rayleigh streaming[49] and Eckart streaming[72]) whose vortex plane contains the axis of the standing or travelling waves. Therefore, despite having been observed experimentally for more than a decade, the mechanism underlying this kind of streaming pattern has not been fully investigated.

In this chapter, a steady, symmetric streaming pattern with the circulation plane parallel to the transducer radiating surface, which has frequently been observed in thin-layered ultrasonic particle manipulation devices, is presented. This pattern has a four-quadrant vortex pattern, which is similar to that described by Hammarstrom *et al.*[154]. As the plane of the vortices is parallel to the transducer face, in the following, it will be referred to as “transducer plane streaming". Understanding its origins is essential for creating designs that limit or control this phenomenon. Therefore, in order to gain insights into the transducer plane streaming pattern a numerical method based on the 3D LVM introduced in ***Chapter 2*** that includes terms ignored in the Rayleigh analysis, and verify its predictions against experimental results in a simple device, is presented. The results show that the modelled particle trajectories match those found experimentally. Analysis of the dominant terms in the driving equations shows that the origin of the transducer plane streaming pattern is related to the circulation of the active sound intensity field.

In Section *4.2*, the experimental measurements are shown, in which the test device, micro-particle-image-velocimetry (μPIV) setup and the motion of particles obtained from PIV measurements are presented. Section *4.3* shows the numerical simulations, including the numerical methods, models and results. In Section *4.4*, a brief discussion of the results, including a comparison between the numerical simulations and the experimental measurements and the mechanism of the observed streaming pattern, is given and overall conclusions are drawn in Section *4.5*.

## 4.2. Experimental Investigations

### 4.2.1. Test Device

The four-quadrant transducer plane streaming pattern was observed in glass capillaries, which have been used for many years to form small acoustofluidic particle manipulation systems [152, 154, 157-162]. The test device is shown in ***Figure 4.1*** (a), which is composed of a PZT4A transducer (Ferroperm, 3 mm × 3 mm × 1 mm thick) glued to a glass capillary of approximately rectangular cross-section. The glass capillary (Vitrocom) had inner dimensions of 0.3 mm × 6 mm, wall thickness of 0.3 mm and length 50 mm, shown in ***Figure 4.1*** (b). To make the top electrode connection a sheet of gold foil was placed between the transducer and the capillary (glues: epoxy, epotek 301 between capillary and leaf, and Circuitworks silver loaded epoxy between leaf and transducer, measured glue layer thicknesses <10 μm). Soldered connections were made between the gold leaf, top electrode and connecting wires. Fluidic connections were made to the capillary via PTFE tubing (ID 1 mm) attached via heat-shrink sleeving. The advantage of a capillary device such as this is that, in contrast to many other layered resonators, there is little energy dissipated into support and clamping structures which makes the modelling of the device more straightforward.

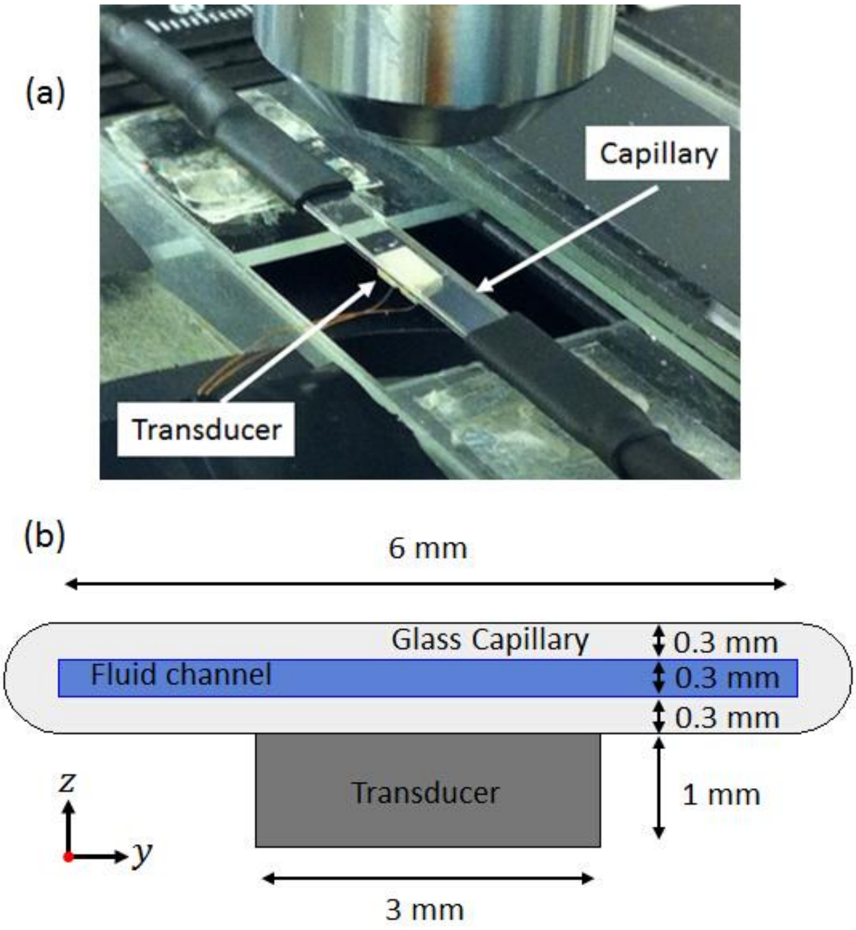

Figure 4.1 (a) An example capillary particle manipulation device, which lacks the gold foil electrode, allowing the transducer to be seen; and (b) dimensions of the cross-section of the device.

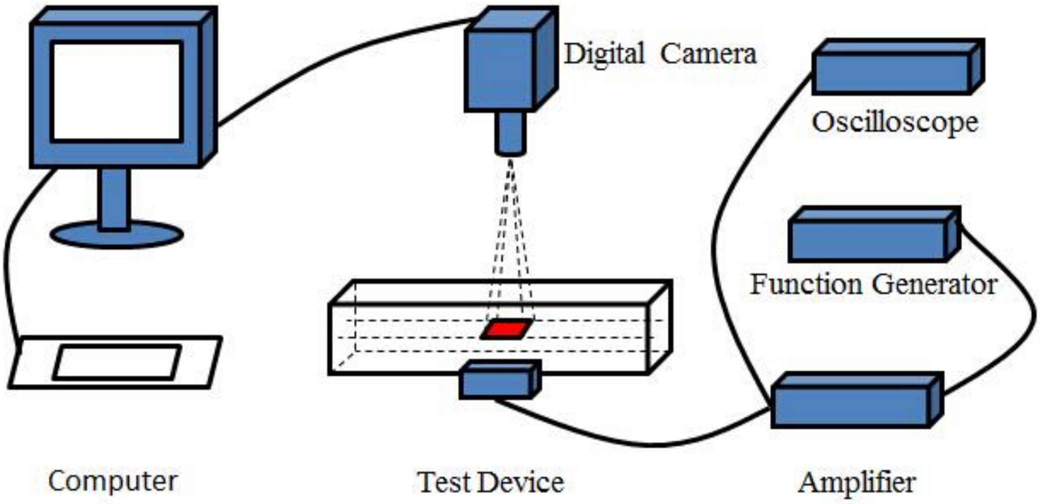

Figure 4.2 A schematic presentation of the experimental arrangements for taking micro-particle-image-velocimetry measurements of acoustic streaming in the device.

### 4.2.2. Experimental Setup

Measurements of the acoustic streaming fields were performed using the experimental arrangement shown in ***Figure 4.2***. A function generator (TTi, TG1304 Programmable) drives an RF amplifier (EIN, Model 240L) that drives the transducer, with signal monitored by an oscilloscope (Agilent Technologies, DOS1102B Digital Storage Oscilloscope). An Olympus BXFM epi-fluorescent microscope with a *pixelfly* dual-frame CCD camera was used to image the fluid motion.

Impedance measurements were firstly used to identify the half-wave resonance frequency in the $z$-direction of the fluid channel in the capillary, which was found at approximately 2.585 MHz. It was found that, at this driving frequency, 10 μm polystyrene beads (Fluoresbrite microspheres, Polysciences Inc.) were levitated in the centre of fluid channel when they were pumped in and slowly agglomerated into clumps in the pressure nodal plane. This relates to radiation forces arising from gradients in predominantly the potential and kinetic energy densities respectively, as discussed by Glynne-Jones *et al*.[163, 164], for beads of this size streaming effects were not in evidence due to the much larger radiation forces. While temperature effects are known to have an influence on the resonances in devices such as this [165], the streaming pattern was found to be reliably present (measured with 1 μm beads) at this frequency and the streaming magnitude similar within the level of accuracy resulting from the approximations made in the modelling below.

Acoustic streaming measurements (μPIV) were performed using green-fluorescent 1 μm polystyrene tracer beads (Fluoresbrite microspheres, Polysciences Inc.). While these experience small radiation forces toward the nodal plane, the streaming forces were found to be a factor of around four stronger. Experiments were conducted with a fresh fill of beads for each measurement to ensure a homogeneous bead distribution. Image pairs (with 10x microscopic objective) were captured at measured time intervals of about 280 ms and processed using the MATLAB based μPIV software, *mpiv*[166].

### 4.2.3. Observed Acoustic Streaming Patterns

As shown in *Figure 4.3*, a four-quadrant, steady acoustic streaming pattern symmetric to the centre of the device was formed. The plane of these vortices is within the visualisation plane, which is parallel to the transducer radiating surface (i.e. perpendicular to the axis of the main standing wave). This is in contrast to the rolls often observed as a result of Rayleigh streaming[49], which have components parallel to the sidewall of chambers. It was found that this acoustic streaming pattern is similar in magnitude at all heights of the fluid channel. This pattern is referred to as “transducer plane streaming” here.

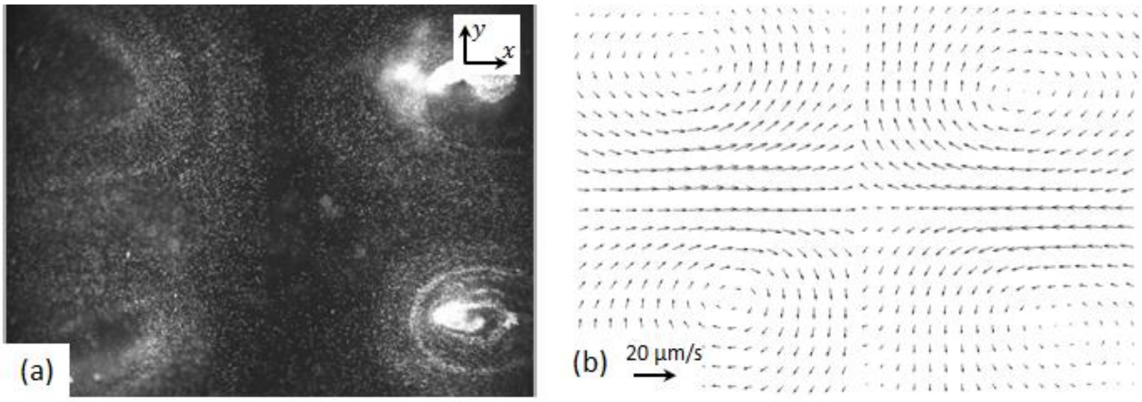

Figure 4.3 (a) A photographic image of distribution of beads in the fluid after some minutes of streaming, where beads can be seen to have agglomerated near the centre of the streaming vortices; (b) µPIV measurements of acoustic streaming (measurements taken after a fresh population of beads have been flowed in to ensure an even distribution). The field of view $(1.8\,\mathrm{mm} \leq x \leq 1.8\,\mathrm{mm}, -1\,\mathrm{mm} \leq y \leq 1\,\mathrm{mm})$ is smaller than the transducer radiating surface.

### 4.2.4. Acoustic Pressure Measurements

In order to compare the measured streaming velocities to the modelling shown later, the acoustic pressure amplitude in the device was measured using the ‘voltage drop’ method described by Spengler *et al.*[155]. In static equilibrium a particle in an ultrasonic force field will settle to a position where the gravitational and buoyancy forces balance with the acoustic forces, which is based on Newton’s first law: $\sum F = 0$. In the transverse direction $(z)$, the particles suffer from gravity force, $F_{Gv}$, buoyance forces, $F_{By}$ and the ARF, $F_{ac}$, shown in *Figure 4.4* (a). Same to the ARF, the gravitational and buoyancy forces are both proportional to the particle volume, so the equilibrium position is independent of particle size. The measurement procedure can be concluded as: 1) a test particle was placed in the field; as the acoustic field is decreased the particle equilibrium position sinks, until it reaches the turning point of the radiation force versus position graph, where further decrease leads to the particle dropping. Since the material properties and hence buoyancy force on the particle are known, the acoustic energy density and hence pressure amplitude can be calculated. The paragraphs below will show the theory in more detail.

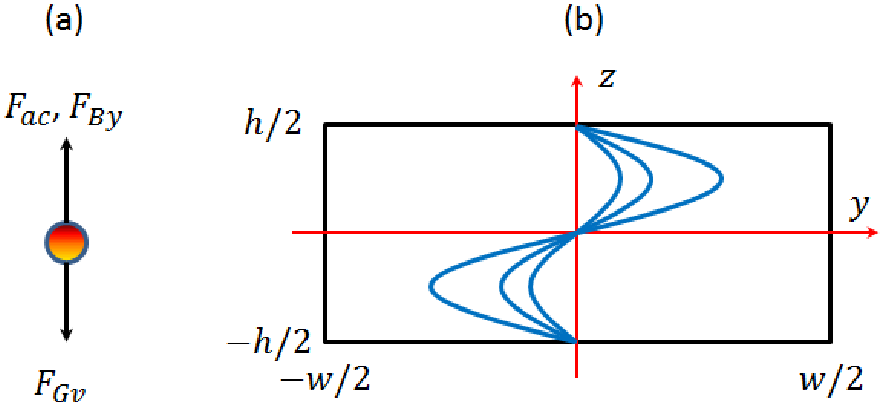

Figure 4.4 (a) Vertical forces on a suspended particle in the fluid channel; and (b) schematic illustration of the acoustic radiation force distribution in the fluid, where a half-wavelength standing wave is established in the $z$-direction. $F_{ac}$, $F_{By}$ and $F_{Gv}$ are the acoustic radiation force, the buoyancy force and the gravity force, respectively.

The vertical ($z$-direction) time averaged ARF can be calculated by the following equation:

$$F_{ac} = 4\pi k r^3 \varepsilon \varphi(\rho, \beta) \sin(2kz), \tag{4.1}$$

where $\varepsilon$ is the acoustic energy density, $k$ is the acoustic wave number, $r$ is the radius of the particles and the factor $\varphi(\rho, \beta)$ is often known as the acoustic contrast factor, which can be calculated from

$$\varphi(\rho, \beta) = \frac{\rho_p + \frac{2}{3}(\rho_p - \rho_f)}{2\rho_p + \rho_f} - \frac{\beta_p}{3\beta_f}, \tag{4.2}$$

where $\beta = 1/\rho c^2$ and $\rho$ are respectively the compressibility and mass density of the fluid and the particle, indicated by subscripts $f$ and $p$, respectively.

For a half-wave standing wave field established in the $z$-direction of the fluid channel, the distribution of ARF on the $yz$ cross-section of the fluid channel can be described in ***Figure 4.4*** (b), which shows that the maximum ARF is distributed at the positions with a distance of quarter height to the upper and bottom boundaries of fluid channel.

Table 4.1 Parameters for acoustic pressure measurements in a thin-layered glass capillary, where $V_{in}$ is the driving voltage.

| Driving frequency, $f$: | 2.585 MHz |
|---:|:---|
| Particle density, $\rho_p$: | 1055 kg·m$^{-3}$ |
| Acoustic speed in particle, $c_p$: | 1962 m·s$^{-1}$ |
| Acoustic pressure amplitude, $\lvert p \rvert$: | (2.685 × 10$^{4}$ × $V_{in}$) Pa |
| Drop voltage, $V_d$: | 1.08 V |
| Particle radius, $r$: | 5 μm |
| Fluid density, $\rho_f$: | 1000 kg·m$^{-3}$ |
| Acoustic speed in fluid, $c_f$: | 1480 m·s$^{-1}$ |
| Energy density, $\varepsilon$: | (0.082 × $V_{in}^2$) J·m$^{-3}$ |

***Table 4.1*** shows the material properties used in the experiment. The ‘drop voltage’, was determined by viewing a 10 μm diameter polystyrene bead with a 50× microscope objective. The system can be approximated as linear since $|p| << (\rho c^2 = 2.2\,\mathrm{GPa})$, so the pressure magnitude is proportional to the driving voltage, and thus the ARF is proportional to the square of the applied voltage.

Therefore, the procedure of measuring the acoustic pressure within the fluid layer can be split into the following steps:

1. A low concentration of fresh 10 μm polystyrene beads was injected into the channel. When a homogeneous distribution of micro beads was observed, the flow was stopped and the ultrasound was turned on at a high driven voltage. Under such a condition, the 10 μm beads would be levitated to a plane, slightly below the pressure nodal plane ($z = 0$) due to the balance of ARF, gravity force and buoyancy force;
2. Focus on one particle at the centre of the fluid channel above the transducer area and gradually decrease the driving voltages until the particle drops towards the bottom of the fluid layer;
3. Record the drop voltage, $V_d$.

Correspondingly, for a given microbeads, the acoustic pressure amplitude can be calculated from the following steps:

1. Firstly, the threshold value of $z$-component of ARF, $F_{ac}$, on the particle equals to the balance between the gravity force and buoyancy force;
2. Then, by inserting the ARF into Equation *(4.1)*, the acoustic energy density can be calculated;
3. Finally, the acoustic pressure amplitude at the driving voltage, $V_{in}$, can be obtained from the calculated acoustic energy density following

$$|p_1| = \sqrt{\frac{F_{ac}\rho_f c_f^2}{\pi k r^3 \varphi(\rho,\beta)}} \cdot \frac{V_{in}}{V_d}. \tag{4.3}$$

### 4.2.5. Effects of Driving Voltages on Acoustic Streaming

The effects of driving voltages on the streaming pattern and magnitude of the streaming velocities were investigated. A series of excitation voltages, ranging from 10 V – 30 V, was considered. At each voltage, the streaming field was measured. To compare the different cases, the maximum streaming velocity (found close to the position $x = 1$ mm, $y = 0$, in ***Figure 4.12***) had been plotted against the pressure amplitude, which will be discussed in comparison to the numerical modelling in Section *4.4*. The large margin of error on this measurement (relationship between the magnitude of acoustic streaming velocity and the acoustic pressure) is due to a number of factors: (a) the difficulty on measuring the ‘drop voltage’ precisely due to uncertainty in knowing when equilibrium has been passed; (b) the difficulty on locating the particle at the centre of the fluid channel (the pressure magnitudes also vary in $x$- and $y$-directions); and (c) uncertainties in the material properties of the bead.

## 4.3. Numerical Simulations

In this section, a 3D model was introduced to simulate the streaming fields observed in thin-layered glass capillary device using the LVM. As described in *Chapter 2*, this method was first introduced by Nyborg[78] and modified by Lee and Wang[88]. It was shown that if the radius of curvature of the boundary is large compared to the viscous boundary layer thickness and height of the fluid channel $h \gg \delta_v$ (here $h \approx 1000\delta_v$) the time averaged velocity at the extremity of the inner streaming (the LV) can be approximated as a function of the local, first order linear acoustic field. The acoustic streaming fields in the bulk of the fluid can then be predicted by a fluidic model that takes the LV as a boundary condition. In the acoustofluidic device working in the MHz region introduced in the previous section, this method is valid as generally only the acoustic streaming fields in the main body of the fluid are of interest in devices where the smallest dimension of the fluid channel is orders of magnitude thicker than the viscous boundary layer thickness, $\delta_v$.

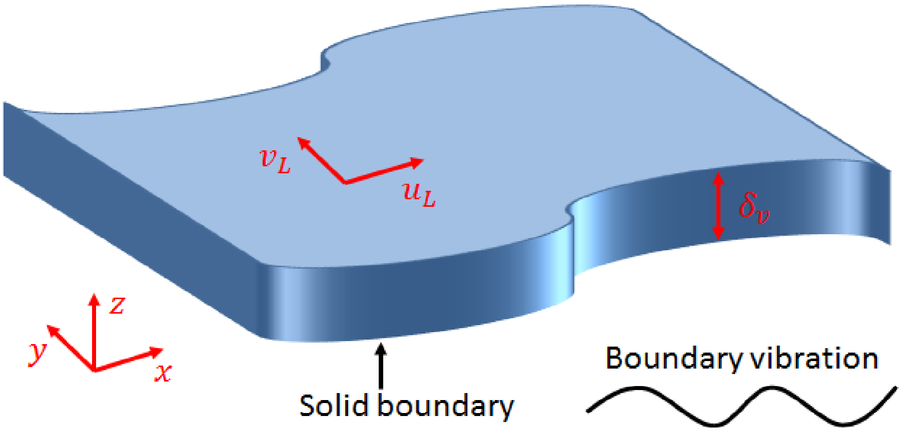

Figure 4.5 Schematic presentation of the limiting velocities over a vibrating surface, where the radius of curvature should be much larger than $\delta_v$. $u_L$ and $v_L$ are the two components of limiting velocities along coordinates $x$ and $y$, and $\delta_v$ is the viscous boundary layer thickness.

The LVM has been fully described in *Chapter 2*. In Section 3.2.2, the LVM for 2D models has been described. Here, the LVM for 3D models used in this chapter is presented in *Figure 4.5*, which solves the acoustic streaming outside the viscous boundary layer with the streaming velocities immediately outside the viscous boundary layer, $u_L$ and $v_L$, acting as slip velocity boundary conditions. The two components of the LV field can be calculated from

Equations *(2.27)*. In a 3D Cartesian coordinates $(x, y, z)$, on a planar surface that is normal to $z$, the equations simplify to the following form:

$$u_L = -\frac{1}{4\omega} Re\left\{u_1 \frac{du_1^*}{dx} + v_1 \frac{du_1^*}{dy} + u_1^*\left[(2+i)(\frac{du_1}{dx} + \frac{dv_1}{dy} + \frac{dw_1}{dz}) - (2+3i)\frac{dw_1}{dz}\right]\right\}, \tag{4.4a}$$

$$v_L = -\frac{1}{4\omega} Re\left\{u_1 \frac{dv_1^*}{dx} + v_1 \frac{dv_1^*}{dy} + v_1^*\left[(2+i)(\frac{du_1}{dx} + \frac{dv_1}{dy} + \frac{dw_1}{dz}) - (2+3i)\frac{dw_1}{dz}\right]\right\}, \tag{4.4b}$$

The model was implemented in the finite element package COMSOL 4.4[167]. The numerical procedure can be split into three steps. First, a linear acoustic model, '*Pressure Acoustics, Frequency Domain*' interface, was used to find the first-order acoustic pressure and velocity fields. Second, the LVs were found using Equations *(4.4)* above, which are functions of the linear acoustic velocities. These were then applied as boundary conditions to a creeping flow model, '*Creeping Flow*' interface, to obtain the time averaged fluid motion (acoustic streaming). Finally, a '*Particle Tracing for Fluid Flow*' interface was used to simulate the particle trajectories under the combined action of ARF and ASF. This decomposition of the problem (into the steps described above) is only valid if the mass source term in the streaming field described by Muller et al.[168] in their Equation (9a) can be ignored. Nyborg[78] justifies this approximation in his derivation of the LVs in the paragraph above his Equation (10).

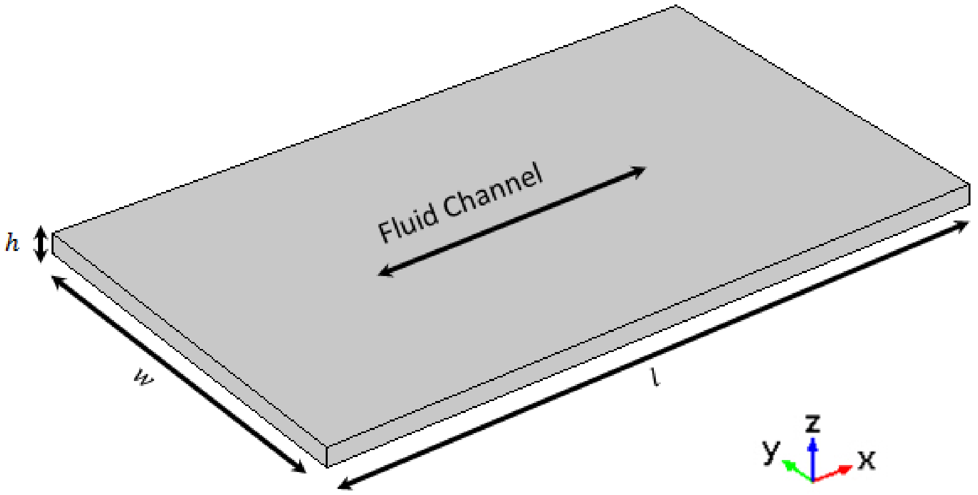

Figure 4.6 The simplified 3D model.

The model geometry was formed from a cuboidal domain of dimensions 0.3 × 6 × 10 mm$^3$ ($h \times w \times l$), shown in ***Figure 4.6***. Here, only the fluid layer within a section of the capillary was modelled for the following reasons: (1) without the transducer and glass walls of the capillary, the whole model is computationally simpler. The numerical process, including the simulation of the first-order acoustic field and the acquisition of the acoustic streaming field can be finished in one hour. While it is possible to model the full device, including piezoelectric and fluid-solid couplings, the additional complexity places high demands on workstation memory; (2) This reduced model is shown below to successfully predict the observed phenomena, which demonstrates that the essential physics is already captured by the model, and thus when I discuss the physical origin of the transducer plane streaming pattern I am in a stronger position to identify the mechanism. The origin of coordinates was set at the centre of the fluid channel such that the model volume is located at coordinates: $-l/2 \leq x \leq l/2, -w/2 \leq y \leq w/2, -h/2 \leq x \leq h/2$. In the following sections, each step is examined in more detail. All the model parameters are summarised in ***Table 4.2***.

Table 4.2 Parameters for four-quadrant transducer plane streaming simulations.

| $l \times w \times h$: | 10×6×0.3 mm$^3$ |
|---:|:---|
| Mesh size: | 100 µm (swept) |
| Excitation, $a_0$: | 3.2 x 10$^5$ m· s$^{-2}$ |
| Density of water, $\rho_p$: | 1000 kg· m$^{-3}$ |
| Excitation frequency, $f$: | 2.484 MHz |
| Speed of sound in water: | 1481.4 m· s$^{-1}$ |
| Dynamic viscosity of water, $\mu$: | 8.9 × 10$^{-4}$ Pa· s |

### 4.3.1. First-order Acoustic Fields

The first-order acoustic pressure and velocity fields in the simplified 3D model shown in ***Figure 4.6*** were modelled using the COMSOL '*Pressure Acoustics, Frequency Domain*' interface. The detailed theory of this interface can be found in Section *3.2.2*.

In this step, the boundary conditions were set as following: the bottom wall was given a normal-acceleration boundary condition, the left and right walls were considered as plane wave radiation boundary conditions (to represent energy that travels down the capillary being largely absorbed by the tubing and connectors at the ends) and the remaining walls were hard boundary conditions. The standing wave field within the fluid layer was generated by a harmonic acceleration of the bottom wall. A 2D normal distribution is used to represent the reduction in vibration amplitude away from the transducer area:

$$a_n = a_0 e^{-ax^2 - by^2}. \tag{4.5}$$

To assess the validity of this approach, the vibration profile was compared with a full model (shown in *Figure 4.7*), which shows that similar acoustic acceleration and velocity distributions on the bottom surface are obtained from these two models. Then, five sets of 'a' and 'b' coefficients (respectively with units m$^{-2}$, $a = 0.22 \times 10^6, b = 0.22 \times 10^6$ ; $a = 0.22 \times 10^6, b = 5 \times 10^5$ ; $a = 0.22 \times 10^6, b = 2 \times 10^6$; $a = 5 \times 10^5, b = 5 \times 10^5$ ; $a = 5 \times 10^5, b = 2 \times 10^6$ ) in the above equation were examined, to represent the area of the excitation from the transducer. It was found that the streaming field was similar from all excitations, suggesting that the streaming pattern is reasonably robust to the precise choice of the excitation shape. This approach is similar to that described by Muller *et al.*[168] who represented ultrasonic actuation with a velocity boundary condition when simulating the Rayleigh streaming in a 2D rectangular chamber. The results presented in this chapter are for an excitation of $a = 5 \times 10^5$ and $b = 2 \times 10^6$ m$^{-2}$.

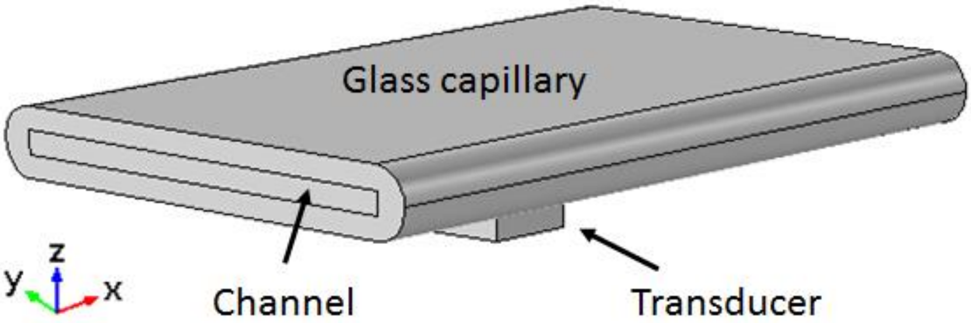

Figure 4.7 Schematic presentation of the 3D full model

The frequency of the half-wave resonance was found at 2.484 MHz by using a parametric sweep to plot the average acoustic energy density in the fluid layer versus the driving frequencies. This method has been found to be more reliable than sorting through the very large number of modes presented by a modal analysis. The modelled acoustic pressure field is shown in *Figure 4.8*. *Figure 4.8* (a) represents the magnitude of the acoustic pressure on the surfaces of the 3D chamber and ***Figure 4.8*** (b) shows the pressure magnitudes on the central $yz$ cross-section ($x = 0$). It can be seen that a half-wave standing wave was established in the $z$-direction of the fluid channel. At this resonance, in addition to the main half-wave standing wave established in the $z$-direction of the 3D chamber, the acoustic pressure along the width of the chamber ($y$-direction) also has an one-wave standing wave variation. Therefore, the resonance established on the $yz$ cross-section can be referred to a (2, 1) cavity mode. In the $x$-direction of the 3D model, as the size of transducer is only a small portion of the channel length ($l$), the pressure magnitudes decay from the maximum value at the centre ($x = 0$) to the two ends ($x = \pm l/2$) of the fluid channel, which makes the 3D acoustic resonance very close the 3D (1, 2, 1) cavity mode.

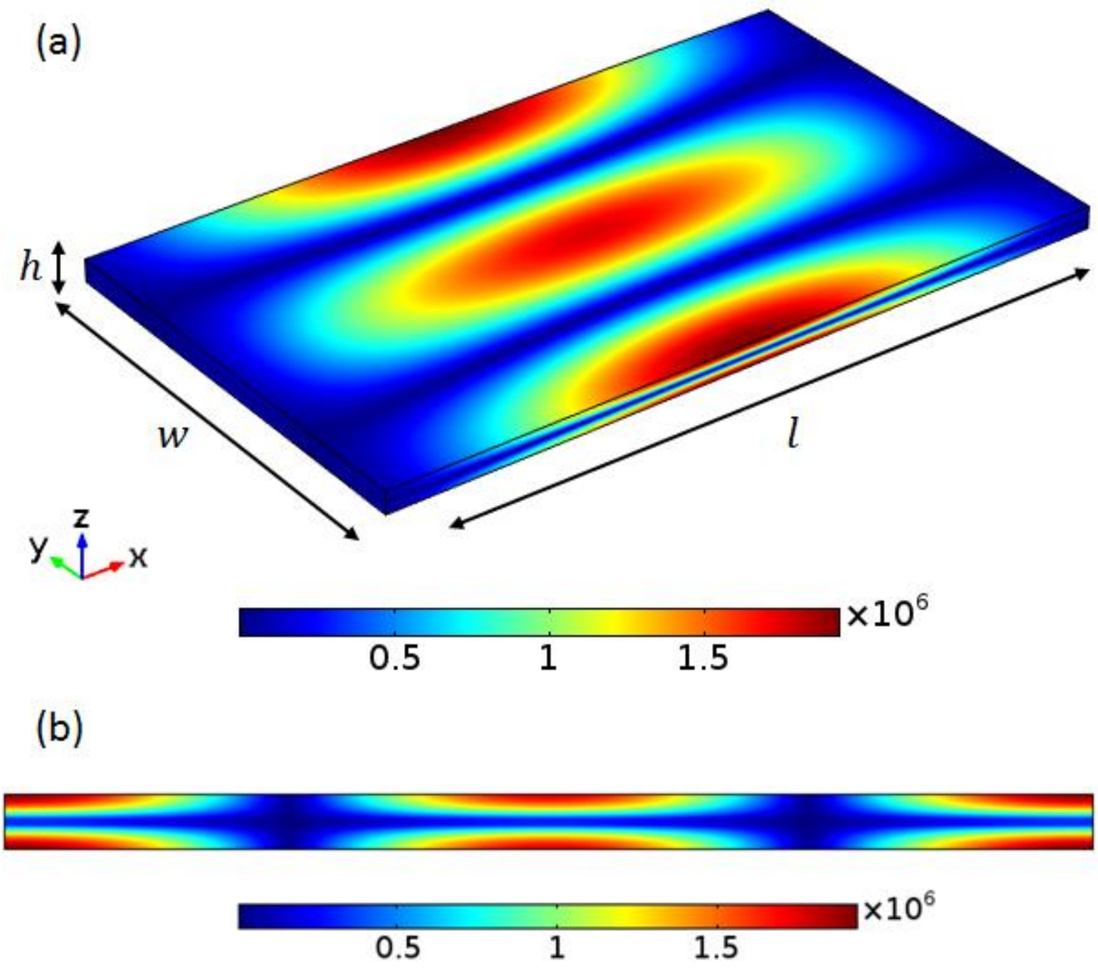

Figure 4.8 The modelled magnitudes of the acoustic pressure (unit of Pa) in the fluid channel on: (a) the surfaces of the modelled volume; and (b) the central $yz$ cross-section, $x = 0$.

### 4.3.2. Acoustic Streaming Fields

The COMSOL '*Creeping Flow*' model was used to simulate the acoustic streaming field. This approximates the fluid as incompressible, and neglects inertial terms (Stokes flow) as the streaming Re is much smaller than one in the experiments presented in this work. The detailed theory of this interface can be found in Section *3.2.4*. In this step, the bottom and top walls were considered as LV boundary conditions while the remaining four walls were considered as nonslip boundary conditions. Initial modelling had represented the side walls (at $y = \pm 3\,\mathrm{mm}$) as LV boundary conditions and the resulting pattern was a combination of classical Rayleigh streaming in the vicinity of the side walls superimposed on the larger scale transducer plane streaming. However, to aid clearer presentation of the results it is limited in this section to presenting the transducer plane streaming generated by the LVs of the floor and ceiling of the device ($z = \pm h/2$) and neglect the localised Rayleigh streaming generated by the side walls.

In order to investigate the effects of mesh sizes on the modelled results, a mesh dependency study of the 3D model was used. A series of tetrahedral meshes with sizes ranging from 30 μm to 170 μm was considered. The average value of the magnitude of streaming velocity in the whole device, $\overline{|\boldsymbol{u}_2|}$, for each case was obtained. The normalised average streaming velocity $\overline{|\boldsymbol{u}_2|}/\overline{\boldsymbol{u}_{2ref}}$, where $\overline{\boldsymbol{u}_{2ref}}$ is the average streaming velocity for a mesh size of 30 μm, is plotted in ***Figure 4.9***. It can be seen that, with the decrease of mesh size corresponding to a finer mesh, the modelled streaming speed becomes larger and approaches a steady value. In order to balance the computational efficiency and the accuracy of simulation, a tetrahedral mesh of size 0.06 mm was used for the remainder of results presented in this chapter, resulting in an estimated mesh-induced numerical error of 0.7%.

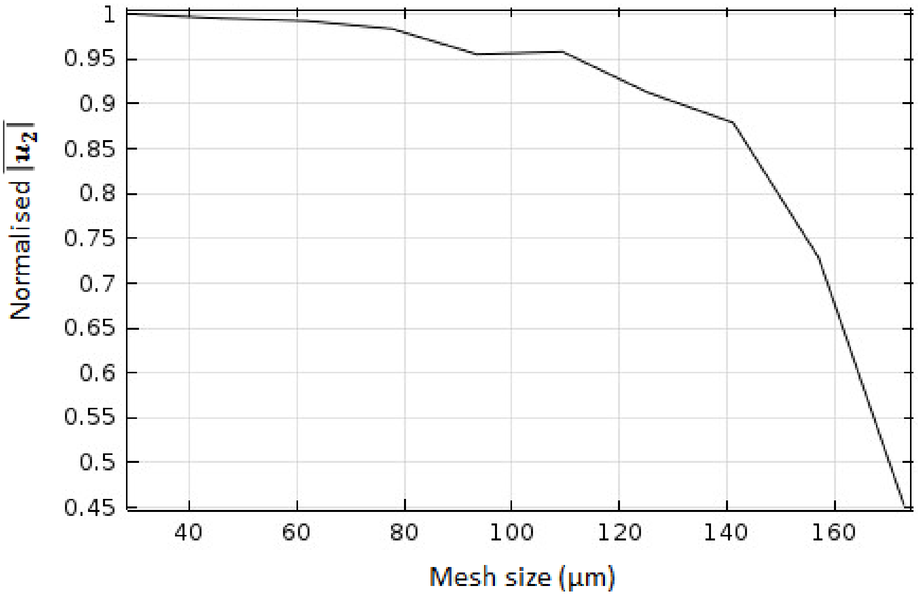

Figure 4.9 The relationship between the average streaming velocity $\overline{|\boldsymbol{u_2}|}$ and mesh size. The normalised $\overline{|\boldsymbol{u_2}|}$ is calculated by $\overline{|\boldsymbol{u_2}|}/\overline{\boldsymbol{u_{2ref}}}$, where $\overline{\boldsymbol{u_{2ref}}}$ is the average streaming velocity for a mesh size of 30 μm.

*Figure 4.10* shows the modelled 3D fluid motion within the fluid layer. It can be seen that a four-quadrant vortex pattern, symmetric to the centre of the device, were obtained. It can be seen from *Figure 4.10* (a)-(b) that the predominant motion is in-plane ($xy$) and that at the centre of the device, all the velocity vectors run parallel to each other and parallel to the top and bottom surfaces (the LV boundaries). *Figure 4.10* (c) plots the streaming field through the central $yz$ cross-section ($x = 0$), from which the in-plane streaming can be seen more clearly. The magnitudes of the in-plane streaming velocities were found almost uniform along different heights of the chamber.

To establish that truncating the length of the capillary that is modelled does not have a significant effect on the results (i.e. investigating whether those regions at some distance from the transducer contribute significantly to the streaming), a range of different values of the capillary lengths ranging from 8 mm to 20 mm was considered. It was found that, in all chosen lengths, the modelled acoustic streaming patterns were the transducer plane streaming with circulations parallel to the bottom surfaces. All the models produced similar results with an error in the maximum velocity of no more than 6 %. The remaining results in this chapter are for a length of 10 mm unless otherwise stated.

Due to the quadratic dependence of the LVs on the linear acoustic quantities, the relationship between the maximum streaming velocity in the device $|\boldsymbol{u_2}|_{max}$ and the maximum acoustic pressure, $|p_1|_{max}$, was expected to take the form:

$$|\boldsymbol{u_2}|_{max} = \alpha \, |p_1|^2_{max}, \tag{4.6}$$

where $\alpha$ is a constant. This was tested by applying to a range of excitation amplitudes to the transducer. The quadratic dependence was valid, and the constant, $\alpha$, was found to take the value 47.23 $\text{m}\cdot \text{s}^{-1}\cdot \text{MPa}^{-2}$ for the stated dimensions. This relationship is discussed further in comparison with experimental results in ***Figure 4.12*** below.

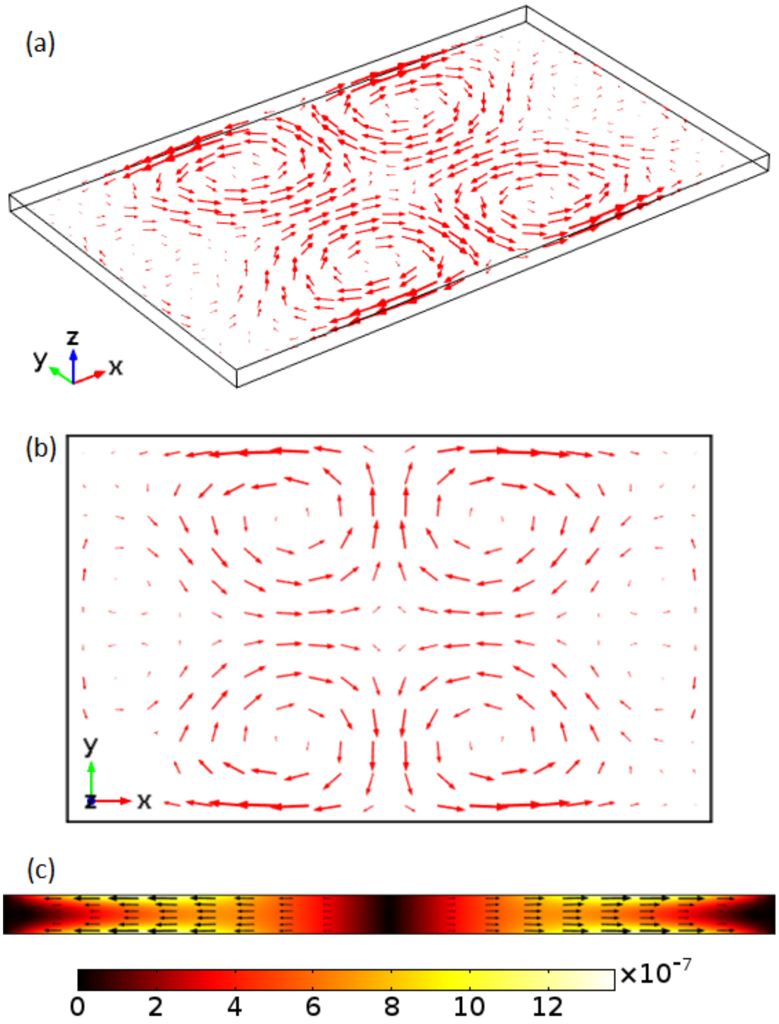

Figure 4.10 The modelled acoustic streaming field, $\boldsymbol{u_2}$: (a) a 3D view of the vector plot of the fluid motion, velocity vectors are shown at three heights within the chamber ($z$-positions of one third and two thirds of the chamber height); (c) the streaming field on central $yz$ cross-section, $x = 0$, where the arrows and colours (unit of m/s) show the in-plane streaming field and the velocity magnitudes.

### 4.3.3. Particle Trajectories

In order to understand the effects of acoustic streaming on particle manipulation and compare to the experimental visualisation, a numerical simulation of particle trajectories was done. Neglecting the gravity force and buoyancy force on a spherical particle, the movement of the particle within a standing wave field is determined by the ARF, $\boldsymbol{F_{ac}}$, and ASF, $\boldsymbol{F_d}$:

$$\frac{d}{dt}(m_p\boldsymbol{v}) = \boldsymbol{F_d} + \boldsymbol{F_{ac}}, \tag{4.7a}$$

$$\boldsymbol{F_{ac}} = -\nabla\left(V_0\left(\frac{3(\rho_p - \rho_f)}{2\rho_p + \rho_f}\overline{E_{kin}} - \left(1 - \frac{\beta_p}{\beta_f}\right)\overline{E_{pot}}\right)\right), \tag{4.7b}$$

$$\boldsymbol{F_d} = 6\mu\pi r(\boldsymbol{u_2} - \boldsymbol{v}), \tag{4.7c}$$

where $m_p$ is the particle mass, $\boldsymbol{v}$ is the velocity of the particle, $\boldsymbol{u_2}$ is the fluid velocity, $\mu$ is the fluid dynamic viscosity, $r$ is the particle radius, $\overline{E_{kin}}$ and $\overline{E_{pot}}$ are the time averaged kinematic and potential energy, $\rho_p$ and $\rho_f$ are respectively the density of particle and fluid, $\beta_p$ and $\beta_f$ are the compressibility of particle and fluid, and $V_0$ is the particle volume. Equation *(4.7b)* is correct for the gradient forces found in both standing waves and in travelling wave fields with energy density gradients (e.g. valid in travelling waves in the near field and in Bessel beams). In the absence of gradient forces an additional, order of magnitude smaller[43], contribution from pure scattering becomes important; however, this will be small here compared to the gradient forces.

From this theory, together with the two interfaces introduced in Sections *4.3.1* and *4.3.2* above, a COMSOL '*Particle Tracing for Fluid Flow*' interface was used to simulate the particle trajectories. The shape of the trajectories are independent of the pressure amplitude, since both the ARF and ASF scale with the square of pressure; results are presented here for an excitation amplitude of $a_0 = 3.2 \times 10^5\ \mathrm{m/s^2}$. An array of tracer particles (given the properties of polystyrene beads of diameter 1 μm) were seeded at $t = 0$. Both ARF and ASF act on the particles, resulting in the motion shown in ***Figure 4.11***. The four-quadrant transducer plane vortex pattern symmetric to the centre of the device is clearly seen, matching that observed in the experimental visualisation. The predominant ARF act perpendicular to the transducer to push the beads towards the pressure nodal plane ($z = 0$). It can be seen that over the course of a single rotation the lateral ARF (acting parallel to the transducer radiating surface) are small in comparison to the forces causing the rotational motion. Particles are firstly driven to the pressure nodal plane and then follow the transducer plane streaming forming a four-quadrant steady, symmetric vortex pattern with circulations parallel to the bottom surface (i.e. the transducer radiating surface).

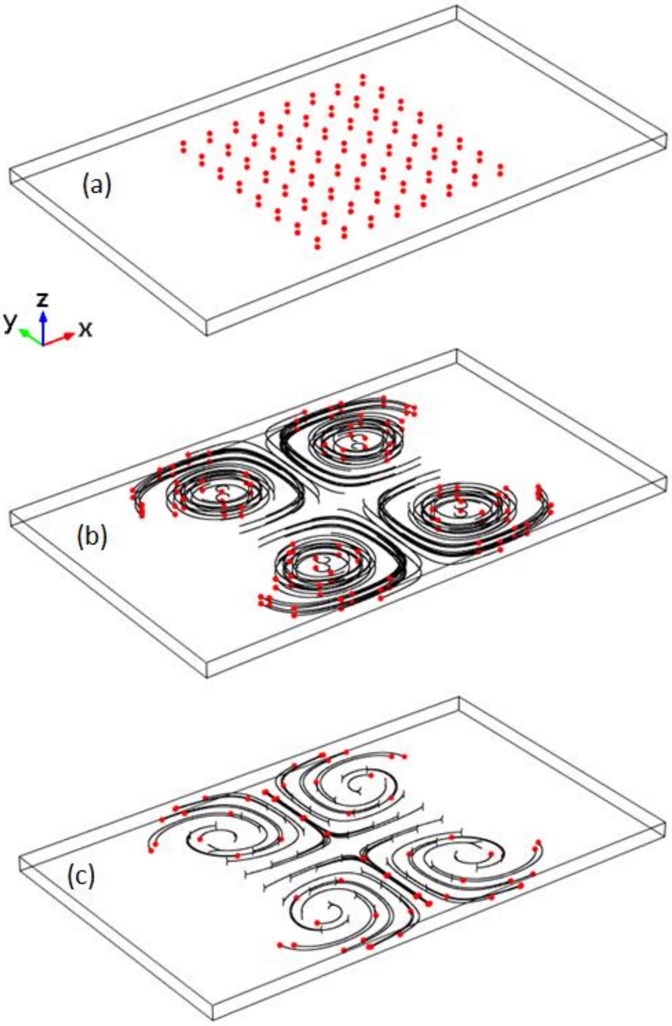

Figure 4.11 3D views of the modelled particle trajectories: (a) an 8×8×2 array of particles is initially arranged at $t = 0$; (b) particle trajectories driven by acoustic streaming induced drag forces; and (c) particle trajectories driven by both acoustic radiation force and streaming-induced drag force, where spheres represent 1 μm beads and the lines show their corresponding trajectories.

## 4.4. Discussion

### 4.4.1. Comparisons between Experiments and Modelling

In the previous sections, the acoustic streaming fields within the thin-layered glass capillary device have been investigated from both experimental and numerical approaches. It can be seen from ***Figure 4.10*** (b) that the modelled four-quadrant streaming pattern, symmetric to the centre of the device and parallel to the transducer face, is in good agreement with the visualised streaming pattern in experiments, ***Figure 4.3*** (b). The magnitudes of acoustic streaming velocities over a series of driving voltages the model and experiments have been plotted in ***Figure 4.12***. It can be seen that the streaming velocity magnitudes obtained from simulations are also in good comparison with the experimental measurements.

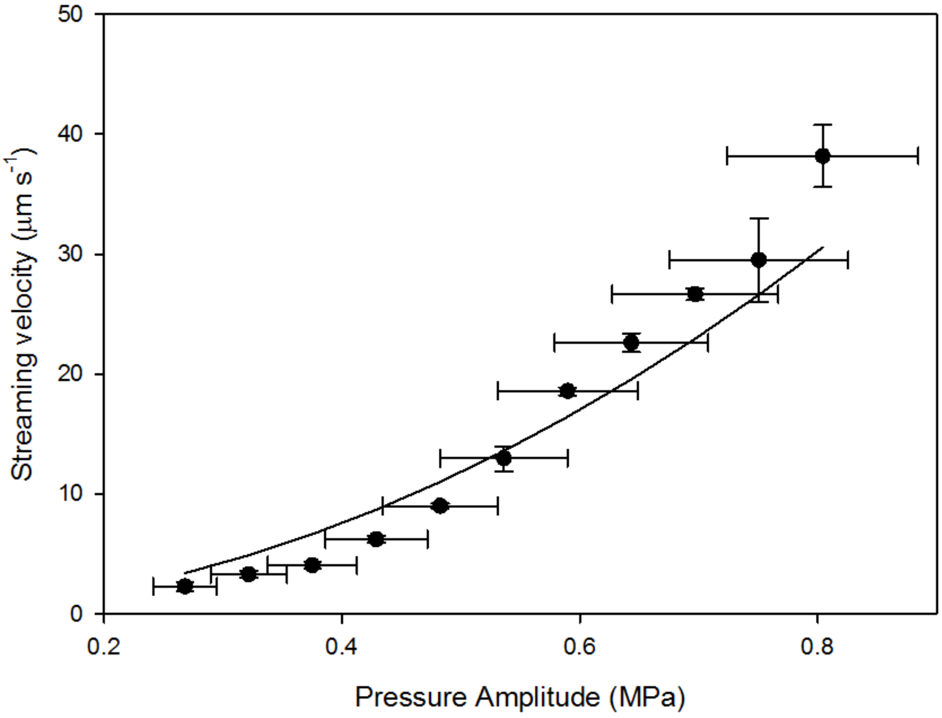

Figure 4.12 The Relationship between the magnitudes of maximum streaming velocity and acoustic pressure, a comparison between μPIV measurements and numerical simulations, where the line and points show the modelled and measured results, respectively.

The differences between the modelled streaming velocity and the measured value may be attributed to the reasons listed below:

1. Acoustic pressure measurement. As described in Section *4.2.4*, the voltage-drop method of pressure measurement is subject to significant errors. Other methods involving μPIV based bead tracking[165] have been shown much more accurate, although this method would be hard to apply in this case due to the radiation force being in line with the viewing direction;
2. The model is a simplification, neglecting coupled resonances that include the transducer and glass walls. Hence the modelled resonance is at a slightly different frequency to that found experimentally (measured: 2.585MHz versus modelled: 2.484MHz);
3. The temperature of the device has not been stabilised. Experiments [165] have shown that self-heating of the transducer and attached structures at higher drive levels can cause a shift in the resonant frequency of the system. It is assumed that this is the cause for the small steepening of the experimental results with frequency (i.e. the curve is steeper than a quadratic one). Temperature stabilisation in this system is not straightforward (compared to the silicon devices presented by Augustsson *et al.*[165]) as the air boundaries of the device are an integral part of the design, and do not allow for thermal connections;
4. Bruus et al.[168] have recently modelled Rayleigh streaming in a glass capillary to a higher level of precision. They show that including thermo-viscous effects, not modelled here, produces a significant correction in systems such as these;
5. The capillary chamber is not perfectly rectangular in cross-section, which will influence the acoustic resonance and resulting streaming pattern;
6. The scale of the fluid channel length ($x$-direction) has tens of acoustic wavelengths, which may allow acoustic attenuation to generate Eckart type streaming that has been ignored in the modelling presented in this chapter.

However, despite these approximations and uncertainties, the model and experiments are sufficient to both demonstrate the existence of the four-quadrant transducer plane streaming patterns, and also deduce the causal mechanism as discussed next.

## 4.4.2. Mechanism of the Transducer Plane Streaming

Equations *(4.4)* for the LVs have a number of terms that are functions of the acoustic velocity components and their derivatives. Numerically examining the LVs on the top ($z = h/2$) and bottom ($z = -h/2$) boundaries (those primarily driving the observed streaming pattern), it was found that they are dominated by the term which is the product of the acoustic velocity parallel to the surface and the $z$-gradient of acoustic velocity in the $z$-direction, $dw_1/dz$. This reflects the strong axial velocity gradients found in planar manipulation devices ($du_1/dx << dw_1/dz$ and $dv_1/dy << dw_1/dz$). For example, the $x$-component LV $u_L$ is approximated by the term,

$$u_L \approx -\frac{1}{4\omega} Re[-2i\, u_1^* \frac{dw_1}{dz}]. \tag{4.8}$$

To find the meaning of the term, $u_1^* dw_1/dz$, the linearized equation of mass conservation was considered

$$\rho_0 \nabla \cdot \boldsymbol{u_1} = -\frac{\partial \rho}{\partial t}. \tag{4.9}$$

In planar acoustofluidic manipulation devices, the gradients of the velocity in the $z$-direction are much greater than in the lateral directions due to the planar geometry[163], hence the left side of Equation *(4.9)* can be approximated as

$$\rho_0 \frac{dw_1}{dz}. \tag{4.10}$$

Meanwhile, using standard relations between density and pressure in linear acoustics[151] and then exploiting the harmonic nature of the excitation, the right-hand-side of Equation *(4.9)* becomes

$$-\frac{\partial \rho}{\partial t} = -\frac{1}{c^2}\frac{\partial p}{\partial t} = -\frac{1}{c^2}(i\omega p_1). \tag{4.11}$$

Thus, Equation *(4.9)* can be written as

$$\frac{dw_1}{dz} \approx -\frac{1}{\rho_0 c^2}(i\omega p_1). \tag{4.12}$$

Using this, the product $u_1^* dw_1/dz$ can be approximated as

$$u_1^* \frac{dw_1}{dz} \approx u_1^* \left(-\frac{i\omega p_1}{\rho_0 c^2}\right) = -\frac{i\omega}{\rho_0 c^2}(u_1^* p_1) = -\frac{i\omega}{\rho_0 c^2} 2\, C_x, \tag{4.13}$$

where the complex intensity, $C_x$, is given by:[169]

$$C_x = \frac{1}{2} u_1^* p_1. \tag{4.14}$$

Thus the $x$-component of the LV can be written

$$u_L \approx \frac{1}{\rho_0 c^2} Re[C_x], \tag{4.15}$$

valid for $du_1/dx \ll dw_1/dz$ and $dv_1/dy \ll dw_1/dz$.

According to Fahy[169], the complex intensity (a harmonic representation of the real, instantaneous intensity, which is a function of time) can be decomposed into two parts: (i) the real part, called the active intensity, which gives the time average energy flow; and (ii) the imaginary part (the reactive intensity) which corresponds to local, oscillatory energy flows with zero time average. It can be seen from Equation *(4.15)* that the LV is proportional to the active intensity. Fahy shows that the active intensity can have a rotational component in fields that have a standing wave component (and that the reactive intensity is irrotational). He states that in standing wave fields this rotation should be interpreted as reflecting the elliptical path of fluid elements rather than a larger scale circulation of energy. The active acoustic intensity vector at the bottom boundary is plotted in ***Figure 4.13***. It can be seen that the pattern it forms at the resonant frequency (***Figure 4.13*** *(e)*) is closely related to the modelled and observed streaming patterns. The active intensity fields in models at various driving frequencies around that resonant frequency are also presented in ***Figure 4.13***. As can be seen from the figures, the four-quadrant vortex pattern can be found in a range of frequencies with different magnitudes on the active intensity. The magnitudes at less resonant frequencies (e.g. ***Figure 4.13*** (b)*)* can be comparable and even bigger than that obtained at the resonant frequency. The insight that these streaming patterns are thus caused, may lead in the future to better control, or elimination of the streaming through more careful control of the interplay between standing and travelling waves in the lateral extents of devices.

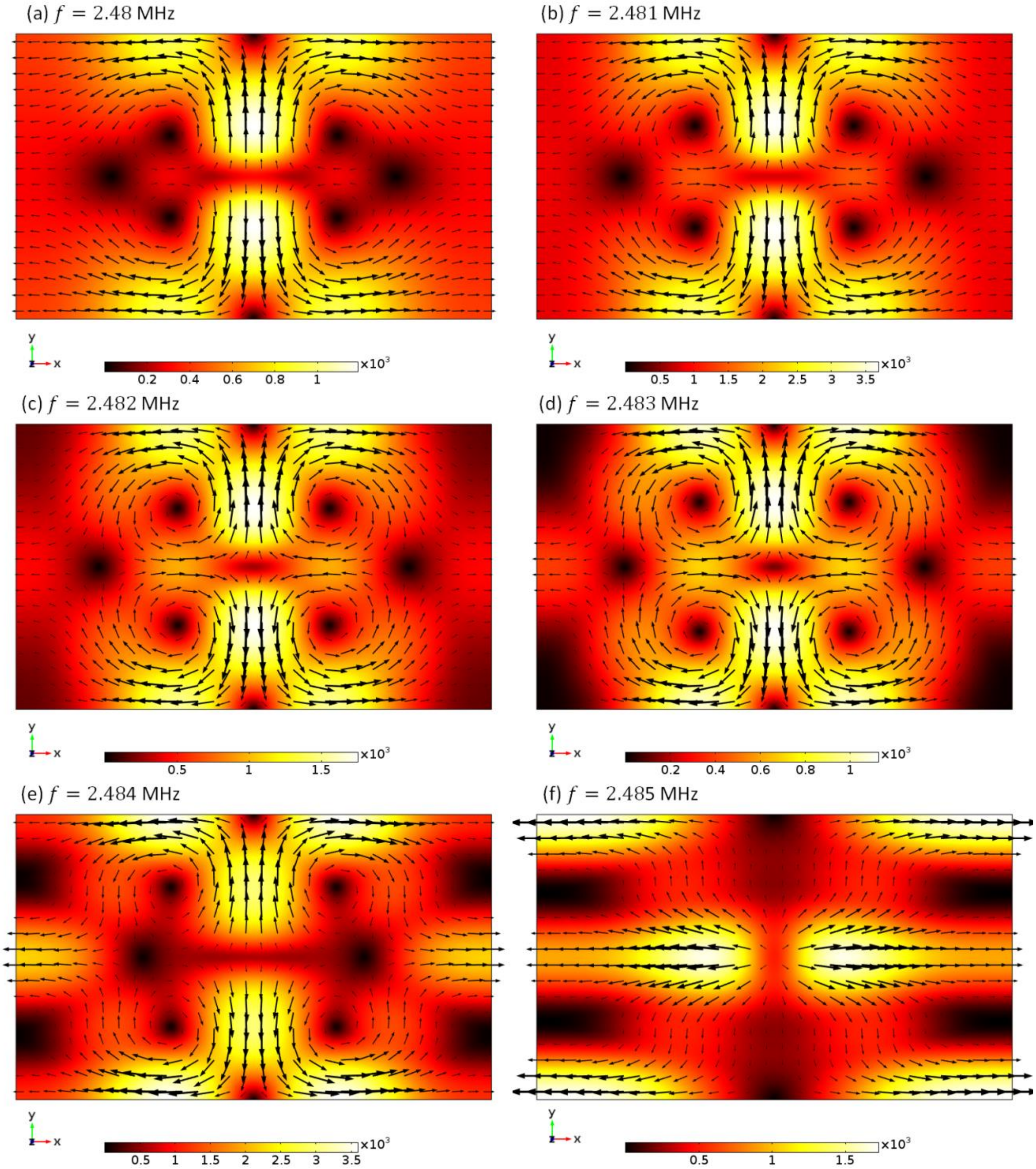

Figure 4.13 The modelled active sound intensity field (unit of W/m$^2$) on the bottom wall of the 3D chamber ($z = -h/2$, the limiting velocity boundary) in models with various driving frequencies: (a) $f = 2.48$ MHz; (a) $f = 2.481$ MHz; (a) $f = 2.482$ MHz; (a) $f = 2.483$ MHz; (a) $f = 2.484$ MHz; (a) $f = 2.485$ MHz, where the arrows and colours show the vector plots and the magnitudes of the active intensity field, respectively.

## 4.5. Conclusions

A four-quadrant transducer plane streaming pattern, symmetric to the centre of the transducer and with the circulation plane parallel to the transducer face, were experimentally visualised and numerically modelled in planar acoustofluidic manipulation devices. This kind of acoustic streaming pattern is different from the better-known Rayleigh and Eckart type pattern both in the shape of streaming flows it generates and in its genesis. The mechanism of the transducer plane streaming has been investigated and presented for the first time. It was found that the transducer plane streaming pattern is related to the active acoustic intensity, which is known to show rotation in acoustic fields. In real acoustic standing wave devices there are also acoustic energy gradients in the lateral directions perpendicular to the standing wave axis. In many cases these are insignificant in comparison with the axial gradients, but they become more significant in planar resonators with large surface areas [164].

Experimental work with tracer beads and µPIV has quantified the streaming flows for a range of excitations. It was found to show good agreement with a finite element model that decomposes the streaming problem into three steps, using results from a linear acoustic analysis to calculate LVs that are applied as boundary conditions to a Stokes flow model.

The explanation on the mechanism of this type of boundary-driven streaming allows us to create designs for controlling or better using of this phenomenon in thin-layered acoustofluidic manipulation systems.

# Chapter 5. Numerical Simulations of 3D Boundary-driven Streaming Fields in Acoustofluidic Systems†

## 5.1. Introduction

As discussed in the previous chapters, acoustic streaming patterns in real acoustofluidic systems are 3D problems so that the results obtained from simplified 2D models cannot always represent the real acoustic streaming conditions. In *Chapter 4*, it has been shown a new type of boundary-driven acoustic streaming pattern, the transducer plane streaming, which is different from the better known classical streaming patterns, *e.g.* Rayleigh streaming[49] and Eckart streaming[72], whose vortex plane is normally perpendicular to the transducer radiating surface. The acoustic streaming patterns simulated from 3D fluid-channel-only models show good consistence with the experimental measurements and it has been analysed that such streaming patterns are typically generated in planar microfluidic resonators where the acoustic energy gradients in the lateral directions parallel to the transducer radiating surface are significant in addition to the gradients perpendicular to the transducer radiating surface. Furthermore, the mechanism behind the transducer plane streaming pattern has been found to be closely related to the active sound intensity field from both numerical and theoretical analyses.

In this chapter, 3D boundary-driven streaming fields in acoustofluidic devices are thoroughly characterised from 3D full configurations of acoustofluidic systems. Firstly, the 3D Rayleigh streaming pattern in a microchannel (mainly 1D standing wave resonance) was simulated and its effect on the movement of micro-particles of various sizes was demonstrated. The results obtained from this model show good comparisons with 3D experimental visualisations shown in literature and demonstrate the fully 3D nature of the acoustic streaming field and the associated acoustophoretic motion of micro-particles in acoustofluidic devices. This method was then applied to another acoustofluidic

---

† A portion of the results presented in this chapter are in ref. 170. Lei, J., M. Hill, and P. Glynne-Jones, *Numerical simulation of 3D boundary-driven acoustic streaming in microfluidic devices.* Ibid. **14**(3): p. 532-41.

device in order to gain insights into an unusual in-plane streaming pattern, the origin of which has not been fully described and its characteristics cannot be explained from the classical theory of Rayleigh streaming. The simulated in-plane streaming pattern was in good agreement with the experimental visualisation. The mechanism behind it was shown to be related to the active sound intensity field, which supports the previous findings on the mechanism of the transducer plane streaming pattern visualised and modelled in a thin-layered acoustofluidic device shown in ***Chapter 4***. To sum up, the LVM was applied to calculate the driving boundary conditions on 3D fluid volumes and model two acoustofluidic manipulation devices described in literature:

a) An acoustofluidic device investigated experimentally by Muller et al.[171]. The simulated results were shown to be in good agreement with the experimental observations and provide evidence of 3D characteristics.
b) The second device was first presented by Hagsater et al.[172]. It was shown to present an unusual pattern of 6×6 in-plane streaming vortices that differed from that predicted by consideration of the Rayleigh streaming pattern and has not previously been explained. By modelling it here we are able to predict the cause of this phenomenon.

In general, this work is trying to demonstrate how full 3D models add to the understanding of the streaming behaviours found in experimental devices. While many systems can be modelled appropriately with suitable 2D approximations, making the correct approximation a-priori is not always straightforward, and can only be judged accurate in hindsight from a 3D representation (be that a model or experimental results). For example in this chapter (Section *5.4*), a 2D model is not sufficient: streaming is driven by a boundary that is parallel to the plane of the observed streaming pattern. In Section *5.2*, the numerical method used to simulate the acoustic streaming field in the main fluid is introduced. Then, the 3D Rayleigh-like streaming pattern in the first device is simulated and analysed in Section *5.3*, where the model, results and a discussion are presented. In Section *5.4*, the unusual acoustic streaming pattern visualised in the second device is investigated and brief conclusions are drawn in Section *5.5*.

## 5.2. Numerical Method

The model in *Chapter 4* presents a 3D fluid-channel-only model while the models in this chapter consider 3D full configurations of the acoustofluidic devices, including the piezoelectric transducer (PZT), carrier layer, fluid channel and the reflector layer. Here, the 3D LVM introduced in *Chapter 4* was used to simulate the acoustic streaming fields in these two acoustofluidic devices. It is the characteristics of the LVM which removes the need for a boundary-layer mesh that reduces the computational load to the point where a 3D full model is viable. This method is generally applicable to acoustofluidic devices working at MHz frequencies where the thickness of viscous boundary layer, $\delta_v$, is typically several orders of magnitude smaller than the dimensions of the fluid chamber so that only the streaming field outside the viscous boundary layer is of interest.

The whole numerical procedure can be split into three steps, which is the same with that used to characterise the transducer plane streaming field in a glass capillary device presented in *Chapter 4*. The finite element package COMSOL 4.4[167] was used to implement each of these steps, described in more detail below. Firstly, the first-order acoustic fields within the devices were simulated using the COMSOL '*Acoustic-Piezoelectric Interaction, Frequency Domain*' interface, which solves the harmonic, linearized acoustic problems, referring to Section *3.2.2*. Secondly, the LVs at all boundaries were calculated as a function of the first order acoustic fields (essentially the streaming is driven by the interaction of the acoustic field with these boundaries). On a planar surface normal to $z$, the LV equations have been derived in Equations *(4.4)*. Finally, a COMSOL '*Creeping Flow*' interface is used to calculate the resulting streaming flows with the LVs acting as slip velocity boundary conditions. This approximates the fluid as incompressible, and neglects inertial terms (Stokes flow) as the streaming Res are much smaller than one in the devices presented in this chapter. The basic theory, governing equations for the second-order streaming velocity field and associated pressure field have been introduced in Section *3.2.4*.

## 5.3. Verification of the 3D Rayleigh Streaming Model in an Acoustofluidic Device

### 5.3.1. Model Configuration and Results

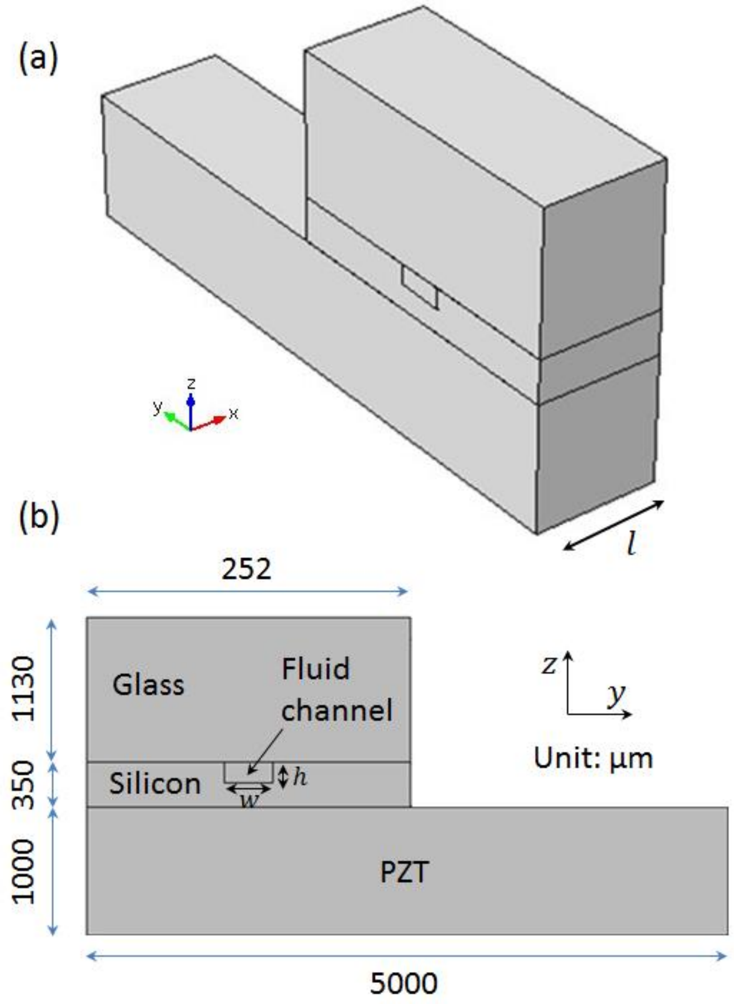

Figure 5.1 (a) The 3D full model considered; and (b) its $yz$ cross-section, including the configuration and dimension.

*Figure 5.1* (a) shows the 3D model considered, which represents a short section of the device (in the $x$-direction) investigated by Muller et al.[171]. A schematic of different layers of the model is shown in *Figure 5.1* (b), composed of a transducer layer (PZT), a carrier layer (silicon), a fluid layer (water), and a reflector layer (glass). The fluid channel has dimensions of 1×0.377×0.157 mm$^3$. The origin of coordinates was set at the centre of the fluid channel such that the fluid channel was located within coordinates: $-l/2 \le x \le l/2, -w/2 \le y \le w/2, -h/2 \le z \le h/2$. The model parameters are summarised in ***Table 5.1***, including particle properties used in particle trajectory simulations. In order to balance the numerical accuracy and the computational load, a uniform distribution of swept mesh with an element size of 50 μm in the fluid channel was used for the results presented here unless otherwise stated, which was chosen based on the mesh dependency study presented in ***Chapter 4***, which shows that $8 \sim 10$ elements within each acoustic wavelength is enough for the simulation of acoustic and streaming fields using the LVM.

Table 5.1 Parameters for the 3D Rayleigh streaming modelling

| | |
|---|---|
| Fluid volume ($l \times w \times h$): | 1 × 0.377 × 0.157 mm$^3$ |
| Driving frequency, $f$: | 1.936 MHz |
| Acoustic speed in fluid, $c_f$: | 1481.4 m·s$^{-1}$ |
| Particle diameter, $d$: | 0.5 & 5 μm |
| Particle density, $\rho_p$: | 1055 kg·m$^{-3}$ |
| Acoustic speed in particle, $c_p$: | 1962 m·s$^{-1}$ |
| Dynamic viscosity of water, $\mu$: | 1.0093 × 10$^{-3}$ Pa·s |
| Fluid density, $\rho_f$: | 999.62 kg·m$^{-3}$ |
| Mesh size: | 5×10$^{-5}$ m |
| Excitation, $\mathrm{V_{pp}}$: | 40 V |

In this step, the left and right walls ($x = \pm 0.5$ mm) were considered as plane wave radiation boundary conditions and the remaining walls as hard boundaries. The resonant frequency was found at 1.963 MHz by using a parametric sweep to find the average acoustic energy density in the fluid layer versus driving frequency (the resonance was taken as the maximum of this function). The modelled acoustic pressure field is shown in ***Figure 5.2***. It can be seen that a lateral half-wavelength ($y$-direction) standing wave field was generated in the fluid channel in this device and the acoustic pressure magnitude decreases from the centre ($x = 0$) to the left and right boundaries ($x = \pm 0.5$ mm) as energy traveling down the channel is largely absorbed by the tubing and connectors at the left and right ends.

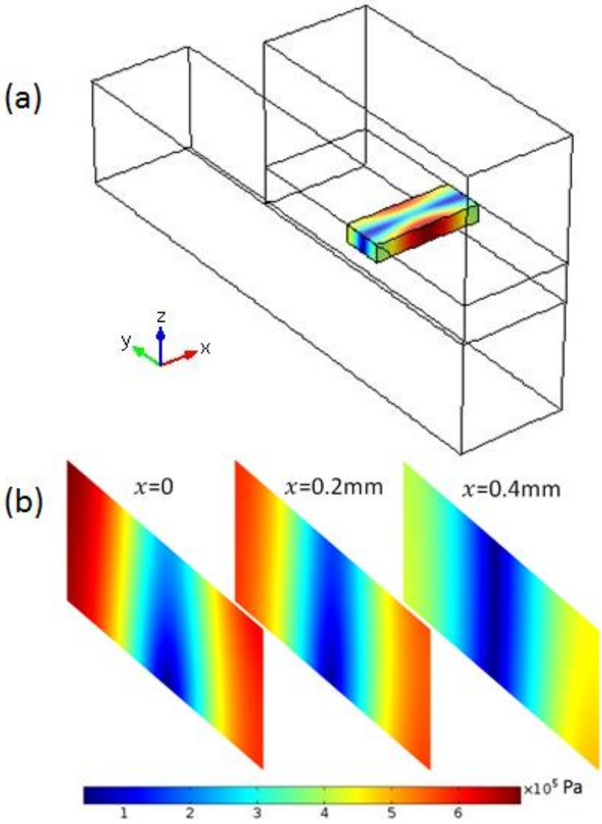

Figure 5.2 Modelled first-order acoustic pressure field: (a) 3D acoustic pressure field within the fluid volume; and (b) acoustic pressure magnitude on three vertical $yz$ planes.

In the '*Creeping Flow*' step of the method, the top and bottom walls of the fluid channel were considered as LV boundary conditions while the remaining four walls were considered as nonslip boundary conditions. ***Figure 5.3*** (a) shows the modelled acoustic streaming velocity magnitudes on the surfaces of fluid channel and ***Figure 5.3*** (b) shows the 3D acoustic streaming field through three $yz$ planes, $x = 0$, $x = 0.2$ mm, and $x = 0.4$ mm. The four counter-rotating vortices that can be seen within the lateral half-wavelength resonator are characteristic of classical Rayleigh streaming. Due to the acoustic variation along the channel axis ($x$-direction), the magnitude of the streaming velocity is at a maximum at the centre ($x = 0$) of the device and decreases with distance from the centre because the acoustic energy density is strongest at the centre ($x = 0$) of the model.

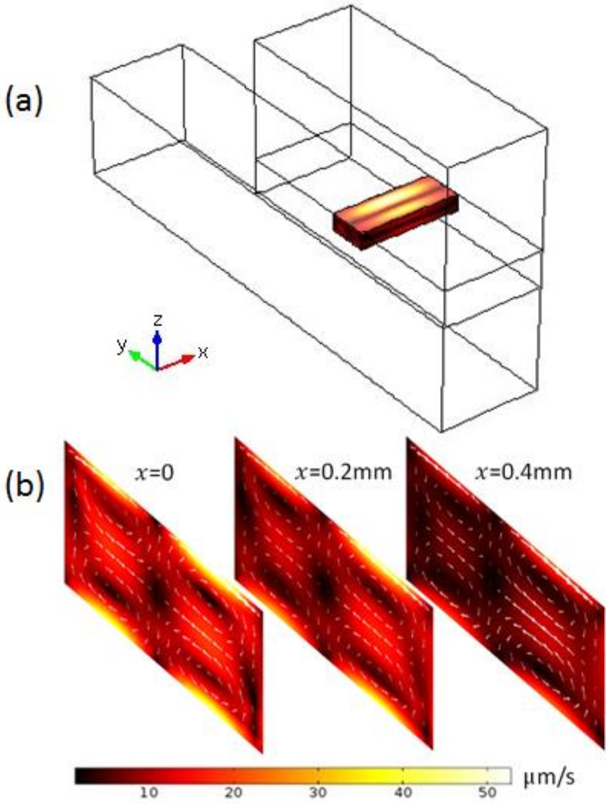

Figure 5.3 Modelled second-order acoustic streaming fields: (a) 3D acoustic streaming field within the fluid volume; and (b) acoustic streaming fields on three vertical $yz$ planes.

In order to understand the effects of acoustic streaming on acoustophoretic motion of microparticles and compare with the experimental visualisation, a numerical simulation of particle trajectories is presented here. Theory of particle movement and the forces on the particles in an acoustofluidic system has been introduced in Section *4.3.3*.

The COMSOL '*Particle Tracing for Fluid Flow*' module was used to implement these equations to simulate the particle trajectories. In order to compare with the experimental investigations shown in ref.[171], the trajectories of 0.5 µm and 5 µm particles were demonstrated here. Both ARF and ASF act on the tracer particles (polystyrene beads of diameter 0.5 µm and 5 µm), resulting in the motion shown in ***Figure 5.4***. It can be seen that the movements of 0.5 µm particles are dominated by the ASF as the pattern the particle trajectories form is closely related to the acoustic streaming field. However, 5 µm particles were firstly driven to the pressure nodal plane by ARF and then slowly dragged to the up and bottom boundaries by ASF. A comparison between numerical simulation and experiments will be shown in the following discussion Section *5.3.2*.

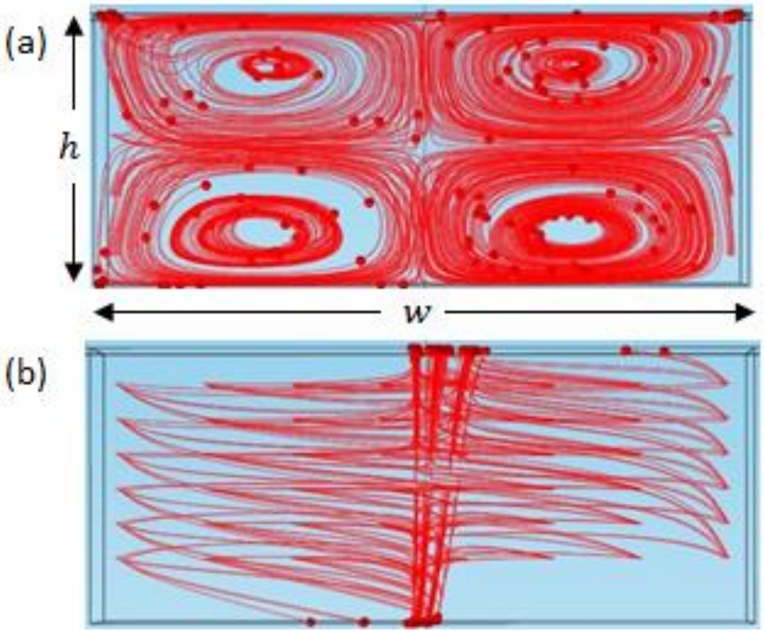

Figure 5.4 Overall views along the channel axis ($x$-direction) of the modelled trajectories of: (a) 0.5 μm particles; and (b) 5 μm particles, which were initially arranged in a 7×8×6 array, where the spheres present the particles and the lines show respectively their trajectories.

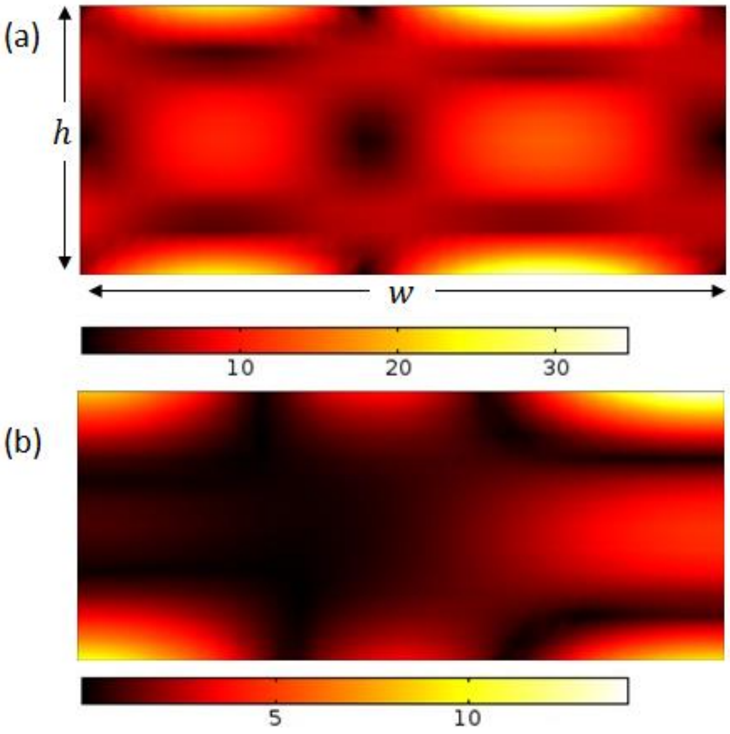

Figure 5.5 A comparison of the magnitudes (unit of μm/s) of acoustic streaming velocity components on a $yz$ plane ($x = -0.3$ mm): (a) In-plane component; and (b) out of plane component (along the channel).

In addition to the dominant Rayleigh streaming pattern in the $yz$-plane, the streaming also has components along the channel axis ($x$-direction), which can cause particle migration along the channel. It can also be seen in ***Figure 5.5*** where the in-plane streaming velocity magnitude (***Figure 5.5*** (a)) can be compared to the smaller but significant out-of-plane component along the channel axis. This exists due to the presence of acoustic energy gradients along the fluid channel ($x$-direction).

### 5.3.2. Discussion

The acoustic streaming pattern obtained from numerical and experimental investigations can be compared from the trajectories of 0.5 μm particles, which are dominated by the ASF. It can be seen from ***Figure 5.4*** (a) and Figure 4 (b) in ref.[171] that classical Rayleigh streaming patterns were obtained from both methods within this lateral half-wavelength resonator.

Due to the quadratic dependence of the LV on the linear acoustic quantities, the relationship between the maximum streaming velocity in the device, $|\boldsymbol{u}_2|_{max}$, and the maximum acoustic pressure, $|p_1|_{max}$, is expected to take the form

$$|\boldsymbol{u}_2|_{max} = \alpha |p_1|_{max}^2, \tag{5.1}$$

where $\alpha$ is a constant. On the other hand, the relationship between the acoustic energy density and acoustic pressure can take the form

$$E = \beta |p_1|_{max}^2, \tag{5.2}$$

where $\beta$ is a constant, so the comparison between experiment and model on the magnitude of acoustic streaming velocity can be achieved from the comparison of relationship between energy density and maximum streaming velocity

$$|\boldsymbol{u}_2|_{max} = \frac{\alpha E_{max}}{\beta} = \gamma E_{max}. \tag{5.3}$$

Experimental work by Muller et al.[171] found that when the energy density measured in the device is approximately $E_{max} = (65 \pm 2)$ J/m³, the corresponding maximum streaming velocity (velocity of 0.5 μm particles) measured is $|\boldsymbol{u_2}|_{max}$ =63 μm/s. Therefore, the measured constant $\gamma$ presented in Equation (5.3) is: $\gamma$ =(0.97±0.03) × $10^{-6}$ $m^4$ $J^{-1}$ $s^{-1}$.

In the model presented here, it was found that when $E_{max} = 54.8$ J/$m^3$ then $|\boldsymbol{u_2}|_{max}$ =52.7 μm/s. Therefore, the constant $\gamma$ of the model is: $\gamma$ = 0.96 x $10^{-6}$ $m^4$ $J^{-1}$ $s^{-1}$.

It can be seen that the magnitude of the acoustic streaming velocities in the model and experiment are also in good agreement.

## 5.4. Investigation of an Unusual Vortex Pattern

### 5.4.1. Background

This section introduces a device presented in 2007 by Hagsater et al.[172] and seeks to explain the unusual streaming pattern observed. *Figure 5.6* shows the chip configuration and the observed in-plane acoustic streaming pattern. It can be seen from *Figure 5.6* (b) that a 6×6 in-plane vortex pattern was generated. However, it can be seen from both the measured trajectories of 5 μm tracer particles (Figure 4 (a) of [172]) and the modelled acoustic pressure Eigen mode (Figure 4 (c) of [172]), a pattern of 6×6 antinodes exists in the square area of the fluid chamber, which would normally be expected to result in a $12 \times 12$ vortex pattern (2 vortices within each half wavelength for the classical Rayleigh streaming pattern). Therefore, the in-plane vortex pattern cannot be explained by classical Rayleigh streaming theory. In order to provide better understanding of this streaming pattern, a finite element model is presented here to simulate the 3D acoustic streaming field in this device and to investigate its origin.

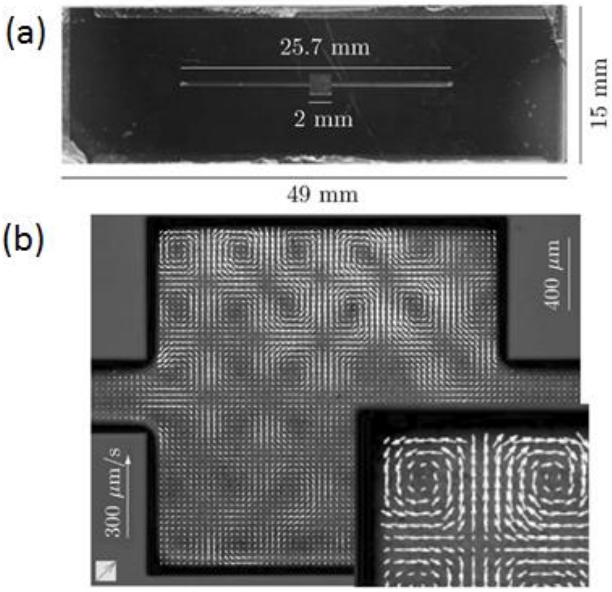

Figure 5.6 Experimental investigation of an unusual in-plane vortex pattern: (a) dimension of the device; (b) visualised in-plane acoustic streaming field, where the inset shows the detail of acoustic streaming field at the top-left corner of chamber. Adapted with permission from Hagsater et al.[172].

### 5.4.2. Finite Element Model and Results

*Figure 5.7* shows the schematic of the model, where (a) is a 3D view of the full device and (b) & (c) are respectively top & side views of the model with dimensioning. The origin of the coordinates was set at the centre of the interface between water and glass. All model parameters are summarised in *Table 5.2*.

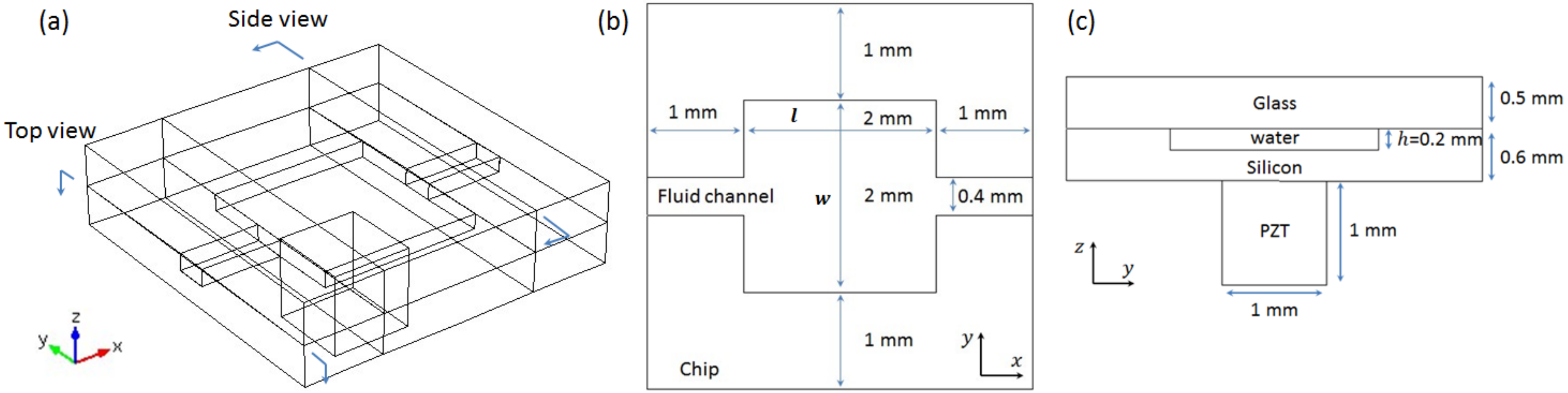

Figure 5.7 (a) 3D full model; (b) top view; (c) side view.

Table 5.2 Parameters for 3D boundary-driven streaming simulations in full configurations of acoustofluidic devices.

| Central square area ($l \times w \times h$): | 2 × 2 × 0.2 mm$^3$ |
|---|---|
| Driving frequency, $f$: | 2.17 MHz |
| Acoustic speed in fluid, $c_f$: | 1481.4 m/s |
| Excitation, $V_{pp}$: | 40 V |
| Dynamic viscosity of water, $\mu$: | 1.0093×10$^{-3}$ Pa s |
| Fluid density, $\rho_f$: | 999.62 kg/m$^3$ |

Firstly the mesh, as with the previous model, was chosen based on the mesh dependency study presented in *Chapter 4* such that 8~10 elements within each acoustic wavelength are enough for the simulation of acoustic and streaming fields using the LVM. In order to balance the computational load and numerical accuracy, a mesh size of 0.08 mm was used for the results presented here, resulting in an estimated mesh-induced numerical error of 2%.

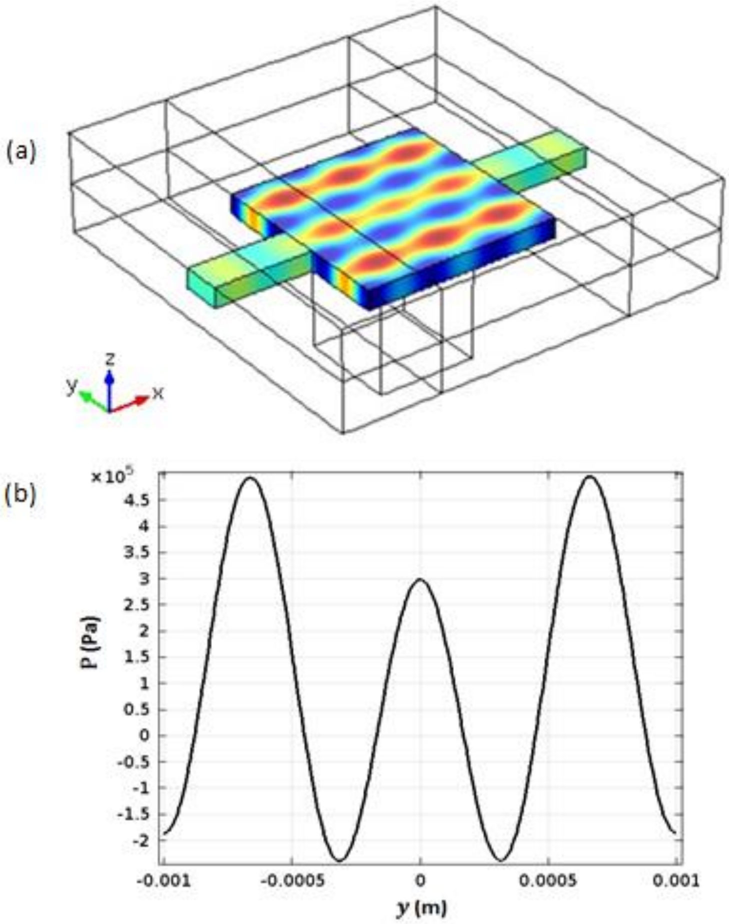

Figure 5.8 Modelled first-order acoustic pressure field: (a) A 3D view; (b) Magnitudes of acoustic pressure along the central line of fluid channel ($x = 0, -1\ \mathrm{mm} \leq y \leq 1\ \mathrm{mm}, z = 0$).

In the acoustic step, the left and right walls of the fluid channel was considered as plane wave radiation boundary conditions and the remaining walls as hard boundaries. The resonant frequency was found at 2.193 MHz using a parametric sweep to find the maximum average acoustic energy density in the fluid layer versus driving frequency. The resonant frequency gives a 2D standing wave in the $x$- and $y$-directions in this shape of fluid channel. A 3D view of the acoustic pressure field within the fluid channel is shown in ***Figure 5.8*** (a). It can be seen that throughout the device the magnitude of acoustic pressure is almost constant along the $z$ axis. In the $xy$-plane, in the central square area of fluid channel (2 mm×2 mm), a primary standing wave field (close to three wavelengths in extent, ***Figure 5.8*** (b)) was established in the $y$-direction and the acoustic pressure distribution also shows a standing wave field of three wavelengths in the $x$-direction due to plane wave radiation boundaries on two ends of fluid channel.

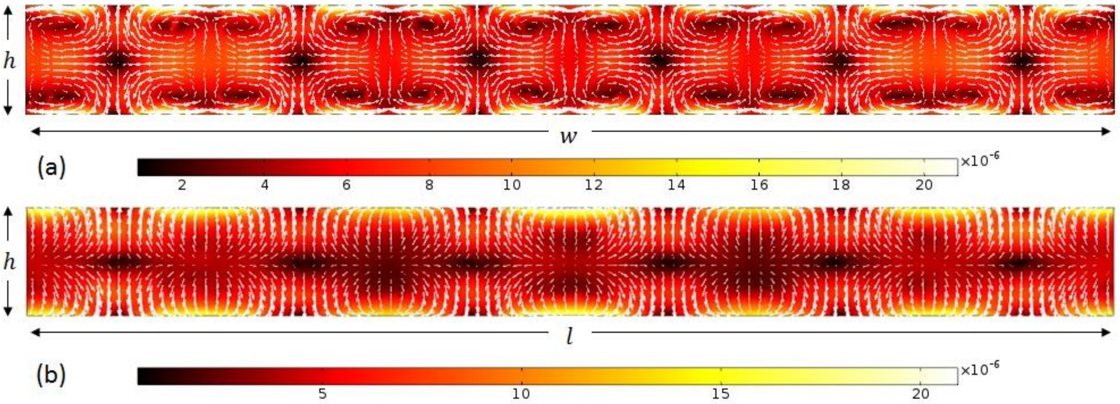

Figure 5.9 The modelled acoustic streaming fields on: (a) a $yz$ cross-section, $x = -0.5$ mm, and (b) a $xz$ cross-section, $y$ = -0.5 mm. The arrows show the orientation of acoustic streaming field and colour bars plot the magnitude of acoustic streaming velocities (unit of μm/s).

In the '*Creeping Flow*' step of the method, the top and bottom boundaries ($z = 0$ and $z = -0.02$ mm) of fluid channel were considered as LV boundary conditions while the other walls were nonslip boundary conditions. In order to help visualise the 3D acoustic streaming field, streaming in both the $yz$ cross-section ($x = 0.5\,\mathrm{mm}$) and $xz$ cross-section ($y = 0.5\,\mathrm{mm}$) in the central square area of fluid channel are plotted in ***Figure 5.9***. Due to a dominant standing wave being established ($3\lambda$) in the $y$-direction and the shape of fluid channel, a classical Rayleigh streaming vortex pattern was observed in the $yz$ cross section, *Figure 5.9* (a). Note that although the chamber is square, the entry and exit channels in the $x$-direction mean that the field is not symmetrical. A similar but weaker vortex pattern was seen in the $xz$ plane, *Figure 5.9* (b), which is the Rayleigh streaming from the weaker $x$-directed standing wave.

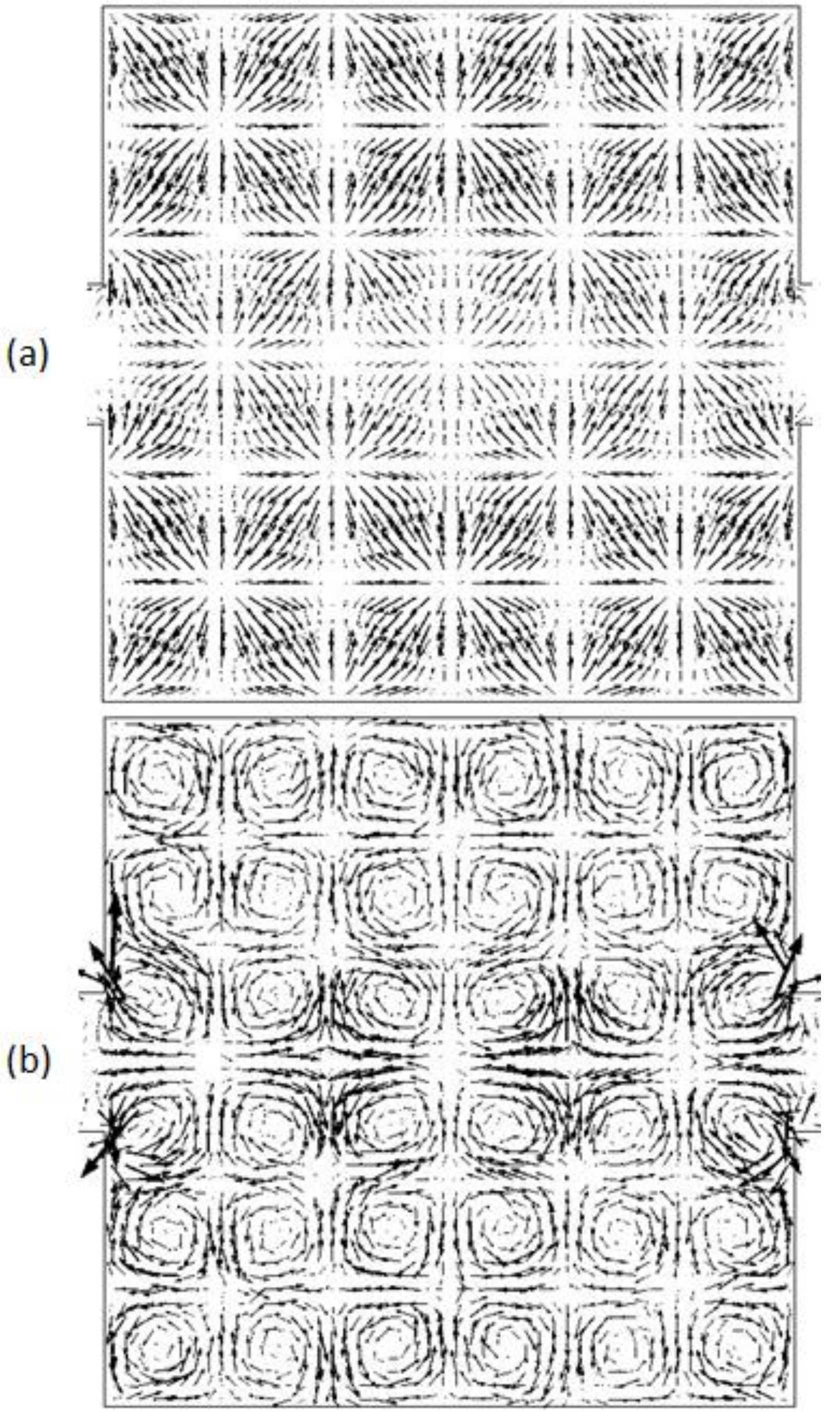

Figure 5.10 Arrow plots of the modelled acoustic streaming fields in the central square area (2 mm × 2 mm) on planes: (a) $z = -0.1\,\text{mm}$; and (b) $z = -0.04\,\text{mm}$.

In order to compare modelled results to the experimentally observed in-plane vortex pattern, a top view of the acoustic streaming field in the central square area of fluid channel is plotted. *Figure 5.10* (a) shows the streaming field at the mid height (plane $z = -0.1\,\mathrm{mm}$) and *Figure 5.10* (b) shows the streaming pattern at plane just below the very top of the fluid channel (plane $z = -0.04$ mm). The reason for choosing this plane to present the in-plane acoustic streaming pattern was that the direction of Rayleigh streaming velocities on this plane was mainly perpendicular to the $xy$ plane, which can be seen from *Figure 5.9* (a), so the in-plane vortex pattern can be seen more clearly. In this $xy$-plane a $6 \times 6$ vortex pattern in the square fluid channel was obtained, which compares well with the experimental visualisation of Hagsater et al.[172]. However, the orientation of acoustic streaming in each single vortex is opposite to the experimental visualisation. Similarly, another 6×6 in-plane vortex pattern can be seen on the plane $z = -0.16$ mm.

In order to investigate the behaviour of this in-plane acoustic streaming pattern in more detail, the model was also run at frequencies around the reported driving frequency. It was found that at all frequencies the 6 × 6 in-plane vortex pattern was observed on the same planes. In addition, another two models were considered with a change in the $x$- and $y$- dimensions of the channel to $1.95 \times 1.95$ mm$^2$ (model 3) and $2.05 \times 2.05$ mm$^2$ (model 4) to investigate the sensitivity of this in-plane streaming pattern to the size of the fluid chamber. It was found that in model 3, both the 6 × 6 vortex pattern and the Rayleigh streaming pattern are close to the results presented here. In model 4, the Rayleigh streaming pattern is similar to the model presented here but the 6×6 in-plane vortex pattern has the direction of rotation of each vortex opposite to that shown in *Figure 5.10* (b) (i.e. the same as that reported in the experimental visualisation). The differences of orientation in each vortex in model 4 and the results presented in *Figure 5.10* are believed to be related to the change of direction of the active sound intensity field in these two models, which will be analysed in more detail in the discussion below.

### 5.4.3. Discussion

#### 5.4.3.1. Mechanism of this 6×6 In-plane Streaming Pattern

It has previously been analysed in *Chapter 4* the transducer plane (i.e. parallel to the transducer face) streaming field in a planar half wave resonator. In that case a $2\times2$ vortex pattern was obtained. For that device the following approximations held:

$$\frac{du_1}{dx} \ll \frac{dw_1}{dz} \text{ and } \frac{dv_1}{dy} \ll \frac{dw_1}{dz}. \tag{5.4}$$

Under these assumptions the LVs shown in Equations *(4.4)* can be approximated to

$$u_L \approx -\frac{1}{4\omega} Re(\,-2i\, u_1^* \frac{dw_1}{dz}), \tag{5.5a}$$

$$v_L \approx -\frac{1}{4\omega} Re(\,-2i\, v_1^* \frac{dw_1}{dz}), \tag{5.5b}$$

which (taking $u_L$ as an example) can also be expressed using the acoustic intensity, $C$,

$$C_x = \frac{1}{2} u_1^* p_1, \tag{5.6a}$$

$$u_L \approx \frac{1}{\rho_0 c^2} Re(C_x). \tag{5.6b}$$

In this device, where the two orthogonal standing waves along $x$ and $y$ are the dominant and which has negligible standing wave in the $z$-direction, a different set of approximations from that in the glass capillary device are valid:

$$\frac{dw_1}{dz} \ll \frac{du_1}{dx} \text{ and } \frac{dw_1}{dz} \ll \frac{dv_1}{dy}. \tag{5.7}$$

In this case, Equations *(4.4)* can now be approximated as

$$u_L \approx -\frac{1}{4\omega} Re\left\{q_x + u_1^* \left[(2+i)\left(\frac{du_1}{dx} + \frac{dv_1}{dy}\right)\right]\right\}, \tag{5.8a}$$

$$v_L \approx -\frac{1}{4\omega} Re\left\{q_y + v_1^* \left[(2+i)\left(\frac{du_1}{dx} + \frac{dv_1}{dy}\right)\right]\right\}. \tag{5.8b}$$

Using Equation *(5.7)* the complex pressure can be written as[151]

$$p_1 \approx \frac{i\rho_0 c^2}{\omega}\left(\frac{du_1}{dx}+\frac{dv_1}{dy}\right). \tag{5.9}$$

Thus Equations *(5.8)* can be expressed in terms of the active sound intensity (the real part) and reactive sound intensity (the imaginary part of complex intensity):

$$u_L = -\frac{1}{4\omega}Re(q_x) - \frac{1}{\rho_0 c^2}Im(C_x) - \frac{1}{2\rho_0 c^2}Re(C_x), \tag{5.10a}$$

$$v_L = -\frac{1}{4\omega}Re(q_y) - \frac{1}{\rho_0 c^2}Im(C_y) - \frac{1}{2\rho_0 c^2}Re(C_y). \tag{5.10b}$$

In order to distinguish the terms that drive the Rayleigh type streaming patterns found in ***Figure 5.9*** (a) from those which produce the in-plane vortex pattern (***Figure 5.10*** (b)), which of the driving terms have rotation in the $xy$ plane (at the boundary where the LVs are calculated, $z = 0$) must be established.

*Firstly, the contribution of the first terms, $q_x$ and $q_y$*: In the linear (inviscid) acoustic approximation the acoustic particle velocity, $\boldsymbol{u_1}$, is irrotational:[151]

$$\nabla \times \boldsymbol{u_1} = 0. \tag{5.11}$$

Using this relation (along with the fact that the spatial derivatives of $\nabla \times \boldsymbol{u_1}$ must also be zero, it was found that the curl of the field $\boldsymbol{Q} = (q_x, q_y, 0)$ is everywhere zero and hence will not contribute to the $xy$ 6×6 in-plane vortex pattern.

*Then, the contribution of the remaining terms*: As discussed in the previous analysis in Section *4.4.2*, according to Fahy[169], only the active intensity, the real part of complex sound intensity can have a rotational component in a standing wave field and this rotation reflects the elliptical path that fluid particles take rather than circulation of energy on a larger scale.

Thus the rotational component of the streaming field in the $xy$ plane is proportional to the active sound intensity components of Equations *(5.10)*. The active sound intensity is plotted in ***Figure 5.11*** and can be seen to closely resemble the rotational part of the modelled and experimental fields found in ***Figure 5.10*** (b) and ***Figure 5.6*** (b). Interestingly the rotation of the LV field is in the opposite direction to that of the active intensity under this approximation (Equation *(5.7)*), compared to that previously investigated where the approximations of Equation *(5.4)* were valid.

Now, it is clear why the direction of $xy$-plane rotation is different in this model and model 4. Examining the models it was found that the change of dimension of fluid chamber changes the relative phases of the $x$- and $y$-components of the standing wave, which thus changes the direction of rotation of the active sound intensity field, and hence the transducer plane streaming field. Detailed information is presented in the section below.

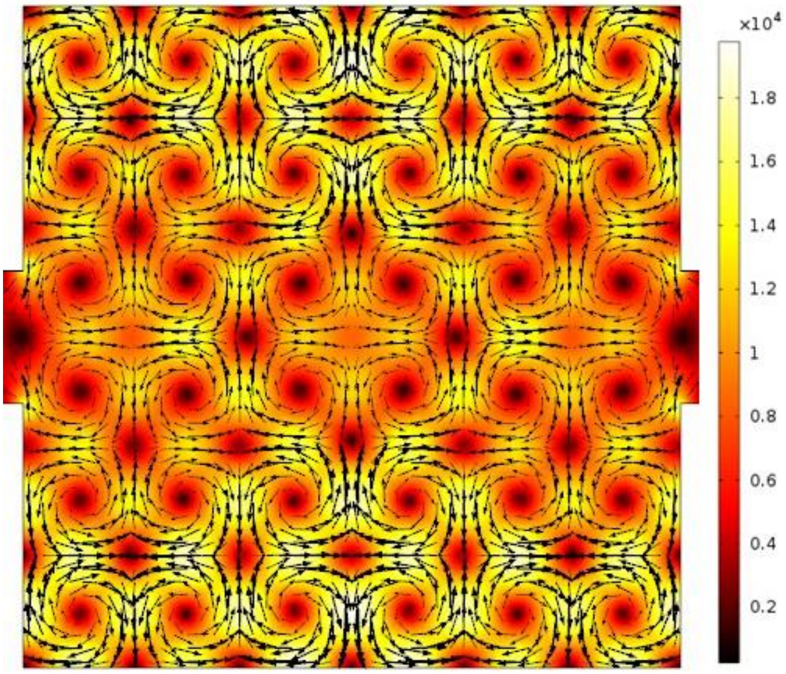

Figure 5.11 The modelled active sound intensity field on a limiting velocity boundary ($z = -0.1$ mm) in the central square area of the fluid channel (2 mm × 2 mm), where the arrows and colours show its vector plots and magnitudes (unit of W/m$^2$), respectively.

#### 5.4.3.2. Effects of Channel Dimensions on the In-plane Streaming Field

In order to investigate the sensitivity of modelled acoustic streaming patterns to channel dimensions, another two models (3 & 4), illustrated in Section *5.4.2* with respectively slight changes on the dimensions in the central square area of the fluid channel, are shown here. The differences on the dimensions for the entire models considered are presented in *Table 5.3* and all other dimensions are the same.

The simulated results for models 3 & 4 are shown in ***Figure 5.12*** and concluded in ***Table 5.3***. It can be seen from ***Figure 5.12*** (a) that, in both cases, two orthogonal standing waves in the $x$- and $y$-directions were established ($\sim 3\lambda$) and 6×6 in-plane vortex pattern with circulation parallel to the bottom surface ($z = -0.1$ mm) were obtained in the central square area of the fluid channel. However, the circulation of each vortex in the 6 × 6 matrix in model 4 is in the opposite direction with that in model 3 as well as that in model 2 (***Figure 5.10*** (b)) although the Rayleigh streaming patterns for all these models have the same distributions (***Figure 5.12*** (c)). This difference emerges due to a change of phase of the standing wave from the modification of the dimension in the central square area of fluid channel. It can be seen from ***Figure 5.12*** (a) that the phase of standing wave in the cutdown model (model 3) is the same with that in model 2, but a phase difference of $\pi$ exists when the dimension of main fluid channel is slightly increased (model 4). This modification on the phase of standing waves in these models can in result affect the active sound intensity field in the main fluid channel, shown ***Figure 5.12*** (d), from which it can be seen the active sound intensity field in these two models are also in opposite direction for each vortex in the same position, which supports the conclusion that has been made in previous section that the in-plane vortex pattern is generated by the active sound intensity field and they are in opposite directions.

Table 5.3 Comparisons of parameters and modelled results for all the models considered in this section on the simulation of an unusual 6 × 6 in-plane vortex pattern, where the pressure field compares the pressure on planes $y = 0$ and the acoustic streaming field and the active sound intensity field compare the orientation of vortex in the top left corner.

| Models | Central area ($l \times w$) | Acoustic pressure | Acoustic streaming | Active sound intensity |
|---|---|---|---|---|
| 2 | 2 x 2 mm$^2$ | Maxima | Clockwise | Anti-clockwise |
| 3 | 1.95 x 1.95 mm$^2$ | Maxima | Clockwise | Anti-clockwise |
| 4 | 2.05 x 2.05 mm$^2$ | Minima | Anti-clockwise | Clockwise |

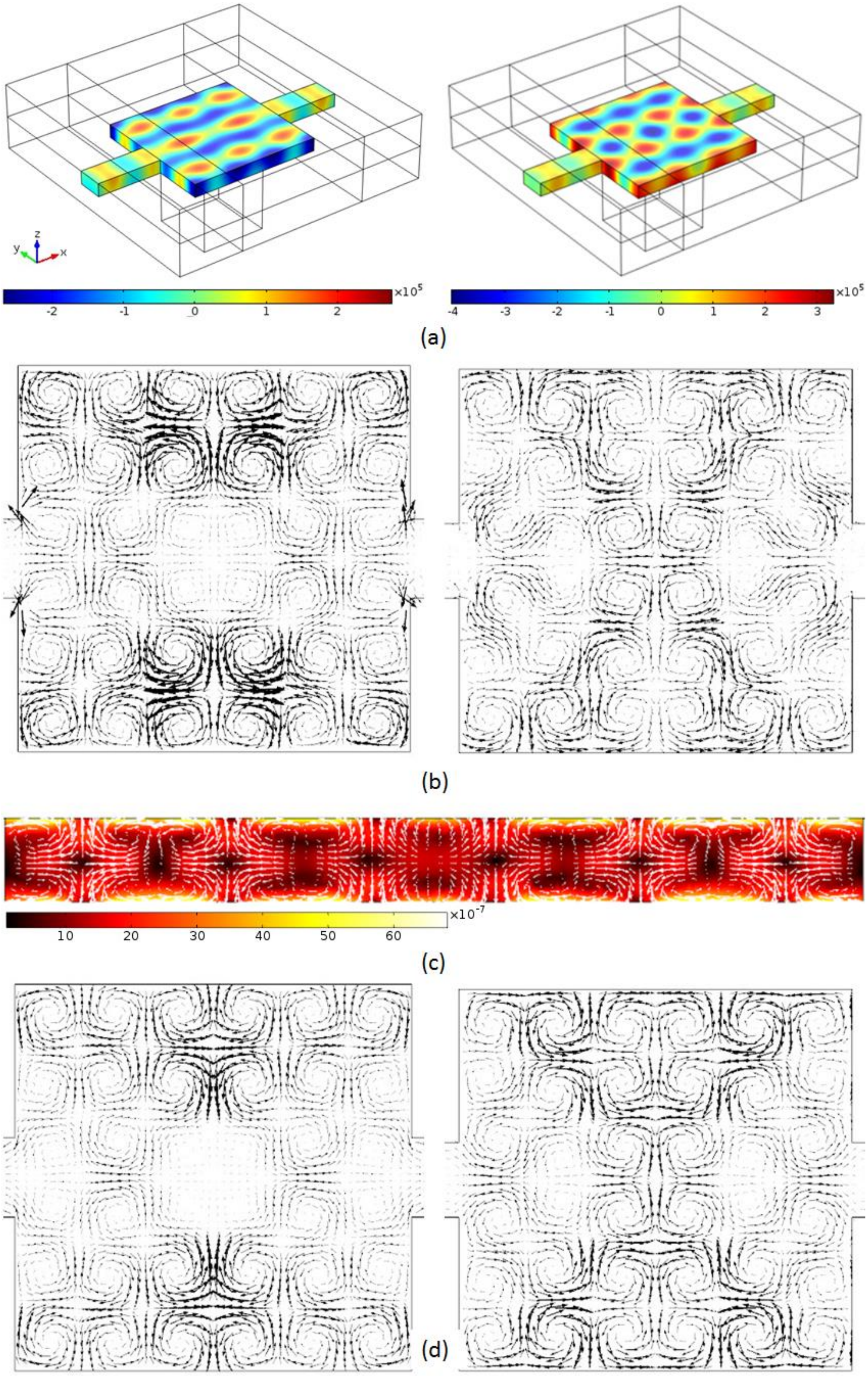

Figure 5.12 Simulated results in models 3 (left column) and 4 (right column): (a) acoustic pressure fields (unit of Pa); (b) in-plane acoustic streaming fields in the central square area of fluid channel (2 mm × 2 mm) on plane $z = -0.04$ mm; (c) Rayleigh streaming field (unit of m/s) in the fluid channel on plane $x = 0$; (d) active sound intensity field on the bottom boundary of the main fluid channel ($z = -0.1$ mm).

## 5.5. Conclusions

The 3D Rayleigh streaming pattern in an acoustofluidic device has been simulated using the LVM and its effects on acoustophoretic motion of microparticles have been presented. While results obtained from 2D simulations of streaming in uniform channels can show good accuracy, this 3D method permits modelling of subtle effects relating to non-uniformities and resonances in the length direction of channels, and also the modelling of more complex structures, suggesting that streaming motion exists in all three directions. The modelled acoustic streaming field compared well with the experimental investigations.

Additionally, acoustic streaming due to two orthogonal standing waves in an acoustofluidic device with a main square area at the centre has been numerically investigated and its mechanism considered. Previous experimental work had reported a regular array of vortices that could not be explained by analogy with Rayleigh streaming since the periodicity of the structure did not match such a hypothesis. It has been demonstrated that in certain planes the model predicts similar circulatory patterns to those found in the experiments, which was found to be closely related to the active sound intensity field. With a slight change on the size of the fluid channel, the direction of orientation of in-plane streaming pattern was changed due to the change of active sound intensity field although the Rayleigh streaming pattern remained the same. Further experimental verification that the pattern found in the model is consistent with that observed is necessary to consider the origin of these vortices *solved,* however the mechanism described here would seem a strong candidate.

As illustrated, numerical results obtained from this computationally efficient method can not only represent 3D acoustic and streaming fields in real micro-acoustofluidic devices but also provide good comparisons with experimental measurements. This should allow such models to be used to predict the streaming fields in micro-acoustofluidic devices to provide optimization of device designs for various applications. This LVM is valid for modelling boundary induced streaming fields when the local radius of curvature of the boundaries is much larger than the viscous penetration depth and the streaming velocities are low enough to be within a strictly laminar regime. It does not, however, model Eckart type streaming[72, 106] induced by bulk absorption of sound, which can be modelled as a volume force on the fluid[173, 174]. Thus this method is not suitable for modelling the majority of streaming found in high frequency SAW systems[175, 176], but it would be interesting to explore to what extent boundary driven streaming contributes in these systems. This work will be investigated in future although it will be not included in this thesis.

# Chapter 6. Modal Rayleigh-like Streaming in Acoustofluidic Systems[‡]

## 6.1. Introduction

In resonant acoustofluidic particle manipulation devices, acoustic streaming flows are typically found in addition to the ARF. These are generally considered as a disturbance as they place a practical lower limit on the particle size that can be manipulated by the primary ARF [153, 178]. However, acoustic streaming can also play an active role in such systems, such as particle trapping[154, 179-182], two-dimensional particle focusing[183] and particle separation[184]. Most acoustofluidic manipulation devices utilise standing wave fields and the acoustic streaming field is generally dominated by boundary-driven streaming which arises from the acoustic attenuation within the viscous boundary layer due to the no-slip condition on the walls of the fluid channel. Another important streaming pattern, Eckart streaming[72], requires acoustic absorption over longer distances (e.g. in SAW devices[175, 176]) than those typically found in the devices of interest here.

While Rayleigh streaming has been recently extensively studied within the field of acoustic particle trapping and manipulation [48, 79, 106, 145, 168, 185], there are acoustic streaming patterns observed experimentally in acoustofluidic manipulation devices that cannot be explained by Rayleigh's classical theory[154, 172, 186]. In the previous chapters, the mechanisms behind the transducer plane streaming and 3D acoustic streaming patterns have been explained. It was shown that, for the transducer plane streaming fields, the LV field was closely related to the active sound intensity field at the driving boundaries. The expressions for the LVs have terms corresponding to acoustic velocity gradients in different directions. Depending on which of these is dominant, different acoustic streaming patterns arise, e.g. transducer plane streaming (streaming vortex parallel to the driving surface, e.g. *Figure 6.1* (b)) and Rayleigh streaming (streaming vortex perpendicular to the driving surface,

---

[‡] A portion of the results presented in this chapter are in ref. 177. Lei, J., P. Glynne-Jones, and M. Hill, *Modal Rayleigh-like streaming in layered acoustofluidic devices.* Physics of Fluids, (under review).

e.g. *Figure 6.1* (d)) for the rotational and irrotational features of respectively the active and reactive intensity patterns in acoustic fields[169].

In this chapter, the conditions under which each of these streaming patterns discussed above is dominant in layered acoustofluidic particle manipulation devices with different channel aspect ratios are addressed and how the LV field for each case relates to different parts of the complex acoustic intensity fields at the driving boundaries are shown. A new boundary-driven streaming pattern, here called modal Rayleigh-like streaming, which has not been discussed or shown experimentally before, is also discussed here. In this regime, the main streaming field is driven by boundaries perpendicular to those that drive conventional Rayleigh patterns, the streaming has a roll size greater than the quarter wavelength of the main acoustic resonance, and the scale is instead related to a cavity mode that drives the four-quadrant transducer plane streaming pattern, *Figure 6.1* (c).

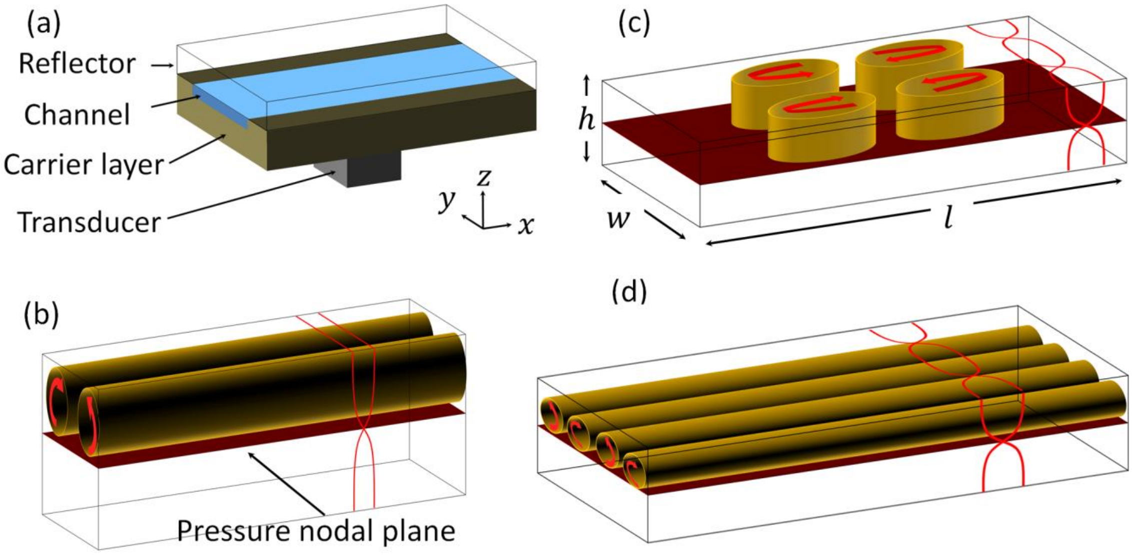

Figure 6.1 Schematic illustrations of: (a) a layered acoustofluidic manipulation device; (b) Rayleigh streaming in a fluid channel with high aspect ratio on its $yz$ cross-section ($h/w > 1$); (c) four-quadrant transducer plane streaming field in a fluid channel with low aspect ratio ($h/w \leq 1/20$); and (d) modal Rayleigh-like streaming in a fluid channel with medium aspect ratio ($1/3 \leq h/w \leq 2/3$); where the waveforms on the surfaces of the 3D volumes show respectively the standing wave fields established in these fluid channels, the planes through the half-heights of the fluid volumes are the pressure nodal planes, and the rolls of cylinders show the paralleled streaming vortices with the arrows representing their orientations.

## 6.2. Statement of the Problem

In ***Chapter 4***, it has been shown that, in thin layered acoustofluidic manipulation devices (***Figure 6.1*** (a)), a (2,1) cavity mode can be easily excited on the $yz$ cross-sections of the fluid channel: in addition to the main half-wave standing wave established in the $z$-direction, the pressure field along the channel width also has a standing wave variation (waveforms in ***Figure 6.1*** (b)). In the discussion Section ***4.4.2***, it was shown that, due to the low aspect ratio of the fluid channel in the $yz$ cross-section ($h/w = 0.05$), $du_1/dx$ and $dv_1/dy$ can be neglected compared to $dw_1/dz$ in the divergence of acoustic velocity vector, $\nabla \cdot \boldsymbol{u_1}$, which approximates the LV field on the top and bottom surfaces to the active intensity field. At this cavity mode, the active intensity field on the top and bottom surfaces of the fluid channel above the transducer area have an in-plane rotational pattern, driving the four-quadrant transducer plane streaming at all heights of the fluid channel.

In the following, it will be demonstrated step by step how the LV fields relate to different parts of the complex intensity and in turn affect the acoustic streaming patterns in various fluid channels with different aspect ratios on the $yz$ cross-sections. In all these fluid channels, the acoustic resonances are assumed to be the same pattern, the cavity mode presented in ***Figure 4.8***. It can be seen from the modelling shown in later sections that it is possible to excite this cavity mode in all the models with various dimensions.

The equations for the two components of the LV field on the top and bottom surfaces of the fluid channel in 3D Cartesian coordinates are shown in Equations ***(4.4)***. Here they are repeated for the clarification of the problem:

$$u_L = -\frac{1}{4\omega} Re\left\{u_1 \frac{du_1^*}{dx} + v_1 \frac{du_1^*}{dy} + u_1^*\left[(2+i)\nabla \cdot \boldsymbol{u_1} - (2+3i)\frac{dw_1}{dz}\right]\right\}, \tag{6.1a}$$

$$v_L = -\frac{1}{4\omega} Re\left\{u_1 \frac{dv_1^*}{dx} + v_1 \frac{dv_1^*}{dy} + v_1^*\left[(2+i)\nabla \cdot \boldsymbol{u_1} - (2+3i)\frac{dw_1}{dz}\right]\right\}. \tag{6.1b}$$

In layered acoustofluidic manipulation devices with the resonances established at the cavity mode shown in ***Figure 4.8***, $du_1/dx$ can be neglected as the half-wave standing wave field in the $x$-direction is established over a much longer distance than that in the other two dimensions (in the modelling, the plane wave radiation boundary conditions on the two ends of the fluid channel allows minimal reflections) and thus gradients in this direction have a lower contribution, compared to the other two acoustic velocity gradients, to the divergence of the acoustic velocity vector, $\nabla\cdot\boldsymbol{u_1}$. Therefore, the LVs can be approximated as

$$u_L \approx -\frac{1}{4\omega}Re\left\{u_1^*\left[i\left(\frac{dv_1}{dy}-2\frac{dw_1}{dz}\right)+2\frac{dv_1}{dy}\right]\right\}, \tag{6.2a}$$

$$v_L \approx -\frac{1}{4\omega}Re\left\{v_1^*\left[i\left(\frac{dv_1}{dy}-2\frac{dw_1}{dz}\right)+3\frac{dv_1}{dy}\right]\right\}. \tag{6.2b}$$

Meanwhile, the complex sound intensity, $C$, can be correspondingly expressed as[151]

$$C_x = \frac{1}{2}u_1^*p_1 \approx \frac{\rho_0 c^2}{2\omega}u_1^*\left[i\left(\frac{dv_1}{dy}+\frac{dw_1}{dz}\right)\right], \tag{6.3a}$$

$$C_y = \frac{1}{2}v_1^*p_1 \approx \frac{\rho_0 c^2}{2\omega}v_1^*\left[i\left(\frac{dv_1}{dy}+\frac{dw_1}{dz}\right)\right]. \tag{6.3b}$$

Combining the Equations *(6.2)*-*(6.3)*, it can be found that, in the LV equations, $dw_1/dz$ only contributes to the active intensity component while $dv_1/dy$ contributes to both active and reactive intensity components. Therefore, following a change of dominant terms in the divergence of the acoustic velocity vector, three regions can be seen:

1. $dw_1/dz$ dominates in $\nabla\cdot\boldsymbol{u_1}$:

$$u_L \approx -\frac{1}{4\omega}Re\left\{u_1^*\left[i\left(-2\frac{dw_1}{dz}\right)\right]\right\} = \frac{1}{\rho_0 c^2}Re[C_x], \tag{6.4a}$$

$$v_L \approx -\frac{1}{4\omega}Re\left\{v_1^*\left[i\left(-2\frac{dw_1}{dz}\right)\right]\right\} = \frac{1}{\rho_0 c^2}Re[C_y]. \tag{6.4b}$$

For this case, the LV fields on the top and bottom surfaces have the same pattern as the active intensity field, which results in transducer plane streaming. (***Chapter 4***)

2. $dv_1/dy$ dominates in $\nabla\cdot\boldsymbol{u_1}$:

$$\begin{aligned} u_L &\approx -\frac{1}{4\omega}Re\left\{u_1^*\left[i\frac{dv_1}{dy}+2\frac{dv_1}{dy}\right]\right\} \approx -\frac{1}{4\omega}Re\left\{u_1^*\cdot 2\frac{dv_1}{dy}\right\} \\ &= -\frac{1}{\rho_0 c^2}Im[C_x], \end{aligned} \tag{6.5a}$$

$$\begin{aligned} v_L &\approx -\frac{1}{4\omega} Re\left\{v_1^*\left[i\frac{dv_1}{dy} + 3\frac{dv_1}{dy}\right]\right\} \approx -\frac{1}{4\omega} Re\left\{v_1^* \cdot 3\frac{dv_1}{dy}\right\} \\ &= -\frac{3}{2\rho_0 c^2} Im[C_y]. \end{aligned} \tag{6.5b}$$

For this case, the imaginary parts in the square brackets can be ignored for the reason that, in a standing wave field, the reactive intensity field is much stronger than the active intensity field[169]. Considering the acoustic pressure distribution on the LV boundary, the following relationship is also established

$$Im[C_x] \ll Im[C_y], \tag{6.6}$$

as the reactive intensity vector field is irrotational, diverging from the acoustic pressure maxima and concentrating at the pressure minima. Therefore,

$$u_L \ll v_L = -\frac{3}{2\rho_0 c^2} Im[C_y]. \tag{6.7}$$

Actually, if the 3D problem is simplified to a 2D problem, assuming an acoustic standing wave in the $y$-direction of the $yz$ cross-section of the fluid channel excited by the boundary $y = -w/2$, the LVs can be turned into the LVs obtained by Rayleigh[75]:

$$u_L = 0, \tag{6.8a}$$

$$v_L = \frac{3}{4\omega} \cdot v_1^* \frac{dv_1}{dy}. \tag{6.8b}$$

3. $dw_1/dz$ and $dv_1/dy$ are comparable in $\nabla \cdot \boldsymbol{u_1}$:
   For this case, the LVs have the same derivation as that for case 2, which can be seen more clearly from the discussion shown below.

Therefore, it can be seen that a change on the dominant terms between the magnitudes of the two significant acoustic velocity gradients, $dw_1/dz$ and $dv_1/dy$, can alter the LV field to be closer to different parts of the complex intensity. In order to predict the acoustic streaming patterns in layered acoustofluidic manipulation devices, it is necessary to understand the sensitivity of the ratio of the two main acoustic velocity gradients to the channel dimensions, defined as

$$r = \frac{dw_1}{dz} \Big/ \frac{dv_1}{dy}. \tag{6.9}$$

In Sections *4.4.2* and *5.4.3.1*, it was shown how the individual terms of the LV equations in two devices were proportional to the active and reactive sound intensity fields, respectively. From the analyses given above, it can be concluded that for $r \gg 1$, the LV field typically has a similar pattern to the active intensity field; while for $r \ll 1$, the LV field is dominated by the reactive intensity fields. In the following, the relationship between this ratio and the aspect ratio of the fluid channel cross-sections are demonstrated.

In order to demonstrate how the ratios $r$ change in devices with various dimensions, the Euler equation is considered:

$$\frac{\partial \boldsymbol{u_1}}{\partial t} + \frac{1}{\rho_0} \nabla p_1 = 0, \tag{6.10}$$

from which the following equations can be deduced

$$v_1 = \frac{i}{\rho_0 \omega} \cdot \frac{dp_1}{dy}, \tag{6.11a}$$

$$w_1 = \frac{i}{\rho_0 \omega} \cdot \frac{dp_1}{dz}. \tag{6.11b}$$

Therefore, it can be seen that the acoustic velocity fields are closely related to the gradients of the acoustic pressure fields and the acoustic velocity gradients can be expressed as the second derivatives of the acoustic pressure, following

$$\frac{dv_1}{dy} = \frac{i}{\rho_0 \omega} \cdot \frac{d^2 p_1}{dy^2}, \tag{6.12a}$$

$$\frac{dw_1}{dz} = \frac{i}{\rho_0 \omega} \cdot \frac{d^2 p_1}{dz^2}. \tag{6.12b}$$

Let's consider the (2, 1) cavity mode established on the $yz$ cross-section of the fluid channels: with respectively half-wave and one-wave in $z$- in the $y$-directions, shown in ***Figure 6.2*** (a), where the distribution of pressure magnitudes on a $yz$ cross-section ( $x = 0$ ) is presented. From these characteristics, an approximation of the ratio of pressure gradients (magnitudes) can be calculated:

$$A\left(\left|\frac{dp_1}{dz}\right|\right) \Big/ A\left(\left|\frac{dp_1}{dy}\right|\right) \approx \frac{w}{2h}, \tag{6.13}$$

where $A(\cdot)$ and $|\cdot|$ represent the spatial average and absolute values over the LV boundary.

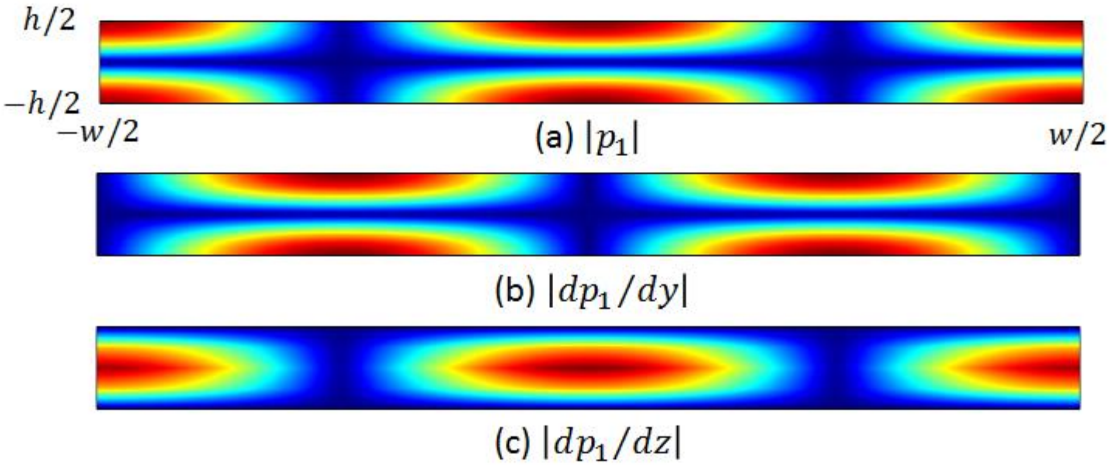

Figure 6.2 Colour plots of the (a) acoustic pressure magnitudes, $|p_1|$; (b) $|dp_1/dy|$; and (c) $|dp_1/dz|$, on a $yz$ cross-section of the fluid channel ($x = 0$), where the red and blue show their maximum and minimum values, respectively.

*Figure 6.2* (b)-(c) show the distributions of two acoustic pressure gradients along $y$- and $z$-directions on a $yz$ cross-section ($x = 0$), respectively. It can be seen that, similar to the acoustic pressure distributions, the two pressure gradients, $|dp_1/dy|$ and $|dp_1/dz|$, also respectively have one wavelength in the $y$-direction and a half wavelength in the $z$-direction of the chamber. Actually, the distributions of the two pressure gradients show respectively the distribution of these corresponding acoustic velocity fields such that the distributions of the acoustic pressure gradients are out of phase with the pressure field (Equation *(6.12)*). Therefore, the following relationship is established

$$A\left(\left|\frac{d^2p_1}{dz^2}\right|\right) \Big/ A\left(\left|\frac{d^2p_1}{dy^2}\right|\right) \approx \left(\frac{w}{2h}\right)^2. \tag{6.14}$$

Combining Equations *(6.12)* & *(6.14)*, thus

$$r = A\left(\left|\frac{dw_1}{dz}\right|\right) \Big/ A\left(\left|\frac{dv_1}{dy}\right|\right) \approx \left(\frac{w}{2h}\right)^2. \tag{6.15}$$

This means that the ratio of the significant acoustic velocity gradients, which determines which part of the complex intensity dominates the LV field, are dependent on the aspect ratio of the fluid channel cross-sections. The simulated $r$ in all the models considered are plotted in *Figure 6.3*, which shows that the approximation of Equation *(6.15)* is accurate to within an error of 2% in all the cases. From this relationship, it can be concluded that a change in the aspect ratio of the fluid channel cross sections could alter the acoustic streaming fields from one pattern to another due to rotational and irrotational properties of the active intensity and reactive intensity fields in acoustic fields respectively and this is investigated further in the modelled 3D acoustic streaming fields shown below.

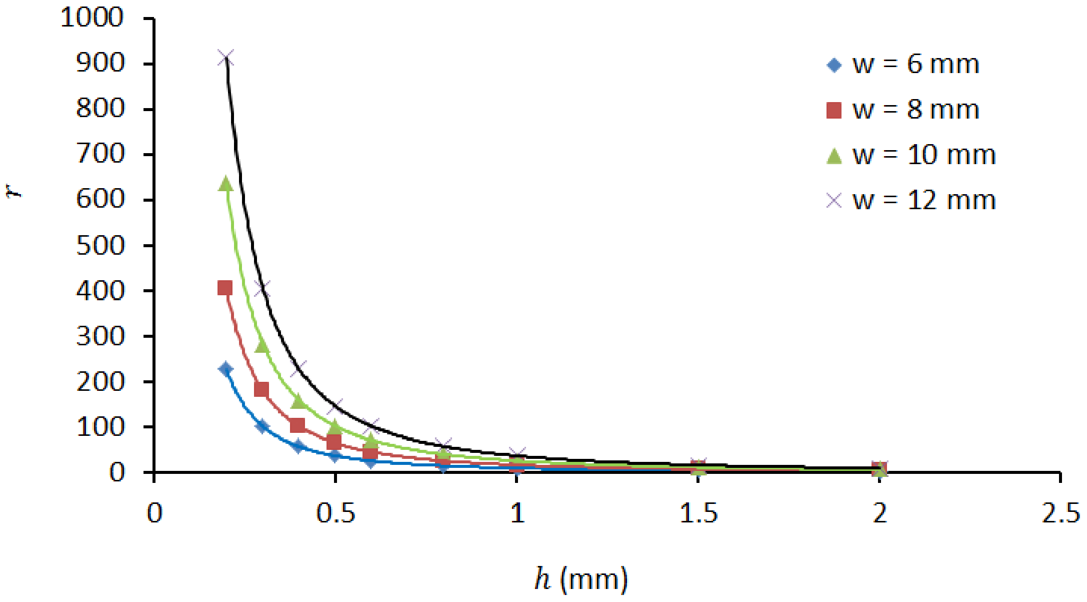

Figure 6.3 The simulated ratios, $r = A(|dw_1/dz|)/A(|dv_1/dy|)$, for all the models excited at the (1, 2, 1) resonant mode, where $A(\cdot)$ and $|\cdot|$ show respectively the average and absolute values over the bottom walls of the fluid channels ($z = -h/2$, the limiting velocity boundary) and the solid lines are those predicted from Equation *(6.15)*.

## 6.3. Modelling

### 6.3.1. Model Configurations

*Figure 6.1* (a) shows the schematic presentation of a classical layered acoustofluidic particle manipulation device, which is, typically, composed of four layers, respectively the transducer, the carrier layer, the fluid channel and the reflector layer[163, 187]. In this chapter, only the fluid layer is considered for the numerical efficiency of 3D acoustic and streaming simulations, which is appropriate as it has been shown previously in *Chapter 4* that this simplified model is sufficient to demonstrate the mechanisms of streaming fields observed in experiments. For a given application, however, a full model may be required to capture more complex combinations of boundary movement to determine which resonance is excited in the fluid layer (*Chapter 5*). In this case the particular cavity mode (see below) that has been presented in *Chapter 4* was excited to explore how the acoustic streaming patterns vary in devices with various channel dimensions through applying a normal acceleration boundary condition on the bottom surfaces of the fluid channels. The whole numerical process was conducted in COMSOL 4.4[167]. As only the fluid layers in the acoustofluidic devices were considered, the procedures for the simulation of acoustic streaming are the same as those described in Section *4.3*.

Table 6.1 Channel dimensions modelled in this chapter, where $l, w, h$ are the length, width and height of the fluid chamber, respectively.

| Case | Channel dimensions |
|---|---|
| a | $l = 10$ mm, $w = 6$ mm, $h$: 0.2 – 2 mm |
| b | $l = 12$ mm, $w = 8$ mm, $h$: 0.2 – 2 mm |
| c | $l = 14$ mm, $w = 10$ mm, $h$: 0.2 – 2 mm |
| d | $l = 16$ mm, $w = 12$ mm, $h$: 0.2 – 2 mm |

In order to investigate the sensitivity of the acoustic streaming patterns to the channel dimensions, a series of models with various channel dimensions were considered, which are summarised in *Table 6.1*, where $l$, $w$ and $h$ are the dimensions of the fluid channels along the coordinates $x$, $y$ and $z$, respectively. Various channel heights ranging from 0.2 to 2 mm for respectively four different channel widths were considered. The models were restricted to the thin-layered acoustofluidic device ($h/w < 1$ and $h/l < 1$) for the reason that the purpose of this work is to demonstrate the transition from streaming fields induced by LVs dominated by active sound intensity to those dominated by the reactive intensity in 3D resonant cavity modes. However, in high aspect-ratio devices ($h/w > 1$), the acoustic field is usually more closely approximated by a 1D acoustic resonance, leading to classical Rayleigh streaming[49], which is a different pattern to the others discussed here. Furthermore, it was found that, only in the thin-layered region, the contribution of the acoustic streaming field generated by the side boundaries ($y = \pm w/2$) to the overall streaming field in the bulk of the fluid channel can be neglected as it only has a size of $h/2$. Hence, in this chapter, only the driving terms on the top and bottom boundaries ($z = \pm h/2$) were taken into consideration for the acoustic streaming simulations unless otherwise stated.

## 6.3.2. First-order Acoustic fields

Firstly, the COMSOL '*Pressure Acoustics, Frequency Domain*' interface was used to model the first-order acoustic fields, which solves the harmonic, linearized acoustic problem. The detailed theory of this interface can be found in Section *3.2.2*.

While there are various resonant acoustofluidic systems, this work investigates those with a half-wave resonance in the $z$-direction, which is a widely used system for particle and cell manipulation [163, 187-195]. In such systems, particles and cells in the fluid channel are expected to be focused at the half-heights of the fluid channels. The origin of the coordinates in these models was set at the centre of the fluid channels such that the fluid channels are located within coordinates: $-l/2 \le x \le l/2, -w/2 \le y \le w/2, -h/2 \le z \le h/2$. In each case the standing wave field was excited through a '*normal acceleration*' boundary condition on the bottom wall. Energy gradients are created by the localised source of excitation in combination with plane wave radiation boundary conditions at the two ends of the flow channels ($x = \pm l/2$). The remaining walls were set as sound reflecting boundary conditions.

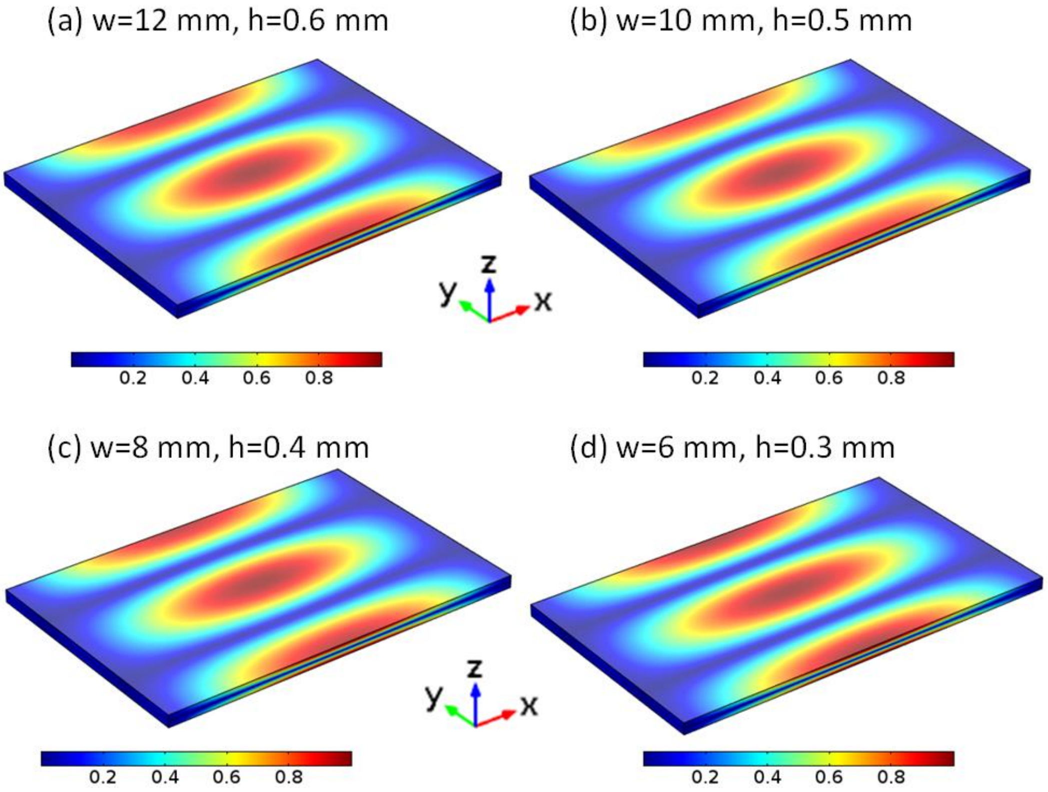

Figure 6.4 Colour plots of the simulated acoustic pressure magnitudes (normalised) on the surfaces of the fluid channels in four models where $l \times w \times h$ are respectively: (a) $16 \times 12 \times 0.6$ mm$^3$; (b) $14 \times 10 \times 0.5$ mm$^3$; (c) $12 \times 8 \times 0.4$ mm$^3$; and (d) $10 \times 6 \times 0.3$ mm$^3$. The red and blue colours show the maximum and minimum values, respectively.

It has been shown previously in *Chapter 4* that for the four-quadrant transducer plane streaming in a resonant cavity the streaming pattern was largely insensitive to the pattern of wall accelerations used to create the resonance. The acceleration distribution used previously of: $a_n = a_0 e^{ax^2+by^2}$ with $a_0 = 5.9 \times 10^4$ m·s$^{-2}$ and $a = b = -2.2 \times 10^5$ m$^{-2}$, was used here. These values match those used in the previous modelling where it was demonstrated that the results are not sensitive to these values. A frequency sweep study was firstly used to find the half-wave resonant frequencies in the $z$-direction of these 3D fluid channels, looking for the frequencies with maximum energy density in the fluid channels. The excitation used above created the required resonance in all the cases examined, shown in *Figure 6.4*, where the acoustic pressure fields on the surfaces of four models are presented. It can be seen that a similar standing wave field is established in all these models. In addition to the main resonance in the $z$-direction, the acoustic pressure field in the $y$ direction has a one-wavelength standing wave variation, and the pressure distribution in the $x$-direction is also close to a half-wavelength standing wave although the left and right walls ($x = \pm l/2$) were considered as plane wave radiation boundary conditions, which thus is referred to as a (1, 2, 1) cavity mode here, which is the same with that presented in Section *4.3.1*. Hence, in the following, it will be referred to as a (1, 2, 1) cavity mode. It will be shown later that the modal Rayleigh-like streaming discussed below are a result of the $z$- and $y$- axis acoustic gradients of this particular cavity mode.

### 6.3.3. Second-order Acoustic streaming Fields

Next, the COMSOL '*Creeping Flow*' interface was used to model the acoustic streaming fields, which approximates the fluid as incompressible and neglects the inertia forces as the streaming Re is much smaller than one for all the cases considered in this chapter. The governing equations for the streaming velocities, $\boldsymbol{u_2}$, and the associated acoustic pressure fields, $p_2$, can be found in Section *3.3.3*.

The LVM, introduced by Nyborg[78], modified by Lee and Wang[88] for 3D simulations, was used to solve the acoustic streaming fields in these layered acoustofluidic devices. For the models shown in this chapter, the LV equations on the driving boundaries ($z = \pm h/2$) can be found in Equations *(4.4)*. More detailed description of this method can be found in Section *4.3*. In this step, the bottom and top walls ( $z = \pm h/2$ ) were considered as LV boundary conditions while the remaining walls were no-slip boundary conditions unless otherwise stated. All the results presented below are for fluid channels with $w = 6$ mm and $l = 10$ mm unless otherwise stated.

The modelled active and reactive sound intensity fields at the bottom surface of the fluid channels ($z = -h/2$) for the pressure distributions shown in ***Figure 6.4*** are plotted in ***Figure 6.5*** (a) and (b), respectively. It has been shown previously that the LV field is negatively proportional to the reactive intensity field. Therefore, for comparison, the negative vector plot of the reactive intensity field is also plotted in (b2). It can be seen that the active (mean) intensity field on the LV boundaries has a regular four-quadrant vortex pattern while the reactive intensity field is irrotational, diverging from the pressure maxima and concentrating at the pressure minima. ***Figure 6.5*** (c)-(g) plots the LV vector fields for five models with different fluid channel heights. It is clear that, for the first model where $r \gg 1$ ($h = 0.2$ mm), shown in *Figure 6.5* (c), the LV field has a similar vortex pattern with that shown in *Figure 6.5* (a) demonstrating that, as predicted, it is dominated by the active sound intensity field. In *Figure 6.5* (d)-(f), the aspect ratio, and hence $r$, becomes steadily smaller and the predicted transition towards a pattern dominated by the vortex pattern of the reactive intensity field is seen.

For the different channel aspect ratios, qualitatively different vortex patterns are also seen in the streaming velocity fields due to the varying contribution of the active and reactive intensity fields discussed above. *Figure 6.6* plots the simulated in-plane acoustic streaming fields on the central $xy$ pressure nodal plane ($z = 0$) of the fluid channels for the five models illustrated above. It can be seen that a well-defined four-quadrant transducer plane streaming pattern is only observed in *Figure 6.6* (a), where $h = 0.2$ mm. With the increase of $h$ and the related decrease in the $r$, the in-plane acoustic streaming vortices transition towards modal Rayleigh-like streaming (see discussion below), as seen in *Figure 6.6* (e). In this case, the in-plane acoustic streaming field was found to be nearly irrotational, as the LVs for this case are dominated by the irrotational reactive intensity field.

In addition, the acoustic streaming fields on the central $yz$ cross-section of the fluid channel ($x = 0$) for all these five models are plotted in *Figure 6.7*. It can be seen that, for the model where $h = 0.2$ mm, the transducer plane streaming vortex pattern is observed and the streaming field is similar at all heights of the fluid channel ($z$-direction) as all the velocities are parallel to the bottom wall (LV boundary), *Figure 6.7* (a). With the increase of $h$ to 0.5 mm, *Figure 6.7* (b), the streaming velocities are non-uniform in the $z$-direction near the channel centre ($y = 0$) and the side walls ($y = \pm w/2$), where the pressure antinodes for the one-wave mode in the $y$-direction are positioned. Further, small vortices appear and increase in size in these areas with the further increase of $h$, forming well developed modal Rayleigh-like streaming when the fluid height $h = 2$ mm, *Figure 6.7* (e).

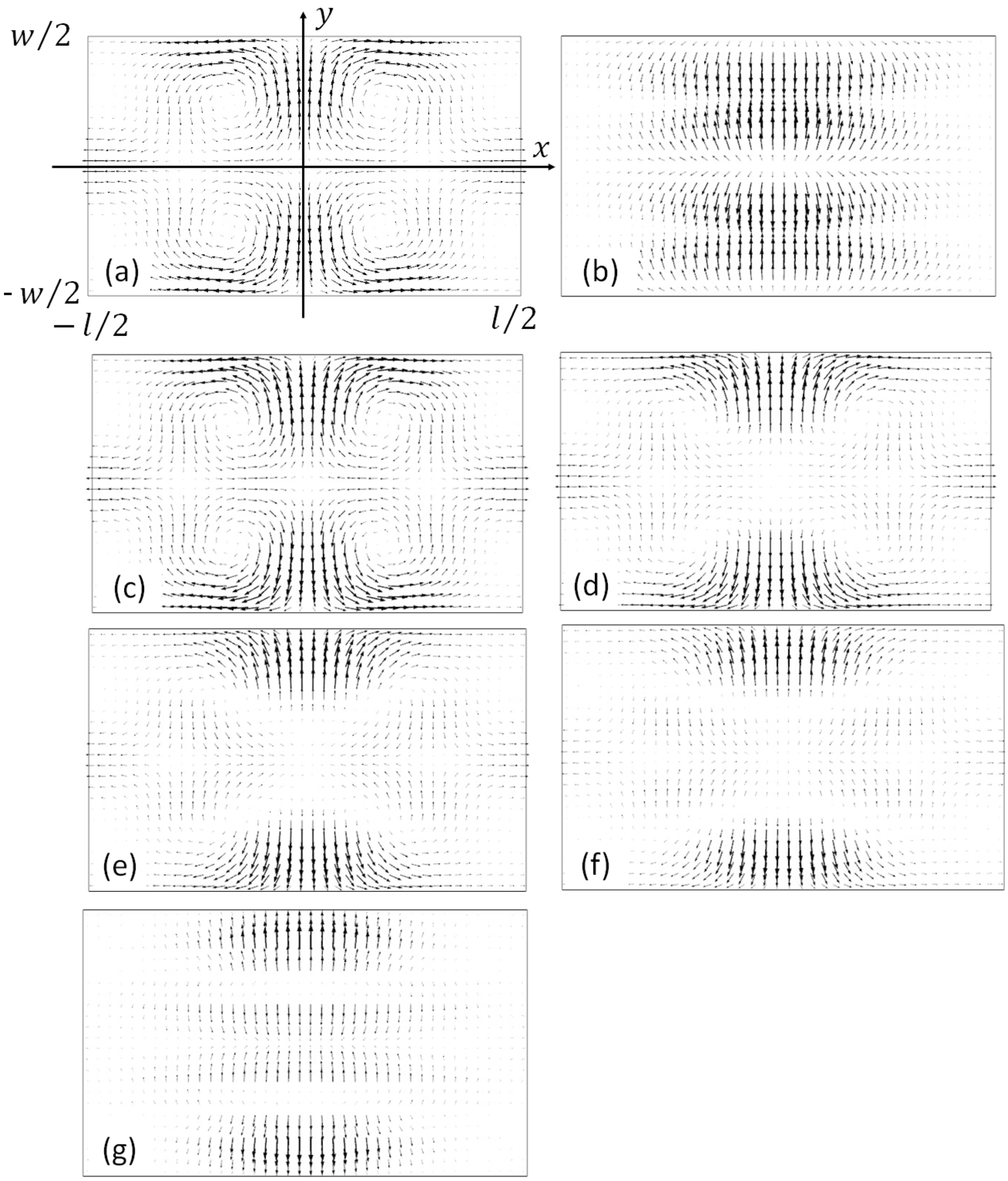

Figure 6.5 Vector plots of the sound intensity and limiting velocity fields on the bottom surface of the 3D fluid channels ($z = -h/2$) with various aspect ratios on their $yz$ cross-sections ($w = 6$ mm, $l = 10$ mm): (a) active (mean) intensity field; (b1) reactive intensity field; (b2) negative vector fields of (b1); (c) - (g) limiting velocity fields for respectively $h = 0.2$ mm; $h = 0.5$ mm; $h = 0.8$ mm, $h = 1$ mm and $h = 2$ mm, where the length of arrows shows their magnitudes.

The vortex pattern seen in *Figure 6.5* (g) and *Figure 6.6* (e) was referred to as “modal Rayleigh-like streaming” as it has a similar pattern to the classical Rayleigh streaming pattern, two vortices per wavelength along the acoustic standing wave. However, it is “Rayleigh-like” as this streaming pattern depends on the resonant cavity mode excited in the 3D rectangular cavities rather than a simple 1D acoustic standing wave. To clarify, the model $h = 2$ mm is taken as an example: the one-wavelength variation of acoustic pressure field generated in the $y$-direction of the fluid channel was excited at the resonant cavity mode at frequency $f \approx 0.45$ MHz, where the main standing wave field is established in the $z$-direction; Thus the observed streaming rolls have a width of $3\lambda/8$ compared to a value of $\lambda/4$ seen in conventional Rayleigh streaming.

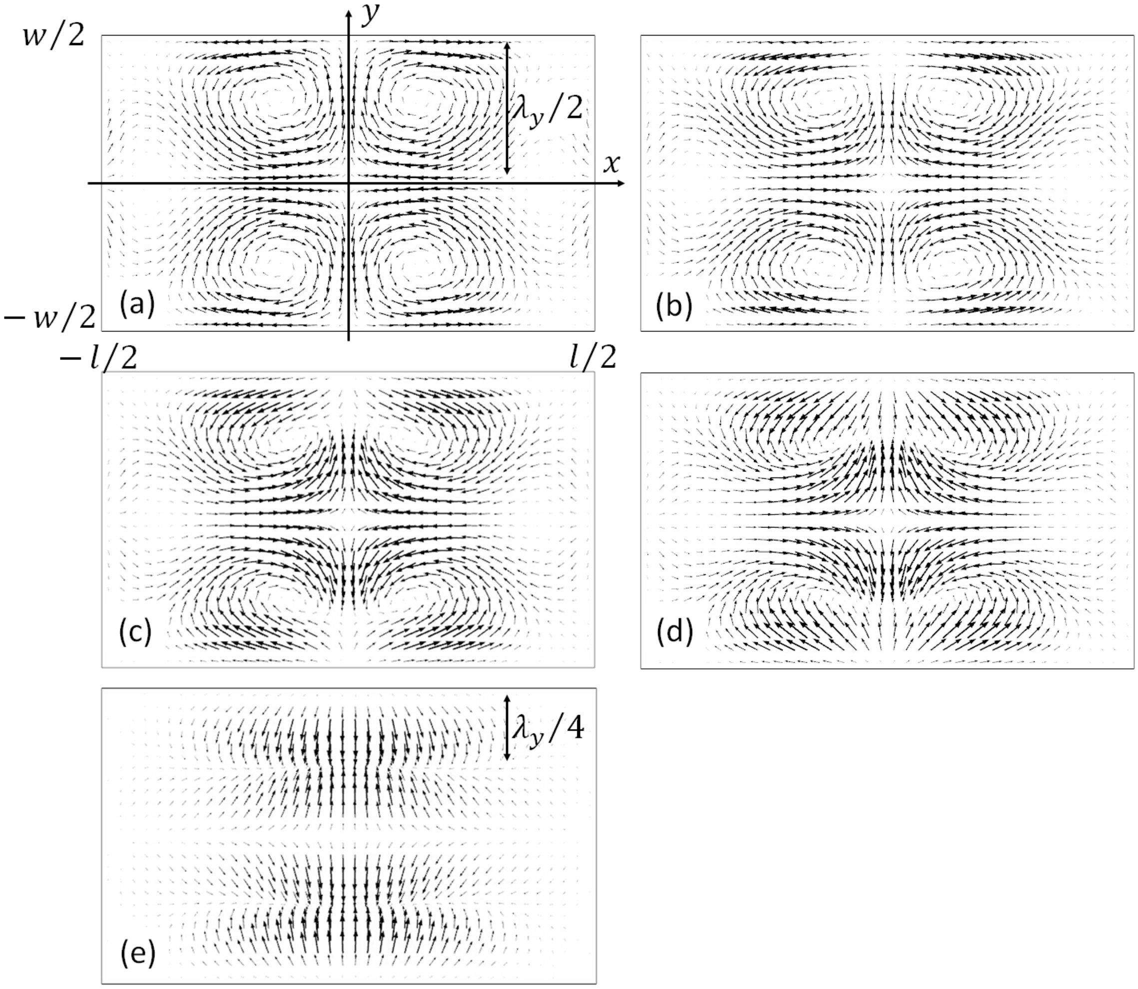

Figure 6.6 Vector plots of the acoustic streaming fields in the central $xy$ plane ($z = 0$) of the fluid channels ($w = 6$ mm, $l = 10$ mm) for: (a) $h = 0.2$ mm; (b) $h = 0.5$ mm; (c) $h = 0.8$ mm; (d) $h = 1$ mm; and (e) $h = 2$ mm, where the maximum streaming velocities shown in models (a)-(e) are respectively 0.14, 1.08, 2.03, 2.83, 12.38 μm/s, which are obtained from an acoustic pressure amplitude of approximately 0.6 MPa. A transition from transducer plane streaming to modal Rayleigh-like streaming is seen with deeper channels. Limiting velocities on the side walls are set to zero for simplicity.

It will be shown below experimental demonstration of modal Rayleigh-like streaming patterns in a layered acoustofluidic particle manipulation device. It should be emphasised that in this section the driving forces resulting from LVs on the $y = \pm 3$ mm sidewalls are not included; this has simplified the streaming fields to help show the transition illustrated, however a model of the case when LVs on all boundaries are included can be seen below.

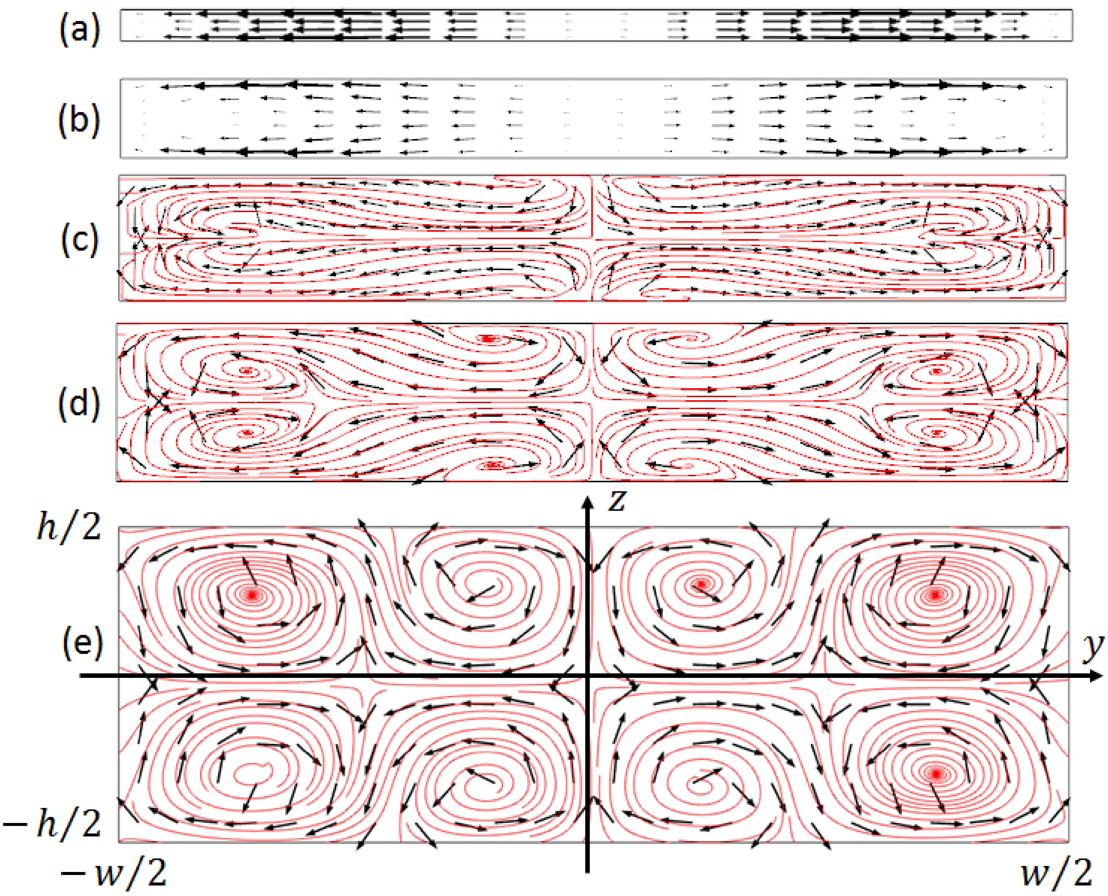

Figure 6.7 Vector plots of the modelled acoustic streaming fields in the central $yz$ plane ($x = 0$) of the fluid channels ($w = 6$ mm, $l = 10$ mm): (a) $h = 0.2$ mm; (b) $h = 0.5$ mm; (c) $h = 0.8$ mm; (d) $h = 1$ mm; and (e) $h = 2$ mm, where the arrows show streaming velocity fields and the red lines show the streamlines. The arrows in (c)-(e) have been normalised in order to show clearly the velocity vectors. A transition from transducer plane streaming to modal Rayleigh-like streaming is seen with deeper channels. Limiting velocities on the side walls are set to zero for simplicity.

## 6.4. Experimental Measurements

The experiments were conducted in glass capillaries, which have been used for many years to form small acoustofluidic particle manipulation systems [152, 154, 157-162]. As the transducer plane streaming has been presented in *Chapter 4* in a low aspect-ratio capillary device ($h/w = 1/20$), in this section, measurements in a higher aspect-ratio glass capillary ($h/w = 1/3$) are presented to show the modal Rayleigh-like streaming in layered acoustofluidic particle manipulation devices. The glass capillary (Vitrocom, USA) has an inner dimension of 2 × 6 mm$^2$ ($h \times w$) and wall thicknesses of 0.8 mm. A function generator (TTi, TG1304 Programmable) drives an RF amplifier (EIN, Model 240L) that drives the transducer, with the signal monitored by an oscilloscope (Agilent Technologies, DOS1102B Digital Storage Oscilloscope). An Olympus BXFM epi-fluorescent microscope with a *pixelfly* dual-frame CCD camera was used to image the device. The detailed experimental setup can be found from Section *4.2*.

The experimental measurements were the same as those shown in Section *4.2*, which can be split into the following steps:

- Impedance measurements were firstly used to identify the resonant frequencies in these two devices;
- 10 μm particles were used to characterise the acoustic fields in the capillaries by examining the ARF on them;
- μPIV measurements of 1 μm polystyrene tracer particles (Fluoresbrite microspheres, Polysciences Inc.) were performed to characterise the acoustic streaming fields;
- The voltage drop method[155], based on the balance of the buoyancy force and ARF on 10 μm particles, was used to estimate the acoustic pressure magnitudes in the fluid channels.

More detailed information on the device configuration, the μPIV setup and the process on measuring and characterising the acoustic streaming fields can be found in Section *4.2*.

As illustrated previously, the main standing wave fields in the capillaries were excited at the half-wave resonance along the height of the fluid channels ($z$-direction). ***Figure 6.8*** shows the alignment of 10 μm polystyrene beads in the

$xy$ plane. It can be seen that most of the particles were aligned to two planes in the fluid channel, $y \approx \pm 1.2$ mm, which proves that, in addition to the primary half-wave standing wave in the $z$-direction of the fluid channels, acoustic pressure fields in the $y$-direction of the fluid channels also have one-wave variations. Therefore, the devices were excited in the (-, 2, 1,) cavity mode matching the modelling above, with '-' showing that the resonance along the fluid channel ($x$-direction) cannot be read from the particle alignment. All the parameters for fluid and microparticles are summarised in *Table 6.2*.

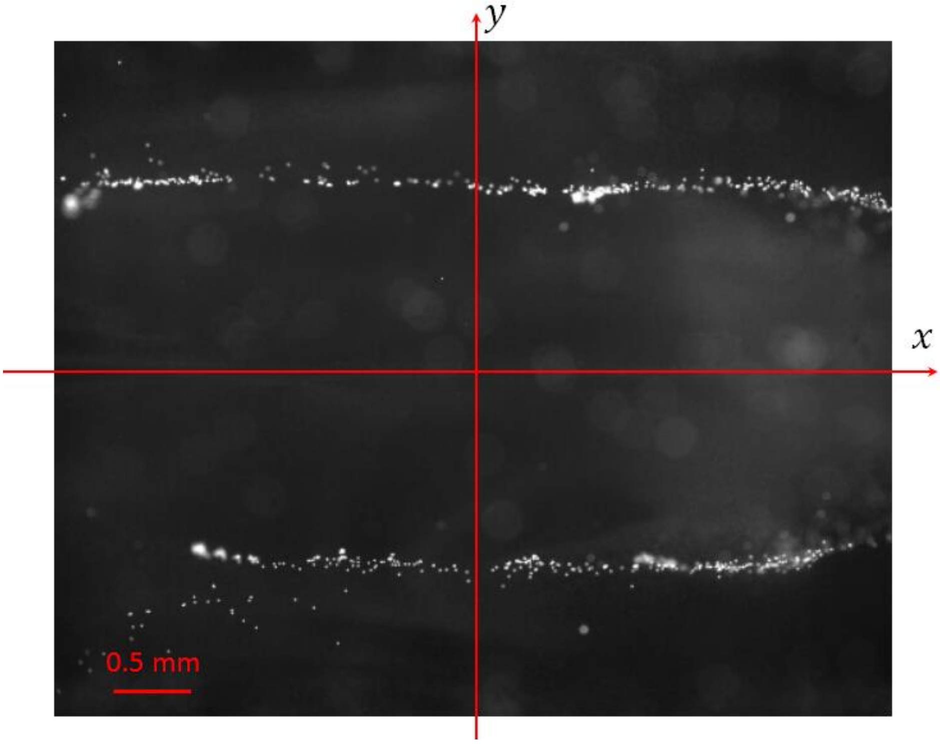

Figure 6.8 A plan view of the alignment of 10 μm polystyrene beads in the glass capillary.

The measured acoustic streaming fields near the centre of the second device are shown in *Figure 6.9*, and correspond to modal Rayleigh-like streaming, where the acoustic streaming fields on two $xy$ planes, $z = 0$ and $z = 0.45h$, are presented. It is clear that there is no in-plane streaming in these $xy$ planes and that there must be vortices in the $yz$ cross-sections (see *Figure 6.10* (c)) to complete the flow field (compare these results to the dashed box in *Figure 6.10* (d)). The size of these vortices is approximately one-quarter of the fluid channel width, $w/4$, which is much bigger than the size of classical Rayleigh streaming vortices, $h/2$, which would be caused from the main half-wave resonance in the $z$-direction. It can be seen that the measured acoustic streaming patterns in the central area compare well with those predicted in *Figure 6.6* (e) and *Figure 6.7* (e). However, in addition to the $y$-directed flows that form the pattern we are describing as modal Rayleigh-like streaming, there are some $x$-components to the flow in the top plane shown in *Figure 6.9* (a). These are also seen in a smaller way in the model (*Figure 6.5* (g)) and result from the gradient of energy density towards the central maximum. We hypothesise that the boundary conditions in the experiments cause larger gradients than those modelled and hence the larger $x$-component of the velocity vectors.

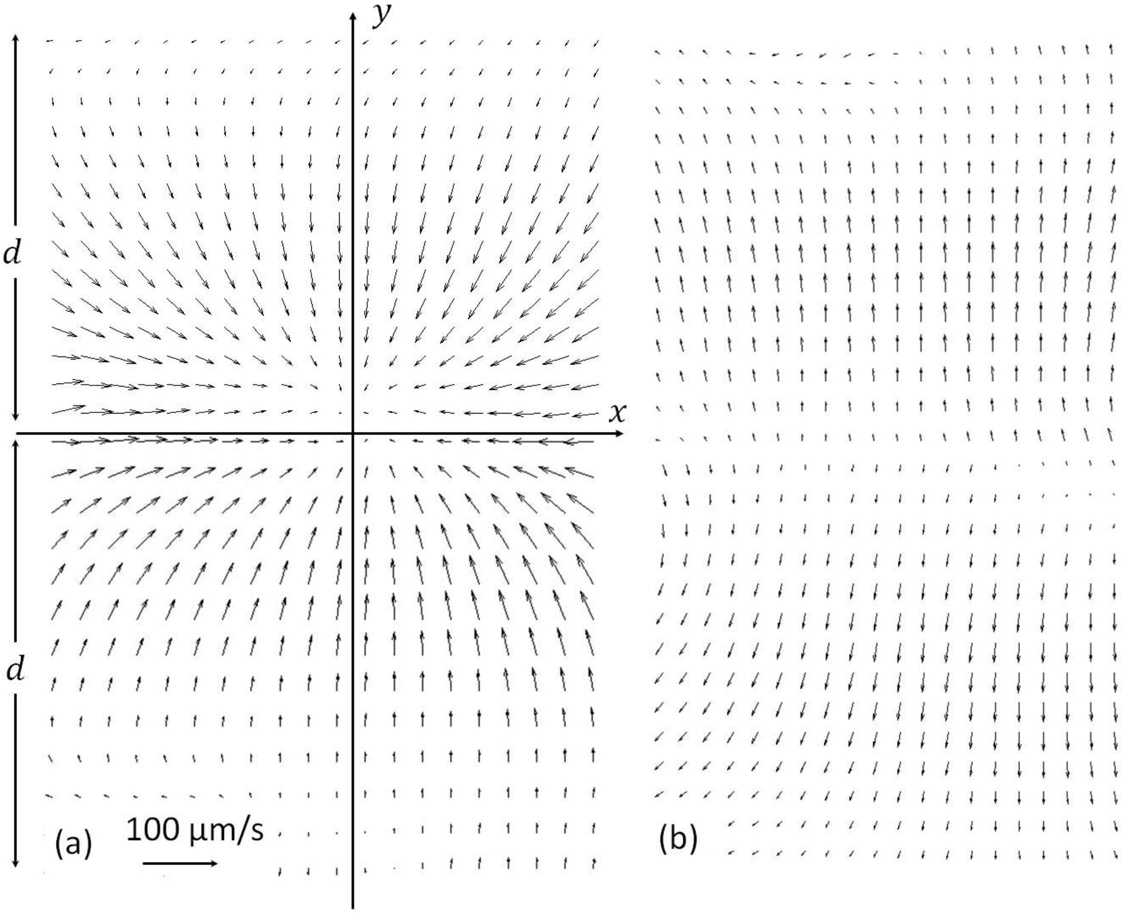

Figure 6.9 Field views ($-1\ \mathrm{mm} \leq x \leq 1\ \mathrm{mm}, -1.5\ \mathrm{mm} \leq y \leq 1.5\ \mathrm{mm}$) of the measured acoustic streaming rolls in the central area of the glass capillary with a fluid channel dimension of $h = 2$ mm and $w = 6$ mm: (a) on plane $z = 0.45h$; and (b) on plane $z = 0$, where $d$ represents the size of the modal Rayleigh-streaming vortices. The streaming velocities presented are obtained from an acoustic pressure amplitude of approximately 0.8 MPa.

In order to accurately accord with experimental results the LVs at the side walls ($y = \pm w/2$) were included in the model results shown in ***Figure 6.10*** (e). This creates a streaming field that has contributions from both Rayleigh streaming (driven by the sidewalls) and modal Rayleigh-like streaming (driven by the upper and lower channel boundaries), resulting in the streaming pattern shown in ***Figure 6.10*** (d). This pattern has extra vortices, which accords well with the measured streaming fields shown in ***Figure 6.10*** (a)-(b).

In the case of boundary-driven streaming, it is acoustic attenuation in the viscous boundary layer, forming RSF fields, that induces streaming vortices in that thin layer. The fluid movement inside the viscous boundary layer induces outer streaming vortices in the bulk of the fluid (***Chapter 3***). This means that the maximum streaming velocities will be no more than a few multiples of $\delta_v$ away from the wall. However, in some regions of the second capillary ($h = 2$ mm), the maximum streaming velocity was found to be further from the boundaries (about 50% higher than at the boundary at a distance of ~ 250 μm), which is not consistent with the characteristics of boundary-driven acoustic streaming described above. Initial modelling suggests that this is due to the energy loss in the bulk of the fluid producing RSF that drive non-negligible Eckart type streaming velocities in the volume of the fluid channel additional to the dominant boundary-driven streaming. This effect is also likely to be observable in acoustofluidic devices with thinner layers, in which the active intensity flow (which generates Eckart streaming) has a significant contribution to the LV fields generating the boundary-driven streaming. The effects of Eckart streaming on the overall streaming fields in planar acoustofluidic devices will be further examined in future work.

Table 6.2 Experimental parameters for modal Rayleigh-like streaming measurements.

| Quantity | Abbreviation | Value | Unit |
|---|---|---|---|
| Capillary size | $l \times h \times w$ | 80 × 6 × 2 | mm$^3$ |
| Dimension of transducer | $l \times h \times w$ | 3 × 3 × 1 | mm$^3$ |
| Fluid density | $\rho_0$ | 998 | kg·m$^{-3}$ |
| Particle radius | $r$ | 1 | μm |
| Dynamic viscosity of fluid | μ | 0.893 | mPa·s |
| Speed of sound in fluid | $c$ | 1480 | m·s$^{-1}$ |

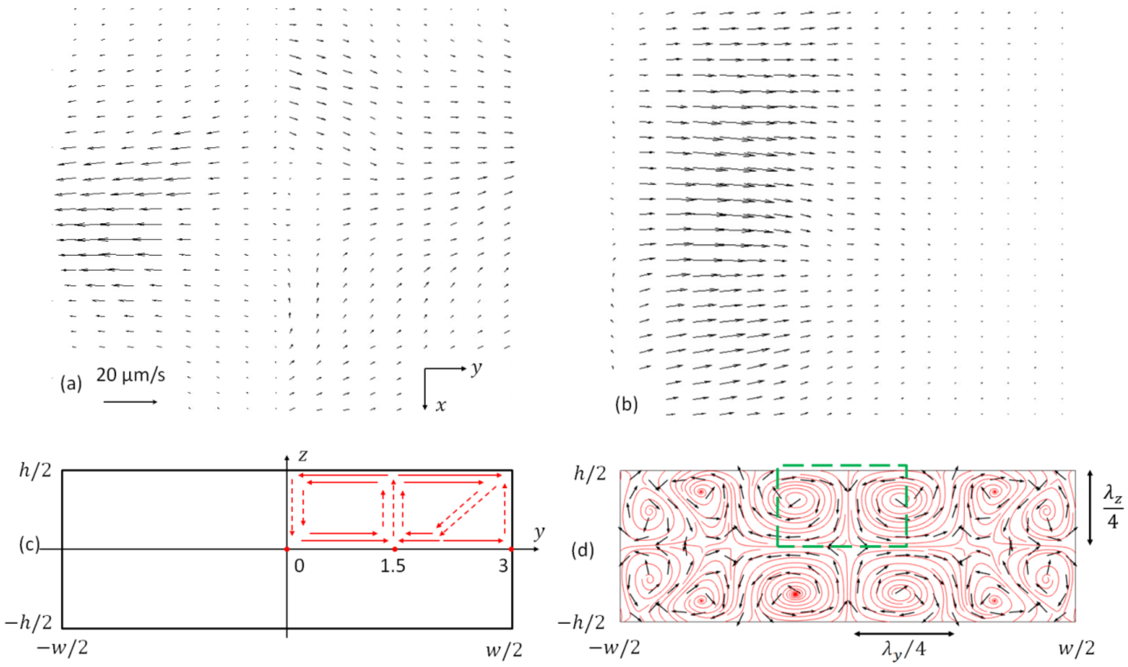

Figure 6.10 (a)–(b) Field views ($-1\,\mathrm{mm} \le x \le 1\,\mathrm{mm}, 1.5\,\mathrm{mm} \le y \le 3\,\mathrm{mm}$) of the measured acoustic streaming fields near a side wall ($y = -w/2$) of the glass capillary on respectively the planes $z = 0$ and the plane $z = 0.45h$; (c) schematic presentation of the acoustic streaming vortices in the whole channel, where solid and dashed arrows show the measured and deduced streaming velocity fields, respectively; (d) the modelled acoustic streaming field in a fluid channel which has a same dimension with the glass capillary with the consideration of Rayleigh streaming driven by the side boundaries ($y = \pm w/2$). The vortices identified by the green dashed line in (d) are discussed in the text. ($w = 6$ mm, $h = 2$ mm, $l =$ 80 mm). The streaming velocities presented in (a) - (b) are obtained from an acoustic pressure amplitude of approximately 0.68 MPa.

## 6.5. Conclusions

The acoustic streaming patterns in 3D rectangular fluid cavities, where a (1, 2, 1) resonant cavity mode was excited, have been investigated. It has been shown that the ratio of the two dominant acoustic velocity gradients, governed by the aspect ratio of the channel, determines the driving terms of the acoustic streaming fields. These driving terms can be identified as having vortex patterns matching those of the active and reactive components of the complex intensity field. This provides a basis for predicting the acoustic streaming patterns in layered acoustofluidic devices, for particle and cell manipulation.

In addition to the well-known Rayleigh streaming and the transducer plane streaming recently described, a third type of boundary-driven streaming, *modal Rayleigh-like streaming*, has been experimentally observed and numerically verified. This streaming field has the same pattern as classical Rayleigh streaming but depends on the resonant cavity mode excited in the 3D cavities rather than simple 1D standing wave patterns.

The modelled and experimental results demonstrate that the acoustic streaming patterns in layered half-wave acoustofluidic particle manipulation devices excited in the resonant cavity modes can be split into three regions, bounded approximately by:

- $h/w \leq 1/20$, transducer plane streaming;
- $1/20 < h/w < 1/3$, transducer plane streaming & modal Rayleigh-like streaming; and
- $h/w \geq 1/3$, modal Rayleigh-like streaming.

The cases considered above focus on the boundary-driven streaming in layered acoustofluidic systems, without considering the Eckart type streaming generated from the energy dissipation from the bulk of the fluid. It would be interesting to investigate the contribution of boundary-driven streaming to the overall streaming field in acoustofluidic systems in which path lengths are larger in comparison with acoustic wavelengths and where Eckart type streaming has a comparable contribution.

# Chapter 7. Effects of Surface Profile on the Acoustic and the Boundary-driven Streaming Fields in Acoustofluidic Systems[§]

## 7.1. Introduction

In previous chapters, it has been demonstrated that 3D boundary-driven streaming fields in the bulk of fluid channels in most practical acoustofluidic systems can be efficiently solved from the LVM from both 3D fluid-channel-only models and full configurations of acoustofluidic models provided that the radius of curvature of the boundary is much greater than the thickness of viscous boundary layer. Most acoustic streaming fields in acoustofluidic devices modelled in literature are generally based on the condition that these fluid channels have flat boundaries. However, it has not been examined whether the curvilinear condition of boundaries has effects on the boundary-driven streaming fields. In acoustofluidic systems where the fluid-solid boundaries do not satisfy the condition stated above, the classical LVM is not applicable for solving the outer streaming fields. Instead, the acoustic streaming fields can be modelled from the RSM, which can be applied to any devices where an acoustic field is established. This method has been shown and validated on the simulation of classical boundary-driven streaming fields in ***Chapter 3***, which decomposes the acoustic streaming problem into three steps: (1) first-order acoustic velocity fields are solved; (2) the RSF distributions are calculated; (3) acoustic streaming fields both inside and outside the viscous boundary layer are solved from the momentum equation with the RSF working as a body force per unit volume on the fluid.

The modelling work presented in this chapter investigates the boundary-driven streaming fields using the RSM in devices where the boundaries have sine-wave shaped curvatures and the effects of both the amplitude and period of the

---

[§] A portion of the results presented in this chapter are in ref. 196. Lei, J., P. Glynne-Jones, and M. Hill, *Effects of surface profile on a boundary-driven acoustic streaming field*, in *The 21st International Congress on Sound and Vibration*. 2014, iiav: Beijing, China. p. 1-5.

sine-wave profile are examined. More specifically, acoustic and streaming fields in devices, where the sine-wave shaped boundaries have amplitudes ranging from negligible to significant values, compared to the thickness of viscous boundary layer, were studied and compared to the work presented in *Chapter 3*. The reason to choose this shape is based on the fact that it is easier to model than a sharper profile.

Section *7.2* shows the model configuration and modelling results are presented in Sections *7.3*. Detailed discussions on the surface profile effects on both the boundary-driven streaming patterns and the magnitudes of streaming velocities are presented in Section *7.4*. An overall conclusion is drawn in Section *7.5*.

## 7.2. Model Configurations

It has been shown in *Chapter 3* that boundary-driven streaming fields inside and outside the viscous boundary layer in 2D models can be effectively solved from its driving force derived from the mean acoustic momentum flux, namely Reynolds stress. Here, this model is emphasised again in order to demonstrate the effects of surface profile on the boundary-driven streaming fields in 2D rectangular chambers.

*Figure 7.1* shows the model configuration. As acoustic streaming fields in 2D rectangular chambers are generally symmetric to the channel axis, only half of the rectangular chamber is modelled here for numerical efficiency and thus, as shown in *Figure 7.1* (a), the bottom wall of chamber was set as a symmetric boundary condition (normal velocity equals to zero). In the acoustic step, the left wall of the chamber was considered as velocity vibration for the generation of a half-wave standing wave in the $x$-direction of the chamber, which represents the boundary vibration generated by the transducer in an acoustofluidic device. The two remaining walls were considered as nonslip boundary conditions. In the CFD step, in addition to a symmetric condition of the bottom wall, all the three walls remaining were nonslip boundary conditions. The origin of coordinates was set at the centre of the bottom wall.

*Figure 7.1* (b) shows a magnification of the sine-wave shaped surface profile, which is determined by two parameters, $h_0$ and $T$, the profile amplitude and profile period, respectively. A range of values for these parameters are explored in the section that follows.

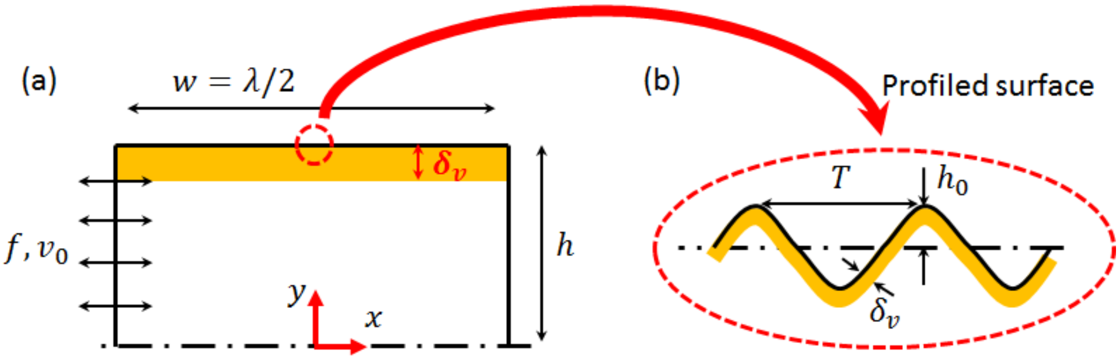

Figure 7.1 Schematic illustration of the model: (a) excitation and coordinates; and (b) a magnification of the profiled surface (exaggerated), where $\delta_v$ is the thickness of the viscous boundary layer (not to scale), $f$ and $v_0$ are respectively the frequency and amplitude of the excitation, and $T$ and $h_0$ are the period and amplitude of the sine-wave shaped boundary, respectively.

## 7.3. Modelled Results

In order to show the reliability and applicability of the modelling work, a series of sine-wave shaped surface profiles in two cases, respectively $h = 40\delta_v$ and $h = 80\delta_v$, are compared in this section. For all the results presented below, the period of the sine-wave shaped surfaces was the same, $T = 3.7$ μm, unless otherwise stated. It is noteworthy to mentioning that the sine-wave shaped surface covers the whole boundary such that the total areas of the chambers are the same, $A = h \times w$, which is the area of the chamber with flat surfaces.

### 7.3.1. First-order Acoustic Fields

The modelled first-order acoustic pressure fields are plotted in *Figure 7.2*. It was found that, under the same velocity excitation, a half-wave standing wave was established in the $x$-direction of the chambers, with pressure node staying at the centre ($x = 0$) and two pressure antinodes at the two ends ($x = \pm w/2$).

However, it was found that the magnitudes of acoustic pressure amplitude vary in these chambers although they were driven with the same excitation. The detailed relationship between the pressure amplitudes and the amplitudes of sine-wave profiled surfaces is shown in ***Figure 7.2*** (b), where the modelled acoustic pressure magnitudes in chambers with various amplitudes on the sine-wave shaped surface for two cases, $h = 40\delta_v$ and $h = 80\delta_v$, are presented.

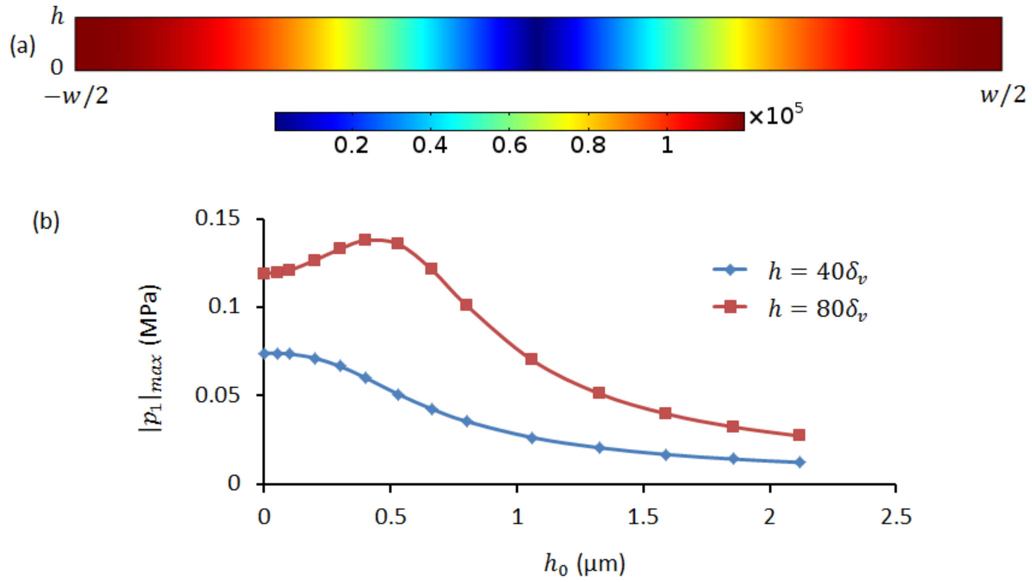

Figure 7.2 (a) The modelled first-order acoustic pressure fields in chambers ($h = 80\delta_v, h_0 = 0$); (b) The relationships between the modelled pressure amplitudes, $|p_1|_{max}$, and the amplitudes of the sine-wave shaped surface profiles, $h_0$, for two cases, $h = 40\delta_v$ (diamond-line) and $h = 80\delta_v$ (square-line), respectively. The pressure amplitudes (unit of Pa) were obtained from the same excitation, $v_0 = 1$ mm/s. The period of these sine-wave shaped surface profiles was the same: $T = 3.7$ μm.

In the first case where $h = 40\delta_v$, as shown in ***Figure 7.2*** (b), a general downward trend on the pressure amplitudes can be found with the rise of $h_0$. The potential reasons for the variation and decreasing of pressure amplitudes in models with sine-wave shaped surfaces, compared to that in devices with flat boundaries, may be attributed to the fact that the viscous boundary layer area is augmented from the curved boundary compared to that in a device with flat boundaries, which results in more attenuation of acoustic energy when the area of the chambers is kept the same. However, in the second case where $h = 80\delta_v$, it can be seen that the change of acoustic pressure amplitudes with respective to $h_0$ can be split into two stages. Firstly, starting from $h_0 = 0$, the pressure amplitudes in the chambers rise slowly with the increase of $h_0$ and reaches the maximum value at $h_0 \approx \delta_v$. Then, it decreases more rapidly with further growth of $h_0$. The interesting increase of pressure amplitude seen in the first stage might be attributed to the scatting of sound waves near the curved surfaces which results in a rise of the sound intensity and thus the acoustic pressure in the whole chambers.

### 7.3.2. Second-order Acoustic Streaming Fields

In this section, the effects of sine-wave shaped surface on the boundary-driven streaming fields, including the acoustic streaming patterns and streaming velocity magnitudes, are presented.

#### 7.3.2.1. Profiles with Fixed Period and Various Amplitudes in nm Region

*Figure 7.3* shows the modelled acoustic streaming fields in chambers with $h_0$ ranging at nm region ($T = 3.7$ μm) to represent insignificant amplitudes (compared to $\delta_v$). It was found that the acoustic pressure fields were the same for all these models, which are shown in *Figure 7.3* (a). For comparison, the modelled streaming field in a device with flat boundaries ($h_0 = 0$) is also presented in *Figure 7.3* (b). *Figure 7.3* (c)-(d) plot the simulated streaming fields in models where $h_0 = 1$ nm and $h_0 = 10.6$ nm, respectively.

In terms of streaming patterns, it can be seen that the modelled outer streaming field has a same pattern in all these models, two vortices within the half-wave standing wave field in the $x$-direction of the chambers, which is the same with that in a device with flat boundaries. However, the regular two-vortex-per-half-wave inner vortex pattern near the top wall in devices with flat boundaries (e.g. *Figure 7.3* (b)) was disrupted by the curved boundaries forming wall dependent vortex patterns (*Figure 7.3* (c)-(d)). The detailed inner streaming patterns will be shown in the next section in order to give a clearer presentation as it was found that the size of these wall dependent streaming vortices increase with $h_0$.

With respect to the streaming velocity magnitudes, it is clear that the maximum streaming velocities vary in these three models shown in *Figure 7.3*. For $h_0 = 0$, the maximum streaming velocity (brightest colour in *Figure 7.3* (b)) stays at $x = \pm w/4$, while the streaming velocities near the top boundary within coordinates: $-w/4 \le x \le w/4$ have comparable magnitudes for $h_0 = 10.6$ nm (*Figure 7.3* (d)) due to the wall dependent velocity generated from the curved surface which have maximum values at the centre ($x = 0$) and decreases to the two ends ($x = \pm w/2$) of the chamber (explained later in the discussion section). The detailed relationship between the magnitudes of the streaming velocities and the amplitudes of the sine-wave shaped profiles will be shown later in the discussion section.

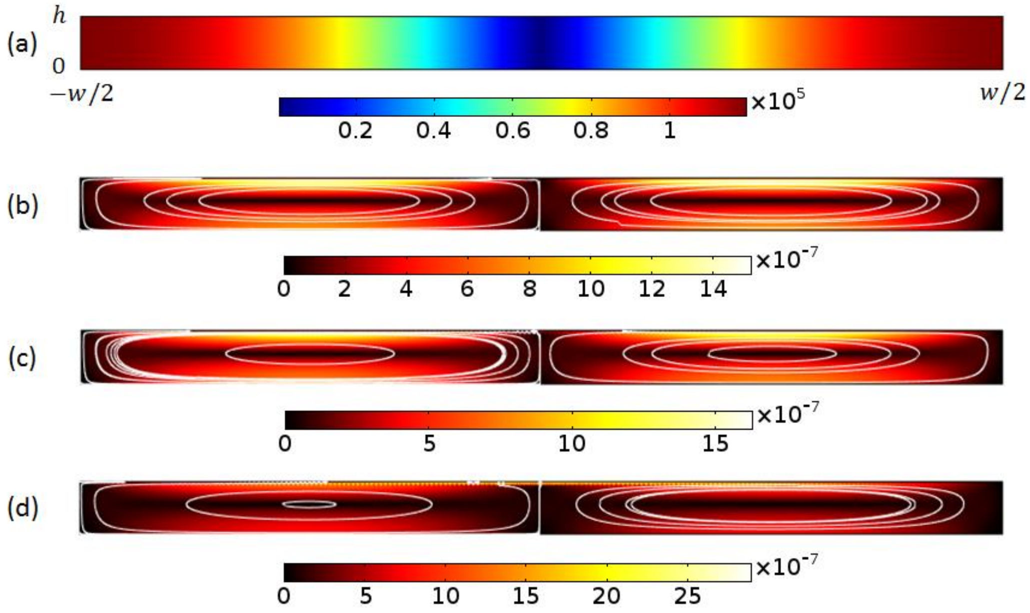

Figure 7.3 The modelled second-order acoustic streaming fields in chambers ($h = 80\delta_v$) where the amplitudes of the sine-wave shaped surface profiles are in the nm region: (a) the acoustic pressure field (unit of Pa) for all these models shown below; (b)-(d) the acoustic streaming fields for $h_0 = 0$, $h_0 = 1$ nm, $h_0 = 10.6$ nm, respectively. The white lines plot the streaming patterns and the colours show the magnitudes of streaming velocities (unit of μm/s). The period of these sine-wave shaped surface profiles was the same: $T = 3.7$ μm.

#### 7.3.2.2. Profiles with Fixed Period and Various Amplitudes in μm Region

Continuing with the work presented in Section *7.3.2.1* above, the modelled acoustic streaming fields in chambers with bigger $h_0$ (non-negligible amplitudes compared to $\delta_v$) on the sine-wave shaped boundaries are compared in this section. ***Figure 7.4*** shows the modelled streaming fields in devices with $h_0 = 0.53$ μm. It can be seen that the outer streaming patterns in models where profile amplitudes are in μm region still show the same pattern as the cases in the previous section with negligible surface profile amplitudes, two vortices within each half-wave standing wave field.

Overall, the magnitudes of streaming velocities in the bulk of the chambers are very small compared to that near the top surfaces due to a dramatic increase of the wall dependent streaming velocities generated by $h_0$ that are comparable or larger than $\delta_v$. In these cases, the streaming velocity magnitudes vary in these models and the maximum streaming velocity (brightest colour) in these models has moved to the centre of the chambers ($x = 0$). The detailed information will be shown in the following discussion section.

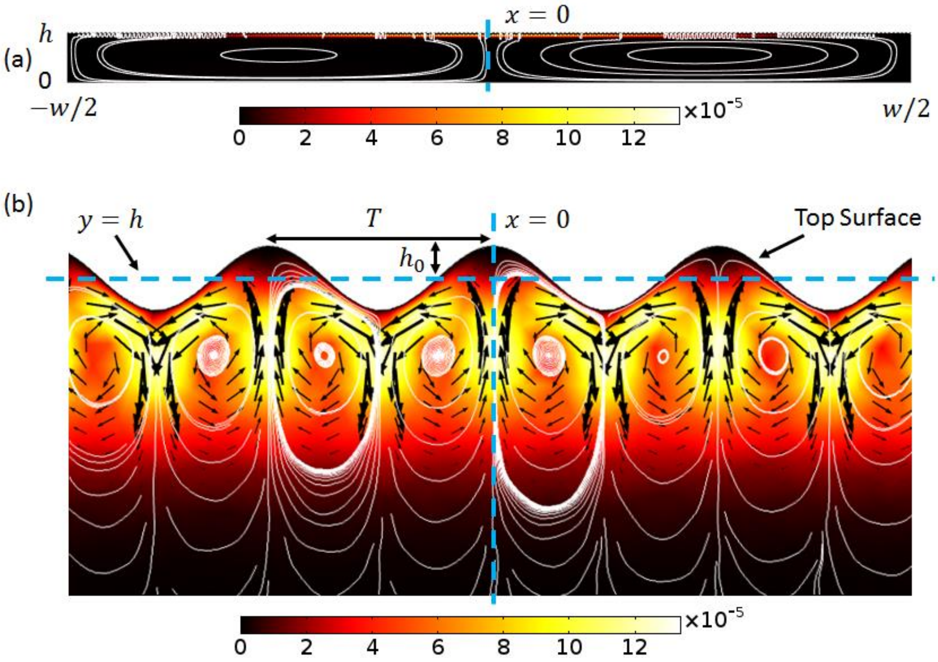

Figure 7.4 (a) The modelled second-order acoustic streaming field in a chamber ($h = 80\delta_v$) where the amplitudes of the sine-wave shaped surface profile is $h_0 = 0.53$ μm; (b) a magnification of near boundary region at the centre of the channel. The white lines plot the streaming patterns and the colours show the magnitudes of streaming velocities (unit of μm/s). The period of these sine-wave shaped surface profile was $T = 3.7$ μm.

In order to demonstrate the detailed inner streaming fields of the models presented in ***Figure 7.4*** *(a)*, a magnification of the local area near the top boundary at the centre of the chamber where $h_0 = \delta_v$, is shown in ***Figure 7.4*** (b). It can be seen that an array of streaming vortices were generated near the top boundary in the $x$-direction of chamber, with the same period as that of the sine-wave shaped boundary, $T$, instead of the regular two-vortices-per-half-wave pattern observed in devices with flat boundaries. The mechanism on the formation of this vortex pattern will be analysed in detail in the discussion section below.

In this chapter, only the modelled acoustic streaming fields in devices where $h_0 \leq 2\delta_v$ have been presented as it is shown that the streaming patterns already tend to be stable when $h_0$ increases to the μm region and the magnitudes of streaming velocities are also predictable with the further increase of $h_0$, which will be shown in the discussion section below (***Figure 7.7***).

## 7.4. Discussion

### 7.4.1. Effects of Surface Profile on the Acoustic Streaming Patterns

In the first part of this section, the formation mechanism of inner streaming patterns in devices with sine-wave shaped boundaries is discussed.

Here the model where $h_0 = \delta_v$ is chosen as an example to illustrate the formation mechanism of the inner streaming pattern in devices with sine-wave shaped surfaces. ***Figure 7.5*** shows the distributions of the modelled acoustic velocity, RSF, vorticity of RSF and the acoustic streaming fields near the top wall of the chamber, respectively. It can be seen that, due to the presence of the sine-wave shaped boundary, both the acoustic velocity magnitudes and the RSF have a periodic distribution (period of $T$) in the $x$-direction of the chamber, with the maximum values staying at locations a vertical distance of approximately $2\delta_v$ and $\delta_v$ from the troughs of the sine-wave, respectively. ***Figure 7.5*** (c) plots the vorticity of the RSF field near the top boundary. As shown, it is zero in most areas of the chamber except those small regions near each trough of sine-wave shaped wall. According to the magnitudes, signs are respectively used to demonstrate the vorticity of the RSF fields following the 'right-hand-rule'. It can be seen that, due to the different rotationality of the RSF at the two sides of each trough of the sine-wave, two vortices can be generated in each period of the sine-wave shaped surface, which can explain the modelled acoustic streaming fields near the top boundary shown in ***Figure 7.5*** (d).

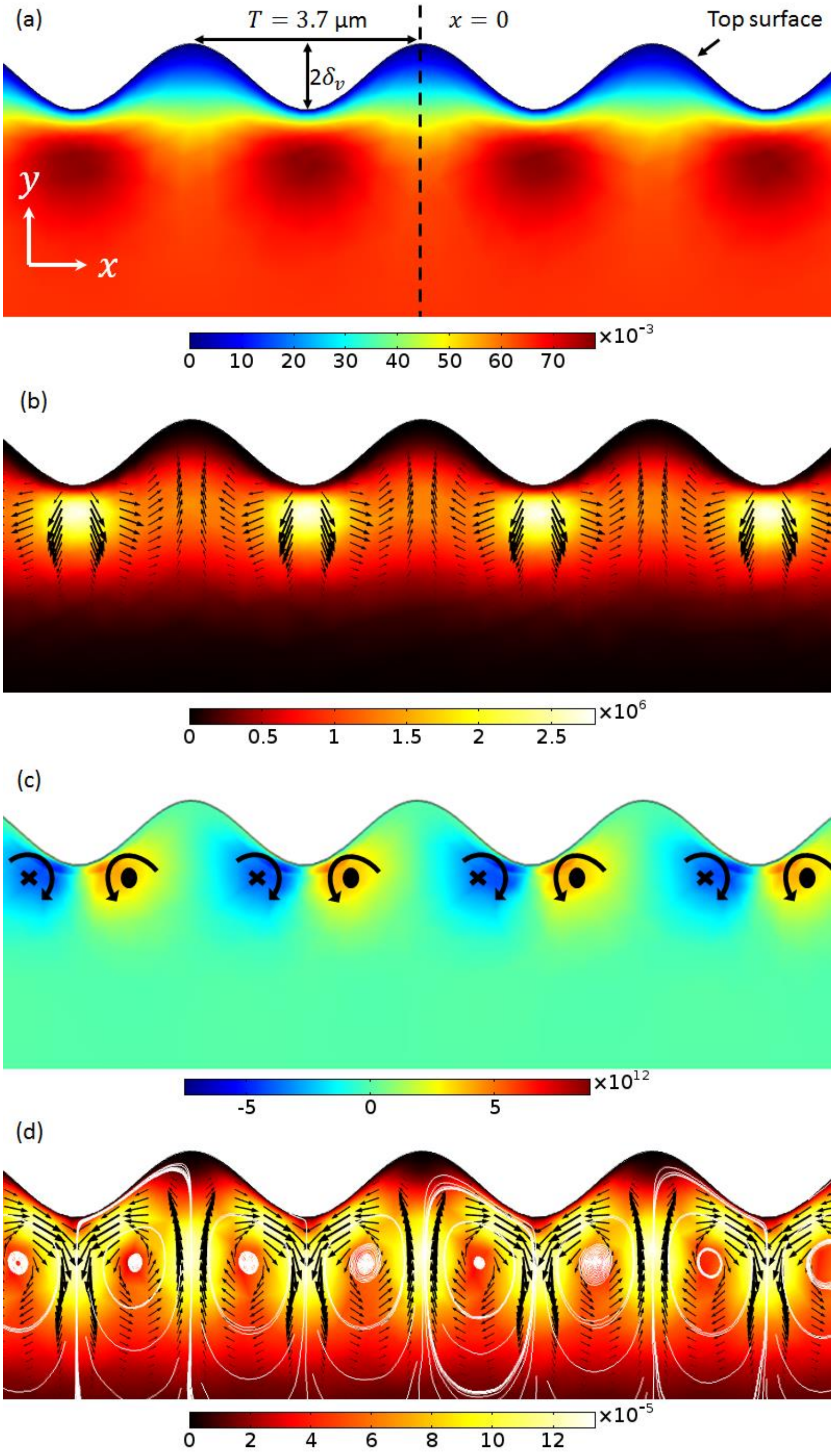

Figure 7.5 Distributions of the modelled results near the top boundary of the chamber where $h_0 = \delta_v$: (a) acoustic velocity (unit of m/s); (b) Reynolds stress force (unit of N/m$^3$); (c) vorticity of the Reynolds stress force (unit of N/m$^4$); and (d) acoustic streaming (unit of m/s), where the arrows and colours show the corresponding vector fields and magnitudes, respectively. The values were obtained from acoustic velocity amplitude of $v_0 = 1$ mm/s.

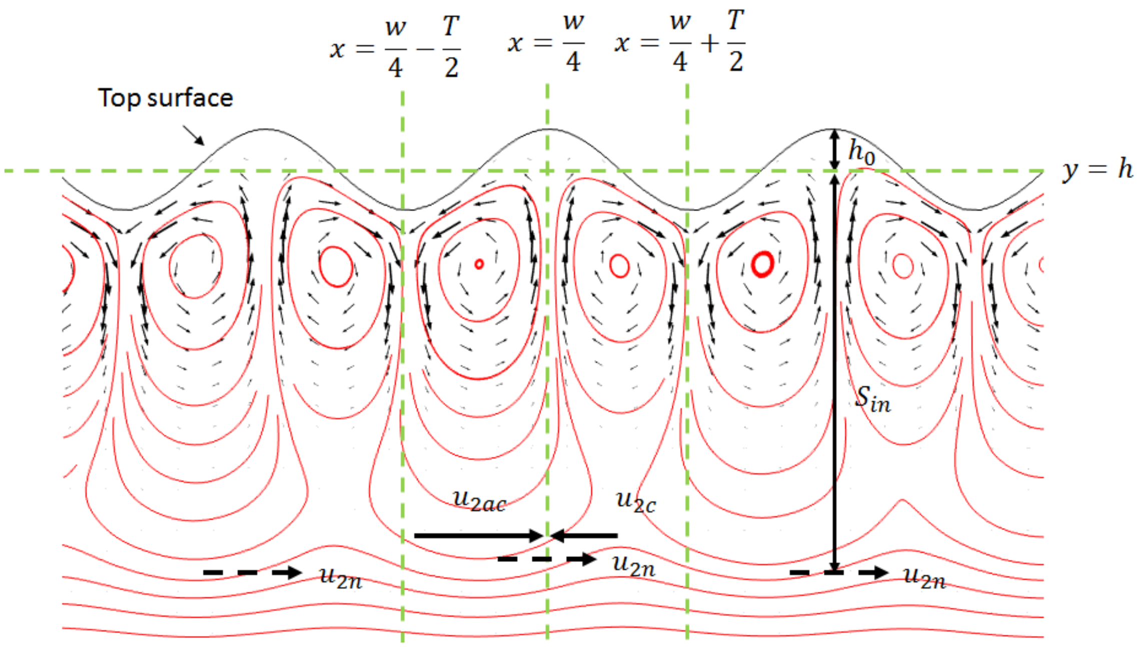

Figure 7.6 Explanations for the formation mechanism of outer streaming vortices – competing of two inner streaming vortices (size of $S_{in}$) in each period of the sine-wave shaped surface, where $u_{2c}$ and $u_{2ac}$ are the $x$-component streaming velocities at the edge of the clockwise and anti-clockwise inner streaming vortex pairs in a period, respectively. $u_{2n} = u_{2ac} - u_{2a}$ is the net $x$ -component streaming velocity of the competing inner streaming vortex pairs, the limiting velocities that drive the outer streaming vortex.

*Figure 7.6* shows the modelled inner streaming field near the top surface of the chamber, where only a portion of the chamber near $x = w/4$ is presented in order to show the detailed information. Here, as emphasized in the figure, the two inner streaming vortices near $x = w/4$ was chosen as an example. It can be seen that the vortex pairs have different strengths, stronger on the left-hand-side one due to the higher acoustic velocities, which decrease from the maximum value at the centre $(x = 0)$ to the side boundary of the chamber $(x = w/2)$. Therefore, there is a net streaming velocity at the edge ($y$-extent) of competing two inner streaming vortices (the vortex edge is defined as the point at which streamlines cease to re-circulate and instead join the outer streaming pattern, shown in detail below) in each period of sine-wave, $u_{2n} = u_{2ac} - u_{2a}$, where $u_{2c}$ and $u_{2ac}$ are the $x$-component streaming velocities at the edge of the clockwise and anti-clockwise inner streaming vortex pairs, respectively. The $y$-extent of inner streaming vortices are controlled by the competition between the rotationality of RSF along the height of the chamber, which is the same as that of a device with flat surfaces. As the inner vortex pattern is continuous along the whole top surface, this net streaming velocities exist in the whole chamber and have the same sign between the acoustic velocity antinode and its adjacent node (change signs in every $\lambda/4$ of the standing wave). This can explain why the modelled outer streaming fields have the same pattern in all the models that two vortices were obtained in each $\lambda/2$ of the standing wave in these half devices.

### 7.4.2. Effects of Surface Profile on the Streaming Velocity Magnitudes

The driving mechanisms of the inner and outer streaming vortices in devices with sine-wave shaped boundaries have been demonstrated in the previous section. In this section, the effects of surface profiles on the magnitude of streaming velocities are analysed. As both the modelled magnitudes of acoustic pressure and acoustic streaming velocity change with the amplitude of the sine-wave shaped surface, $h_0$, in order to quantify the effects of $h_0$ on the streaming velocity, here a coefficient $\gamma$, defined as the ratio of the maximum streaming velocity and the square of acoustic pressure amplitudes, is introduced. The reason for choosing this coefficient to characterise the magnitudes of acoustic streaming velocities is based on the fact that the amplitude of the streaming velocity scales with the square of the pressure amplitude in an acoustic standing wave field, and it is independent of the variations in damping (which determines the pressure amplitude for a given excitation) that are seen with different values of $h_0$.

Two coefficients, $\gamma_{in}$ and $\gamma_{out}$, are used to characterise respectively the inner streaming velocity and the streaming velocity in the bulk of the chamber, which are calculated by

$$\gamma_{in} = \frac{|\boldsymbol{u}_2|_{max}}{|p_1|_{max}^2}, \tag{7.1a}$$

$$\gamma_{out} = \frac{|u_2|}{|p_1|_{max}^2}, \tag{7.1b}$$

where $|p_1|_{max}$ is the pressure amplitude, $|\boldsymbol{u}_2|_{max}$ is the streaming velocity amplitude, and $|u_2|$ is the magnitude of streaming velocity at ($w/4$, 0) used to represent the outer streaming velocity amplitude. *Figure 7.7* plots the relationship between $\gamma_{in}$ and the amplitudes of sine-wave shaped surface, $h_0$, where the maximum streaming velocities for two cases, $h = 40\delta_v$ (diamond-line) and $h = 80\delta_v$ (square-line), are shown. It can be seen that a similar relationship was obtained from these two cases that the magnitudes of streaming velocities rise rapidly with the increase of $h_0$.

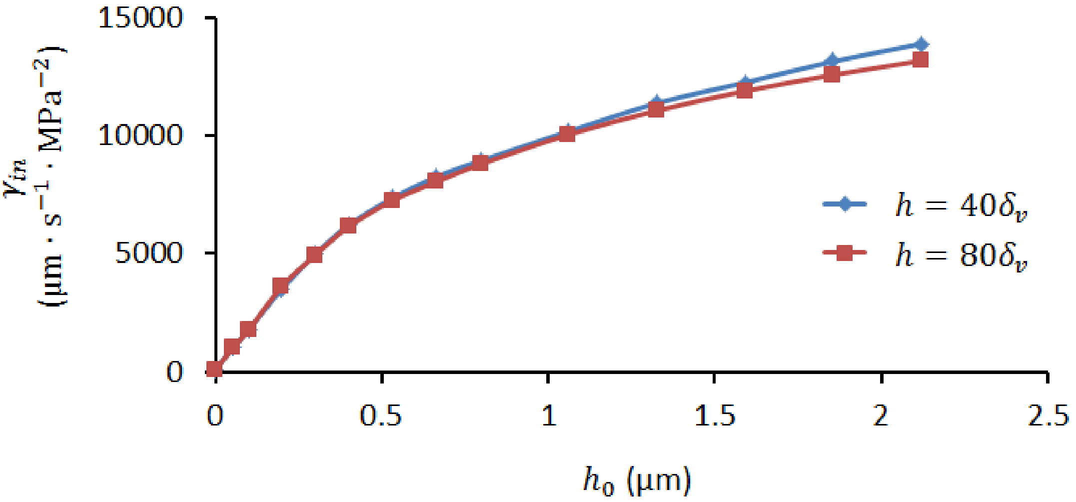

Figure 7.7 The relationships between the maximum streaming velocity, $\gamma_{in}$, and the amplitudes of sine-wave shaped surface, $h_0$, for two cases, $h = 40\delta_v$ (diamond-line) and $h = 80\delta_v$ (square-line), respectively. $\gamma_{in} = |\boldsymbol{u}_2|_{max}/|p_1|^2_{max}$, where $|\cdot|_{max}$ means the maximum absolute value. $r_{in}$ for $h = 40\delta_v$ and $h = 80\delta_v$ at $h_0 = 0$ are 96 and 107, respectively. The period of these sine-wave shaped surface profiles was the same: $T = 3.7$ μm.

It has been shown in *Chapter 3* that the maximum streaming velocity in devices with flat boundaries stays at $x = \pm w/4$ near the boundary due to the sinusoidal shaped distribution of the $x$-component RSF along the axis of the chamber with the maximum values at $x = \pm w/4$ (*Figure 3.6*). In such devices, the dominant force is $F_x$, which is approximately several orders of magnitude bigger than $F_y$ (*Figure 3.5*) due to the huge difference on the magnitudes of first-order acoustic velocity components, $u_1$ and $v_1$ (Equations *(3.3)*). However, the situation in devices with sine-wave shaped boundaries can be different. As shown in the vector field of the RSF field (*Figure 7.5* (b)), in the near boundary region, $F_y$ is non-negligible compared to $F_x$ in the present model. It can be seen that in areas below the troughs of the sine-wave surface profile, $F_y$ dominates in the resultant force, which drives the fluid away from the troughs (shown in *Figure 7.5* (d)). $F_y$ may be further enhanced with the increase of $h_0$ (when $T$

remains the same), resulted in higher streaming velocities in the inner streaming vortices, which can explain the relationship shown in ***Figure 7.7***.

Comparing cases with significant $h_0$ to a flat-walled chamber, it is seen that the largest RSFs are found near the centre of the chamber (for the profiled case) as a result of the larger acoustic velocities there inducing larger maxima of the type seen in ***Figure 7.5*** (a) (due to the need for fluid to flow over the profile). This is in contrast to the flat wall case, where the gradient of the larger scale half-wave resonance acoustic velocity field is the main source of the RSFs; In this case the maximum RSFs are found at $w/4$. This can be seen in ***Figure 7.3*** and ***Figure 7.4***.

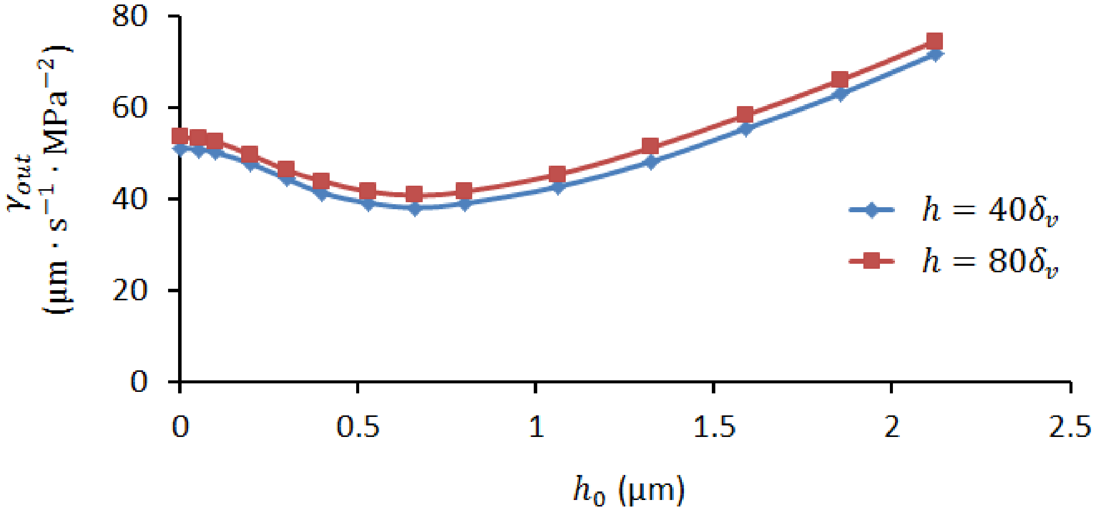

Figure 7.8 The relationships between the $x$ -component streaming velocity at $(w/4, 0)$, $\gamma_{out}$, and the amplitudes of sine-wave shaped surface, $h_0$, for two cases, $h = 40\delta_v$ (diamond-line) and $h = 80\delta_v$ (square-line), respectively. $\gamma_{out} = |u_2|_{max}/|p_1|^2_{max}$, where $|\cdot|_{max}$ means the maximum absolute value. The period of these sine-wave shaped surface profiles was the same: $T = 3.7$ μm.

***Figure 7.8*** plots the relationship between $\gamma_{out}$ and the amplitudes of sine-wave shaped surface, $h_0$, where the maximum outer streaming velocities for two cases, $h = 40\delta_v$ (diamond-line) and $h = 80\delta_v$ (square-line), are shown. It can be seen, similar to the inner streaming velocities, that the relationships between these two cases on the outer streaming velocities are also very close. According to the graph, with the growth of $h_0$, $\gamma_{out}$ firstly decreases slowly to the minimum value while $h_0$ is just over $\delta_v$ and then rises gradually with the further increase of $h_0$.

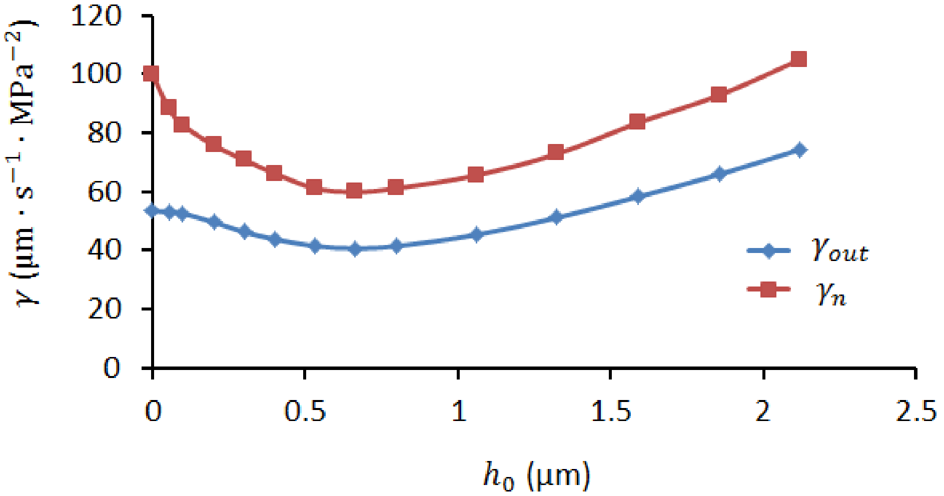

Figure 7.9 The relationships between the $x$ -component streaming velocity, $\gamma$, and the amplitudes of sine-wave shaped surface, $h_0$, in chambers where$h = 80\delta_v$. $\gamma_{out} = |u_2|_{max}/|p_1|^2_{max}$, the streaming velocity at position ($w/4$, 0), and $\gamma_n = |u_{2n}|/|p_1|^2_{max}$, the net limiting velocity on line $x = w/4$, where $|\cdot|_{max}$ means the maximum absolute value. The period of these sine-wave shaped surface profiles was the same: $T = 3.7$ μm.

In ***Chapter 3***, the viability and applicability of the LVM on the modelling of boundary-driven streaming fields in 2D rectangular chambers have been analysed. It was shown that, in a device with flat surfaces, the magnitude of streaming velocity in the bulk of the fluid at ($w/4$, 0) is closely related to the magnitude of the LV at $x = w/4$ on the slip velocity boundary. The ratio between them depends on the height of the chamber (when the other parameters, e.g. $w$ and $\lambda$, are the same). In the previous section, it has been analysed that it is the net streaming velocity of vortex pairs in each period of the sine-wave shaped surface that drives the outer streaming vortices. In order to clarify the relationship presented in ***Figure 7.8***, it is necessary to understand how the net streaming velocity changes with $h_0$. ***Figure 7.9*** plots the relationships between the net streaming velocity, $\gamma_n$, and the amplitudes of sine-wave shaped surface, $h_0$, in chambers where $h = 80\delta_v$. For comparison, the outer streaming velocities, $\gamma_{out}$, are also plotted in the same graph. It is clear that they have similar changing trends with respect to $h_0$, which can further verify the statement that the streaming velocity in the bulk of the fluid is closely related to the magnitude of LV.

The size of the inner streaming vortex (y-extent) varies with $h_0$. In order to determine the vortex size, the vortex edge is defined as the point at which streamlines cease to re-circulate and instead join the outer streaming pattern. By plotting sufficient density of streamlines in COMSOL, this could be determined with good accuracy.

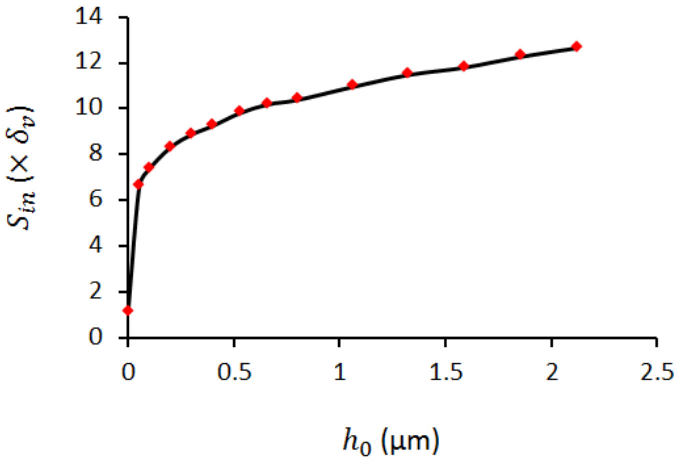

Figure 7.10 The relationship between the sizes of inner streaming vortex, $s_{in}$, near $x = w/4$ and the amplitudes of sine-wave shaped surface, $h_0$, in models where $h = 80\delta_v$. The period of these sine-wave shaped surface profiles was the same: $T = 3.7$ μm.

***Figure 7.10*** plots the modelled sizes of inner vortex (that near $x = w/4$) with respect to $h_0$ in devices where $h = 80\delta_v$. According to the figure, the sizes of inner streaming vortices increase rapidly with the introduction of the sine-wave shaped surface and rise slowly with the further increase of $h_0$. As can be seen from ***Figure 7.11***, in the vertical direction ($y$), the magnitude of the streaming velocities grows rapidly from 0 at the surface to its maximum value where the distance to the surface is approximately $1.5\delta_v$ and then drops dramatically with the increase of distance to the surface. Therefore, a fall on the net streaming velocity, $u_{2n}$, is expected with the increase of $h_0$ as the sizes of the inner streaming vortex grow. At the initial stage shown in ***Figure 7.10*** (small $h_0$), as the sizes of inner vortices grow rapidly, there was a huge drop on the net streaming velocity, $u_{2n}$, and thus on the outer streaming velocity, $|u_2|$, although the inner streaming velocity magnitudes also increases. This can explain the drop of outer streaming velocity shown in ***Figure 7.9***. With the further increase of $h_0$, the size of inner vortices grows much slower and so does the decrease rate of $u_{2n}$. However, the magnitudes of inner streaming velocity magnitude still keep a rapid growth, which results in an increase on the outer streaming velocity shown in ***Figure 7.9***.

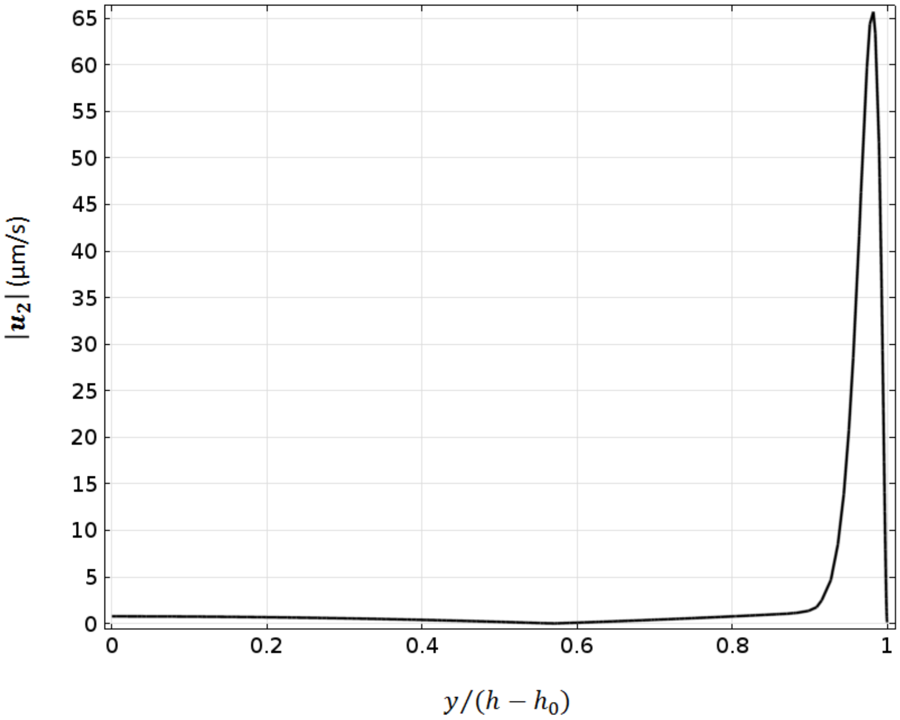

Figure 7.11 The magnitudes of acoustic streaming velocities along $x = w/4 - T/2$ shown in *Figure 7.9*. $v_0 = 1$ mm/s.

### 7.4.3. Effects of the Period of the Surface Profile, $T$, on the Acoustic Streaming Fields

The effects of $h_0$ on the boundary-driven acoustic streaming fields have been fully discussed in the previous sections. Explicit analyses have been given in order to explain the interesting phenomena observed in models with various amplitudes of surface profiles. In a similar way, the effects of profile period, $T$, on the acoustic pressure and streaming fields can be demonstrated. In the following, only the modelled results are shown and the corresponding explanations can be found similar to that shown in previous sections.

The acoustic and streaming fields in four chambers where the sine-wave shaped boundaries have fixed $h_0 = 0.53$ μm and various $T$ ranging from 2.5 μm to 5 μm were modelled in this section. In all these cases, a half-wave standing wave in the $x$-direction of the chambers was established in all these chambers. Under the same excitation, the magnitudes of pressure amplitudes and streaming velocities vary in these models. In terms of acoustic streaming patterns, two vortices along the half-wave standing wave were generated in the bulk of all the chambers and vortex pairs in each period of the sine-wave shaped boundary near the top surfaces were generated. These are similar to those described in the previous Section *7.3*.

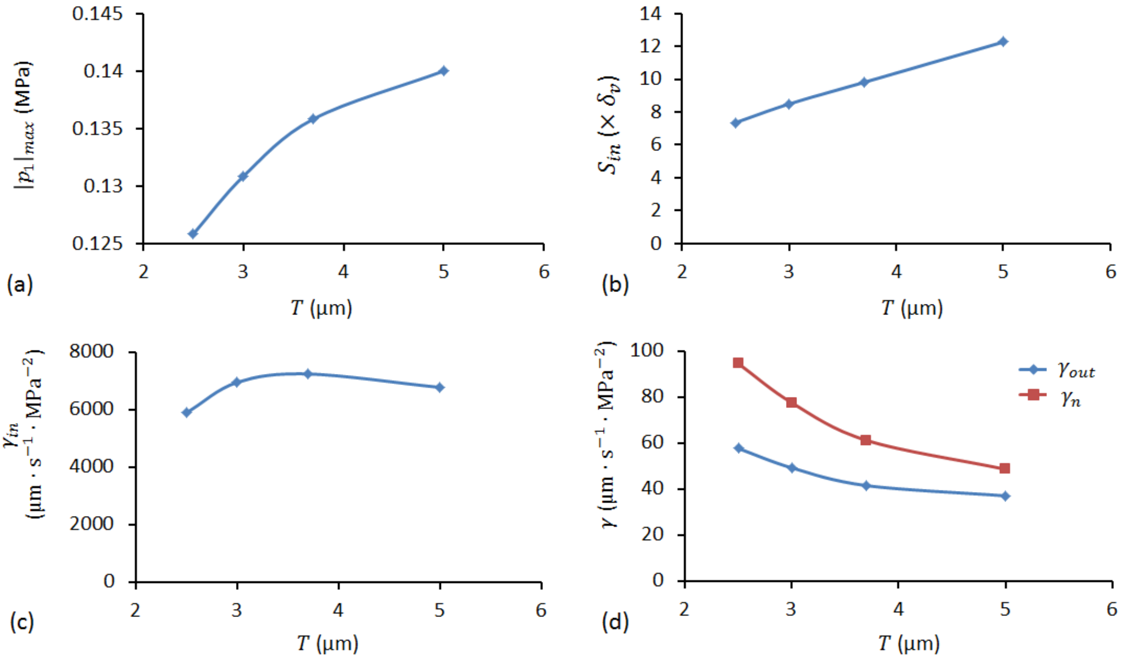

Figure 7.12 The relationships between the modelled results and the periods of the sine-wave shaped boundary, $T$: (a) the acoustic pressure amplitudes; (b) the size of inner streaming vortex near $x = w/4$; (c) the maximum streaming velocity, $\gamma_{in}$; and (d) the outer streaming velocity, $\gamma_{out}$, and net streaming velocity, $\gamma_n$ . The amplitude of these sine-wave shaped boundaries was the same: $h_0 = \delta_v$.

***Figure 7.12*** shows the comparisons of the simulated results in all the models. The parameters plotted are those that have been discussed in previous sections. In each graph, the variation of these terms with respect to the periods of the sine-wave shaped boundaries is plotted. According to ***Figure 7.12***, in all the models considered, with the increase of period, $T$: (1) a global growth can be seen on the modelled acoustic pressure amplitudes (***Figure 7.12*** (a)); (2) the inner streaming vortices near $x = w/4$ increase in size (***Figure 7.12*** (b)); (3) the maximum streaming velocities in the chambers firstly experience a rise and then see a slight drop (***Figure 7.12*** (c)); and (4) a similar distribution on the variations of the net streaming velocity and the outer streaming velocity, a general fall on the magnitudes, can be seen.

Compared to the effect of profile amplitude on the modelled streaming fields, it can be seen that the period of the sine-wave surface profile has less impact on the streaming velocities.

## 7.5. Conclusions

In this chapter, the effects of sine-wave shaped boundaries on the boundary-driven streaming fields in 2D rectangular chambers were numerically investigated. The sine-wave shaped profile was placed on the walls parallel to the axis of the standing wave. The effects of the two parameters of the sine-wave, respectively the amplitude, $h_0$, and the period, $T$, were analysed. It was shown that this kind of surface profile has dramatic influences not only on the magnitudes of first-order acoustic fields, but also on the second order acoustic streaming patterns and velocity magnitudes (around 100 fold).

In term of first-order acoustic fields, it was shown that the sine-wave shaped surfaces do not have any effect on the standing wave pattern but affect the magnitude of pressure amplitudes.

With respect to the acoustic streaming patterns, it was found that the regular two-vortices-per-half-wave inner streaming pattern was disrupted by the curved surface profile. A pair of wall dependent inner streaming vortices with much higher velocity is generated within each period of the sine-wave resulting from the additional driving terms created by the gradients in acoustic velocity near the profiled surface. The outer streaming pattern in devices with profiled surfaces was found to have similar structure to that found in devices with flat surfaces. The outer streaming pattern can be considered to be generated from small differences in the rotational velocity of adjacent vortex pairs near the surface. This difference has a similar origin (a result of the larger scale acoustic gradients in the body of the chamber) to the flat walled case.

In regards to the magnitudes of streaming velocities, the inner streaming velocity is seen to increase rapidly with increasing profile amplitude, $h_0$. In comparison, the outer streaming velocities stay within the same order of magnitude over the range $h_0 = 0 - 2$ μm. The effect of profile period, $T$, is much less significant.

The wall dependent inner streaming vortex pattern and the dramatic increase of acoustic streaming velocities in regions near the boundary could be useful for applications where the near-boundary fluid flow is essential. For instance, in flow battery systems, where the charging and discharging processes are limited by the formation of a diffusion limited boundary layer near the surfaces of electrodes, the introduce of small acoustic streaming vortices to the interface of electrodes and electrolyte could be useful for disturbing this boundary layer and thus enhancing the charging and discharging processes. In addition, this could also be useful for removing biofouling formed on the surfaces that are not accessible by other mechanical forces, e.g. in microfluidic systems.

# Chapter 8. Concluding Remarks and Future Work

Acoustic streaming is a steady flow that can be visualised in acoustofluidic manipulation devices, which is generally considered as a disturbance in the process of acoustofluidic particle manipulation as it usually occurs unexpectedly and disrupts the process of particle manipulation predicted by the ARF. On the other hand, it can be found useful in various applications, such as fluid mixing, heat and mass transfer, fluid pumping, etc. Understanding the formation mechanism of acoustic streaming patterns is very important to create designs to suppress it or to generate desired vortex pattern for particular applications.

In this thesis, several boundary-driven streaming patterns, considered as the dominant pattern (compared to the Eckart type streaming) in most bulk acoustofluidic manipulation devices, have been analysed with formation mechanisms proposed. Specifically, boundary-driven streaming patterns in devices due to respectively 1D standing wave, 2D standing wave and 3D cavity modes have been presented.

To be more specific, this thesis has mainly shown the work listed below:

- Previous work on acoustic streaming (mainly focusing on the boundary-driven streaming) ranging from the first observation of air circulation over an oscillating plate to the mostly recent work, including theoretical analyses, experimental measurements and numerical simulations, has been reviewed. (*Chapter 1*)
- Two numerical methods, the RSM and LVM, have been introduced for the simulation of boundary-driven streaming fields in acoustofluidic systems. The RSM solves both inner and outer streaming fields and investigates the origin of the boundary-driven streaming, the rotational RSF distributions inside and outside the viscous boundary layer. The LVM solves the outer streaming field in the bulk of the fluid with the LVs derived from the irrotational acoustic velocity field working as slip velocity boundary conditions. (*Chapter 2*)
- Classical boundary-driven streaming fields, Rayleigh-Schlichting streaming, in 2D rectangular chambers have been numerically simulated

from the RSM. Acoustic velocity, RSF and acoustic streaming fields were presented. The modelled streaming fields were found in good comparisons with that obtained from Hamilton et al.'s analytical solution; Rayleigh streaming in 2D rectangular chambers has been numerically modelled from the LVM. The modelled results were compared to that obtained from Rayleigh's analytical solution, which show good consistency. (***Chapter 3***)

- The scope of application of the LVM has been demonstrated from a comparison of the two numerical methods above, which shows that, in addition to the low curvature condition on the surfaces of the fluid channel, the LVM can have high accuracy on modelling the magnitudes of streaming velocities provided that the dimension of the fluid channel cross-section exceeds $\sim 50\delta_v$ ($< 10\%$ of error). This means that the outer streaming fields in both 2D and 3D models within large chambers (>$100\delta_v$), where only the streaming fields in the bulk of the fluid are usually of interest, can be effectively solved from the LVM. (***Chapter 3***)
- The driving mechanism for the classical boundary-driven streaming in 2D rectangular channels has been presented in depth. It was found that it is the acoustic energy attenuation due to the presence of viscous boundary layer that generates rotational RSF fields, which have distinct vorticity in the viscous boundary layer and that immediately outside it. The balanced streaming velocity in the juncture of the two streaming vortices driven by the distinct rotational RSF is the LV that drives both the inner and outer streaming vortices, forcing the inner vortex in the viscous boundary layer with a size of $\sim\delta_v$ in devices where $h \gg \delta_v$. (***Chapter 3***)
- A four-quadrant acoustic streaming pattern with circulations parallel to the transducer radiating surface was observed in low aspect-ratio glass capillaries ($h/w = 0.05$), referred to as transducer plane streaming. It is different from the better-known streaming patterns, e.g. Rayleigh streaming and Eckart streaming, whose circulations are perpendicular to the transducer radiating surfaces. The LVM was applied to solve the streaming fields in the glass capillaries through a fluid-layer-only model. The modelled trajectories of microparticles were in good agreement with the experimental observations. The mechanism of this transducer plane streaming pattern has been presented for the first time, which

was found to be closely related to the active sound intensity field, which is shown to be rotational in acoustic fields. (*Chapter 4*)

- 3D boundary-driven streaming fields in acoustofluidic manipulation devices have been modelled from the LVM with a consideration of the full configuration of acoustofluidic systems. It was shown that both the acoustic streaming patterns and magnitudes of acoustic streaming velocities were in good agreements with the experimental measurements. The high accuracy on modelling the acoustic streaming fields has proved the LVM a numerical efficient method for the prediction of 3D boundary-driven streaming in acoustofluidic systems. (*Chapter 5*)
- A new acoustic streaming pattern has been analysed in medium aspect-ratio channels from both numerical and experimental methods, referred to as “modal Rayleigh-like streaming”. It was found that the modelled acoustic streaming pattern in the fluid-channel-only model compared well with the measured streaming fields in a glass capillary device where the size of the fluid channel was the same with that modelled. It was found that the overall acoustic streaming field in the bulk of the channel was driven by the boundaries parallel to the transducer face at the cavity mode obtained the transducer plane streaming but has a pattern similar to the Rayleigh streaming: circulations of the streaming vortices are perpendicular to the transducer radiating surface and there are two vortices within each half-wave standing wave along the axis of the cavity. (*Chapter 6*)
- The conditions, under which each of the acoustic streaming patterns illustrated above is dominant in layered acoustofluidic manipulation devices, have been established. (*Chapter 6*)
- The effects of sine-wave shaped surfaces on boundary-driven streaming fields have been numerically investigated. It was found that it has dramatic effects not only on the first-order acoustic fields but also on the acoustic streaming fields. Detailed comparisons on the acoustic velocity and RSF fields between models with flat surfaces and those with sine-wave shaped surfaces, have allowed explanations on the mechanism behind the sine-wave shaped surfaces on the acoustic and streaming fields. This has opened a wide range of applications where the fluid flow near the solid surfaces is essential. (*Chapter 7*)

In future, this research can possibly be extended in the following directions:

- Contribution of Eckart type streaming to the boundary-driven streaming fields in bulk acoustofluidic manipulation devices, e.g. Rayleigh streaming, transducer plane streaming and modal Rayleigh-like streaming. In most layered bulk acoustofluidic manipulation devices, the dimension of fluid channel cross-sections is in the same order of magnitude to the acoustic wavelength. However, along the fluid channel, it usually has a scale of hundreds of acoustic wavelengths, which may allow acoustic energy attenuation to generate Eckart type streaming comparable to and ever greater than the boundary-driven streaming velocities.
- Acoustic streaming in SAW systems, the contribution of Eckart streaming and boundary-driven streaming, respectively. Recent work[197, 198] have shown the modelling of acoustic streaming fields in standing SAW devices, which though still needs to be validated from experimental measurements. The numerical methods on predicting the acoustic streaming fields in SAW devices are far from complete. Especially in SAW systems where the dimension of the fluid channel is comparable to the acoustic wavelength, it will be interesting to know how big effects boundary-driven streaming has on the overall streaming fields.
- Focusing of submicron particles in acoustofluidic systems is useful for many promising applications, which requires better control of the acoustic streaming fields to remove its side effects. There is still some work to do in order to accomplish this although some work has shown focusing of particles with sizes down to ~0.5 μm.
- The work presented in *Chapter 7* has opened a broad field of applications where the near-boundary streaming field is essential. Therefore, this technique can be applied to fulfil particular applications.

# Appendix 1

## Paper published in Lab on a Chip

### Acoustic streaming in the transducer plane in ultrasonic particle manipulation devices

**Junjun Lei, Peter Glynne-Jones and Martyn Hill**

**Abstract:** In acoustofluidic manipulation and sorting devices, Rayleigh streaming flows are typically found in addition to the acoustic radiation forces. However, experimental work from various groups has described acoustic streaming that occurs in planar devices in a plane parallel to the transducer face. This is typically a four-quadrant streaming pattern with the circulation parallel to the transducer. Understanding its origins is essential for creating designs that limit or control this phenomenon. The cause of this kind of streaming pattern has not been previously explained as it is different from the well-known classical streaming patterns such as Rayleigh streaming and Eckart streaming, whose circulation planes are generally perpendicular to the face of the acoustic transducer. In order to gain insight into these patterns we present a numerical method based on Nyborg's limiting velocity boundary condition that includes terms ignored in the Rayleigh analysis, and verify its predictions against experimental PIV results in a simple device. The results show that the modelled particle trajectories match those found experimentally. Analysis of the dominant terms in the driving equations shows that the origin of this kind of streaming pattern is related to the circulation of the acoustic intensity.

**DOI:** 10.1039/C3LC00010A

Lab on a Chip

RSCPublishing

PAPER

View Article Online
View Journal | View Issue

# Acoustic streaming in the transducer plane in ultrasonic particle manipulation devices†

**Cite this:** *Lab Chip*, 2013, **13**, 2133

Junjun Lei, Peter Glynne-Jones* and Martyn Hill

Received 3rd January 2013,
Accepted 8th April 2013

DOI: 10.1039/c3lc00010a

**www.rsc.org/loc**

In acoustofluidic manipulation and sorting devices, Rayleigh streaming flows are typically found in addition to the acoustic radiation forces. However, experimental work from various groups has described acoustic streaming that occurs in planar devices in a plane parallel to the transducer face. This is typically a four-quadrant streaming pattern with the circulation parallel to the transducer. Understanding its origins is essential for creating designs that limit or control this phenomenon. The cause of this kind of streaming pattern has not been previously explained as it is different from the well-known classical streaming patterns such as Rayleigh streaming and Eckart streaming, whose circulation planes are generally perpendicular to the face of the acoustic transducer. In order to gain insight into these patterns we present a numerical method based on Nyborg's limiting velocity boundary condition that includes terms ignored in the Rayleigh analysis, and verify its predictions against experimental PIV results in a simple device. The results show that the modelled particle trajectories match those found experimentally. Analysis of the dominant terms in the driving equations shows that the origin of this kind of streaming pattern is related to the circulation of the acoustic intensity.

## I. Introduction

Particle manipulation using acoustic radiation forces from ultrasonic standing waves, recently reviewed in *Review of Modern Physics*[1] and *Lab on a Chip*,[2] has gained increased attention in recent years and is recognised as being well-suited to particle handling in microfluidic channels as it is non-invasive and requires no pre-treatment of the particles regardless of their optical or charge properties. When an ultrasonic standing wave field is established in a microfluidic channel, the particles suspended in the fluid experience two main forces: acoustic radiation forces (ARF) from their interaction with the sound field; and acoustic streaming induced drag forces (ASF). Previous experimental work on acoustophoresis has shown both ARF-dominated motion and ASF-dominated motion. Typically, in a low MHz field the motion of particles of diameters larger than about 2 μm is dominated by the ARF. Recent experimental work[3–5] has shown excellent agreement with theoretical predictions based on well-established theory.[6,7] However, during the process of particle manipulation, acoustic streaming can disrupt the manipulation of particles with diameter smaller than 2 μm. As Spengler *et al.*[8] demonstrated, streaming currents can significantly influence the manipulation because the convective drag, generated by acoustic streaming can be comparable to the lateral direct radiation force in the nodal plane. Kuznetsova and Coakley[9] later investigated the roles of acoustic streaming on microparticle concentration and found that 1 μm particles in a half wavelength resonator were convected by streaming from the centre to the edge of the chamber thus undermining the concentration process.

In microfluidic ultrasonic particle manipulation devices, the acoustic streaming field is generally dominated by boundary-driven streaming (Eckart streaming requires acoustic absorption over longer distances than those typically found in such devices[10]). Boundary streaming is a result of the interaction between the acoustic oscillation and solid boundaries. Rayleigh[11] was the first to present a theoretical analysis of a boundary layer driven acoustic streaming field. With a series of assumptions, he obtained equations for the steady motion of periodic vortices within a standing wave field, comprising four pairs of counter-rotating vortices within each wavelength. His solution only describes the fluid motion outside the viscous boundary layer, so it is commonly referred to as 'outer streaming' as well as 'Rayleigh streaming'. Subsequently, a series of modifications of Rayleigh's solution have been proposed, most notably by Westervelt,[12] Nyborg[13] and Schlichting,[14] reviewed by Boluriaan *et al.*[15] and Wiklund *et al.*[16] Hamilton *et al.*[17] derived an analytical solution for the acoustic streaming generated by a standing wave confined by parallel plates that described the streaming field inside the viscous boundary layer in addition to the outer streaming field. These theoretical analyses have been complemented by

---

*Faculty of Engineering and the Environment, University of Southampton, Southampton, UK. E-mail: P.Glynne-Jones@soton.ac.uk*

† Electronic supplementary information (ESI) available: A 3D animation of the simulated particle trajectories and a video of the four quadrant streaming observed experimentally. See DOI: 10.1039/c3lc00010a

experimental work in acoustofluidic systems and numerical simulations. The acoustic streaming in a standing wave field in an air-filled closed duct was simulated by Kawahashi and Arakawa[18] by applying a fourth-order spatial difference method and by Aktas and Farouk[19] using a flux-corrected transport algorithm. They directly solved the compressible Navier–Stokes equations using a control-volume-based finite-volume method based on the flux-corrected transport (FCT) algorithm. The classical Rayleigh streaming field in a cylindrical tube was numerically simulated by Sastrapradja and Sparrow[20] using the vorticity transport equation (VTE). Recently, Rayleigh streaming in a silicon-glass chip was modelled by Muller *et al.*[21] Simulations showing the transition of acoustophoretic motion from that dominated by ASF to that dominated by ARF were numerically studied.

The literature discussed above generally describe cases in which the plane of the streaming vortices contains the axis of the standing or travelling waves (in most cases this axis is perpendicular to the transducer). However experimental observations in planar microfluidic resonators have described streaming patterns with vortices flowing parallel to the transducer plane.[16,22] Similar vortices had previously been described by Spengler *et al.*[23] and later work from Kuznetsova and Coakley[9] also discusses 'unexpected wall-independent' suspension vortices with circulation planes parallel to the transducer radiating surface. They called this streaming pattern ''unexpected'' for the reason that this kind of streaming pattern is different from the classical streaming (*e.g.* Rayleigh streaming[11] and Eckart streaming[24]) whose vortex plane contains the axis of the standing or travelling waves. In real standing wave devices there are also acoustic energy gradients in the lateral directions perpendicular to the standing wave axis. In many cases these are insignificant in comparison with the axial gradients, but they become more significant in planar resonators with large surface areas.[25] This paper investigates whether these lateral energy gradients may be the cause of some of the unexpected streaming patterns observed in planar microfluidic resonators.

Despite having been observed experimentally for more than a decade, the mechanism underlying this kind of streaming pattern has not been fully investigated. In this paper, we present a steady, four-quadrant, symmetric streaming pattern with the circulation plane parallel to the transducer plane, which has frequently been observed in our ultrasonic particle manipulation devices and is similar to that described by Hammarstrom *et al.*[22] A Finite element method is used to numerically simulate the streaming field and particle trajectories in relevant devices in order to understand the mechanism of this type of streaming pattern. In section II we present the numerical simulations, including the numerical methods, models and results, numerical accuracy, and particle trajectory simulation. Section III shows experiments in which the test device, micro-PIV setup and the motion of particles obtained from PIV measurement are presented. In section IV, a brief discussion of the results, including a comparison between the numerical simulation and the experimental measurement and the mechanism of the observed streaming pattern, is given and overall conclusions are drawn in section V.

## II. Numerical simulation

### 1. Background – limiting velocity method

In this section, a numerical model is introduced to simulate the three dimensional streaming field in our capillary device, described below, using the *limiting velocity method*. This method was first introduced by Nyborg[26] in 1958 and modified by Lee and Wang[27] in 1988. It was shown that if the boundary has a radius of curvature that is large compared to the acoustic viscous boundary layer, then the time averaged velocity at the extremity of the inner streaming (the ''limiting velocity'') can be approximated as a function of the local, first order linear acoustic field (when solved with the surface replaced by a slip boundary condition). The streaming in the bulk of the fluid can then be predicted by a fluidic model that takes the limiting velocity as a boundary condition. A schematic of the streaming flow over a vibrating surface is shown in Fig. 1.

Thus, this approach only predicts the velocity of the streaming field *outside* the viscous boundary layer, and does not calculate the streaming field inside the acoustic viscous boundary layer. In typical acoustofluidic devices working in the MHz region this is useful as we are generally interested in the main body of the fluid which is typical several orders of magnitude thicker than the acoustic viscous boundary layer which has thickness:[28]

$$\delta_v = \sqrt{\frac{2v}{\omega}}, \tag{1}$$

where $v$ is the kinematic viscosity of the fluid and $\omega$ is the angular frequency. At 1 MHz in water this has a value of about 0.6 μm.

This decomposition of the problem (into the steps described below) is only valid if the mass source term in the streaming field described by Muller *et al.*[29] in their eqn (9a) can be ignored. Nyborg[26] justifies this approximation in his derivation of the limiting velocity in the paragraph above his eqn (10).

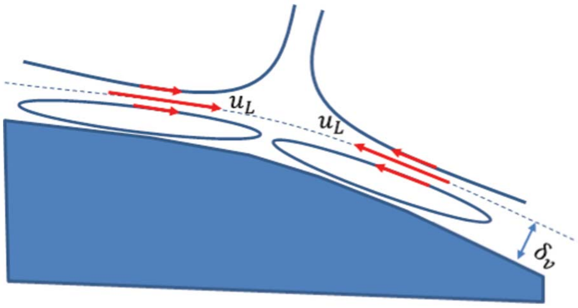

**Fig. 1** Schematic of the streaming field over a vibrating surface, where $u_L$ is the limiting velocity and $\delta_v$ is the viscous penetration depth.

The limiting velocity represents the streaming immediately outside the viscous boundary layer, and has components, $u_L$ and $v_L$, given by:[27]

$$u_{\mathrm{L}} = -(4\omega)^{-1} \operatorname{Re}\left\{ q_x + u_1^* \left[ (2+i)\nabla\cdot\boldsymbol{u}_1 - (2+3i)\frac{\partial w_1}{\partial z} - (2-i)H\, w_1 \right] \right\}, \quad (2)$$

$$v_{\mathrm{L}} = -(4\omega)^{-1} \operatorname{Re}\left\{ q_y + v_1^* \left[ (2+i)\nabla\cdot\boldsymbol{u}_1 - (2+3i)\frac{\partial w_1}{\partial z} - (2-i)H\, w_1 \right] \right\}, \quad (3)$$

where

$$q_x = u_1\left(\frac{\partial u_1^*}{\partial x} + v_1^* T_{121}\right) + v_1\left(\frac{\partial u_1^*}{\partial y} + v_1^* T_{122}\right), \quad (4)$$

$$q_y = u_1\left(\frac{\partial v_1^*}{\partial x} + u_1^* T_{121}\right) + v_1\left(\frac{\partial v_1^*}{\partial y} + u_1^* T_{122}\right), \quad (5)$$

Where $u_1$, $v_1$ and $w_1$ are components of the complex acoustic velocity vector, $\boldsymbol{u}_1$ (the subscript helps distinguish this first order term from the second order streaming velocity, $\boldsymbol{u}_2$, described later). The superscript, *, is the complex conjugate. The indices $i$, $j$, and $k$ represent the three coordinates $x$, $y$ and $z$. $T_{ijk}$ and $H$ are geometric parameters (of units [$\mathrm{m}^{-1}$] and [non-dimensional] respectively) that relate to the curvature and orientation of the surface relative to the coordinate system,[27] making this expression general for limiting velocities on all shapes and orientations of boundaries (subject to the constraint that the curvature is small compared to the viscous boundary layer).

On a planar surface that is normal to $z$, the equations simplify to the following form:

$$u_{\mathrm{L}} = -\frac{1}{4\omega}\operatorname{Re} \left\{ u_1\frac{du_1^*}{dx} + v_1\frac{du_1^*}{dy} + u_1^*\left[(2+i)\left(\frac{du_1}{dx} + \frac{dv_1}{dy} + \frac{dw_1}{dz}\right) - (2+3i)\frac{dw_1}{dz}\right]\right\}, \quad (6)$$

$$v_{\mathrm{L}} = -\frac{1}{4\omega}\operatorname{Re} \left\{ u_1\frac{dv_1^*}{dx} + v_1\frac{dv_1^*}{dy} + v_1^*\left[(2+i)\left(\frac{du_1}{dx} + \frac{dv_1}{dy} + \frac{dw_1}{dz}\right) - (2+3i)\frac{dw_1}{dz}\right]\right\}. \quad (7)$$

## 2. Finite element models

The model was implemented in the finite element package COMSOL.[30] The numerical procedure can be split into three steps. First, a linear acoustic model is used to find the first-order resonant acoustic pressure and velocity fields, from which the limiting velocities can be derived. Second, the limiting velocities are found using eqn (6) and (7) above, which are functions of the linear acoustic velocities. These are then applied as boundary conditions to a Navier–Stokes creeping flow model to obtain the time averaged fluid motion (the streaming). Finally, a 'particle tracing for fluid flow' model was used to simulate the particle trajectories under the combined action of ARF and ASF.

The model geometry is formed from a cuboidal domain of dimensions 0.3 × 6 × 10 $\mathrm{mm}^3$ (height × width × length). Here, only the fluid layer within a section of the capillary was modelled for the following reasons: (1) without the transducer and glass walls of the capillary, the whole model is computationally simpler. The numerical process, including the simulation of the first-order acoustic field and the acquisition of the acoustic streaming field can be finished in one hour. While it is possible to model the full device, including piezoelectric and fluid-solid couplings, the additional complexity places high demands on workstation memory; (2) This reduced model is shown below to successfully predict the observed phenomena, which demonstrates that the essential physics is already captured by the model, and thus when we discuss the physical origin of this type of streaming pattern we are in a stronger position to identify the mechanism. In the following sections, each step is examined in more detail.

**A. Comparison of the approach with classical solutions.** Firstly, the applicability of this approach to modelling the streaming is ascertained by applying the methodology described above to a 2 dimensional model of a rectangular chamber (Fig. 2 (a)) with an aspect ratio chosen so that classical Rayleigh streaming predominates. The parameters used in the 2D and 3D models are summarised in Table 1 and Table 2, respectively. The small mesh size is required to accurately resolve the inner streaming vortex. The linear acoustic step has the left wall excited by a sinusoidal pressure fluctuation of amplitude 0.2 MPa, with the remaining boundaries set to be reflecting. In the fluid motion step, the bottom and top walls are set to have limiting velocity boundary conditions (derived from the linear acoustic quantities) and the left and right walls are slip boundaries. It can be seen from Fig. 2 (b) and (c) that the model is in good agreement with the classical results of Rayleigh.[11]

**B. First-order acoustic field.** Having established the viability of the approach by comparison with Rayleigh streaming solutions, the capillary device shown in Fig. 3 was modelled using the COMSOL 'pressure acoustic' option to obtain the first-order acoustic field. This solves the harmonic, linearized acoustic problem, which takes the form:[31]

$$\nabla^2 p = -\frac{\omega^2}{c^2}p \quad (8)$$

where $p$ is the complex pressure defined at position $r$ using the relation,

$$p_t(r,t) = \operatorname{Re}\{p(r)\mathrm{e}^{-j\omega t}\} \quad (9)$$

and makes the assumptions[31] of small acoustic disturbances, an inviscid and Newtonian fluid, and adiabatic processes. The fluid is also assumed at rest so the streaming velocities must be small in comparison to acoustic velocities. It can be seen in the following that all of these approximations are upheld in the device presented here.

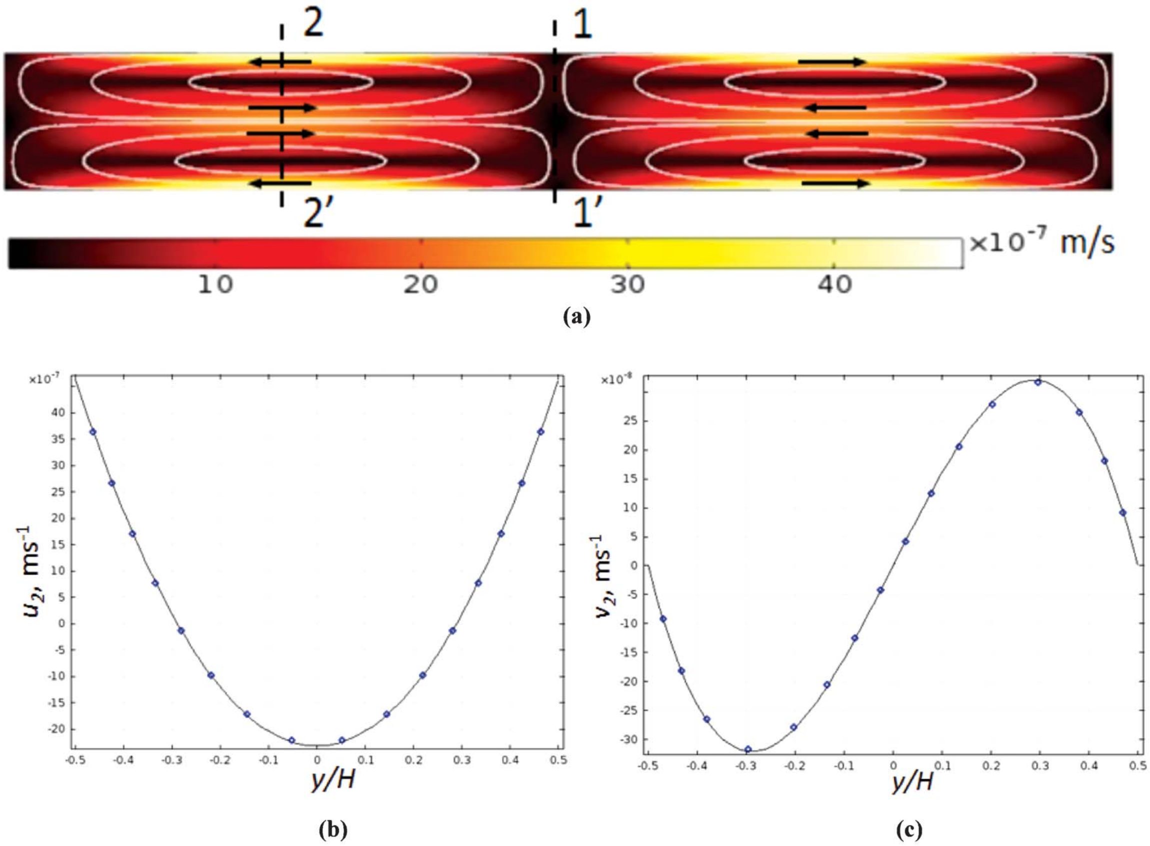

**Fig. 2** (a) Modelled Rayleigh streaming in a 2D rectangular chamber (b) $u_2$, the *x*-component of streaming velocity, along line 1–1′ ($x = -L/4$); (c) $v_2$, the *y*-component of streaming velocity, along line 2–2′ ($x = 0$). Diamonds show model results and solid lines are the results obtained from Rayleigh's analytical solution.

**Table 1** 2D Rayleigh streaming model parameters

| | | | |
|---|---|---|---|
| Dimension of enclosure (length $L$ × height $H$): | 0.74 mm × 84.8 µm | Driven frequency, $f$: | 1 MHz |
| Excitation pressure amplitude, $p$: | 0.2 MPa | Dynamic viscosity of water, $\mu$: | $8.9 \times 10^{-4}$ Pa s |
| Density of water, $\rho_p$: | 1000 kg m$^{-3}$ | Mesh size: | 1 µm |

The bottom surface was given a normal-acceleration boundary condition, the left and right walls were considered as plane wave radiation boundary conditions (to represent energy that travels down the capillary being largely absorbed by the tubing and connectors at the ends), and the remaining side walls and roof were hard boundary conditions. The standing wave field within the fluid layer was generated by a sinusoidal acceleration of the bottom wall. A 2D normal distribution is used to represent the reduction in vibration amplitude away from the transducer area:

$$a_\mathrm{n} = a_0 \mathrm{e}^{-ax^2 - by^2}. \tag{10}$$

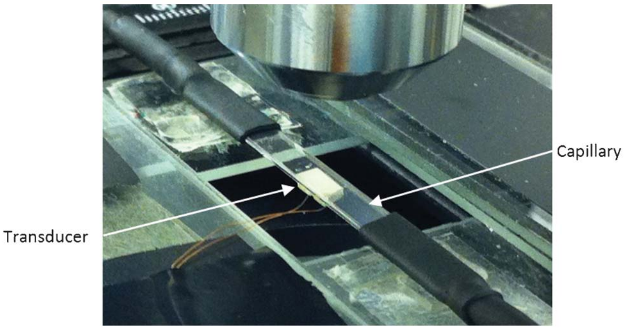

**Fig. 3** An example capillary particle manipulation device. This particular device lacks the gold foil electrode, allowing the transducer to be seen.

To assess the validity of this approach, the vibration profile was compared with a full model (composed of transducer and glass capillary), which shows that similar acoustic acceleration and velocity distributions on the bottom surface were obtained from these two models. Then, five sets of '$a$' and '$b$' coefficients (respectively, with units m$^{-2}$, $a = 0.22 \times 10^6$, $b = 0.22 \times 10^6$; $a = 0.22 \times 10^6$, $b = 5 \times 10^5$; $a = 0.22 \times 10^6$, $b = 2 \times 10^6$; $a = 5 \times 10^5$, $b = 5 \times 10^5$; $a = 5 \times 10^5$, $b = 2 \times 10^6$) in the

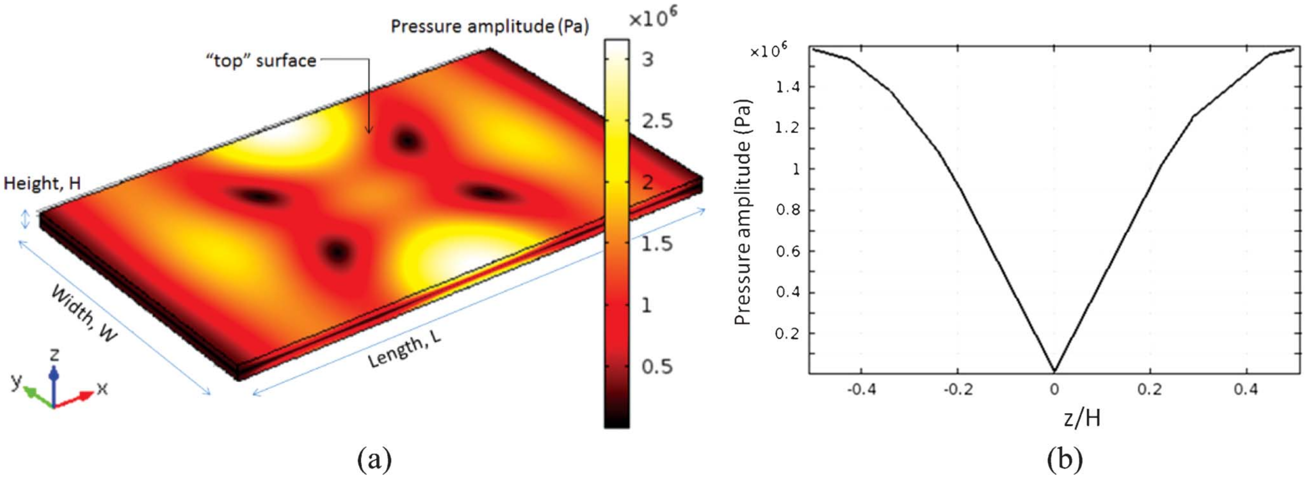

**Fig. 4** (a) Magnitude of the acoustic pressure in the fluid layer at the surfaces of the modelled volume; (b) acoustic pressure amplitude distribution at the centre line ($x = 0$, $y = 0$, $-H/2 \leqslant z \leqslant H/2$).

above equation were examined, to represent the area of the excitation from the transducer. It was found that the streaming field was similar from all excitations, suggesting that the streaming pattern is reasonably robust to the precise choice of the excitation shape. This approach is similar to that described by Muller *et al.*[29] who represented ultrasonic actuation with a velocity boundary condition when simulating the Rayleigh streaming in a 2D rectangular chamber. The results presented in this paper are for an excitation of $a = 5 \times 10^5$ and $b = 2 \times 10^6\ \mathrm{m}^{-2}$.

The frequency of the half-wave resonance was found at 2.479 MHz by using a parametric sweep to plot the average acoustic energy density in the fluid layer *versus* driving frequency. This method has been found to be more reliable than sorting through the very large number of modes presented by a modal analysis. The simulated acoustic pressure field is shown in Fig. 4. Fig. 4 (a) represents the magnitude of the acoustic pressure on the surfaces of the chamber and Fig. 4 (b) the magnitude along the centre line ($x = 0, y = 0, -H/2 \leqslant z \leqslant H/2$).

**C. Acoustic streaming field.** The COMSOL 'creeping flow' model was used to simulate the acoustic streaming field. This approximates the fluid as incompressible, and neglects inertial terms (Stokes flow) as the Reynolds number is much smaller than one in the experiments presented in this paper. In the body of the fluid the governing equations for the streaming velocity field, $\boldsymbol{u_2}$, and associated pressure field, $p_2$, are

$$\nabla p_2 = \mu \nabla^2 \boldsymbol{u_2} \qquad (11a)$$

$$\nabla . \boldsymbol{u_2} = 0 \qquad (11b)$$

The bottom and top walls were considered as limiting velocity boundary conditions while the remaining four walls were considered as slip boundary conditions. Initial modelling had represented the side walls (at $y = \pm 3$ mm) as limiting velocity boundary conditions and the resulting pattern was a combination of classical Rayleigh streaming in the vicinity of the side walls superimposed on the larger scale transducer-plane streaming. However, to aid clearer presentation of the results we limit ourselves in this paper to presenting the transducer-plane streaming generated by the limiting velocities of the floor and ceiling of the device and neglect the localised Rayleigh streaming generated by the side walls.

In order to investigate the effects of mesh size on the modelled results, a mesh dependency study of the 3D model is presented here. A series of tetrahedral meshes with size ranging from 0.03 mm to 0.17 mm was simulated. The average value of the magnitude of streaming velocity in the whole device, $\bar{u}$, for each case was obtained. The normalised average streaming speed $\bar{u}/\bar{u}_{\mathrm{ref}}$ where $\bar{u}_{\mathrm{ref}}$ is the average streaming speed for a mesh size of 30 μm is plotted in Fig. 5. It can be seen clearly that, with the decrease of mesh size corresponding to a finer mesh, the modelled streaming speed becomes larger and approaches a steady value. In order to balance the computer efficiency and the accuracy of simulation, a tetrahedral mesh of size 0.06 mm was used for the remainder of results presented in this paper, resulting in an estimated mesh-induced numerical error of 0.7%.

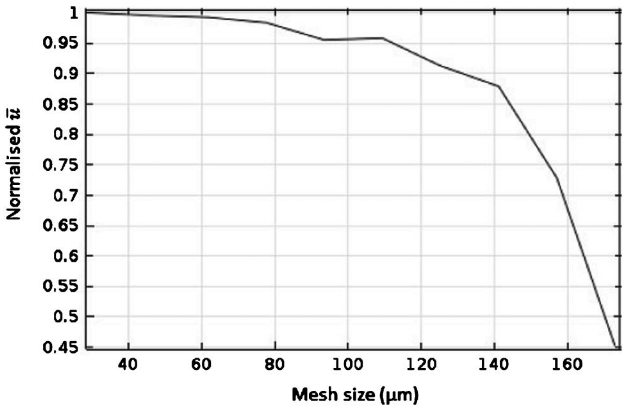

**Fig. 5** Relationship between the average streaming speed $\bar{u}$ and mesh size.

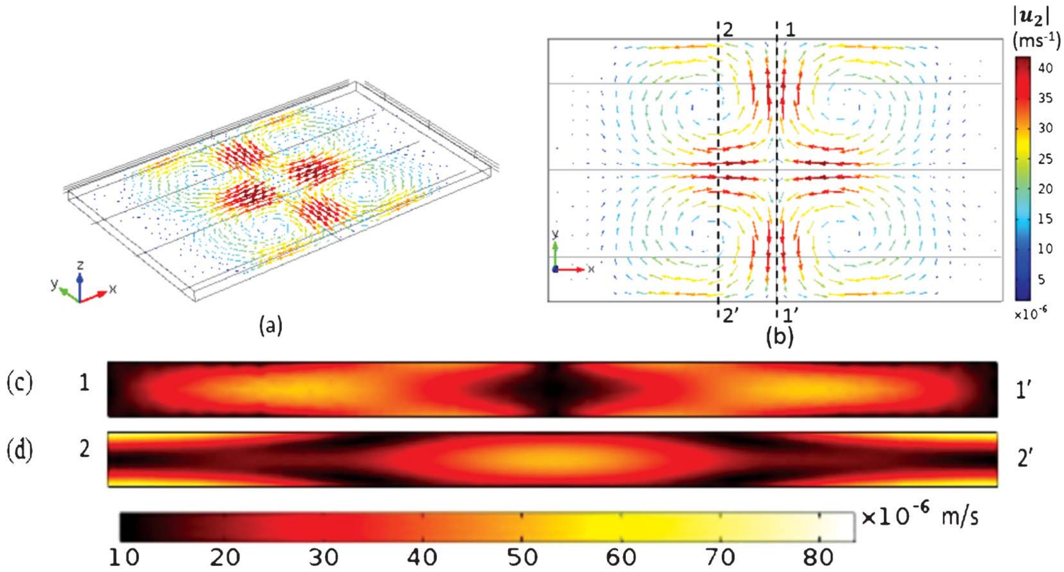

**Fig. 6** Acoustic streaming velocity field, $u_L$: (a,b) The modelled 3D fluid motion, velocity vectors are shown at two heights within the chamber (*z*-positions of one third and two thirds of the chamber height); (c,d) streaming velocity magnitude on cross-sections 1–1′ and 2–2′ (not to scale: *z* dimension has been stretched for clarity).

Fig. 6 shows the modelled 3D fluid motion within the fluid layer. It can be seen clearly that four quadrant streaming vortices, symmetric to the centre of the device, are obtained. Fig. 6 (c)–(d) shows the streaming velocity magnitude through cross-sections in the *yz* plane 1–1′ and 2–2′, shown in Fig. 6 (b). From Fig. 6 (a) and (b), we can see that the predominant motion is in-plane and that at the centre of the device, all the velocity vectors run parallel to each other.

To establish that truncating the length of the capillary that is modelled does not have a significant effect on the results (*i.e.* investigating whether those regions at some distance from the transducer contribute significantly to the streaming) we considered a range of different values of the capillary lengths: 8, 10, 16 and 18 mm. It was found that at 8 mm (when the length is comparable to the width) the truncation had significant effect on the acoustic field, and actually caused streaming vortices with rotation in the opposite direction to the other cases. The remaining lengths produced similar results, with an error in the maximum velocity of no more than 6%. The remaining results in this paper are for a length of 10 mm unless otherwise stated.

Due to the quadratic dependence of the limiting velocity on the linear acoustic quantities, the relationship between the maximum streaming velocity in the device $u_{2\max}$ and the maximum acoustic pressure, $p_{\max}$, was expected to take the form

$$u_{2\max} = \alpha p_{\max}{}^2, \tag{12}$$

where $\alpha$ is a constant. This was tested by applying to a range of excitation amplitudes to the transducer. The quadratic dependence was valid, and the constant, $\alpha$, was found to take the value 47.23 m s$^{-1}$ MPa$^{-2}$ for the stated dimensions. This relationship is discussed further in comparison with experimental results in Fig. 10 below.

**D. Particle trajectories.** In order to understand the effects of acoustic streaming on particle manipulation, a numerical simulation of particle trajectories is presented here. Neglecting the gravity force and buoyancy force on a spherical particle, the movement of the particle within a standing wave field is determined by the acoustic radiation force,[32] $F_{\mathrm{ac}}$, and streaming drag force, $F_{\mathrm{d}}$:

$$\frac{d}{dt}(m_{\mathrm{p}}v) = F_{\mathrm{d}} + F_{\mathrm{ac}}, \tag{13}$$

$$F_{\mathrm{ac}} = -\nabla\left(V_0\left(\frac{3(\rho_{\mathrm{p}}-\rho_{\mathrm{f}})}{2\rho_{\mathrm{p}}+\rho_{\mathrm{f}}}\overline{E_{\mathrm{kin}}} - \left(1-\frac{\beta_{\mathrm{p}}}{\beta_{\mathrm{f}}}\right)\overline{E_{\mathrm{pot}}}\right)\right), \tag{14}$$

$$F_{\mathrm{d}} = 6\mu\pi r(u - v), \tag{15}$$

where $m_{\mathrm{p}}$ is the particle mass, $v$ is the velocity of the particle, $u$ is the fluid velocity, $\mu$ is the fluid viscosity, $r$ is the particle

**Table 2** 3D Model parameters

| | | | |
|---|---|---|---|
| Domain size (length, $L$, × Width, $W$, × height, $H$): | 10 mm × 6 mm × 0.8 mm | Excitation frequency, $f$: | 2.479 MHz |
| Mesh size: | 60 μm, tetrahedral | Dynamic viscosity of water, $\mu$: | 8.9 × 10$^{-4}$ Pa s |
| Density of water, $\rho_{\mathrm{p}}$: | 1000 kg m$^{-3}$ | Speed of sound, water: | 1481.4 m s$^{-1}$ |
| Excitation: peak normal acceleration: | 3.2 × 10$^5$ m s$^{-2}$ | | |

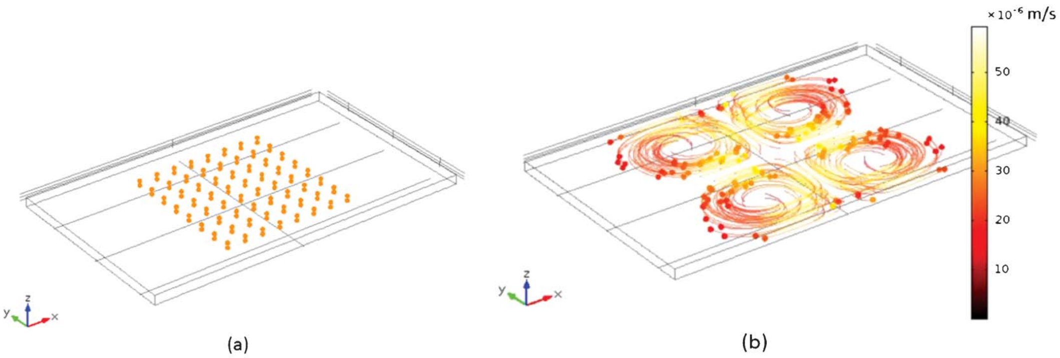

**Fig. 7** Three-dimensional view of modelled particle trajectories: spheres represent 1 μm beads (initially arranged in an 10 × 8 × 2 array) with lines showing their corresponding trajectories. Colour shows velocity according to legend. A full animation of this simulation can be seen in the Electronic Supplementary Information.†

radius, $\overline{E_{\mathrm{kin}}}$ and $\overline{E_{\mathrm{pot}}}$ are the time average kinematic and potential energy, $\rho_{\mathrm{p}}$ and $\rho_{\mathrm{f}}$ are respectively the density of particle and fluid, $\beta_{\mathrm{p}}$ and $\beta_{\mathrm{f}}$ are the compressibility of particle and fluid, and $V_0$ is the particle volume. Eqn (14) is correct for the gradient forces found in both standing waves and in travelling wave fields with energy density gradients (*e.g.* valid in travelling waves in the near field and in Bessel beams). In the absence of gradient forces an additional, order of magnitude smaller,[7] contribution from pure scattering become important; however, this will be small here compared to the gradient forces.

From this theory, together with the two models introduced in Sections B and C above, a COMSOL 'Particle Tracing for Fluid Flow' model was used to simulate the particle trajectories. The shape of the trajectories are independent of the pressure amplitude, since both the radiation forces and induced drag forces scale with the square of pressure; results are presented here for an excitation amplitude of $a_0 = 3.2 \times 10^5$ m s$^{-2}$. An array of tracer particles (given the properties of polystyrene beads of diameter 1 μm) are seeded at time $t = 0$. Both acoustic radiation forces and streaming drag forces act on the particles, resulting in the motion shown in Fig. 7. The quadrant vortex pattern symmetric to the centre of the device is clearly seen, matching that observed in the experimental visualisation. The predominant acoustic radiation forces act perpendicular to the transducer to push the beads towards the nodal plane. It can be seen that over the course of a single rotation the lateral acoustic radiation forces (acting parallel to the transducer) are small in comparison to the forces causing the rotational motion.

## III. Experimental

### 1. Test device

The test device was composed of a PZT4A transducer (Ferroperm, 3 mm × 3 mm × 1 mm thick) glued to a glass capillary of approximately rectangular cross-section, as shown in Fig. 8. The glass capillary (Vitricom) had inner dimensions of 0.3 mm × 6 mm, wall thickness of 0.3 mm, and length 50 mm. To make the top electrode connection a sheet of gold foil was placed between the transducer and the capillary (glues: epoxy, epotek 301 between capillary and leaf, and Circuitworks silver loaded epoxy between leaf and transducer, measured glue layer thicknesses <10 μm). Soldered connections were made between the gold leaf, top electrode and connecting wires. Fluidic connections were made to the capillary *via* PTFE tubing (ID 1 mm) attached *via* heat-shrink sleeving. The advantage of a capillary device such as this is that, in contrast to many other layered resonators, there is little energy dissipated into support and clamping structures which makes the modelling of the device more straightforward.

### 2. PIV setup

Measurements of the acoustic streaming field were performed using the experimental arrangement shown in Fig. 3. A function generator (TTi, TG1304 Programmable) drives an RF amplifier (EIN, Model 240L) that drives the transducer, with signal monitored by an oscilloscope (Agilent Technologies, DOS1102B Digital Storage Oscilloscope). An Olympus BXFM epi-fluorescent microscope with a *pixelfly* dual-frame CCD camera was used to image the device.

Impedance measurements were used to identify the half-wave resonance frequency (corresponding to a half wavelength within the fluid layer of the capillary in the $z$ direction), at 2.585 MHz. At this frequency it was observed that if 10 μm polystyrene beads were introduced they were both levitated in the $z$-direction, and more slowly agglomerated into a clump above the centre of the transducer. This relates to radiation forces arising from gradients in predominantly the potential

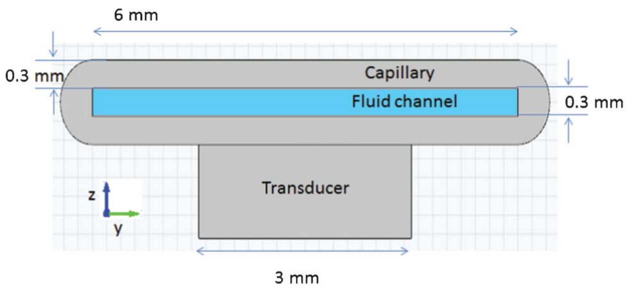

**Fig. 8** Cross-section of the device.

and kinetic energy densities respectively as discussed by Glynne-Jones *et al.*[25,33] For beads of this size streaming effects were not in evidence due to the much larger radiation forces. While temperature effects are known to have an influence on the resonances in devices such as this,[34] the streaming pattern was found to be reliably present at this frequency and the streaming magnitude similar and within the level of accuracy resulting from the approximations made in the modelling below.

PIV measurements were performed using green-fluorescent 1 μm polystyrene tracer beads (Fluoresbrite microspheres, Polysciences Inc.). While these experience small radiation forces toward the nodal plane, the streaming forces are found to be a factor of around 4 stronger. Experiments were conducted with a fresh fill of beads for each measurement to ensure a homogeneous bead distribution. Image pairs were captured at measured intervals of about 280 ms and processed using the *Matlab* based Micro-particle-image-velocimetry (μPIV) software, *mpiv*.[35]

### 3. Observed streaming patterns

A four quadrant, steady acoustic streaming pattern symmetric to the centre of the device was formed, shown in Fig. 9. The plane of these vortices is parallel to the transducer plane (*i.e.* perpendicular to axis of the standing wave). This is in contrast to the rolls often observed as a result of Rayleigh streaming,[11] which have components parallel to the sidewall of chambers.

**A. Acoustic pressure measurement.** The acoustic pressure amplitude in the device was measured using the 'voltage drop' method described by Spengler *et al.*[23] In static equilibrium a particle in an ultrasonic force-field will settle to a position where the gravitational and buoyancy forces balance with the acoustic forces. Like the acoustic radiation force, gravitational and buoyancy forces are both proportional to particle volume, so the equilibrium position is independent of particle size. A test particle is placed in the field; as the acoustic field is decreased the particle equilibrium position sinks, until it reaches the turning point of the radiation force *vs.* position graph, where further decrease leads to the particle dropping. Since the material properties and hence buoyancy force on the particle are known, the acoustic energy density and hence pressure amplitude can be calculated.

Table 3 shows the material properties used in the experiment. The 'drop voltage', was determined by viewing a 10 μm diameter polystyrene bead with a 50× microscope objective. The system can be approximated as linear since $|p| \ll (\rho c^2 = 2.2\ \text{GPa})$, so the pressure magnitude is proportional to the driving voltage, and therefore the acoustic radiation force is proportional to the square of the applied voltage.

Thus, the pressure amplitude above the transducer at voltage, $V_{\text{in}}$, was calculated to be given by

$$|p| = \sqrt{\frac{F_{\text{ac}}\rho_{\text{f}} c_{\text{f}}^2}{\pi k r^3 \varphi(\rho,\beta)}}\cdot\frac{V_{\text{in}}}{V_{\text{d}}}, \tag{16}$$

where all the variables are defined and summarised in Table 3, except $\varphi(\rho, \beta)$, which, is often known as acoustic contrast factor and can be calculated from

$$\varphi(\rho,\beta) = \frac{\rho_{\text{p}} + \frac{2}{3}(\rho_{\text{p}} - \rho_{\text{f}})}{2\rho_{\text{p}} + \rho_{\text{f}}} - \frac{\beta_{\text{p}}}{3\beta_{\text{f}}}, \tag{17}$$

where $\beta$, the compressibility is equal to $^{1}/_{\rho c^2}$.

**B. Effects of driving voltage on acoustic streaming.** The effects of driving voltage on the streaming pattern and magnitude of the streaming velocities were investigated. A series of excitation voltages, ranging from 10 V to 30 V, was considered. For each condition the streaming field was measured. The large margin of error on this measurement is due to a number of factors: (a) the difficulty of measuring the 'drop voltage' precisely due to uncertainty in knowing when equilibrium has been passed (b) uncertainties in the material properties of the bead. To compare the different cases, the maximum streaming velocity (found close to the position $x = 1$ mm, $y = 0$, in Fig. 9) had been plotted against maximum pressure amplitude, which will be discussed in comparison to the numerical modelling in section IV.

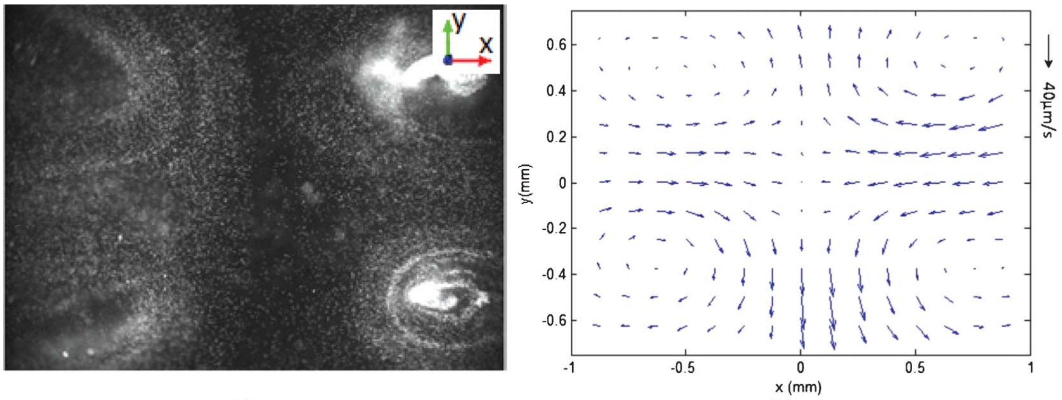

(a) (b)

Fig. 9 (a) A photographic image of distribution of beads in the fluid after some minutes of streaming. Beads can be seen to have agglomerated near the centre of the streaming vortices; (b) PIV measurements of acoustic streaming (measurements taken after a fresh population of beads have been flowed in to ensure an even distribution). The field of view is smaller than the transducer area. A video of this behaviour can be seen in the Electronic Supplementary Information.†

**Table 3** Acoustic pressure measurement

| | | | |
|---|---|---|---|
| Driving frequency, *f*: | 2.585 MHz | Particle radius, *r*: | 5 μm |
| Particle density, $\rho_p$: | 1055 kg m$^{-3}$ | Fluid density, $\rho_f$ : | 1000 kg m$^{-3}$ |
| Acoustic speed in particle, $c_p$: | 1962 m s$^{-1}$ | Acoustic speed in fluid, $c_f$: | 1480 m s$^{-1}$ |
| Acoustic pressure amplitude, $\lvert p \rvert$: | $(2.685 \times 10^4 \times V_d)$ Pa | Energy density, ε: | $(0.082 \times V_d^2)$ J m$^{-3}$ |
| Drop voltage, $V_d$: | 1.08 V | | |

## IV. Discussion

### 1. Comparison between experiment and model

The acoustic streaming field within the transducer-capillary device has been investigated using both experimental and numerical approaches. It can be seen from Fig. 9 that the modelled four-quadrant streaming pattern, symmetric to the centre of the device and parallel to the transducer plane, is in good agreement with the visualised streaming pattern in experiments. The magnitude of streaming velocity obtained from simulation also compares well with the experimental measurement, shown Fig. 10.

The differences between the modelled streaming velocity and the measured value may be attributed to the reasons listed below:

1. Acoustic pressure measurement. As described above, the voltage-drop method of pressure measurement is subject to significant errors. Other methods involving PIV based bead tracking[4] have been shown much more accurate, although this method would be hard to apply in this case due to the radiation force being in line with the viewing direction.

2. The model is a simplification, neglecting coupled resonances that include the transducer and glass walls. Hence the modelled resonance is at a slightly different frequency to that found experimental (2.585 MHz measured *vs.* 2.479 MHz modelled).

3. The temperature of the device has not been stabilised. Experiments[4] have shown that self-heating of the transducer and attached structures at higher drive levels can cause a shift in the resonant frequency of the system. We hypothesise that this is the cause for the small steepening of the experimental results with frequency (*i.e.* the curve is steeper than a quadratic one). Temperature stabilisation in this system is not straightforward (compared to the silicon devices presented by Augustsson *et al.*[4]) as the air boundaries of the device are an integral part of the design, and do not allow for thermal connections.

4. Bruus *et al.*[21] have recently modelled Rayleigh streaming in a glass capillary to a higher level of precision. They show that including thermo-viscous effects, not modelled here, produces a significant correction in systems such as these.

5. The capillary chamber is not perfectly rectangular in cross-section, which will influence the acoustic resonance and resulting streaming pattern.

However, despite these approximations and uncertainties, the model and experiments are sufficient to both demonstrate the existence of the transducer-plane streaming patterns, and also deduce the causal mechanism as discussed next.

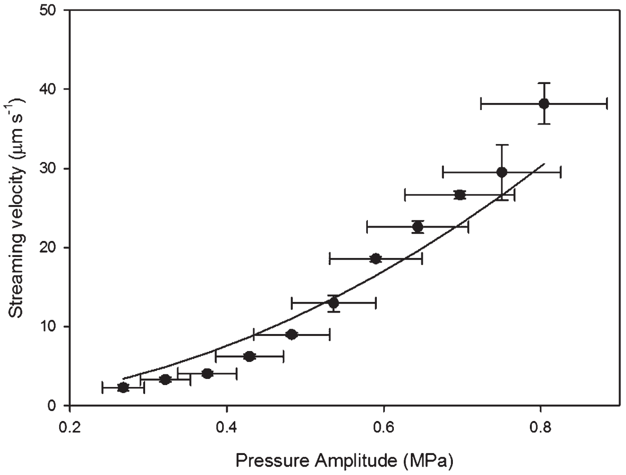

**Fig. 10** Relationship between the magnitude of maximum streaming velocity and driven acoustic pressure, a comparison between PIV measurement and numerical simulation, where the line and points show respectively the simulated and measured results.

### 2. Mechanism of the in-plane streaming pattern

Eqn (6) and (7) for the limiting velocity have a number of terms that are functions of the acoustic velocity components and their derivatives. Numerically examining the limiting velocities on the $z = -H/2$ and $z = H/2$ boundaries (those primarily driving the observed pattern), we find that they are dominated by the term which is the product of the acoustic velocity parallel to the surface and the *z*-gradient of acoustic velocity in the *z*-direction, $dw_1/dz$. This reflects the strong axial velocity gradients found in planar manipulation devices ($du_1/dx \ll dw_1/dz$ and $dv_1/dy \ll dw_1/dz$). For example, the *x*-component limiting velocity $u_L$ is approximated by the term,

$$u_L \approx -\frac{1}{4\omega}\mathrm{Re}\left[-2iu_1^*\frac{dw_1}{dz}\right] \tag{18}$$

where the superscript, *, shows the conjugate value of the complex acoustic velocity. To find the meaning of the term, $u_1{}^*dw_1/dz$, we consider the linearized equation of mass conservation,

$$\rho_0\nabla\cdot\boldsymbol{u}_1 = -\frac{\partial\rho}{\partial t}. \tag{19}$$

In planar manipulation devices the gradients of the velocity in the *z*-direction are much greater than in the lateral directions due to the planar geometry,[36] hence the left side of eqn (19) can be approximated as

$$\rho_0 \frac{dw_1}{dz}. \tag{20}$$

Meanwhile, using standard relations between density and pressure in linear acoustics[31] and then exploiting the harmonic nature of the excitation, the right hand side of eqn (19) becomes

$$-\frac{\partial \rho}{\partial t} = -\frac{1}{c^2}\frac{\partial p}{\partial t} = \frac{1}{c^2}(i\omega p). \tag{21}$$

Thus, eqn (19) can be written

$$\frac{dw_1}{dz} \approx \frac{1}{\rho_0 c^2}(i\omega p). \tag{22}$$

Using this, the product $u_1{}^* dw_1/dz$ can be approximated as

$$u_1^* \frac{dw_1}{dz} \approx u_1^* \left(\frac{i\omega p}{\rho_0 c^2}\right) = \frac{i\omega}{\rho_0 c^2}(u_1^* p) = \frac{i\omega}{\rho_0 c^2} 2C_x. \tag{23}$$

where the complex intensity, $C_x$, is given by:[37]

$$C_x = \frac{1}{2} u_1^* p \tag{24}$$

Thus the $x$ component of the limiting velocity can be written

$$u_L \approx \frac{-1}{\rho_0 c^2}\mathrm{Re}[C_x] \quad \text{valid for } du_1/dx \ll dw_1/dz \text{ and } dv_1/dy \ll dw_1/dz \tag{25}$$

According to Fahy,[37] the complex intensity (a harmonic representation of the real, instantaneous intensity, which is a function of time) can be decomposed into two parts: (i) the real part, called the active intensity, which gives the time average energy flow; and (ii) the imaginary part (the reactive intensity) which corresponds to local, oscillatory energy flows with zero time average. We see from eqn (25) that the limiting velocity is proportional to the active intensity. Fahy shows that the active intensity can have a rotational component in fields that have a standing wave component (and that the reactive intensity is irrotational). He states that in standing wave fields this rotation should be interpreted as reflecting the elliptical path of fluid elements rather than a larger scale circulation of energy. The active acoustic intensity vector at the bottom boundary is plotted in Fig. 11. It can be seen clearly that the pattern it forms is closely related to the modelled and observed streaming patterns. The insight that these streaming patterns are thus caused, may lead in the future to better control, or elimination of the streaming through more careful control of the interplay between standing and travelling waves in the lateral extents of devices.

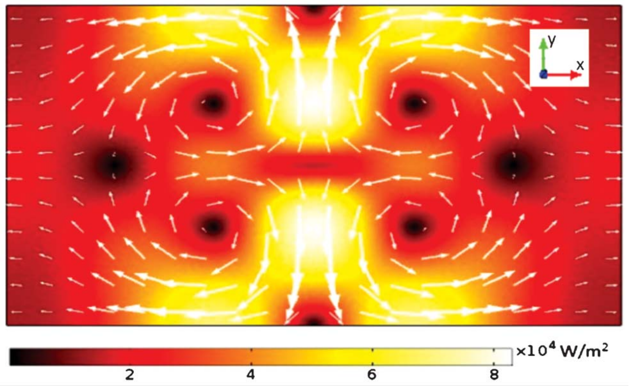

**Fig. 11** Active acoustic intensity field at the bottom wall (limiting velocity boundary).

## V. Conclusions

A four-quadrant acoustic streaming pattern, symmetric to the centre of the transducer and with the circulation plane parallel to the transducer plane, was experimentally visualised in our planar cell manipulation devices. This kind of acoustic streaming pattern is different from the better-known Rayleigh and Eckart type pattern, both in the shape of streaming flows it generates and in its genesis. The pattern described by Coakley *et al.* in 2004 has not previously been explained; we have presented for the first time an investigation into its mechanism, and have shown that the streaming pattern is related to the active acoustic intensity, which is known to show rotation in a standing wave field.

Experimental work with tracer beads and micro-PIV has quantified the streaming flows for a range of excitations. It has been found to show good agreement with a finite element model that decomposes the streaming problem into three steps, using results from a linear acoustic analysis to calculate limiting velocities that are applied as boundary conditions to a Stokes flow model.

## Acknowledgements

The authors gratefully acknowledge the financial support for this work received from China Scholarship Council (CSC) and the EPSRC under the Sonotweezers project (EP/G012075/1)

## References

1 J. Friend and L. Y. Yeo, *Rev. Mod. Phys.*, 2011, **83**, 647–704.
2 H. Bruus, J. Dual, J. Hawkes, M. Hill, T. Laurell, J. Nilsson, S. Radel, S. Sadhal and M. Wiklund, *Lab Chip*, 2011, **11**, 3579–3580.
3 R. Barnkob, P. Augustsson, T. Laurell and H. Bruus, *Lab Chip*, 2010, **10**, 563–570.
4 P. Augustsson, R. Barnkob, S. T. Wereley, H. Bruus and T. Laurell, *Lab Chip*, 2011, **11**, 4152–4164.

5 R. Barnkob, I. Iranmanesh, M. Wiklund and H. Bruus, *Lab Chip*, 2012, **12**, 2337–2344.

6 K. Yosioka and Y. Kawasima, *Acustica*, 1955, **5**, 167–173.

7 L. P. Gor'kov, *Sov. Phys. Dokl.*, 1962, **6**, 773–775.

8 J. F. Spengler, W. T. Coakley and K. T. Christensen, *AIChE J.*, 2003, **49**, 2773–2782.

9 L. A. Kuznetsova and W. T. Coakley, *J. Acoust. Soc. Am.*, 2004, **116**, 1956–1966.

10 J. Lighthill, *J. Sound Vib.*, 1978, **61**, 391–418.

11 Lord Rayleigh, *Philos. Trans. R. Soc. London*, 1884, **175**, 1–21.

12 P. J. Westervelt, *J. Acoust. Soc. Am.*, 1952, **25**, 60–67.

13 W. L. Nyborg, *J. Acoust. Soc. Am.*, 1953, **25**, 68–75.

14 H. Schlichting, *Physikalische Zeitschrift*, 1932, **33**, 327–335.

15 S. Boluriaan and P. J. Morris, *Aeroacoustics*, 2003, **2**(3&4), 255–292.

16 M. Wiklund, R. Green and M. Ohlin, *Lab Chip*, 2012, **12**, 2438–2451.

17 M. F. Hamilton, Y. A. Ilinskii and E. A. Zabolotskaya, *J. Acoust. Soc. Am.*, 2003, **113**, 153–160.

18 M. Kawahashi and M. Arakawa, *JSME Int. J., Ser. B*, 1996, **39**, 280–286.

19 M. K. Aktas and B. Farouk, *J. Acoust. Soc. Am.*, 2004, **116**, 2822–2831.

20 D. Sastrapradja and V. W. Sparrow, *Innovations in Nonlinear Acoustics*, 2006, **838**, 465–468.

21 P. B. Muller, R. Barnkob, M. J. H. Jensen and H. Bruus, *Lab Chip*, 2012, **12**, 4617–4627.

22 B. Hammarstrom, T. Laurell and J. Nilsson, *Lab Chip*, 2012, **12**, 4296–4304.

23 J. F. Spengler, M. Jekel, K. T. Christensen, R. J. Adrian, J. J. Hawkes and W. T. Coakley, *Bioseparation*, 2001, **9**, 329–341.

24 C. Eckart, *Phys. Rev.*, 1947, **73**, 68–76.

25 P. Glynne-Jones, C. E. M. Demore, C. W. Ye, Y. Q. Qiu, S. Cochran and M. Hill, *IEEE T Ultrason Ferr*, 2012, **59**, 1258–1266.

26 W. L. Nyborg, *J. Acoust. Soc. Am.*, 1958, **30**, 329–339.

27 C. P. Lee and T. G. Wang, *J. Acoust. Soc. Am.*, 1989, **85**, 1081–1088.

28 H. Bruus, *Lab Chip*, 2012, **12**, 1578–1586.

29 P. B. Muller, R. Barnkob, M. J. H. Jensen and H. Bruus, *Lab Chip*, 2012, **12**, 4617–4627.

30 Comsol Multiphysics 4.3, http://www.comsol.com/.

31 L. E. Kinsler, A. R. Frey, A. B. Coppens and J. V. Saunders, *Fundamentals of acoustics*, Wiley, New York, 2000.

32 L. P. Gor'kov, *Sov. Phys. Dokl.*, 1962, **6**, 773–775.

33 P. Glynne-Jones, R. J. Boltryk and M. Hill, *Lab Chip*, 2012, **12**, 1417–1426.

34 P. Augustsson, R. Barnkob, S. T. Wereley, H. Bruus and T. Laurell, *Lab Chip*, 2011, **11**, 4152–4164.

35 N. Mori and C. K-A, mpiv-MATLAB PIV Toolbox, http://www.oceanwave.jp/softwares/mpiv/.

36 P. Glynne-Jones, R. J. Boltryk and M. Hill, *Lab Chip*, 2012, **12**, 1417–1426.

37 F. J. Fahy, *Sound intensity*, E & FN Spon, London, 1995.

# Appendix 2

## Paper published in Lab on a Chip

### Numerical simulation of 3D boundary-driven acoustic streaming in microfluidic devices

**Junjun Lei, Martyn Hill and Peter Glynne-Jones**

**Abstract:** This article discusses three-dimensional (3D) boundary-driven streaming in acoustofluidic devices. Firstly, the 3D Rayleigh streaming pattern in a microchannel is simulated and its effect on the movement of microparticles of various sizes is demonstrated. The results obtained from this model show good comparisons with 3D experimental visualisations and demonstrate the fully 3D nature of the acoustic streaming field and the associated acoustophoretic motion of microparticles in acoustofluidic devices. This method is then applied to another acoustofluidic device in order to gain insights into an unusual in-plane streaming pattern. The origin of this streaming has not been fully described and its characteristics cannot be explained from the classical theory of Rayleigh streaming. The simulated in-plane streaming pattern was in good agreement with the experimental visualisation. The mechanism behind it is shown to be related to the active sound intensity field, which supports our previous findings on the mechanism of the in-plane acoustic streaming pattern visualised and modelled in a thin-layered capillary device.

**DOI:** 10.1039/C3LC50985K

Lab on a Chip

PAPER

View Article Online
View Journal | View Issue

Cite this: *Lab Chip*, 2014, **14**, 532

# Numerical simulation of 3D boundary-driven acoustic streaming in microfluidic devices†

Junjun Lei, Martyn Hill* and Peter Glynne-Jones

Received 27th August 2013,
Accepted 7th November 2013

DOI: 10.1039/c3lc50985k

www.rsc.org/loc

This article discusses three-dimensional (3D) boundary-driven streaming in acoustofluidic devices. Firstly, the 3D Rayleigh streaming pattern in a microchannel is simulated and its effect on the movement of microparticles of various sizes is demonstrated. The results obtained from this model show good comparisons with 3D experimental visualisations and demonstrate the fully 3D nature of the acoustic streaming field and the associated acoustophoretic motion of microparticles in acoustofluidic devices. This method is then applied to another acoustofluidic device in order to gain insights into an unusual in-plane streaming pattern. The origin of this streaming has not been fully described and its characteristics cannot be explained from the classical theory of Rayleigh streaming. The simulated in-plane streaming pattern was in good agreement with the experimental visualisation. The mechanism behind it is shown to be related to the active sound intensity field, which supports our previous findings on the mechanism of the in-plane acoustic streaming pattern visualised and modelled in a thin-layered capillary device.

## I. Introduction

Particle manipulation using ultrasonic standing waves has gained increased attention in recent years as it is efficient and non-invasive. During the process of manipulation, acoustic streaming is typically found in addition to the acoustic radiation forces. In acoustofluidic particle manipulation devices, the acoustic streaming field is generally dominated by boundary-driven streaming, which is a result of the interaction between the acoustic oscillation and solid boundaries. Rayleigh[1] was the first to present a theoretical analysis of a boundary layer driven acoustic streaming field. His solution only describes the fluid motion outside the viscous boundary layer, so it is commonly referred to as 'outer streaming' as well as 'Rayleigh streaming'. Subsequently, modifications to Rayleigh's solution have been proposed, most notably by Westervelt,[2] Nyborg[3] and Schlichting,[4] reviewed by Boluriaan *et al.*[5] and Wiklund *et al.*[6] Hamilton *et al.*[7] derived an analytical solution for the acoustic streaming generated by a standing wave confined by parallel plates that solved the streaming field both inside and outside the viscous boundary layer. Another kind of boundary-driven streaming is transducer-plane streaming. Different from the better known classical streaming pattern, *e.g.* Rayleigh streaming[1] and Eckart streaming,[8] whose vortex plane is normally perpendicular to the transducer face, the circulation of transducer-plane streaming is parallel to the transducer face. Such streaming patterns are typically generated in planar microfluidic resonators where the acoustic energy gradients in the lateral directions parallel to the transducer face are significant in addition to the gradients perpendicular to the transducer face.[9,10] The mechanism behind the transducer-plane streaming pattern was recently analysed and shown to be related to the acoustic intensity field.[9]

These theoretical analyses have been complemented by experimental work in acoustofluidic systems and numerical simulations. On the one hand, acoustic streaming and acoustophoretic motion of microparticles in acoustofluidic devices have been measured using various methods, most notably micro particle image velocimetry (μPIV) and particle tracking velocimetry (PTV). Experimental investigations have shown that μPIV[11–13] and PTV[14,15] are powerful tools for analysing 2D microchannel acoustophoresis. Fully 3D particle tracking has been demonstrated using μPIV with depth of correlations[16] and astigmatism particle tracking velocimetry.[17–19] On the other hand, numerical simulations of acoustophoretic motion of microparticles can provide efficient prediction of experiments and provide effective guidance and optimization on the design of acoustofluidic devices to enhance or improve experiments. Many existing models of acoustic streaming simulation are based on 2D simplifications that consider only a cross-sectional area of the fluid chamber due to the high computational demand of 3D simulations. In these models, the acoustic field in the fluid layer is generally assumed to have a periodic

---

*Faculty of Engineering and the Environment, University of Southampton, Southampton, UK. E-mail: m.hill@soton.ac.uk*

† Electronic supplementary information (ESI) is available: 3D, top and side views of the simulated trajectories of 0.5 μm particles are included. See DOI: 10.1039/c3lc50985k

distribution of constant amplitude as it is obtained from a uniform distribution of boundary vibration.[20–22] However, in real acoustofluidic devices, the acoustic field generated from the transducer does not always have a perfectly uniform distribution along the channel axis due to lateral modes, structural modes, transducer inhomogeneities and acoustic absorption at the ends of channels. Therefore, results obtained from simplified 2D models cannot fully represent real acoustofluidic devices and 3D models are necessary to provide better understanding and prediction of experiments. Recently, Lei *et al.*[9] successfully simulated the transducer-plane streaming in a glass capillary by considering a 3D model using the computationally efficient limiting velocity finite element method.

In this paper we apply the limiting velocity finite element method to calculate the driving boundary conditions on a 3D fluid volume. We model two acoustofluidic devices described in the literature:

a) An acoustofluidic device investigated experimentally by Muller *et al.*[23] Our simulated results are shown to be in good agreement with the experimental observations and provide evidence of 3D characteristics.

b) The second device was first presented by Hagsater *et al.*[13] It was shown to present an unusual pattern of 6 × 6 in-plane streaming vortices that differed from that predicted by consideration of the Rayleigh streaming pattern and has not previously been explained. By modelling it here we are able to make suggestions as to the cause of this phenomenon.

In section II, the numerical method used to simulate the acoustic streaming field in the main fluid is introduced. Then, the 3D Rayleigh streaming pattern in the first device is simulated and analysed in section III, where the model, results and a discussion are presented. In section IV, the unusual acoustic streaming pattern visualised in the second device is investigated and brief conclusions are drawn in section V.

This paper demonstrates how 3D models add to our understanding of the streaming behaviours found in experimental devices. While many systems can be modelled appropriately with suitable 2D approximations, making the correct approximation *a priori* is not always straightforward, and can only be judged accurate in hindsight from a 3D representation (be that a model or experimental results). For example in this paper (section IV), a 2D model is not sufficient: streaming is driven by a boundary that is parallel to the plane of the observed streaming pattern.

## II. Numerical method

Fig. 1 shows the schematic of the *limiting velocity method* we use to simulate the streaming field which is based on the analytical solutions first introduced by Nyborg[3] and later modified by Lee and Wang.[24] This method decomposes the problem into three steps: (a) a linear acoustic model predicts the first order acoustic fields; (b) the *limiting velocity* is calculated at all boundaries as a function of the first order acoustic fields (essentially the streaming is driven by the interaction of the acoustic field with these boundaries); (c) a creeping flow model is used to calculate the resulting streaming flows. The limiting velocity only predicts the streaming field outside the viscous boundary layer, removing the need for a boundary-layer mesh and hence reducing computational load to the point where a 3D model is viable. We previously[9] verified a 2D version of this method against Rayleigh's analytical solution[5] and used a 3D version to model and explain unexpected vortex patterns in the plane of the transducer in planar devices. This method is generally applicable to acoustofluidic devices working at MHz frequencies where the thickness of viscous boundary layer, described as $\delta_v$ in Fig. 1, is typically several orders of magnitude smaller than the dimensions of the fluid chamber so that only the streaming field outside the viscous boundary layer is of interest. The finite element package COMSOL[25] was used to implement each of these steps, described in more detail below.

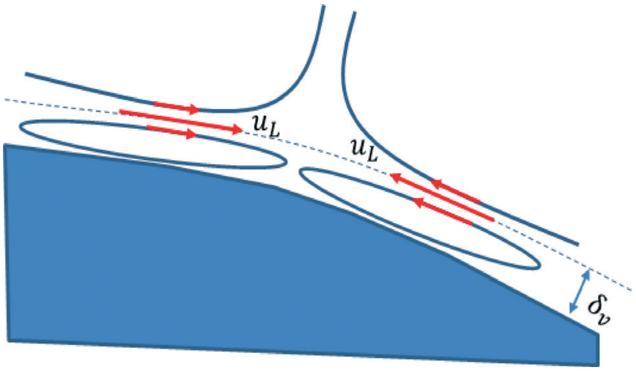

**Fig. 1** Schematic of the limiting velocities over a solid surface, where $u_L$ is the limiting velocity and $\delta_v$ is the viscous penetration depth. Reprinted from ref. 9.

The first-order acoustic fields within the devices are simulated using COMSOL's 'pressure acoustic' physics, which solves the harmonic, linearized acoustic problem and takes the form:

$$\nabla^2 p = -\frac{\omega^2}{c^2} p, \tag{1}$$

where $\omega$ is the angular frequency, $c$ is the sound speed, and $p$ is the complex pressure defined at position $r$ using the relation,

$$p_t(r,t) = \mathrm{Re}[p(r)\mathrm{e}^{-\mathrm{i}\omega t}]. \tag{2}$$

On a planar surface normal to $z$, the limiting velocity equations can be written as[9]

$$u_\mathrm{L} = -\frac{1}{4\omega}\mathrm{Re}\left\{q_x + u_1^*\left[(2+\mathrm{i})\left(\frac{\mathrm{d}u_1}{\mathrm{d}x}+\frac{\mathrm{d}v_1}{\mathrm{d}y}+\frac{\mathrm{d}w_1}{\mathrm{d}z}\right)-(2+3\mathrm{i})\frac{\mathrm{d}w_1}{\mathrm{d}z}\right]\right\}, \tag{3}$$

$$v_L = -\frac{1}{4\omega}\mathrm{Re}\left\{q_y + v_1^*\left[(2+\mathrm{i})\left(\frac{\mathrm{d}u_1}{\mathrm{d}x}+\frac{\mathrm{d}v_1}{\mathrm{d}y}+\frac{\mathrm{d}w_1}{\mathrm{d}z}\right)-(2+3\mathrm{i})\frac{\mathrm{d}w_1}{\mathrm{d}z}\right]\right\}, \tag{4}$$

$$q_x = u_1\frac{\mathrm{d}u_1^*}{\mathrm{d}x}+v_1\frac{\mathrm{d}u_1^*}{\mathrm{d}y}, \tag{5}$$

$$q_y = u_1\frac{\mathrm{d}v_1^*}{\mathrm{d}x}+v_1\frac{\mathrm{d}v_1^*}{\mathrm{d}y}, \tag{6}$$

where $u_L$ and $v_L$ are the two components of the limiting velocities over a vibrating surface, $\omega$ is the angular frequency, $u_1$, $v_1$ and $w_1$ are the three components of acoustic velocities along coordinates $x$, $y$ and $z$, $\mathrm{i} = \sqrt{-1}$, and the superscript, *, denotes the conjugate value of the complex acoustic velocity.

COMSOL's 'creeping flow' physics was used to simulate the second-order acoustic streaming fields. This approximates the fluid as incompressible, and neglects inertial terms (Stokes flow) as the Reynolds numbers are much smaller than one in the devices presented in this paper. The governing equations for the streaming velocity field, $\boldsymbol{u}_2$, and associated pressure field, $p_2$, are

$$\nabla p_2 = \mu\nabla^2\boldsymbol{u}_2, \tag{7}$$

$$\nabla\cdot\boldsymbol{u}_2 = 0. \tag{8}$$

## III. Verification of the 3D streaming model within an acoustofluidic device

### 1. Model configuration and results

Fig. 2(a) shows the 3D model considered, which represents a short section of the device investigated by Muller *et al.*[23] A schematic of different layers of the model is shown in Fig. 2(b), composed of a transducer layer (PZT), a matching layer (silicon), a fluid layer (water), and a reflector layer (glass). The model parameters are summarised in Table 1, including particle properties used in particle trajectory simulations. In order to balance the numerical accuracy and the computational load, a uniform distribution of swept mesh with an element size of 50 μm in the fluid channel was used for the results presented here unless otherwise stated, which is chosen based on the mesh dependency study presented in ref. 9 which shows that 8–10 elements within each acoustic wavelength is enough for the simulation of acoustic and streaming fields.

The left and right walls ($x$ = ±0.5 mm) were considered as plane wave radiation boundary conditions and the remaining walls as hard boundaries. The resonant frequency was found at 1.963 MHz by using a parametric sweep to find the average acoustic energy density in the fluid layer *versus* driving frequency (the resonance was taken as the maximum of this function). The simulated acoustic pressure field is shown in Fig. 3. It can be seen that a lateral half-wavelength ($y$ direction) standing wave field is generated in the fluid channel in this device and the acoustic pressure magnitude decreases from the centre ($x$ = 0) to the left and right boundaries ($x$ = ±0.5 mm) as energy traveling down the channel is largely absorbed by the tubing and connectors at the left and right ends.

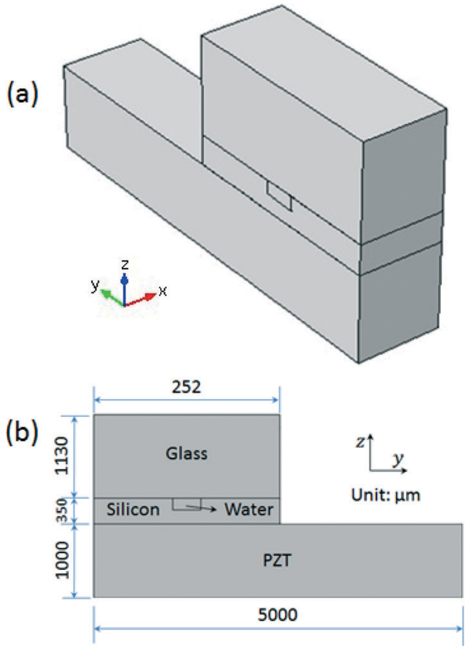

**Fig. 2** (a) The 3D full model considered; (b) *yz* cross-section of (a).

In the creeping flow step of the method, the top and bottom walls of the fluid channel were considered as limiting velocity boundary conditions while the remaining four walls were considered as slip boundary conditions. Fig. 4(a) shows the modelled acoustic streaming velocity magnitude on the surfaces of fluid channel. Fig. 4(b) shows the 3D acoustic streaming field through three $yz$ planes, $x$ = 0, $x$ = 0.2 mm, and $x$ = 0.4 mm. The four counter-rotating vortices that can be seen within the lateral half-wavelength resonator are characteristic of classical Rayleigh streaming. Due to the acoustic variation along the channel axis ($x$-direction), the magnitude of the streaming velocity is at a maximum at the centre ($x$ = 0) of the device and decreases with distance from the centre because the acoustic energy density is strongest at the centre ($x$ = 0) of the model.

In order to understand the effects of acoustic streaming on acoustophoretic motion of microparticles and compare with the experimental visualisation, a numerical simulation of particle trajectories is presented here. Neglecting the gravity force and buoyancy force, the movement of the particle within a standing wave field is determined by the combination of acoustic radiation force (ARF),[26] $F_{\mathrm{ac}}$, inertia, and the viscous drag on the particle, $F_{\mathrm{d}}$ (sometimes called the

**Table 1** 3D Rayleigh streaming and particle trajectory model parameters

| | | | |
|---|---|---|---|
| Fluid volume ($x \times y \times z$): | $1 \times 0.377 \times 0.157$ mm$^3$ | Excitation: | 40 V$_{pp}$ |
| Driving frequency, $f$: | 1.936 MHz | Fluid density, $\rho_f$: | 999.62 kg m$^{-3}$ |
| Acoustic speed in fluid, $c_f$: | 1481.4 m s$^{-1}$ | Dynamic viscosity of water, $\mu$: | $1.0093 \times 10^{-3}$ Pa s |
| Particle diameter, $d$: | 0.5 μm & 5 μm | Acoustic speed in particle, $c_p$: | 1962 m s$^{-1}$ |
| Particle density, $\rho_p$: | 1055 kg m$^{-3}$ | Mesh size: | $5 \times 10^{-5}$ m |

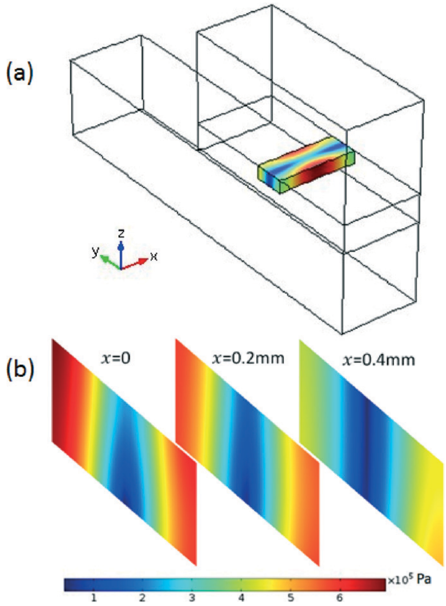

**Fig. 3** (a) 3D acoustic pressure field within the fluid volume; (b) acoustic pressure magnitude on three vertical *yz* planes.

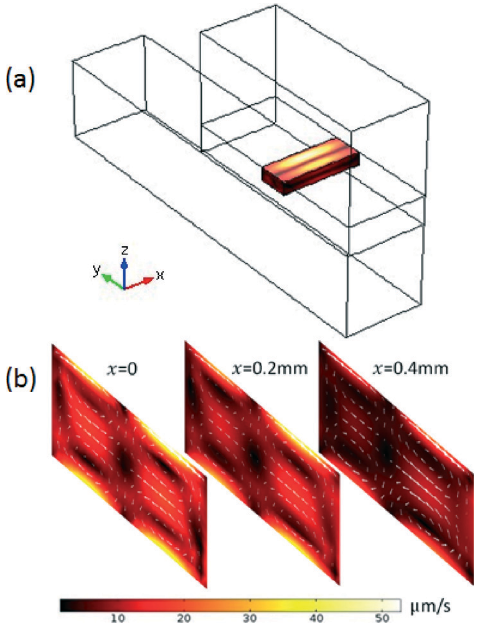

**Fig. 4** (a) 3D acoustic streaming field within the fluid volume; (b) acoustic streaming field on three vertical *yz* planes.

acoustic streaming force, ASF, when the drag is caused by streaming motion).

$$\frac{\mathrm{d}}{\mathrm{d}t}\left(m_p v\right) = F_d + F_{ac}, \tag{9}$$

$$F_{ac} = -\nabla\left(V_0\left(\frac{3\left(\rho_p - \rho_f\right)}{2\rho_p + \rho_f}\overline{E_{kin}} - \left(1 - \frac{\beta_p}{\beta_f}\right)\overline{E_{pot}}\right)\right), \tag{10}$$

$$F_d = 6\mu\pi r(u - v), \tag{11}$$

where $m_p$ is the particle mass, $v$ is the velocity of the particle, $u$ is the fluid velocity, $\mu$ is the fluid viscosity, $r$ is the particle radius, $\overline{E_{kin}}$ and $\overline{E_{pot}}$ are the time average kinematic and potential energy, $\rho_p$ and $\rho_f$ are respectively the density of particle and fluid, $\beta_p$ and $\beta_f$ are the compressibility of particle and fluid, and $V_0$ is the particle volume.

The COMSOL 'Particle Tracing for Fluid Flow' module is used to implement these equations to simulate the particle trajectories. In order to compare with the experimental investigations shown in ref. 23, the trajectories of 0.5 μm and 5 μm particles are demonstrated here. Both ARF and ASF act on the tracer particles (polystyrene beads of diameter 0.5 μm and 5 μm), resulting in the motion shown in Fig. 5. It can be seen that the movements of 0.5 μm particles are dominated by the ASF as the pattern the particle trajectories form is closely related to the acoustic streaming field. However, 5 μm particles are firstly driven to the pressure nodal plane by ARF and then slowly dragged to the top and bottom boundaries by

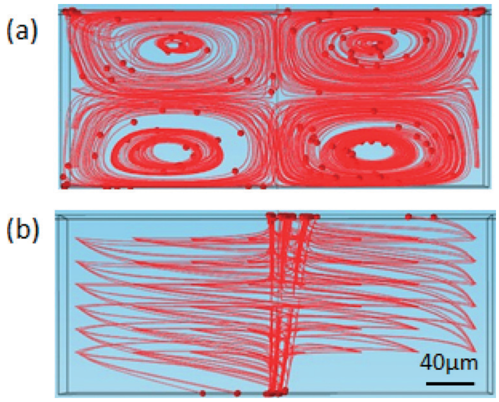

**Fig. 5** Overall views along the channel axis (*x*-direction) of modelled trajectories of 0.5 μm particles (a) and 5 μm particles (b), initially arranged in a 7 × 8 × 6 array, where the spheres present the particles and the lines show respectively their trajectories.

ASF. A comparison between numerical simulation and experiments will be shown in the following discussion section.

In addition to the dominant Rayleigh streaming pattern in the *yz* plane, the streaming also has components along the channel axis (*x* direction), which can cause particle migration along the channel, and is seen most clearly in the animation attached as ESI.† It can also be seen in Fig. 6 where the in-plane streaming velocity magnitude (Fig. 6(a)) can be compared to the smaller but significant out-of-plane component along the channel axis. This exists due to the presence of acoustic energy gradients along the fluid channel (*x*-direction).

### 2. Discussion

The acoustic streaming pattern obtained from numerical and experimental investigations can be compared from the trajectories of 0.5 μm particles, which are dominated by the ASF. It can be seen from Fig. 5(a) and Fig. 4(b) in ref. 23 that classical Rayleigh streaming pattern is obtained from both methods within this lateral half-wavelength resonator.

Due to the quadratic dependence of the limiting velocity on the linear acoustic quantities, the relationship between the maximum streaming velocity in the device, $u_{2\max}$, and the maximum acoustic pressure, $p_{\max}$, is expected to take the form

$$u_{2\max} = \alpha {p_{\max}}^2, \tag{12}$$

where $\alpha$ is a constant. On the other hand, the relationship between acoustic energy density and acoustic pressure can take the form

$$E = \beta p^2, \tag{13}$$

where $\beta$ is a constant, so the comparison between experiment and model on the magnitude of acoustic streaming velocity can be achieved from the comparison of relationship between energy density and maximum streaming velocity

$$u_{2\max} = \frac{\alpha E_{\max}}{\beta} = \gamma E_{\max}. \tag{14}$$

Experimental work by Muller *et al.*[23] found that when the energy density measured in the device is approximately $E_{\max} = (65 \pm 2)\ \mathrm{J\ m^{-3}}$, the corresponding maximum streaming velocity (velocity of 0.5 μm particles) measured is $(u_2)_{\max} = 63\ \mu\mathrm{m\ s^{-1}}$. Therefore, the measured constant $\gamma$ presented in eqn (14) is: $\gamma = (0.97 \pm 0.03) \times 10^{-6}\ \mathrm{m^4\ J^{-1}\ s^{-1}}$.

In the model presented here, it is found that when $E_{\max} = 54.8\ \mathrm{J\ m^{-3}}$ then $(u_2)_{\max} = 52.7\ \mu\mathrm{m\ s^{-1}}$. Therefore, the constant $\gamma$ of the model is: $\gamma = 0.96 \times 10^{-6}\ \mathrm{m^4\ J^{-1}\ s^{-1}}$.

It can be seen that the magnitude of the acoustic streaming velocities in the model and experiment are also in good agreement.

## IV. Investigation of an unusual vortex pattern

### 1. Background

This section introduces a device presented in 2007 by Hagsater *et al.*[13] and seeks to explain the unusual streaming pattern observed. Fig. 7 shows the chip configuration and the observed in-plane acoustic streaming pattern. It can be seen from Fig. 7(b) that a 6 × 6 in-plane vortex pattern was generated. However, from both the measured trajectories of 5 μm tracer particles (Fig. 4 (a) of ref. 13) and the simulated acoustic pressure Eigen mode (Fig. 4(c) of ref. 13), we can see a pattern of 6 × 6 antinodes in the square area of the fluid chamber, which would normally be expected to

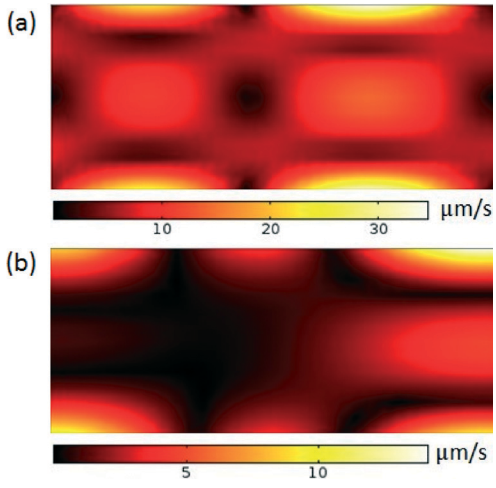

**Fig. 6** A comparison of the magnitude of austic streaming velocity components on a *yz* plane ($x = -0.3$ mm, corresponding to the animation in the ESI†): (a) in plane components; (b) out of plane component, (along channel).

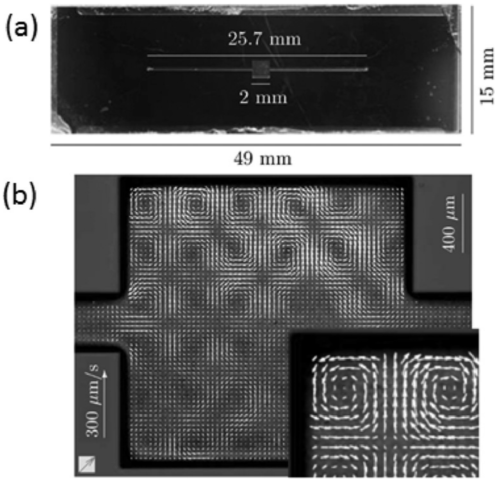

**Fig. 7** Experimental investigation of Hagsater *et al.*[13] (a) Chip configuration; (b) Measured in-plane streaming field, where inset shows detail at top-left corner of chamber. Adapted from ref. 13.

result in a 12 × 12 vortex pattern (2 vortices within each half wavelength for the classical Rayleigh streaming pattern). Therefore, the in-plane vortex pattern cannot be explained by classical Rayleigh streaming theory. In order to provide better understanding of this streaming pattern, a finite element model is presented here to simulate the 3D acoustic streaming field in this device and to investigate its origin.

## 2. Finite element model and results

Fig. 8 shows the schematic of our model, where (a) is a 3D view of the full device and (b) & (c) are respectively top & side views of the model with dimensioning. The origin of the coordinates was set at the centre of the interface between water and glass. All model parameters are summarised in Table 2.

Firstly the mesh, as with the previous model, was chosen based on the mesh dependency study presented in ref. 9 such that 8–10 elements within each acoustic wavelength are enough for the simulation of acoustic and streaming fields. In order to balance the computational load and numerical accuracy, a mesh size of 0.08 mm was used for the results presented here, resulting in an estimated mesh-induced numerical error of 2%.

The resonant frequency was found at 2.193 MHz by using a parametric sweep to find the maximum average acoustic energy density in the fluid layer *versus* driving frequency. The resonant frequency gives a 2D standing wave in the $x$ and $y$ directions in this shape of fluid channel. In order to match the experimental measurement, the results shown below were obtained from the model run at frequency of 2.17 MHz. A 3D view of the acoustic pressure field within the fluid channel is plotted, Fig. 9(a). It can be seen that throughout the device the magnitude of acoustic pressure is almost constant along the $z$ axis. In the $xy$ plane, in the central square area of fluid channel (2 mm × 2 mm), a primary standing wave field (close to three wavelengths in extent, Fig. 9(b)) is established in the $y$ direction and in the $x$ direction the acoustic pressure distribution also shows a standing wave field of three wavelengths due to plane wave radiation boundaries on two ends of fluid channel.

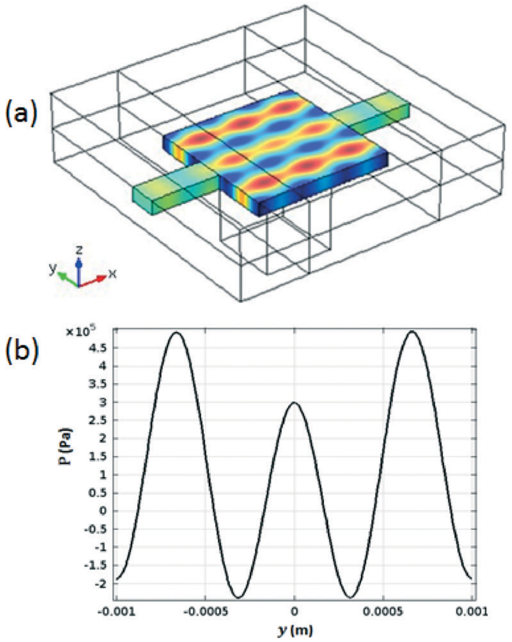

**Fig. 9** Simulated acoustic pressure field: (a) a 3D view; (b) magnitude of acoustic pressure along the central line of fluid channel ($x$ = 0, −1 mm ≤ $y$ ≤ 1 mm, $z$ = 0).

In the creeping flow step of the method, the top and bottom boundaries ($z$ = 0 and $z$ = −0.02 mm) of the fluid channel were considered as limiting velocity boundary conditions while the other walls were slip boundary conditions. In order to help visualise the 3D acoustic streaming field, streaming in both the $yz$ cross-section ($x$ = 0.5 mm) and $xz$ cross-section ($y$ = 0.5 mm) in the central square area of fluid channel are plotted in Fig. 10. Due to a dominant standing wave being established (3$\lambda$) in the $y$ direction and the shape of fluid channel, a classical Rayleigh streaming vortex pattern is observed in the $yz$ cross section, Fig. 10(a). Note

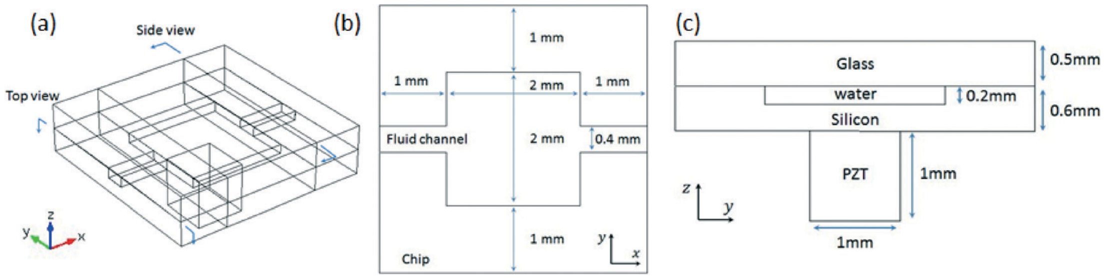

**Fig. 8** (a) 3D full model; (b) top view; (c) side view.

**Table 2** Model parameters

| | | | |
|---|---|---|---|
| Central square area ($x \times y \times z$): | 2 × 2 × 0.2 $\text{mm}^3$ | Excitation: | 40 $V_{pp}$ |
| Driving frequency, $f$: | 2.17 MHz | Fluid density, $\rho_f$: | 999.62 kg $m^{-3}$ |
| Acoustic speed in fluid, $c_f$: | 1481.4 m $s^{-1}$ | Dynamic viscosity of water, $\mu$: | $1.0093\times10^{-3}$ Pa s |

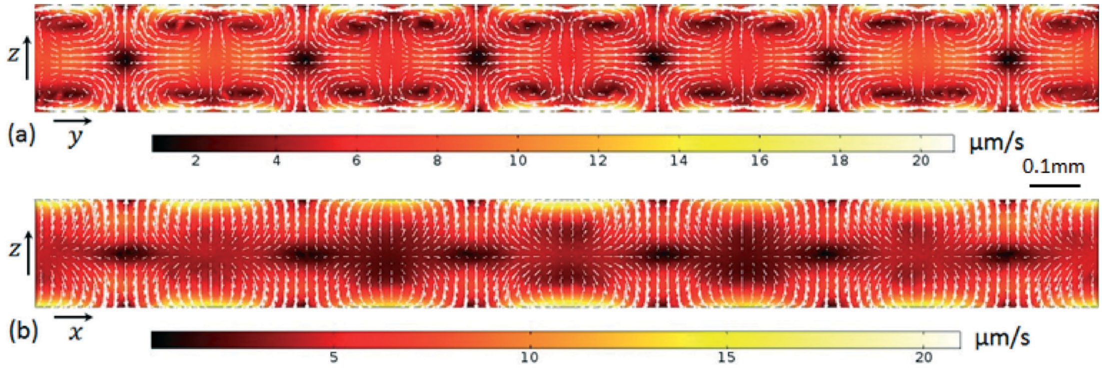

**Fig. 10** Acoustic streaming field on (a) a *yz* cross-section at $x = -0.5$ mm, and (b) a *xz* cross-section at $y = -0.5$ mm. The arrows show the orientation of acoustic streaming field and colour bars plot the magnitude of acoustic streaming velocities.

that although the chamber is square, the entry and exit channels in the *x* direction mean that the field is not symmetrical. A similar but weaker vortex pattern is seen in the *zx* plane, Fig. 10(b), which is the Rayleigh streaming from the weaker *x*-directed standing wave.

In order to compare modelled results to the experimentally observed in-plane vortex pattern, a top view of the acoustic streaming field in the central square area of fluid channel is plotted. Fig. 11(a) shows the streaming field at the mid height (plane $z = -0.1$ mm) and Fig. 11(b) shows the streaming pattern at plane just below the very top of the fluid channel (plane $z = -0.04$ mm). The reason for choosing this plane to present the in-plane acoustic streaming pattern is that the direction of Rayleigh streaming velocities on this plane is mainly perpendicular to the *xy* plane, which can be seen from Fig. 10(a), so the in-plane vortex pattern can be seen more clearly. In this *xy* plane a 6 × 6 vortex pattern in the square fluid channel is obtained, which compares well with the experimental visualisation of Hagsater *et al.*[13] However, the orientation of acoustic streaming in each single vortex is opposite to the experimental visualisation. Similarly, another 6 × 6 in-plane vortex pattern can be seen on the plane $z = -0.16$ mm.

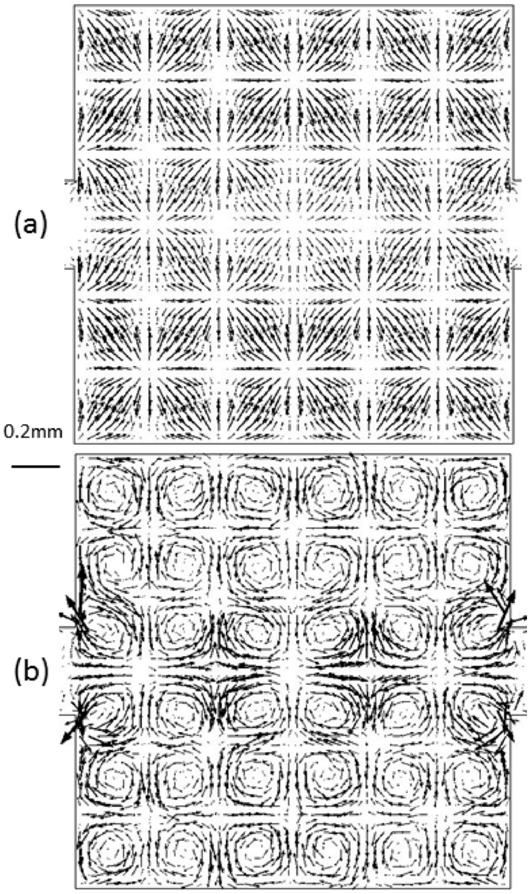

**Fig. 11** (a) Modelled acoustic streaming field (a) on plane $z = -0.1$ mm; (b) on the plane $z = -0.04$ mm.

In order to investigate the behaviour of this in-plane acoustic streaming pattern in more detail, the model was also run at frequencies around the reported driving frequency. It was found that at all frequencies the 6 × 6 in-plane vortex pattern was observed on the same planes. In addition, another two models (included as ESI†) were considered with a change in the *x* and *y* dimensions of the channel to $1.95 \times 1.95$ mm$^2$ (model 3) and $2.05 \times 2.05$ mm$^2$ (model 4) to investigate the sensitivity of this in-plane streaming pattern to the size of the fluid chamber. It was found that in model 3, both the 6 × 6 vortex pattern and the Rayleigh streaming pattern was close to the results presented here. In model 4, the Rayleigh streaming pattern is similar to the model presented here but the 6 × 6 in-plane vortex pattern has the direction of rotation of each vortex opposite to that shown in Fig. 11(b) (*i.e.* the same as that reported in the experimental visualisation). The differences of orientation in each vortex in model 4 and the results presented in this paper are believed to be related to the change of direction of the active sound intensity field in these two models, which will be analysed in more detail in the discussion below.

## 3. Discussion

We have previously analysed the in-plane (*i.e.* parallel to the transducer face) streaming patterns in a planar half wave resonator. In that case we found that a 2 × 2 vortex pattern was obtained regardless of the multiple wavelengths in the

$x$ and $y$ directions. For that device the following approximations held:

$$\frac{\mathrm{d}u_1}{\mathrm{d}x} \ll \frac{\mathrm{d}w_1}{\mathrm{d}z} \text{ and } \frac{\mathrm{d}v_1}{\mathrm{d}y} \ll \frac{\mathrm{d}w_1}{\mathrm{d}z}. \tag{15}$$

Under these assumptions the limiting velocity shown in eqn (3)–(4) can be approximated to[9]

$$u_\mathrm{L} \approx -\frac{1}{4\omega}\mathrm{Re}(-2\mathrm{i}\, u_1^* \frac{\mathrm{d}w_1}{\mathrm{d}z}), \tag{16}$$

$$v_\mathrm{L} \approx -\frac{1}{4\omega}\mathrm{Re}(-2\mathrm{i}\, v_1^* \frac{\mathrm{d}w_1}{\mathrm{d}z}), \tag{17}$$

which (taking $u_\mathrm{L}$ as an example) can also be expressed using the acoustic intensity, $C$,

$$C_x = \frac{1}{2}u_1^* p, \tag{18}$$

$$u_\mathrm{L} \approx \frac{1}{\rho_0 c^2}\mathrm{Re}(C_x). \tag{19}$$

Please note an error in our previous paper:[9] eqn (19) was presented there with a minus before the expression for $u_\mathrm{L}$ (a result of a sign error in eqn (21) of that paper). This error does not change the results and conclusions of that paper as the modelling there was performed with the full expression for limiting velocity (found in eqn (6) and (7) of that paper).

In this device, where the two orthogonal standing waves along $x$ and $y$ are the dominant and which has negligible standing wave in the $z$ direction, a different set of approximations are valid:

$$\frac{\mathrm{d}w_1}{\mathrm{d}z} \ll \frac{\mathrm{d}u_1}{\mathrm{d}x} \text{ and } \frac{\mathrm{d}w_1}{\mathrm{d}z} \ll \frac{\mathrm{d}v_1}{\mathrm{d}y}. \tag{20}$$

In this case, eqn (3)–(4) can now be approximated as

$$u_\mathrm{L} \approx -\frac{1}{4\omega}\mathrm{Re}\left\{q_x + u_1^*\left[(2+\mathrm{i})\left(\frac{\mathrm{d}u_1}{\mathrm{d}x} + \frac{\mathrm{d}v_1}{\mathrm{d}y}\right)\right]\right\}, \tag{21}$$

$$v_\mathrm{L} \approx -\frac{1}{4\omega}\mathrm{Re}\left\{q_y + v_1^*\left[(2+\mathrm{i})\left(\frac{\mathrm{d}u_1}{\mathrm{d}x} + \frac{\mathrm{d}v_1}{\mathrm{d}y}\right)\right]\right\}. \tag{22}$$

Using eqn (20) we can write the complex pressure as[27]

$$p \approx \frac{\mathrm{i}\rho_0 c^2}{\omega}\left(\frac{\mathrm{d}u_1}{\mathrm{d}x} + \frac{\mathrm{d}v_1}{\mathrm{d}y}\right). \tag{23}$$

Thus eqn (21)–(22) can be expressed in terms of the active sound intensity (the real part) and reactive sound intensity (the imaginary part of complex intensity):

$$u_\mathrm{L} = -\frac{1}{4\omega}\mathrm{Re}(q_x) - \frac{1}{\rho_0 c^2}\mathrm{Im}(C_x) - \frac{1}{2\rho_0 c^2}\mathrm{Re}(C_x), \tag{24}$$

$$v_\mathrm{L} = -\frac{1}{4\omega}\mathrm{Re}(q_y) - \frac{1}{\rho_0 c^2}\mathrm{Im}(C_y) - \frac{1}{2\rho_0 c^2}\mathrm{Re}(C_y). \tag{25}$$

In order to distinguish the terms that drive the Rayleigh type streaming patterns found in Fig. 10 (a) from those which produce the in-plane vortex pattern (Fig. 11 (b)), we must establish which of the driving terms have rotation in the $xy$ plane (at the boundary where the limiting velocity is calculated, $z = 0$).

*Firstly, the contribution of the first terms, $q_x$ and $q_y$.* In the linear (inviscid) acoustic approximation the acoustic particle velocity, $\boldsymbol{u}$, is irrotational:[27]

$$\nabla \times \boldsymbol{u} = 0. \tag{26}$$

Using this relation (along with the fact that the spatial derivatives of $\nabla \times \boldsymbol{u}$ must also be zero, we find that the curl of the field $\boldsymbol{Q} = (q_x, q_y, 0)$ is everywhere zero and hence will not contribute to the $xy$ plane 6 × 6 vortex pattern.

*Then, the contribution of the remaining terms.* As discussed in our previous analysis,[9] according to Fahy,[28] only the active intensity, the real part of complex sound intensity can have a rotational component in a standing wave field and this rotation reflects the elliptical path that fluid particles take rather than circulation of energy on a larger scale.

Thus the rotational component of the streaming field in the $xy$ plane is proportional to the active sound intensity components of eqn (24)–(25). The active sound intensity is plotted in Fig. 12 and can be seen to closely resemble the rotational part of the modelled and experimental fields found in Fig. 11(b) and 7(b). Interestingly the rotation of the limiting velocity is in the opposite direction to that of the active intensity under this approximation (eqn (20)), compared to that previously investigated where the approximations of eqn (15) were valid.

We are now in a position to understand why the direction of $xy$ plane rotation is different in this model and model 4. Examining the models we find what the change of dimension

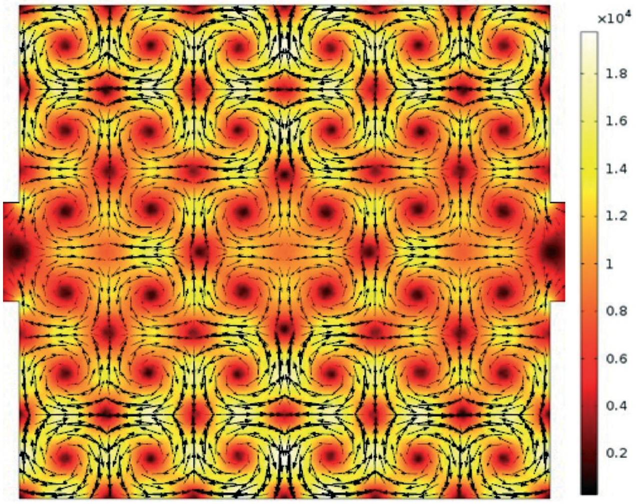

**Fig. 12** Modelled active sound intensity field (W m$^{-2}$) on a limiting velocity boundary in the main fluid channel.

of fluid chamber changes the relative phases of the standing waves in the $x$ and $y$ directions, which in turn changes the direction of rotation of the active sound intensity field, and hence streaming field.

## V. Conclusions

The 3D Rayleigh streaming pattern in an acoustofluidic device has been simulated using the limiting velocity method and its effects on acoustophoretic motion of microparticles are presented. While results from 2D simulations of streaming in uniform channels can show good accuracy, this 3D method permits modelling of subtle effects relating to non-uniformities and resonances in the length direction of channels, and also the modelling of more complex structures, suggesting that streaming motion exists in all three directions. The simulated acoustic streaming field compared well with the experimental investigations.

Additionally, acoustic streaming due to two orthogonal standing waves in a square device was numerically simulated and its mechanism considered. Previous experimental work had reported a regular array of vortices that could not be explained by analogy with Rayleigh streaming since the periodicity of the structure did not match such a hypothesis. We find that in certain planes our model predicts similar circulatory patterns to those found in the experiments, which was found to be closely related to the active sound intensity field. With a slight change on the size of the fluid channel, the direction of orientation of in-plane streaming pattern was changed due to the change of active sound intensity field although the Rayleigh streaming pattern remained the same. Further experimental verification that the pattern found in the model is consistent with that observed is necessary to consider the origin of these vortices *solved*, however the mechanism described here would seem a strong candidate.

As illustrated, numerical results obtained from this computationally efficient method can not only represent 3D acoustic and streaming fields in real acousto-microfluidic devices but also provide good comparisons with experimental measurements. This should allow such models to be used to predict the streaming fields in microfluidic devices to provide optimization of device designs. This limiting velocity method is valid for modelling boundary induced streaming fields when the local curvatures of the boundaries are large in comparison to the viscous penetration depth and the streaming velocities are low enough to be within a strictly laminar regime. It does not, however, model Eckart type streaming[8,29] induced by bulk absorption of sound, which can be modelled as a volume force on the fluid.[30,31] Thus this method is not suitable for modelling the majority of streaming found in high frequency surface acoustic wave systems,[32,33] but it would be interesting to explore to what extent boundary driven streaming contributes in these systems.

## Acknowledgements

The authors gratefully acknowledge the financial support for this work received from China Scholarship Council (CSC) and the EPSRC under the Sonotweezers project (EP/G012075/1).

## References

1 Lord Rayleigh, *Philos. Trans. R. Soc. London*, 1883, **175**, 1–21.
2 P. J. Westervelt, *J. Acoust. Soc. Am.*, 1952, **25**, 60–67.
3 W. L. Nyborg, *J. Acoust. Soc. Am.*, 1953, **25**, 68–75.
4 H. Schlichting, *Phys. Z.*, 1932, **33**, 327–335.
5 S. Boluriaan and P. J. Morris, *Int. J. Aeroacoust.*, 2003, **2**(3&4), 255–292.
6 M. Wiklund, R. Green and M. Ohlin, *Lab Chip*, 2012, **12**, 2438–2451.
7 M. F. Hamilton, Y. A. Ilinskii and E. A. Zabolotskaya, *J. Acoust. Soc. Am.*, 2003, **113**, 153–160.
8 C. Eckart, *Phys. Rev.*, 1947, **73**, 68–76.
9 J. Lei, P. Glynne-Jones and M. Hill, *Lab Chip*, 2013, **13**, 2133–2143.
10 P. Glynne-Jones, C. E. M. Demore, C. W. Ye, Y. Q. Qiu, S. Cochran and M. Hill, *IEEE Trans. Ultrason. Ferroelectr. Freq. Control*, 2012, **59**, 1258–1266.
11 M. W. Thompson and A. A. Atchley, *J. Acoust. Soc. Am.*, 2005, **117**, 1828–1838.
12 M. Nabavi, M. H. K. Siddiqui and J. Dargahi, *Meas. Sci. Technol.*, 2007, **18**, 1811–1817.
13 S. M. Hagsater, T. G. Jensen, H. Bruus and J. P. Kutter, *Lab Chip*, 2007, **7**, 1336–1344.
14 R. Barnkob, P. Augustsson, T. Laurell and H. Bruus, *Lab Chip*, 2010, **10**, 563–570.
15 M. Koklu, A. C. Sabuncu and A. Beskok, *J. Colloid Interface Sci.*, 2010, **351**, 407–414.
16 M. Rossi, R. Segura, C. Cierpka and C. J. Kahler, *Exp. Fluids*, 2012, **52**, 1063–1075.
17 C. Cierpka, R. Segura, R. Hain and C. J. Kahler, *Meas. Sci. Technol.*, 2010, **21**, 1–13.
18 C. Cierpka, M. Rossi, R. Segura and C. J. Kahler, *Meas. Sci. Technol.*, 2011, **22**, 1–10.
19 C. Cierpka, M. Rossi, R. Segura, F. Mastrangelo and C. J. Kahler, *Exp. Fluids*, 2012, **52**, 605–615.
20 M. Kawahashi and M. Arakawa, *JSME Int. J., Ser. B*, 1996, **39**, 280–286.
21 M. K. Aktas and B. Farouk, *J. Acoust. Soc. Am.*, 2004, **116**, 2822–2831.
22 P. B. Muller, R. Barnkob, M. J. H. Jensen and H. Bruus, *Lab Chip*, 2012, **12**, 4617–4627.
23 P. B. Muller, M. Rossi, Á. G. Marín, R. Barnkob, P. Augustsson, T. Laurell, C. J. Kähler and H. Bruus, *Phys. Rev. E: Stat., Nonlinear, Soft Matter Phys.*, 2013, **88**, 023006.
24 C. P. Lee and T. G. Wang, *J. Acoust. Soc. Am.*, 1989, **85**, 1081–1088.
25 *Comsol Multiphysics 4.3*, http://www.comsol.com/.
26 H. Bruus, *Lab Chip*, 2012, **12**, 1014–1021.
27 L. E. Kinsler, *Fundamentals of acoustics*, Wiley, New York, 2000.

28 F. J. Fahy, *Sound intensity*, E & FN Spon, London, 1995.

29 S. S. Sadhal, *Lab Chip*, 2012, **12**, 2292–2300.

30 A. L. Bernassau, P. Glynne-Jones, F. Gesellchen, M. Riehle, M. Hill and D. R. S. Cumming, *Ultrasonics*, 2014, **54**, 268–274.

31 D. Möller, T. Hilsdorf, J. Wang and J. Dual, *AIP Conf. Proc.*, 2012, **1433**, 775–778.

32 X. Ding, P. Li, S.-C. S. Lin, Z. S. Stratton, N. Nama, F. Guo, D. Slotcavage, X. Mao, J. Shi, F. Costanzo and T. J. Huang, *Lab Chip*, 2013, **13**, 3626–3649.

33 S. Li, X. Ding, F. Guo, Y. Chen, M. I. Lapsley, S.-C. S. Lin, L. Wang, J. P. McCoy, C. E. Cameron and T. J. Huang, *Anal. Chem.*, 2013, **85**, 5468–5474.

# Appendix 3

## Paper published in Journal of Nanobiotechnology

### The effect of ultrasound-related stimuli on cell viability in microfluidic channels

**Dyan N Ankrett, Dario Carugo, Junjun Lei, Peter Glynne-Jones, Paul A Townsend, Xunli Zhang and Martyn Hill**

**Abstract:** In ultrasonic micro-devices, contrast agent micro-bubbles are known to initiate cavitation and streaming local to cells, potentially compromising cell viability. Here we investigate the effects of ultrasound alone by omitting contrast agent and monitoring cell viability under moderate-to-extreme ultrasound-related stimuli.

**DOI:** 10.1186/1477-3155-11-20

Ankrett *et al. Journal of Nanobiotechnology* 2013, **11**:20
http://www.jnanobiotechnology.com/content/11/1/20

JOURNAL OF NANOBIOTECHNOLOGY

METHODOLOGY **Open Access**

# The effect of ultrasound-related stimuli on cell viability in microfluidic channels

Dyan N Ankrett[1*†], Dario Carugo[1,2†], Junjun Lei[1], Peter Glynne-Jones[1], Paul A Townsend[3], Xunli Zhang[2] and Martyn Hill[1]

## Abstract

**Background:** In ultrasonic micro-devices, contrast agent micro-bubbles are known to initiate cavitation and streaming local to cells, potentially compromising cell viability. Here we investigate the effects of US alone by omitting contrast agent and monitoring cell viability under moderate-to-extreme ultrasound-related stimuli.

**Results:** Suspended H9c2 cardiac myoblasts were exposed to ultrasonic fields within a glass micro-capillary and their viability monitored under different US-related stimuli. An optimal injection flow rate of 2.6 mL/h was identified in which, high viability was maintained (~95%) and no mechanical stress towards cells was evident. This flow rate also allowed sufficient exposure of cells to US in order to induce bioeffects (~5 sec), whilst providing economical sample collection and processing times. Although the transducer temperature increased from ambient 23°C to 54°C at the maximum experimental voltage (29 $V_{pp}$), computational fluid dynamic simulations and controls (absence of US) revealed that the cell medium temperature did not exceed 34°C in the pressure nodal plane. Cells exposed to US amplitudes ranging from 0–29 $V_{pp}$, at a fixed frequency sweep period ($t_{sw} = 0.05$ sec), revealed that viability was minimally affected up to ~15 $V_{pp}$. There was a ~17% reduction in viability at 21 $V_{pp}$, corresponding to the onset of Rayleigh-like streaming and a ~60% reduction at 29 $V_{pp}$, corresponding to increased streaming velocity or the potential onset of cavitation. At a fixed amplitude (29 $V_{pp}$) but with varying frequency sweep period ($t_{sw} = 0.02$-$0.50$ sec), cell viability remained relatively constant at $t_{sw} \geq 0.08$ sec, whilst viability reduced at $t_{sw} < 0.08$ sec and minimum viability recorded at $t_{sw} = 0.05$ sec.

**Conclusion:** The absence of CA has enabled us to investigate the effect of US alone on cell viability. Moderate-to-extreme US-related stimuli of cells have allowed us to discriminate between stimuli that maintain high viability and stimuli that significantly reduce cell viability. Results from this study may be of potential interest to researchers in the field of US-induced intracellular drug delivery and ultrasonic manipulation of biological cells.

**Keywords:** Ultrasound (US), Micro-device, Cardiac myoblasts, Cell viability

## Background

In ultrasonic cell stimulation micro-devices, the inclusion of ultrasound (US) contrast agent (CA) to enhance US bioeffects or increase cell membrane permeability is common [1]. However, CAs can initiate cavitation and streaming [2] local to cells, potentially compromising cell viability [3,4]. Thus, higher cell viability is likely to be maintained in the absence of CA [5-7]. In our previous study we reported on ultrasonically induced membrane poration of a cardiac myoblast cell line (H9c2) in the absence of CA by generating an ultrasonic field within a biocompatible glass micro-capillary [3]. Notably, high cell viability was maintained in the absence of CA [3]. Following a similar approach, Longsine-Parker *et al.* recently demonstrated effective cell membrane poration in a microfluidic device by combining the action of electric fields and US waves in a CA-free environment [8].

Here we investigate US-"alone"-related physical stimuli of H9c2 cells. We expose suspended cells to gentle, moderate and extreme US amplitudes. Extreme amplitudes also initiate an increase in transducer temperature; therefore we also

---

* Correspondence: D.Ankrett@soton.ac.uk
†Equal contributors
[1] Electromechanical Engineering Group, Faculty of Engineering and the Environment, University of Southampton, Southampton SO17 1BJ, UK
Full list of author information is available at the end of the article

investigated the effect of US-related temperature increase on cell viability. Cell viability was also measured following infusion into the micro-device at varying flow regimes in order to optimise the flow rate. Of particular interest to us is the effect of frequency sweeping on cells as a means of controllably stressing cells and potentially increasing membrane permeability.

## Results

Cells were subjected to a variety of US-related stimuli (summarised in Table 1) in order to assess the effect of US alone on cell viability in the absence of CA.

At 2.6 mL/h viability was uncompromised, likely due to low mechanical stress (Figure 1). This flow rate also provided economical sample collection and processing times whilst allowing sufficient exposure of cells to US ($t_{exp} \cong 5$ sec) for generating observable bioffects. Furthermore, no cell trapping was evident, providing homogeneous exposure of cells to US.

During US applied at the maximum experimental voltage, 29 $V_{pp}$, the transducer temperature was noted to increase from ambient 23°C to a biologically unfavourable 54°C. However, CFD simulations revealed that the temperature of the liquid medium at the capillary centerline only increased up to a maximum of ~34°C (Figure 2a). To validate the simulations, control experiments (absence of US), replacing the transducer with a hot plate fixed at 54°C, revealed that cell viability was minimally affected (92.12±2.94%), while during US exposure at 29 $V_{pp}$, viability reduced to 43.28±5.54% (Figure 2b). This suggests that PZT heating *per se* did not compromise cell viability. However, the CFD simulations did not take into account the effect of acoustic streaming on heat transfer within the fluidic domain, which may have contributed to the reduction in cell viability.

Cell viability was measured immediately following exposure to US amplitudes ranging from 0–29 $V_{pp}$, using a fixed frequency sweep period of 0.05 sec. Figure 3 demonstrates that cell viability was not compromised up to ~15 $V_{pp}$. However a ~17% reduction in cell viability was measured at 21 $V_{pp}$, corresponding to the onset of streaming, assigned as Rayleigh-like (observed with fluorescent tracers under static conditions), characterised by the formation of toroidal axially centred vortices [10]. A ~60% viability reduction was measured at 29 $V_{pp}$, corresponding to an observed increase of the streaming velocity. Furthermore, the acoustic pressure (measured by drop-voltage analysis at a fixed $f = 2.18$ MHz) was $\sim 2.05 \times 10^4 \times V_{pp}$ Pa. This corresponded to pressures in the range 0.12–0.59 MPa, thus suggesting that cavitation may have occurred at $V_{pp} > 20$. Notably, Apfel and Holland determined a minimum pressure threshold of ~0.4 MPa for cavitation to occur in water, at a frequency of ~2 MHz [6,11].

**Table 1 Summary of the experiments performed to investigate the effect of US-related stimuli on H9c2 cell viability**

| Experiment | Operating conditions | Figure |
|---|---|---|
| Flow rate through the micro-capillary | Inlet flow rate: 1.3–13.0 mL/h | Figure 3 |
| US-induced thermal variations | PZT temperature measurements and CFD simulations of fluid temperature distribution | Figure 4a |
| | Controls (correspondent PZT temperatures, absence of US) | Figure 4b |
| Amplitude variations | Driving voltage: 6–29 $V_{pp}$ | Figure 5 |
| Sweep period variations | Sweep period: 0.02–0.50 sec | Figure 1 |

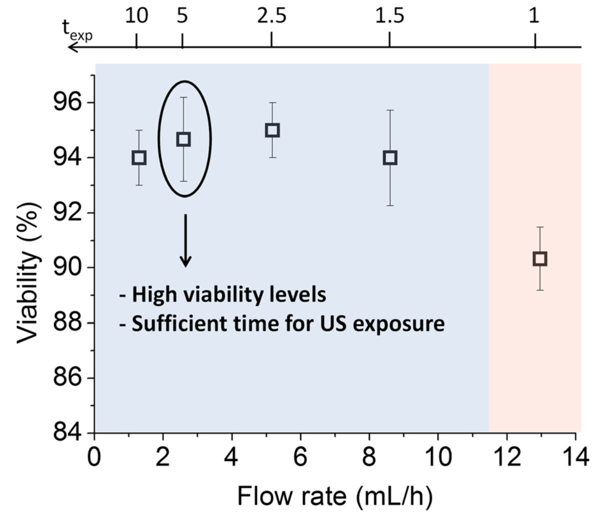

**Figure 1 Effect of fluid flow rate on cell viability.** Cell viability was measured at flow rates ranging from 1.3-13.0 mL/h. At 2.6 mL/h cell viability was uncompromised (control viability = 97±1%), cells were allowed sufficient US exposure ($t_{exp} \cong 5$ sec), and trapping was not evident (n = 3).

At a fixed amplitude (29 $V_{pp}$) but varying the sweep period ($t_{sw} = 0.02$-$0.50$ sec), cell viability was virtually unaffected by frequency sweep periods $t_{sw} \geq 0.08$ sec. However, at sweep periods $t_{sw} < 0.08$ sec cell viability decreased, with minimum viability (~41%) measured at $t_{sw} = 0.05$ sec (Figure 4a). Under identical acoustic conditions, 20 $\mu$m diameter fluorescent beads were observed to rapidly oscillate across a relatively smaller distance away from the nodal plane at $t_{sw} = 0.1$ sec, compared with $t_{sw} = 0.5$ sec where bead oscillation was visibly slower over increased distances away from the nodal plane (Figure 4b).

## Discussion

The effect of individual US-related physical parameters (fluid flow rate, US heat generation, amplitude and frequency sweep period) on H9c2 cell viability was assessed within a microfluidic device. The optimised flow rate did not inflict any detectable mechanical stress, and thus high cell viability was maintained. Moreover cells were allowed

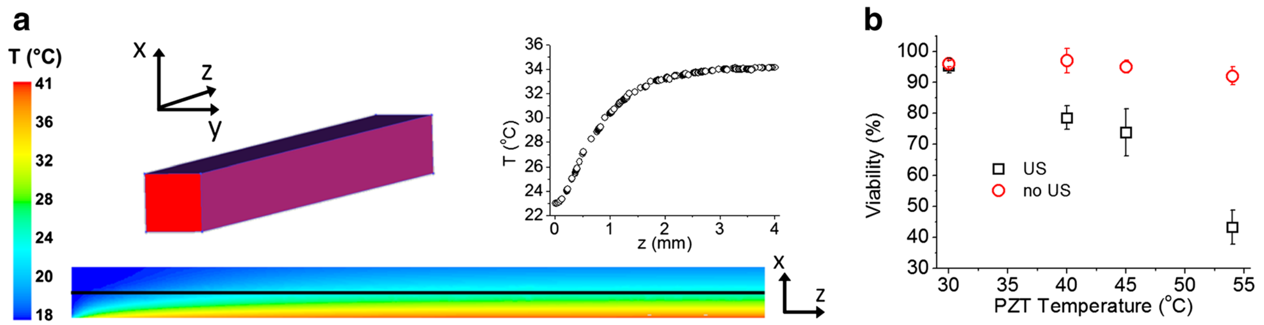

**Figure 2 Effect of temperature on cell viability. a**] Fluid temperature profile along the glass microchannel centerline and contours of fluid temperature determined computationally. **b**] Cell viability during US exposure (black squares), and absence of US (red circle) with PZT substituted by a hot plate at corresponding temperatures (n = 4).

sufficient exposure to US in order to elicit bioeffects, whilst providing economical sample processing times and minimising cell trapping. High cell viability was maintained at amplitudes where streaming was not evident. However, when more extreme amplitudes were employed, streaming velocities increased and cell viability significantly decreased. Extreme amplitudes also initiated an increase in PZT temperature, however cell viability was unaffected by this increase due to heat dissipation, confirmed by controls and CFD simulations. Longer duration frequency sweeps were identified to have little or no effect on cell viability, whereas short sweeps resulted in reduced cell viability. This effect may be attributed to mechanical stress generated by rapid oscillatory movements of the cell within the fluidic domain [12]. Notably, experiments with fluorescent tracer beads revealed that bead oscillation frequency increased with reducing the sweep interval, which may explain the reduction in cell viability at the shorter $t_{sw}$. However, an in depth investigation into the effects of frequency sweeping on cell viability is currently underway in our laboratories.

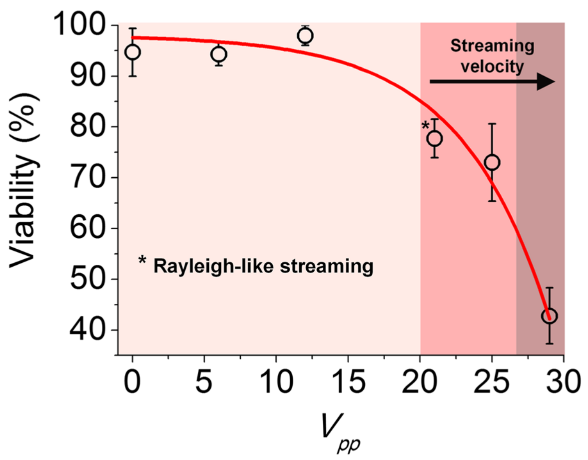

**Figure 3 Effect of US amplitude on cell viability.** Up to ~15 $V_{pp}$ cell viability was unaffected, a ~17% reduction in viability was measured at 21 $V_{pp}$ (corresponding to the onset of Rayleigh-like streaming) and a ~60% reduction was measured at 29 $V_{pp}$ (corresponding to increased streaming velocities) (n = 4).

## Conclusion

Our CA-free investigation into the effects of US on cell viability has enabled us to discriminate between US-related stimuli that do not compromise cell viability and stimuli that significantly reduce cell viability within our micro-device. Our findings may be of potential interest to researchers in the field of US-induced intracellular drug delivery and ultrasonic manipulation of biological cells.

## Methods

The micro-device (Figure 5a), comprising of a squared cross-section borosilicate glass micro-capillary (length: 50 mm, internal width: 300 $\mu$m, wall thickness: 150 $\mu$m; VitroCom, Ilkley, UK), was acoustically coupled to a piezoelectric transducer (PZT; PZ26 Ferroperm, Kvistgard, Denmark) using glycerol. The transducer (length: 40 mm, width: 9 mm and thickness: 1 mm) was fixed to a glass platform and driven by an RF power amplifier (240 L ENI, New York, USA) fed from a signal generator (TG103 TTI, Cambridgeshire, UK). A time varying ultrasonic field was generated within the capillary and the operating frequency determined through electrical impedance measurements (C-60 impedance analyser, Cypher Instruments Ltd., London, UK) of the capillary both air-filled and fluid-filled (Figure 2b).

H9c2 cardiac myoblasts were grown in Dulbecco's Modified Eagle Medium (DMEM) culture medium supplemented with 10% (v/v) foetal calf serum and 1% (v/v) penicillin-streptomycin (media and supplements purchased from Fisher Scientific, Loughborough, UK). Cells were maintained at 37°C, 5% $CO_2$ in air with 95% humidity. Cells were routinely harvested and suspended at a density of $2\times10^6$ cells/mL in serum free DMEM within a 1 mL sterile, plastic syringe (BD Bioscience, Oxford, UK).

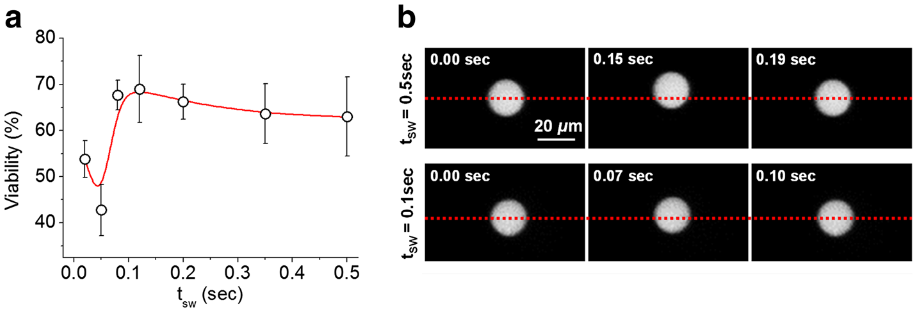

**Figure 4 Effect of frequency sweep on cell viability and bead oscillatory dynamics. a**] Cell viability was unaffected by $t_{sw}$ ≥ 0.08 sec but decrease ≥ 0.08 sec using a frequency range: 2.13-2.40 MHz and at a fixed 29 $V_{pp}$. **b**] Oscillatory dynamics of 20 μm diameter fluorescent polystyrene beads at a sweep period of 0.5 and 0.1 sec.

Cells were infused into the device using a syringe pump (KD100, KD Scientific Inc., Holliston, USA) and subjected to ultrasound-related physical stimuli. Cells were captured in 1 mL sterile tubes, followed by counting and viability assessment using a Neubauer haemocytometer (depth: 0.1 mm, area: 0.04 mm$^2$) and trypan blue exclusion dye. All viability measurements were in triplicate or greater.

To optimise the flow rate, cell viability was measured following infusion into the device at a range of flow rates (1.3-13.0 mL/h), which were prior calculated in order to: i) provide sufficient exposure of cells to US, ii) provide economical cell collection and processing times, iii) minimise flow-induced mechanical stress on cells and iv) minimise cell trapping.

To assess US-related thermal effects on cell viability, cells were infused into the device at a fixed flow rate (2.6 mL/h) and exposed to US (6–29 $V_{pp}$), whilst thermocouples were attached to the transducer, and temperatures recorded using a thermometer (HH11 Omega®, Manchester, UK). Controls were produced in the absence of US by replacing the transducer with a hot plate (Fisher Scientific, Loughborough, UK) at identical temperatures to the recorded transducer temperatures. Additionally, computational fluid dynamic (CFD) simulations were performed to predict the transfer of heat from the transducer to the cell medium within the capillary.

The effect of US amplitude on cell viability was investigated by varying the $V_{pp}$, ranging from 0–29 $V_{pp}$, using a fixed frequency sweep period of 0.05 sec in the frequency range 2.13-2.40 MHz. Additionally, flow visualisation experiments, using 1 μm diameter fluorescent tracers (Polysciences, Inc., Warrington, USA), were performed to characterise the fluid dynamic environment under "gentle" (6 $V_{pp}$) to "extreme" (29 $V_{pp}$) US amplitudes. The acoustic pressure within the capillary was measured through drop-voltage analysis [9], using 20 μm diameter fluorescent polystyrene beads. A fixed resonance frequency of 2.18 MHz was set in this case, due to the difficulty in obtaining acoustic pressure values during frequency sweeping.

The effect of frequency sweep duration on cell viability was investigated by varying the sweep period (0.02-0.50 sec) at a fixed voltage (29 $V_{pp}$).

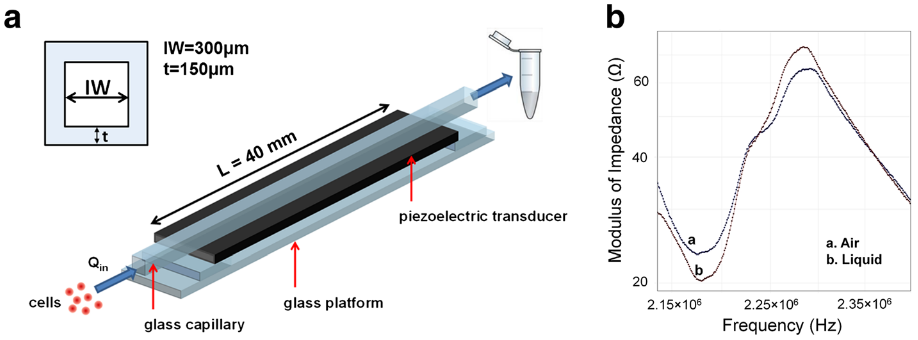

**Figure 5 Microfluidic device. a**] device comprising of a squared cross-section glass capillary (length: 50 mm, internal width: 300 μm and wall thickness: 150 μm), coupled to a PZT transducer (length: 40 mm, width: 9 mm and thickness: 1 mm) and mounted on a glass platform. **b**] Modulus of impedance (Ω) for the air-filled and the liquid-filled micro-capillary, respectively. Frequency range: 2.13-2.40 MHz.

## Competing interests

The authors declare that they have no competing interests.

## Authors' contributions

Conceived, designed and performed experiments: DA and DC. Data analysis: DA and DC. Wrote the paper: DA and DC. Device design: PGJ. Invaluable advice provided on microfluidics: XZ, acoustics: JL and MH and biology: PAT. All authors read and approved the final manuscript.

## Acknowledgements

We are very grateful to Agilent Technologies, Santa Clara, CA, USA for funding this research (University Relations Grant 2012, Gift# 2700).

## Author details

[1]Electromechanical Engineering Group, Faculty of Engineering and the Environment, University of Southampton, Southampton SO17 1BJ, UK. [2]Bioengineering Sciences Group, Faculty of Engineering and the Environment, University of Southampton, Southampton SO17 1BJ, UK. [3]Faculty Institute for Cancer Sciences, Faculty of Medical and Health Sciences, Manchester Academic Health Science Centre, University of Manchester, Manchester M13 9WL, UK.

Received: 17 June 2013 Accepted: 17 June 2013
Published: 28 June 2013

## References

1. Le Gac S, Zwaan E, Van Den Berg A, Ohl C-D: **Sonoporation of suspension cells with a single cavitation bubble in a microfluidic confinement.** *Lab Chip* 2007, **7**(12):1666–1672.
2. Collis J, Manasseh R, Liovic P, Tho P, Ooi A, Petkovic-Duran K, Zhu Y: **Cavitation microstreaming and stress fields created by microbubbles.** *Ultrasonics* 2010, **50**(2):273–279.
3. Carugo D, Ankrett DN, Glynne-Jones P, Capretto L, Boltryk RJ, Zhang X, Townsend PA, Hill M: **Contrast agent-free sonoporation: the use of an ultrasonic standing wave microfluidic system for the delivery of pharmaceutical agents.** *Biomicrofluidics* 2011, **5**(4):044108.
4. Brayman AA, Azadniv M, Cox C, Miller MW: **Hemolysis of albunex-supplemented, 40% hematocrit human erythrocytes *in vitro* by 1-MHz pulsed ultrasound: Acoustic pressure and pulse length dependence.** *Ultrasound Med Biol* 1996, **22**(7):927–938.
5. Hultström J, Manneberg O, Dopf K, Hertz HM, Brismar H, Wiklund M: **Proliferation and viability of adherent cells manipulated by standing-wave ultrasound in a microfluidic chip.** *Ultrasound Med Biol* 2007, **33**(1):145–151.
6. Wiklund M: **Acoustofluidics 12: Biocompatibility and cell viability in microfluidic acoustic resonators.** *Lab Chip* 2012, **12**:2018–2028.
7. Evander M, Johansson L, Lilliehorn T, Piskur J, Lindvall M, Johansson S, Almqvist M, Laurell T, Nilsson J: **Noninvasive acoustic cell trapping in a microfluidic perfusion system for online bioassays.** *Anal Chem* 2007, **79**(7):2984–2991.
8. Longsine-Parker W, Wang H, Koo C, Kim J, Kim B, Jayaraman A, Han A: **Microfluidic electro-sonoporation: a multi-modal cell poration methodology through simultaneous application of electric field and ultrasonic wave.** *Lab Chip* 2013, **13**:2144–2152.
9. Glynne-Jones P, Boltryk RJ, Hill M, Zhang F, Dong L, Wilkinson JS, Melvin T, Harris NR, Brown T: **Flexible acoustic particle manipulation device with integrated optical waveguide for enhanced microbead assays.** *Anal Sci* 2009, **25**(2):285–291.
10. Sorando AC, Hawkes JJ, Fielden PR, González I: **Patterns of particles aggregation and streaming in resonating fluids.** *AIP Conference Proceedings* 2012, **1433**:757.
11. Apfel RE, Holland CK: **Gauging the likelihood of cavitation from short-pulse, low-duty cycle diagnostic ultrasound.** *Ultrasound Med Biol* 1991, **17**(2):179–185.
12. Radel S, McLoughlin A, Gherardini L, Doblhoff-Dier O, Benes E: **Viability of yeast cells in well controlled propagating and standing ultrasonic plane waves.** *Ultrasonics* 2000, **38**(1):633–637.

doi:10.1186/1477-3155-11-20
**Cite this article as:** Ankrett *et al.*: The effect of ultrasound-related stimuli on cell viability in microfluidic channels. *Journal of Nanobiotechnology* 2013 **11**:20.

# Appendix 4

## Paper submitted to Physics of Fluids

## Modal Rayleigh-like streaming in layered acoustofluidic devices

**Junjun Lei, Peter Glynne-Jones and Martyn Hill**

**Abstract:** Classical Rayleigh streaming is well known and can be modelled using Nyborg's limiting velocity method as driven by fluid velocities adjacent to the walls parallel to the axis of the main acoustic resonance. We have demonstrated previously the existence and the mechanism of four-quadrant transducer plane streaming pattern in thin-layered acoustofluidic devices which are driven by the limiting velocities on the walls perpendicular to the axis of the main acoustic propagation. We have recently found experimentally that there is a third case which resembles Rayleigh streaming, but is a more complex pattern related to three-dimensional cavity modes of an enclosure. This streaming has vortex sizes related to the effective wavelength in each cavity axis of the modes which can be much larger than those found in the one-dimensional case with Rayleigh streaming. We will call this here *modal Rayleigh-like streaming*, and show that it can be important in layered acoustofluidic manipulation devices. This paper seeks to establish the conditions under which each of these is dominant and shows how the limiting velocity field for each relates to different parts of the complex acoustic intensity patterns at the driving boundaries.

# Modal Rayleigh-like streaming in layered acoustofluidic devices

Junjun Lei, Peter Glynne-Jones and Martyn Hill*

*Faculty of Engineering and the Environment, University of Southampton,*

*University Road, Southampton, SO17 1BJ, United Kingdom*

m.hill@soton.ac.uk

Classical Rayleigh streaming is well known and can be modelled using Nyborg's limiting velocity method as driven by fluid velocities adjacent to the walls parallel to the axis of the main acoustic resonance. We have demonstrated previously the existence and the mechanism of four-quadrant transducer plane streaming pattern in thin-layered acoustofluidic devices which are driven by the limiting velocities on the walls perpendicular to the axis of the main acoustic propagation. We have recently found experimentally that there is a third case which resembles Rayleigh streaming, but is a more complex pattern related to three-dimensional cavity modes of an enclosure. This streaming has vortex sizes related to the effective wavelength in each cavity axis of the modes which can be much larger than those found in the one-dimensional case with Rayleigh streaming. We will call this here *modal Rayleigh-like streaming*, and show that it can be important in layered acoustofluidic manipulation devices. This paper seeks to establish the conditions under which each of these is dominant and shows how the limiting velocity field for each relates to different parts of the complex acoustic intensity patterns at the driving boundaries.

## I. INTRODUCTION

In resonant acoustofluidic particle manipulation devices, acoustic streaming flows are typically found in addition to the acoustic radiation forces. These are generally considered as a disturbance as they place a practical lower limit on the particle size that can be manipulated by the primary acoustic radiation force.[1, 2] However, acoustic streaming can also play an active role in such systems, such as particle trapping[3-7], two-dimensional particle focusing[8] and particle separation[9]. Most acoustofluidic particle manipulation devices utilise standing wave fields, and the acoustic streaming field is generally dominated by boundary-driven streaming which arises from the acoustic attenuation within the acoustic boundary layer due to the non-slip condition on the walls of the fluid channel. Another significant streaming pattern, Eckart streaming[10], requires acoustic absorption over longer distances (as is the case in surface acoustic wave devices[11, 12]) than those found in these bulk acoustic wave resonators.

Classical boundary-driven streaming includes streaming vortices both inside and outside of the acoustic boundary layer, which are respectively referred to as Schlichting streaming[13] (or inner streaming) and Rayleigh streaming[14, 15] (or outer streaming) in recognition of their contributions to analysing these streaming patterns for the first time. Following Rayleigh's early work, a series of modifications to his solution have been proposed[16-18]. The boundary-driven streaming vortices both inside and outside of the acoustic boundary layer can be modelled by considering Reynolds stresses, the volume forces representing the time-averaged acoustic momentum flux due to the acoustic dissipation near the no-slip walls[19]. Alternatively, the streaming field in the bulk of the fluid can be effectively modelled using the *limiting velocity method*[20, 21], in which the acoustic boundary layer with its non-slip boundary condition on the walls parallel to the axis of acoustic resonances is replaced by a slip boundary condition with a limiting velocity derived from the acoustic field. The former method is computationally expensive, especially for three-dimensional (3D) models, as tiny mesh elements near the no-slip walls are required to resolve the acoustic and streaming fields within the acoustic boundary layer. In contrast, the limiting velocity method is more computationally efficient and is valid so long as the boundaries have curvature that is negligible compared to the viscous boundary layer thickness. In practical acoustofluidic particle manipulation devices working in the MHz region this approximation is usually valid, and since the fluid channel dimensions are typically several orders larger than the acoustic boundary layer thicknesses only the acoustic streaming field in the bulk of the fluid is usually of interest.

While Rayleigh streaming has been recently extensively studied within the field of acoustic particle trapping and manipulation[22-29], there are acoustic streaming patterns observed experimentally in acoustofluidic particle manipulation devices that cannot be explained by Rayleigh's classical theory[3, 30-33]. Recently, we have explained the mechanism behind the four-quadrant transducer-plane streaming, which has a vortex pattern parallel to the transducer face and is driven by the limiting velocity on the walls perpendicular to the axis of main acoustic propagation[34]. In this case, the limiting velocity field was shown to be closely related to the sound intensity field at the driving boundaries. The expression for the limiting velocity has terms corresponding to acoustic velocity gradients in different directions. Depending on which of these is dominant, different acoustic streaming patterns arise, e.g. transducer-plane streaming[34] (streaming vortex parallel to the driving surface, FIG. 1 (b)) and Rayleigh streaming[27] (streaming vortex perpendicular to the driving surface, FIG. 1 (d)) corresponding to the rotational and irrotational features of, respectively, the active and reactive intensity patterns in acoustic fields[35].

In this paper, we address the conditions under which each of these streaming patterns discussed above is dominant in layered acoustofluidic particle manipulation devices with different channel aspect ratios and show how the limiting velocity for each case relates to different parts of the complex acoustic intensity fields at the driving boundaries. We also show a case, here called modal Rayleigh-like streaming, which has not been discussed or shown experimentally before. In this regime, the streaming is driven by boundaries perpendicular to those driving conventional Rayleigh patterns, and has a roll size greater than the quarter wavelength of the main acoustic resonance: the scale is instead related to a cavity mode, FIG. 1 (c).

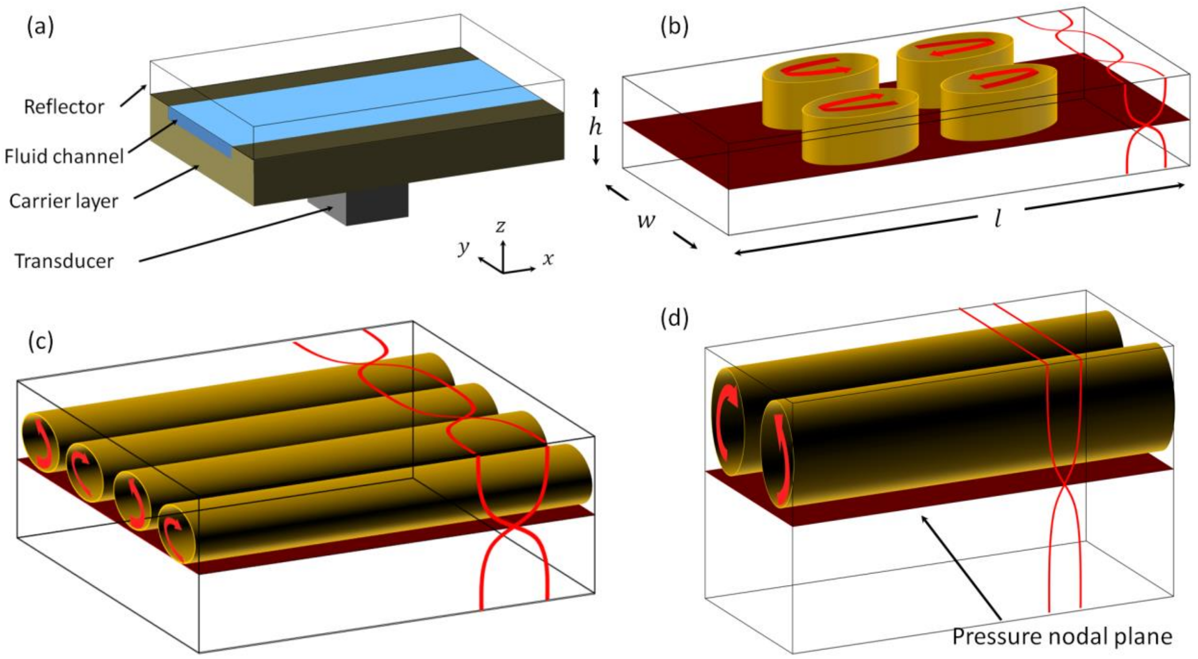

FIG. 1 (colour online). Schematic illustrations of: (a) a layered acoustofluidic particle manipulation device; (b) four-quadrant transducer-plane streaming field in a fluid channel with low aspect ratio in its $yz$ cross-section ($h/w \leq 1/20$); (c) modal Rayleigh-like streaming (as introduced in this paper) in a fluid channel with medium aspect ratio ($1/3 \leq h/w \leq 1/2$); and (d) Rayleigh streaming in a fluid channel with high aspect ratio ($h/w > 1$), where the waveforms on the surfaces of the 3D volumes show respectively the standing wave fields established in these fluid channels, the planes through the half-heights of the fluid volumes are the pressure nodal planes, and the rolls of cylinders show the paralleled streaming vortices with the arrows representing their orientations.

## II. MODELLING

The numerical process was conducted in COMSOL 4.4[36]. FIG. 1 (a) shows the schematic presentation of a classical layered acoustofluidic particle manipulation device, which is, typically, composed of four layers: the transducer, the carrier layer, the fluid channel and the reflector layer[37, 38]. In this paper, only the fluid layer was considered for the numerical efficiency of 3D acoustic and streaming simulations, which is appropriate as it has been shown previously[34] that this simplified model is sufficient to demonstrate the fundamental behaviour of streaming fields. For a given application, however, a full model may be required to capture more complex combinations of boundary movement to determine which resonance is excited in the fluid layer[27]. In this case we excite a particular cavity mode (see below) through applying a normal acceleration boundary condition on the bottom surfaces of the fluid channels.

In order to investigate the sensitivity of the acoustic streaming patterns to the channel dimensions, a series of models with various channel dimensions were considered, which are summarised in TABLE I, where $l$, $w$ and $h$ are the dimensions of the fluid channel along the coordinates $x$, $y$ and $z$, respectively. Various channel heights ranging from 0.2 to 2 mm for four different channel widths were considered. We restrict our models to the thin-layered acoustofluidic devices ($h/w < 1$ and $h/l < 1$) for the reason that the purpose of this paper is to demonstrate the transition from streaming fields induced by limiting velocities dominated by active sound intensity to that dominated by the reactive intensity in 3D resonant cavity modes. However, in high aspect-ratio device ($h/w > 0.5$), the acoustic field is usually more closely approximated by a one-dimensional (1D) acoustic resonance[26, 27], leading to the classical Rayleigh streaming[14], which is a different pattern to the others discussed here. Furthermore, it was found that in the thin-layered regime the contribution of the acoustic streaming field generated by the side boundaries ($y = \pm w/2$) to the overall streaming field in the bulk of the fluid channel is small. Hence, in this paper, only the driving terms on the top and bottom boundaries ($z = \pm h/2$) were taken into consideration for the acoustic streaming simulations unless otherwise stated.

TABLE I Channel dimensions modelled

| Case | Channel dimensions |
|---|---|
| a | $l = 10$ mm, $w = 6$ mm, $h$: 0.2 – 2 mm |
| b | $l = 12$ mm, $w = 8$ mm, $h$: 0.2 – 2 mm |
| c | $l = 14$ mm, $w = 10$ mm, $h$: 0.2 – 2 mm |
| d | $l = 16$ mm, $w = 12$ mm, $h$: 0.2 – 2 mm |

Firstly, the COMSOL '*Pressure Acoustics, Frequency Domain*' interface was used to simulate the first-order acoustic fields, which solves the harmonic, linearized acoustic problem, taking the form:

$$\nabla^2 p = -\frac{\omega^2}{c^2} p, \tag{1}$$

where $p$ is the complex pressure, $\omega$ is the angular frequency and $c$ is the sound speed in the fluid. While there are various resonant acoustofluidic systems, we investigated here the half-wave resonance in the $z$-direction, which is a widely used system for particle and cell manipulation[37-46]. The origin of the coordinates in these models was set at the centre of the fluid channels such that the fluid channels are located within coordinates: $-l/2 \leq x \leq l/2, -w/2 \leq y \leq w/2,\ -h/2 \leq z \leq h/2$. We excited in each case the standing wave field through a '*normal acceleration'* boundary condition on the bottom wall. Energy gradients are created by the localised source of excitation in combination with radiation boundary conditions at the two ends of the flow channels ($x = \pm l/2$). The remaining walls were set as sound reflecting boundary conditions.

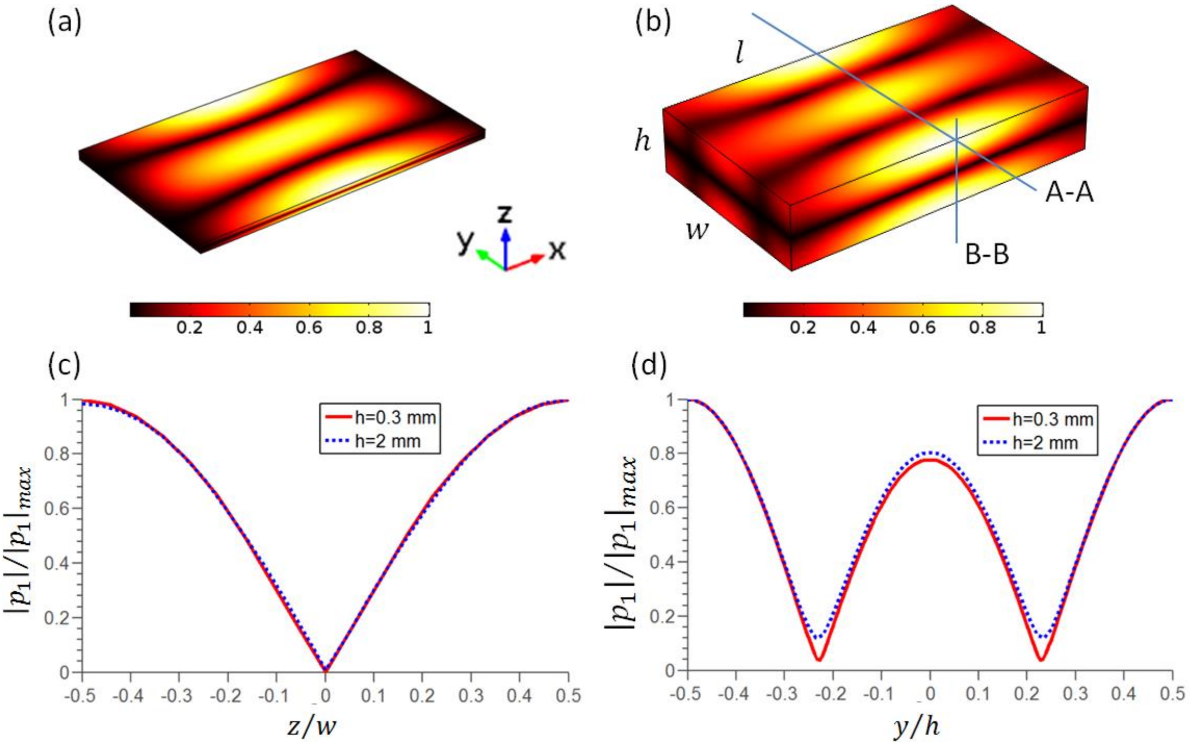

FIG. 2 (colour online). Simulated acoustic pressure distributions (normalised) in two models. (a) - (b) colour plots of the pressure distributions on the surfaces of the fluid channels with dimensions of $w = 6$ mm, $h = 0.3$ mm and $w = 6$ mm, $h = 2$ mm, respectively; (c) - (d) pressure distributions along lines B-B and A-A shown in (b). The origin of the coordinates in these models was set at the centre of the fluid channels such that the fluid channels are located within coordinates: $-l/2 \leq x \leq l/2, -w/2 \leq y \leq w/2, -h/2 \leq z \leq h/2$.

We showed previously that for the four-quadrant transducer-plane streaming in a resonant cavity the streaming pattern was largely insensitive to the pattern of wall accelerations used to create the resonance. We thus used the acceleration distribution used previously[34] of: $a_n = a_0 e^{ax^2+by^2}$ with $a_0 = 5.9 \times 10^4$ m·s$^{-2}$ and $a = b = -2.2 \times 10^5$ m$^{-2}$. These values match those used in our previous modelling where we demonstrated there that the results are not sensitive to these values. A frequency sweep study was firstly used to find the half-wave resonant frequency in the $z$ direction of these 3D fluid channels, looking for the frequency with maximum energy density in the fluid. The excitation used above created the required resonance in all the cases examined, shown in FIG. 2, where the acoustic pressure distributions on the surfaces of two models are presented. It can be seen that a similar standing wave field was established in both models. In addition to the main resonance in the $z$-direction, the acoustic pressure field in the $y$ direction has a one-wavelength standing wave variation. There is a smaller gradient in the $x$ direction resulting from a resonance formed by reflections from the plane-wave radiation boundary conditions at $x = \pm l/2$; Although these boundaries are formulated with the intention of transmitting acoustic energy, in a closed duct significant reflections do occur, and mimic the conditions we expect in the experimental device. Thus, the overall cavity mode in the device is a (1, 2, 1) mode. In each channel dimension shown in TABLE I, the (1, 2, 1) mode is found to show the similar distribution of acoustic field (FIG. 2). It will be shown later that the four-quadrant transducer-plane streaming pattern observed in thin-layered acoustofluidic particle manipulation devices[3, 34] and the modal Rayleigh-like streaming discussed below are a result of the $z$ and $y$ axis acoustic gradients of this particular cavity mode.

In a second step, the *limiting velocity method*, introduced by Nyborg[20], modified by Lee and Wang[21] and applied by Lei *et al.*[27, 34] for 3D simulations, was used to solve the acoustic streaming fields in these layered acoustofluidic devices. Driven by the limiting velocities, the COMSOL '*Creeping Flow*' interface was used to simulate the acoustic streaming fields, which approximates the fluid as incompressible and neglects inertial forces. The governing equations for the streaming velocities, $\boldsymbol{u_2}$, and the associated acoustic pressure fields, $p_2$, are

$$\nabla p_2 = \mu \nabla^2 \boldsymbol{u_2}, \tag{2a}$$

$$\nabla \cdot \boldsymbol{u_2} = 0, \tag{2b}$$

where $\mu$ is the dynamic viscosity of the fluid. For the models shown in this paper, the limiting velocity equations on the driving boundaries ($z = \pm h/2$) take the form:

$$\begin{aligned} u_L = -\frac{1}{4\omega} Re \Bigg\{ u_1 \frac{du_1^*}{dx} + v_1 \frac{du_1^*}{dy} \\ + u_1^* \left[ (2+i)(\frac{du_1}{dx} + \frac{dv_1}{dy} + \frac{dw_1}{dz}) - (2+3i)\frac{dw_1}{dz} \right] \Bigg\}, \end{aligned} \tag{3a}$$

$$\begin{aligned} v_L = -\frac{1}{4\omega} Re \Bigg\{ u_1 \frac{dv_1^*}{dx} + v_1 \frac{dv_1^*}{dy} \\ + v_1^* \left[ (2+i)(\frac{du_1}{dx} + \frac{dv_1}{dy} + \frac{dw_1}{dz}) - (2+3i)\frac{dw_1}{dz} \right] \Bigg\}, \end{aligned} \tag{3b}$$

where $u_L$ and $v_L$ are the two components of limiting velocities on a driving boundary, and $u_1, v_1$ and $w_1$ are components of the complex acoustic velocity vector, $\boldsymbol{u_1}$ (the subscript helps distinguish this first order term from the second order streaming velocity, $\boldsymbol{u_2}$), along the coordinates $x$, $y$ and $z$, respectively. The superscript, $*$, represents the complex conjugate. More detailed description of this method can be found in Lei *et al.*[34] The bottom and top walls ($z = \pm h/2$) were considered as limiting velocity boundary conditions while the remaining walls were no-slip boundary conditions unless otherwise stated. All the results presented in this paper are for fluid channels with $w = 6$ mm and $l = 10$ mm.

In layered acoustofluidic particle manipulation devices excited in the mode shown in FIG. 2, on the top and bottom surfaces ($z = \pm h/2$), $du_1/dx$ can be neglected[34] as it has low contribution, compared to the other two acoustic gradients in the bulk of the fluid channel, to the divergence of the acoustic velocity vector. Therefore, the relative importance of the remaining terms in the limiting velocity equations will depend on the ratio of velocity gradients,

$$r = \frac{dw_1}{dz} \Big/ \frac{dv_1}{dy}. \tag{4}$$

We previously showed how the individual terms of the limiting velocity equation were proportional to the active and reactive sound intensity fields[27, 34]. Thus for $r \gg 1$, the limiting velocity field typically has a similar pattern to the active intensity field, while for $r \ll 1$, the limiting velocity field is dominated by the reactive intensity fields. More detailed explanations for this can be found in the Supplementary Material at [URL will be inserted by AIP]. We show in the Supplementary Material (at [URL will be inserted by AIP]) that, in a resonant cavity shown in FIG. 2, $r$ can be approximated as

$$r \approx \left(\frac{w}{2h}\right)^2 . \tag{5}$$

This means that the ratio of the significant acoustic velocity gradients, which determines which part of the complex acoustic intensity field dominates the limiting velocity field, is dependent on the aspect ratio of the fluid channel cross-section. Our numerical models show that the approximation of Equation (5) is accurate to within an error of 2% in all the cases shown in TABLE I. This relationship implies that a change in the aspect ratio of the fluid channel cross sections can alter the acoustic streaming field from one pattern to another due to rotational and irrotational properties of the active intensity and reactive intensity fields respectively, and this is investigated further in the modelled 3D acoustic streaming fields shown below. The modelled results shown below are in devices where $w = 6$ mm unless otherwise stated.

The modelled active and reactive sound intensity fields at the bottom surface of the fluid channels ($z = -h/2$) for the pressure distributions shown in FIG. 2 are plotted in FIG. 3 (a) and FIG. 3 (b), respectively. It can be seen that the active (mean) intensity fields on the limiting velocity boundaries have a regular four-quadrant vortex pattern while the reactive intensity field is irrotational, diverging from the pressure maxima and concentrating at the pressure minima. FIG. 3 (c)-(g) plots the limiting velocity vector fields for five models with different fluid channel heights. It is clear that, for the first model where $r \gg 1$ ($h = 0.2$ mm), shown in FIG. 3 (c), the limiting velocity field has a similar vortex pattern to that shown in FIG. 3 (a) demonstrating that, as predicted, it is dominated by the active sound intensity field. In FIG. 3 (d)-(f), the aspect ratio, and hence $r$, becomes steadily smaller and the predicted transition towards a pattern dominated by the vortex pattern of the reactive intensity field is seen.

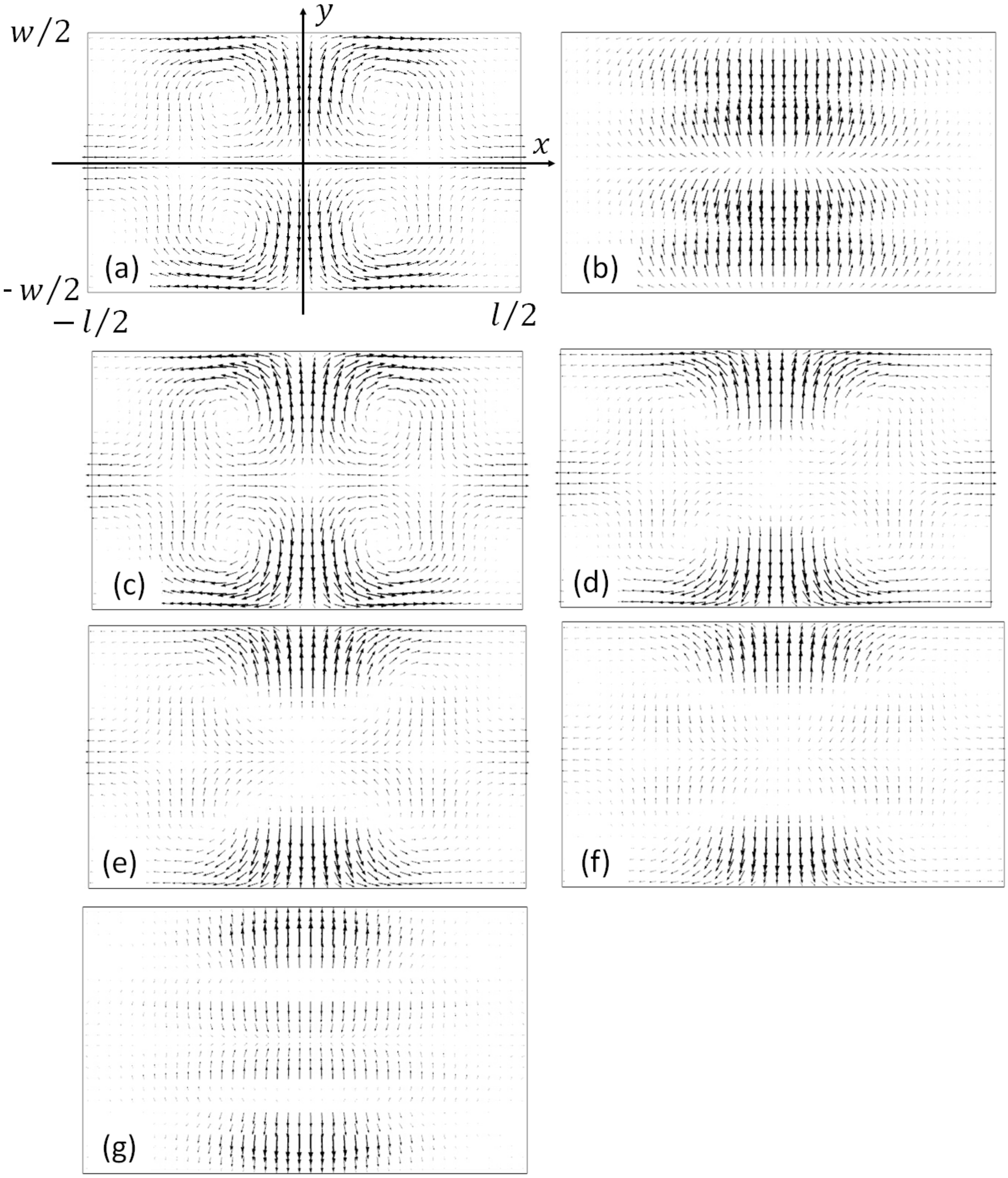

FIG. 3 Vector plots showing the relation between the active and reactive components of sound intensity and the limiting velocity fields on the bottom surface of the 3D fluid channels ($z = -h/2$) for various aspect ratios of their $yz$ cross-sections ($w = 6$ mm, $l = 10$ mm): (a) active (mean) intensity field; (b) reactive intensity field; (c) - (g) limiting velocity fields for respectively: $h = 0.2$ mm; $h = 0.5$ mm; $h = 0.8$ mm, $h = 1$ mm and $h = 2$ mm, where the length of arrows shows normalised magnitudes.

For the different channel aspect ratios, qualitatively different vortex patterns are also seen in the streaming velocity fields due to varying contribution of the active and reactive intensity fields discussed above. FIG. 4 plots the simulated in-plane acoustic streaming fields on the central $xy$ pressure nodal plane ($z = 0$) of the fluid channels for the five models illustrated above. It can be seen that a well-defined four-quadrant transducer-plane streaming pattern[3, 34] is only observed in FIG. 4 (a), where $h = 0.2$ mm. With the increase of $h$ and the related decrease in $r$, the in-plane acoustic streaming vortices transition towards modal Rayleigh-like streaming (see discussion below), as seen in FIG. 4 (e). In this case, the in-plane acoustic streaming field was found to be nearly irrotational, as the limiting velocities for this case are dominated by the irrotational reactive intensity field.

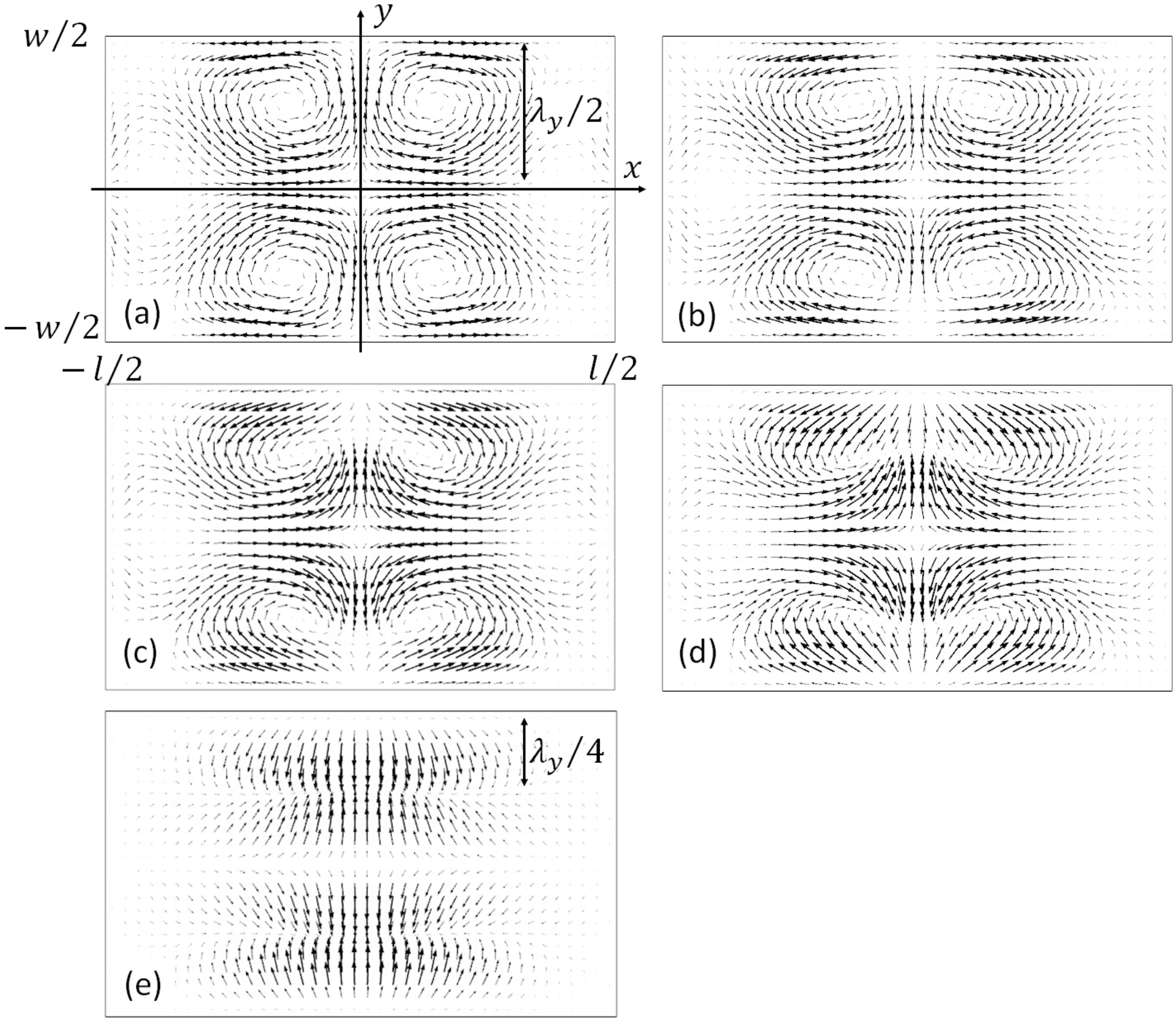

FIG. 4 Vector plots of the modelled acoustic streaming fields in the central $xy$ plane ($z = 0$) of the fluid channels ($w = 6$ mm, $l = 10$ mm) for: (a) $h = 0.2$ mm; (b) $h = 0.5$ mm; (c) $h = 0.8$ mm; (d) $h = 1$ mm; and (e) $h = 2$ mm, where the maximum streaming velocities shown in models (a) - (e) are respectively 0.14, 1.08, 2.03, 2.83, 12.38 μm/s, which are obtained from an acoustic pressure amplitude of approximately 0.6 MPa. A transition from transducer plane streaming to modal Rayleigh-like streaming is seen with deeper channels. Limiting velocities on the side walls are set to zero for simplicity.

In addition, the acoustic streaming fields on the central $yz$ cross-section of the fluid channel ($x = 0$) for all these five models are plotted in FIG. 5. It can be seen that for the model $h = 0.2$ mm, where the transducer-plane streaming vortex pattern is observed, the streaming field is similar at all heights of the fluid channel ($z$-direction) as all the velocities are parallel to the bottom wall (limiting velocity boundary), FIG. 5 (a). With the increase of $h$ to 0.5 mm, FIG. 5 (b), the streaming velocities are non-uniform in the $z$-direction near the channel centre

($y = 0$) and the side walls ($y = \pm w/2$), where the pressure antinodes for the one-wave mode in the $y$-direction are positioned. Further, small vortices appear and increase in size in these areas with the further increase of $h$, forming well developed modal Rayleigh-like streaming when the fluid height $h = 2$ mm, FIG. 5 (e).

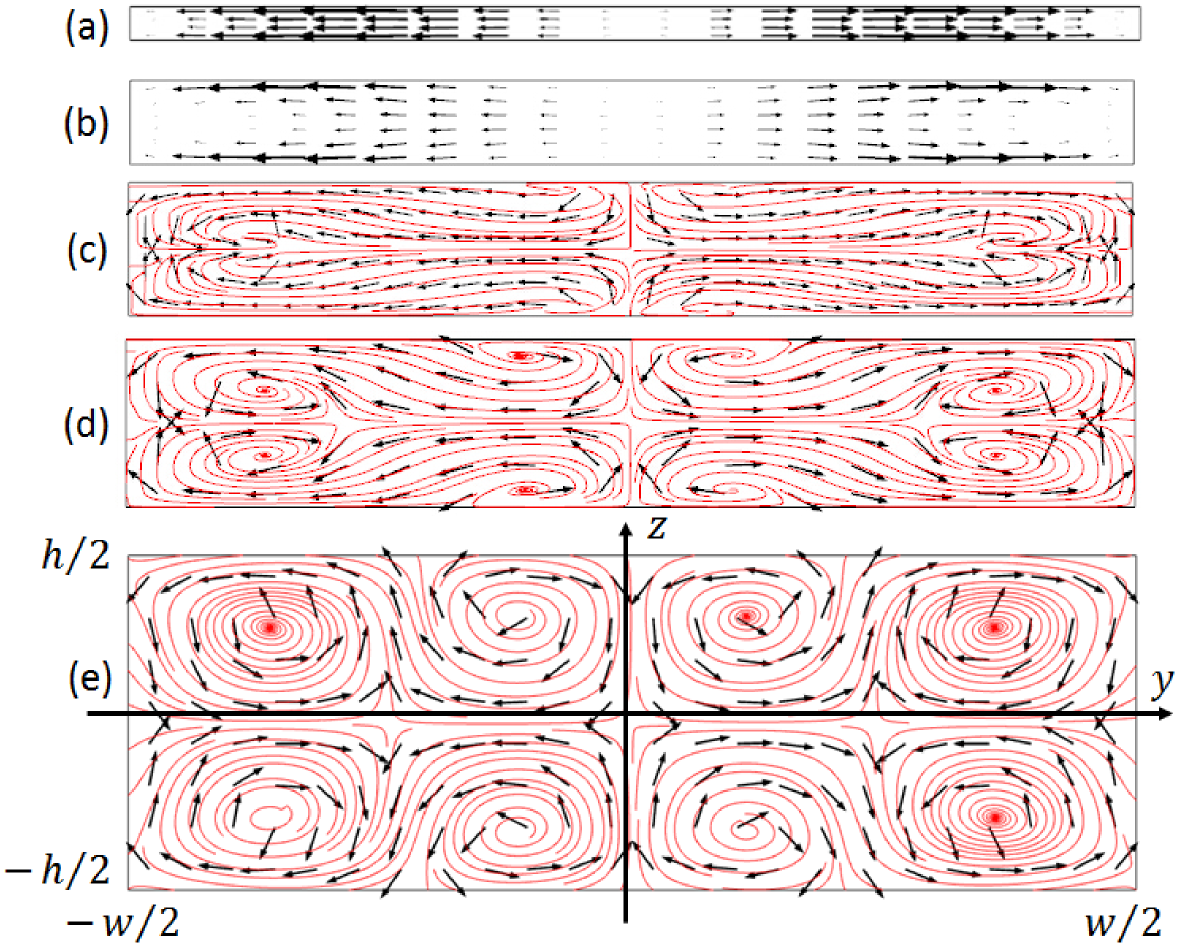

FIG. 5 (colour online) Vector plots of the modelled acoustic streaming fields in the central $yz$ plane ($x = 0$) of the fluid channels ($w = 6$ mm, $l = 10$ mm): (a) $h = 0.2$ mm; (b) $h = 0.5$ mm; (c) $h = 0.8$ mm; (d) $h = 1$ mm; and (e) $h = 2$ mm, where the arrows show streaming velocity fields and the red lines show the streamlines. The arrows in (c) – (e) have been normalised in order to show clearly the velocity vectors. A transition from transducer plane streaming to modal Rayleigh-like streaming is seen with deeper channels. Limiting velocities on the side walls are set to zero for simplicity.

We refer to the vortex pattern seen FIG. 4 (e) and FIG. 5 (e) as "modal Rayleigh-like streaming" as it has a similar pattern to the classical Rayleigh streaming pattern, four vortex pairs per wavelength along the acoustic standing wave. However, it is "Rayleigh-like" as this streaming pattern depends on the resonant cavity mode excited in the 3D rectangular cavities rather than a simple one-dimensional acoustic standing wave. To clarify, we can take the model $h = 2$ mm as an example: the one-wavelength variation of acoustic pressure field generated in the $y$-direction of the fluid channel was excited at the resonant cavity mode at frequency $f \approx 0.45$ MHz, where the main standing wave field is established in the $z$-direction; Thus the observed streaming rolls have a width related to the cavity resonance, and its characteristic wavelength rather than the wavelength of sound in an unbounded medium as seen in conventional Rayleigh streaming. We show below experimental demonstration of both transducer-plane streaming patterns and modal Rayleigh-like streaming patterns in layered acoustofluidic particle manipulation devices with different channel aspect ratios. It should be emphasised that in this section we have not including the driving forces resulting from limiting velocities on the $y = \pm 3$ mm sidewalls; this has simplified the streaming fields to help show the transition we wish to illustrate, however a model of the case when limiting velocities on all boundaries are included can be seen below.

## III. EXPERIMENTAL

The experiments were conducted in glass capillaries, which have been widely used to form small acoustofluidic particle manipulation systems[3, 34, 47-52]. In this paper, measurements performed in two glass capillaries are presented to show respectively the transducer-plane streaming and the *modal Rayleigh-like streaming* in layered acoustofluidic particle manipulation devices. The two glass capillaries (Vitrocom, USA) have inner dimensions of $0.3 \times 6$ mm$^2$ and $2 \times 6$ mm$^2$ ($h \times w$) and wall thicknesses of 0.3 mm and 0.8 mm, respectively. A function generator (TTi, TG1304 Programmable) drives an RF amplifier (ENI, Model 240L) that powers the transducer, with a signal monitored by an oscilloscope (Agilent Technologies, DOS1102B Digital Storage Oscilloscope). An Olympus BXFM epi-fluorescent microscope with a *pixelfly* dual-frame CCD camera was used to image the device. The experimental measurements can be split into the following steps:

- Impedance measurements were firstly used to identify the resonant frequencies in these two devices;
- 10 µm particles were used to characterise the acoustic fields in the capillaries by examining acoustic radiation forces on them;
- Micro-particle-image-velocimetry (*µpiv*) measurements of 1 µm polystyrene tracer particles (Fluoresbrite microspheres, Polysciences Inc.) were performed to characterise the acoustic streaming fields;
- The *voltage drop method*[53], based on the balance of the buoyancy force and acoustic radiation force on 10 µm particles, was used to estimate the acoustic pressure magnitudes in the fluid channels.

TABLE II Experimental parameters

| Quantity | Abbreviation | Value | Unit |
|---|---|---|---|
| First capillary size | $l \times h \times w$ | $80 \times 6 \times 0.3$ | mm$^3$ |
| Second capillary size | $l \times h \times w$ | $80 \times 6 \times 2$ | mm$^3$ |
| Dimension of transducer | $l \times h \times w$ | $3 \times 3 \times 1$ | mm$^3$ |
| Fluid density | $\rho_0$ | 998 | kg·m$^{-3}$ |
| Particle radius | $r$ | 1 | µm |
| Dynamic viscosity of fluid | µ | 0.893 | mPa·s |
| Speed of sound in fluid | $c$ | 1480 | m·s$^{-1}$ |

More detailed information regarding the device configuration, the *µpiv* setup and the process of measuring and characterising the acoustic streaming fields can be found in our previous work[34]. It was found (see Fig. 2 in supplementary material at [URL will be inserted by AIP]) that most of the 10 µm particles used to characterise the fields were aligned to two planes in the fluid channel, $y \approx \pm 1.2$ mm, suggesting that, in addition to the primary half-wave standing wave in the $z$-direction of the fluid channels, acoustic pressure fields in the $y$-

direction of the fluid channels also have one-wave variations. This confirms that the devices were excited in the (1, 2, 1,) cavity mode matching the modelling above. All the parameters for fluid and microparticles are shown in TABLE II.

FIG. 6 shows the measured acoustic streaming fields in the first glass capillary ($h = 0.3$ mm), in which the acoustic streaming fields on two $xy$ planes, respectively $z = 0$ and $z = 0.45h$, are presented. It can be seen that, in this low aspect ratio device, four-quadrant transducer-plane streaming pattern is seen on both planes with the same orientation on each vortex, which compares well with that shown in FIG. 4 (a) and FIG. 5 (a). However, in the second glass capillary ($h = 2$ mm), instead of uniform transducer-plane streaming pattern along the height of the fluid channel, vortices on the $yz$ cross-sections were observed.

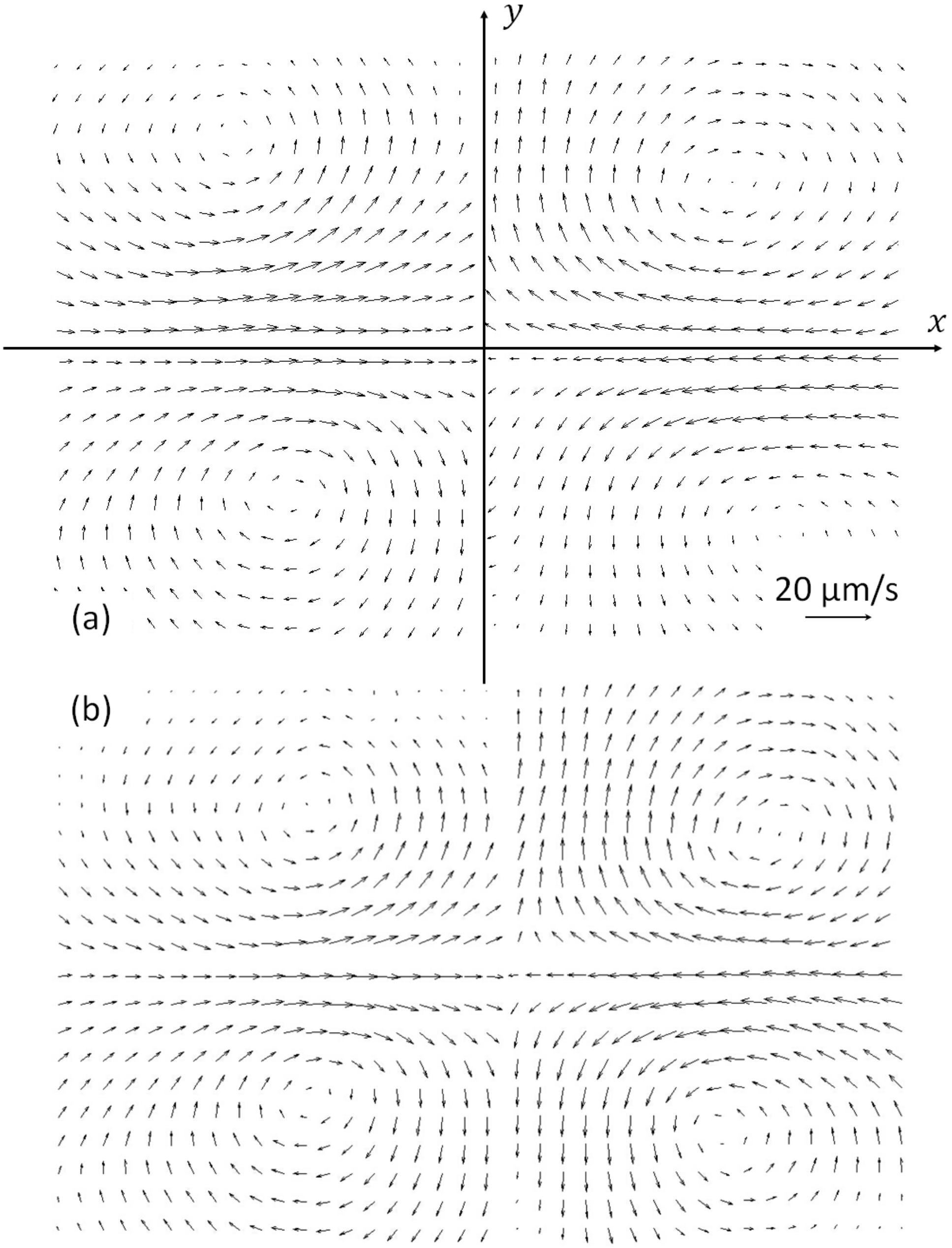

FIG. 6 Experimentally measured streaming field near device centre (field of view:$1.8 \text{ mm} \le x \le 1.8 \text{ mm}, -1 \text{ mm} \le y \le 1 \text{ mm}$) in the first glass capillary ($h = 0.3$ mm and $w = 6$ mm). (a) on plane $z = 0.4h$; and (b) on plane $z = 0$. The streaming velocities presented are obtained from an acoustic pressure amplitude of approximately 0.8 MPa.

The measured acoustic streaming fields near the centre of the second device are shown in FIG. 7, and correspond to modal Rayleigh-like streaming. The acoustic streaming fields on two $xy$ planes, $z = 0$ and $z = 0.45h$, are presented in order to compare with those measured in the first device. It is clear that there is no in-plane streaming vortex in these $xy$ planes and that there must be vortices in the $yz$ cross-sections (see FIG. 8 (c)) to complete the flow field (compare these results to the dashed box in FIG. 8 (d)). The size of these vortices is approximately one-quarter of the fluid channel width, $w/4$, which is much bigger than the size of classical Rayleigh streaming vortices, $h/2$, which would be caused from the main half-wave resonance in the $z$-direction. It can be seen that the measured acoustic streaming patterns in the central area compare well with those predicted in FIG. 4 (e) and FIG. 5 (e). However, in addition to the $y$-directed flows that form the pattern we are describing as modal Rayleigh-like streaming, there are some $x$-components to the flow in the top plane shown in FIG. 7 (a). These are also seen in a smaller way in the model (FIG. 3 (g)) and result from the gradient of energy density towards the central maximum. We hypothesise that the boundary conditions in the experiments cause larger gradients than those modelled and hence the larger $x$-component of the velocity vectors.

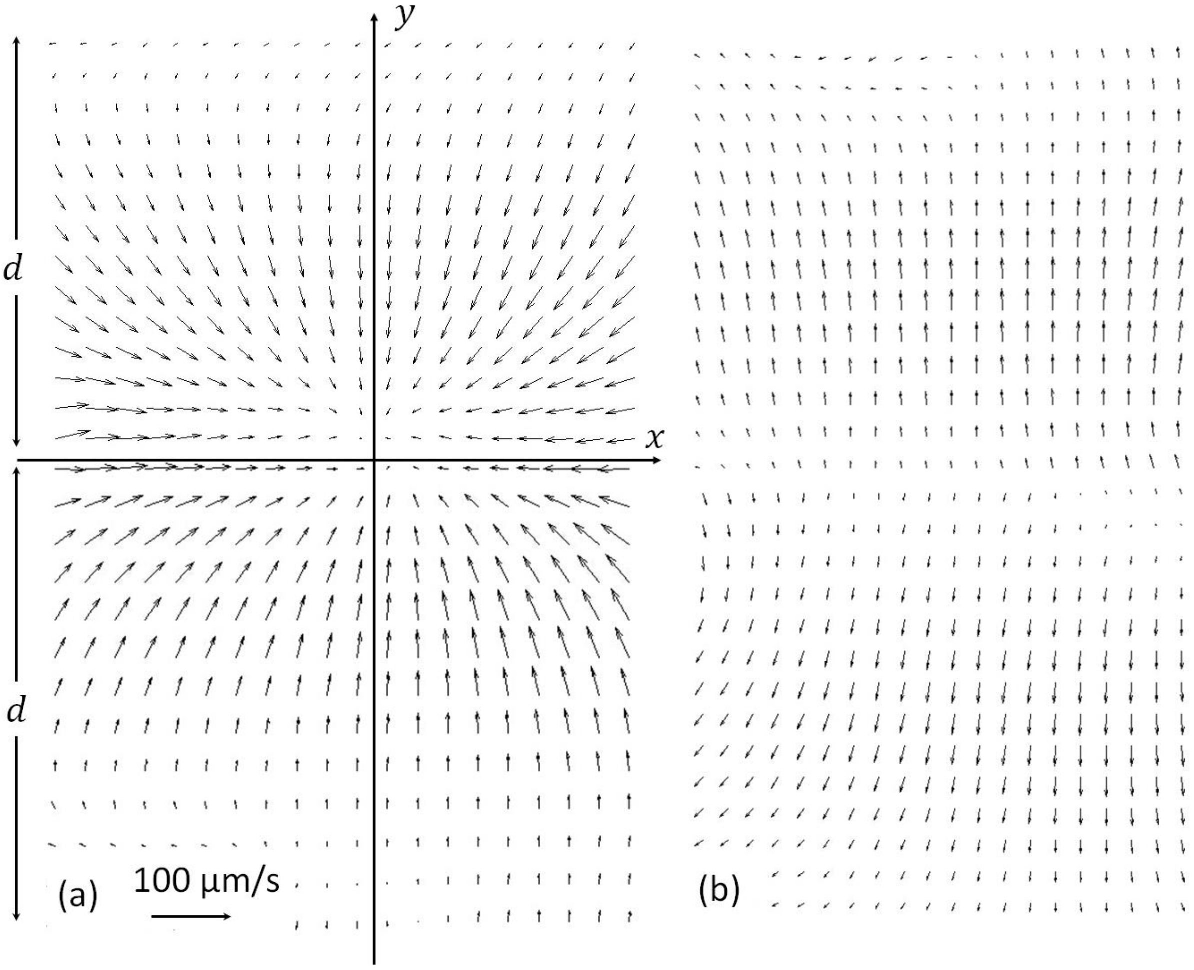

FIG. 7 Experimentally measured streaming field near device centre (field of view: $-1$ mm $\leq x \leq 1$ mm, $-1.5$ mm $\leq y \leq 1.5$ mm) in the second glass capillary ($h = 2$ mm and $w = 6$ mm). (a) on plane $z = 0.45h$; and (b) on plane $z = 0$, where $d$ shows the size of the modal Rayleigh-like streaming vortices. The streaming velocities presented are obtained from an acoustic pressure amplitude of approximately 0.68 MPa.

In order to accurately accord with experimental results the limiting velocities at the side walls ($y = \pm w/2$) were included in the model results shown in FIG. 5 (e). This creates a streaming field that has contributions from both Rayleigh streaming (driven by the sidewalls) and modal Rayleigh-like streaming (driven by the upper and lower channel boundaries), resulting in the streaming pattern shown in FIG. 8 (d). This pattern has extra vortices, which accords well with the measured streaming fields shown in FIG. 8 (a)-(b).

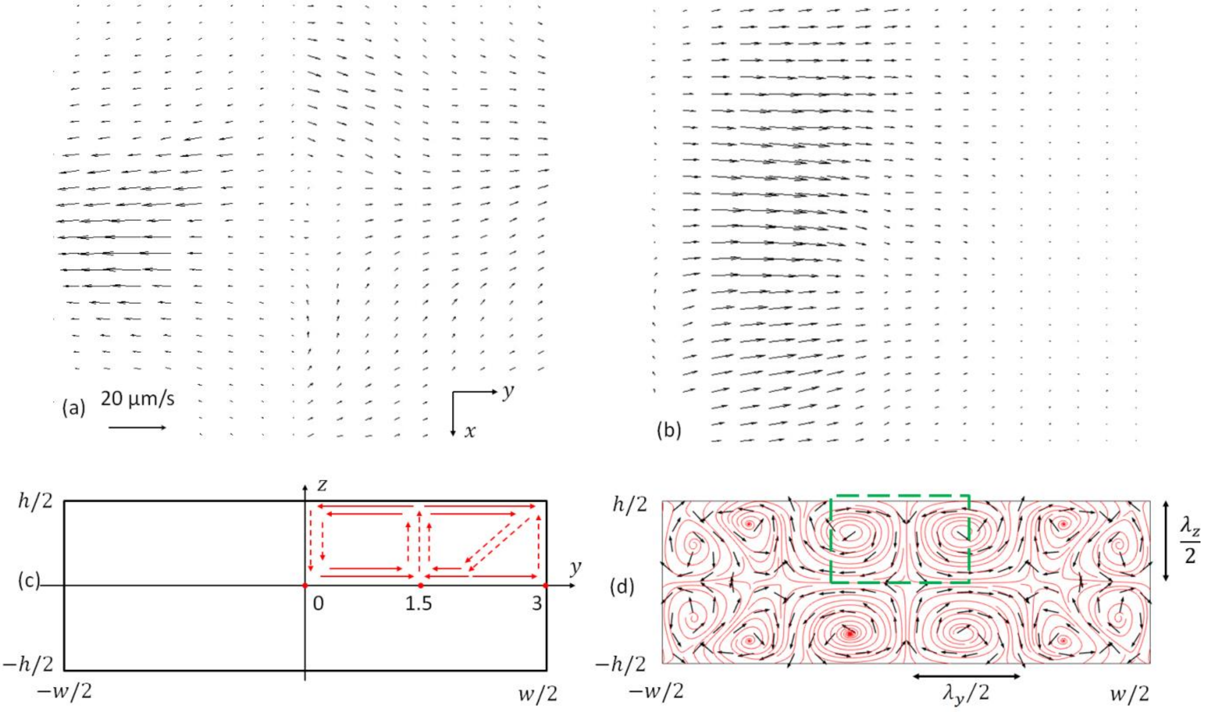

FIG. 8 (Colour online). (a),(b) Measured streaming field near the side wall (field of view: $-1\ \text{mm} \le x \le 1\ \text{mm},\ 1.5\ \text{mm} \le y \le 3\ \text{mm}$) in the second glass capillary on the plane $z = 0$ and the plane $z = 0.45h$ respectively; (c) schematic representation of the acoustic streaming vortices in the whole channel, where solid and dashed arrows show the measured and deduced streaming fields, respectively; (d) the modelled acoustic streaming field including Rayleigh streaming driven by limiting velocities at the side boundaries ($y = \pm w/2$). The vortices identified by the green dashed line in (d) are discussed in the text. ($w = 6$ mm, $h = 2$ mm, $l =$ 80 mm). The streaming velocities presented in (a) - (b) are obtained from an acoustic pressure amplitude of approximately 0.68 MPa.

In the case of boundary-driven streaming, it is acoustic attenuation in the viscous boundary layer, forming Reynolds stress force fields, that induces streaming vortices in that thin layer. The fluid movement inside the viscous boundary layer induces outer streaming vortices in the bulk of the fluid. This means that the maximum streaming velocities will be no more than a few multiples of $\delta_v$ away from the wall. However, in some regions of the second capillary ($h = 2$ mm), the maximum streaming velocity was found to be further from the boundaries (about 50% higher than at the boundary at a distance of ~ 250µm), which is not consistent with our modelling. Initial modelling suggests that this is due to the energy loss in the bulk of the fluid producing Reynolds stress forces that drive non-negligible Eckart type streaming velocities in the volume of the fluid channel additional to the dominant boundary-driven streaming. This effect is also likely to be observable in acoustofluidic devices with thinner layers, in which the active intensity flow (which generates Eckart streaming) has a significant contribution to the limiting velocity fields generating the boundary-driven streaming. The effects of Eckart streaming on the overall streaming fields in planar acoustofluidic devices will be further examined in future work.

## IV. CONCLUSION

The acoustic streaming patterns in 3D rectangular fluid cavities, where a (1, 2, 1) resonant cavity mode was excited, have been investigated. It has been shown that the ratio of the two dominant acoustic velocity gradients, governed by the aspect ratio of the channel, determines the driving terms of the acoustic streaming fields. These driving terms can be identified as having vortex patterns matching those of the active and reactive components of the complex streaming field. This provides a basis for predicting the acoustic streaming patterns in layered acoustofluidic devices, for particle and cell manipulation.

In addition to the well-known Rayleigh streaming and the transducer-plane streaming recently described, a third type of boundary-driven streaming, *modal Rayleigh-like streaming*, has been experimentally observed and numerically verified. This streaming field is driven by limiting velocities that have the same pattern as classical Rayleigh streaming but it depends on the resonant cavity mode excited in a 3D cavity rather than simple one-dimensional standing wave patterns. Since cavity modes can have much larger characteristic wavelengths than a 1D mode, the resulting streaming patterns can have much larger vortex sizes than those found in classical Rayleigh streaming.

The modelled and experimental results demonstrate that the acoustic streaming patterns in layered half-wave acoustofluidic particle manipulation devices excited in the resonant cavity modes can be split into three regions, bounded approximately by:

(1) $h/w \leq 1/20$, transducer-plane streaming;

(2) $1/20 < h/w < 1/3$, transducer-plane streaming & modal Rayleigh-like streaming; and

(3) $h/w \geq 1/3$, modal Rayleigh-like streaming.

The cases considered above focus on the boundary-driven streaming in layered acoustofluidic systems, without considering the Eckart type streaming generated from the energy dissipation from the bulk of the fluid. It would be interesting to investigate the contribution of boundary-driven streaming to the overall streaming field in acoustofluidic systems in which path lengths are larger in comparison with acoustic wavelengths and where Eckart type streaming has a comparable contribution.

## ACKNOWLEDGEMENTS

This work was support by the China Scholarship Council (CSC) and the EPSRC under the Sonotweezers project (EP/G012075/1) and Fellowship EP/L025035/1.

Models used to generate the simulation data, and experimental data supporting this study are openly available from the University of Southampton repository at http://dx.doi.org/10.5258/SOTON/xxxxx.

## REFERENCES

1. H. Bruus, J. Dual, J. Hawkes, M. Hill, T. Laurell, J. Nilsson, S. Radel, S. Sadhal and M. Wiklund, "Forthcoming Lab on a Chip tutorial series on acoustofluidics: Acoustofluidics-

exploiting ultrasonic standing wave forces and acoustic streaming in microfluidic systems for cell and particle manipulation," Lab Chip **11**, 3579 (2011).
2. M. Wiklund, R. Green and M. Ohlin, "Acoustofluidics 14: Applications of acoustic streaming in microfluidic devices," Lab Chip **12**, 2438 (2012).
3. B. Hammarstrom, T. Laurell and J. Nilsson, "Seed particle-enabled acoustic trapping of bacteria and nanoparticles in continuous flow systems," Lab Chip **12**, 4296 (2012).
4. B. Hammarstrom, B. Nilson, T. Laurell, J. Nilsson and S. Ekstrom, "Acoustic Trapping for Bacteria Identification in Positive Blood Cultures with MALDI-TOF MS," Analytical chemistry **86**, 10560 (2014).
5. S. K. Chung and S. K. Cho, "On-chip manipulation of objects using mobile oscillating bubbles," J Micromech Microeng **18**, (2008).
6. B. R. Lutz, J. Chen and D. T. Schwartz, "Hydrodynamic tweezers: 1. Noncontact trapping of single cells using steady streaming microeddies," Analytical chemistry **78**, 5429 (2006).
7. S. Yazdi and A. M. Ardekani, "Bacterial aggregation and biofilm formation in a vortical flow," Biomicrofluidics **6**, (2012).
8. M. Antfolk, P. B. Muller, P. Augustsson, H. Bruus and T. Laurell, "Focusing of sub-micrometer particles and bacteria enabled by two-dimensional acoustophoresis," Lab Chip **14**, 2791 (2014).
9. C. Devendran, I. Gralinski and A. Neild, "Separation of particles using acoustic streaming and radiation forces in an open microfluidic channel," Microfluidics and Nanofluidics 1 (2014).
10. C. Eckart, "Vortices and streams caused by sound waves," Phys. Rev. **73**, 68 (1947).
11. L. Y. Yeo and J. R. Friend, "Surface Acoustic Wave Microfluidics," Annu Rev Fluid Mech **46**, 379 (2014).
12. X. Y. Ding, P. Li, S. C. S. Lin, Z. S. Stratton, N. Nama, F. Guo, D. Slotcavage, X. L. Mao, J. J. Shi, F. Costanzo and T. J. Huang, "Surface acoustic wave microfluidics," Lab Chip **13**, 3626 (2013).
13. H. Schlichting, "Berechnung ebener periodischer Grenzschichtstromungen (Calculation of plane periodic boundary layer streaming)," Physikalische Zeitschrift **33**, 327 (1932).
14. Lord Rayleigh, "On the circulation of air observed in Kundt's tube, and on some allied acoustical problems.," Phil. Trans. **175**, 1 (1883).
15. Lord Rayleigh, *The theory of sound* (Dover publications, New York, 1896).
16. P. J. Westervelt, "The theory of steady rotational flow generated by a sound field," J. Acoust. Soc. Am. **25**, 60 (1952).
17. W. L. Nyborg, "Acoustic streaming due to attenuated plane waves," J. Acoust. Soc. Am. **25**, 68 (1953).
18. S. Boluriaan and P. J. Morris, "Acoustic streaming: from Rayleigh to today," Aeroacoustics **2 (3&4)**, 255 (2003).
19. J. Lighthill, "Acoustic Streaming," J Sound Vib **61**, 391 (1978).
20. W. L. Nyborg, "Acoustic streaming near a boundary," J. Acoust. Soc. Am. **30**, 329 (1958).
21. C. P. Lee and T. G. Wang, "Near-Boundary Streaming around a Small Sphere Due to 2 Orthogonal Standing Waves," J Acoust Soc Am **85**, 1081 (1989).
22. M. F. Hamilton, Y. A. Ilinskii and E. A. Zabolotskaya, "Acoustic streaming generated by standing waves in two-dimensional channels of arbitrary width," J Acoust Soc Am **113**, 153 (2003).
23. M. K. Aktas and B. Farouk, "Numerical simulation of acoustic streaming generated by finite-amplitude resonant oscillations in an enclosure," J Acoust Soc Am **116**, 2822 (2004).

24. R. Barnkob, P. Augustsson, T. Laurell and H. Bruus, "Acoustic radiation- and streaming-induced microparticle velocities determined by microparticle image velocimetry in an ultrasound symmetry plane," Phys Rev E **86**, (2012).
25. P. B. Muller, R. Barnkob, M. J. H. Jensen and H. Bruus, "A numerical study of microparticle acoustophoresis driven by acoustic radiation forces and streaming-induced drag forces," Lab Chip **12**, 4617 (2012).
26. P. B. Muller, M. Rossi, A. G. Marin, R. Barnkob, P. Augustsson, T. Laurell, C. J. Kahler and H. Bruus, "Ultrasound-induced acoustophoretic motion of microparticles in three dimensions," Phys Rev E **88**, (2013).
27. J. Lei, M. Hill and P. Glynne-Jones, "Numerical simulation of 3D boundary-driven acoustic streaming in microfluidic devices," Lab Chip **14**, 532 (2013).
28. J. Lei, P. Glynne-Jones and M. Hill, *Effects of surface profile on a boundary-driven acoustic streaming field* (iiav, Beijing, China, 2014).
29. S. S. Sadhal, "Acoustofluidics 13: Analysis of acoustic streaming by perturbation methods Foreword," Lab Chip **12**, 2292 (2012).
30. S. M. Hagsater, T. G. Jensen, H. Bruus and J. P. Kutter, "Acoustic resonances in microfluidic chips: full-image micro-PIV experiments and numerical simulations," Lab Chip **7**, 1336 (2007).
31. S. M. Hagsater, A. Lenshof, P. Skafte-Pedersen, J. P. Kutter, T. Laurell and H. Bruus, "Acoustic resonances in straight micro channels: Beyond the 1D-approximation," Lab Chip **8**, 1178 (2008).
32. N. Nama, P. H. Huang, T. J. Huang and F. Costanzo, "Investigation of acoustic streaming patterns around oscillating sharp edges," Lab Chip **14**, 2824 (2014).
33. M. Ovchinnikov, J. B. Zhou and S. Yalamanchili, "Acoustic streaming of a sharp edge," J Acoust Soc Am **136**, 22 (2014).
34. J. Lei, P. Glynne-Jones and M. Hill, "Acoustic streaming in the transducer plane in ultrasonic particle manipulation devices," Lab Chip **13**, 2133 (2013).
35. F.J.Fahy, *Sound intensity* (E & FN Spon, London, 1995).
36. *COMSOL Multiphysics 4.4* (COMSOL Multiphysics 4.4, http://www.comsol.com/, 2014).
37. A. Lenshof, M. Evander, T. Laurell and J. Nilsson, "Acoustofluidics 5: Building microfluidic acoustic resonators," Lab Chip **12**, 684 (2012).
38. P. Glynne-Jones, R. J. Boltryk and M. Hill, "Acoustofluidics 9: Modelling and applications of planar resonant devices for acoustic particle manipulation," Lab Chip **12**, 1417 (2012).
39. J. J. Hawkes and W. T. Coakley, "Force field particle filter, combining ultrasound standing waves and laminar flow," Sensor Actuat B-Chem **75**, 213 (2001).
40. J. J. Hawkes, R. W. Barber, D. R. Emerson and W. T. Coakley, "Continuous cell washing and mixing driven by an ultrasound standing wave within a microfluidic channel," Lab Chip **4**, 446 (2004).
41. M. Hill, R. J. Townsend and N. R. Harris, "Modelling for the robust design of layered resonators for ultrasonic particle manipulation," Ultrasonics **48**, 521 (2008).
42. P. Augustsson and T. Laurell, "Acoustofluidics 11: Affinity specific extraction and sample decomplexing using continuous flow acoustophoresis," Lab Chip **12**, 1742 (2012).
43. M. Evander and J. Nilsson, "Acoustofluidics 20: Applications in acoustic trapping," Lab Chip **12**, 4667 (2012).
44. A. Lenshof, C. Magnusson and T. Laurell, "Acoustofluidics 8: Applications of acoustophoresis in continuous flow microsystems," Lab Chip **12**, 1210 (2012).

45. J. F. Spengler, W. T. Coakley and K. T. Christensen, "Microstreaming effects on particle concentration in an ultrasonic standing wave," Aiche Journal **49**, 2773 (2003).

46. Y. Q. Qiu, H. Wang, C. E. M. Demore, D. A. Hughes, P. Glynne-Jones, S. Gebhardt, A. Bolhovitins, R. Poltarjonoks, K. Weijer, A. Schonecker, M. Hill and S. Cochran, "Acoustic Devices for Particle and Cell Manipulation and Sensing," Sensors-Basel **14**, 14806 (2014).

47. M. K. Araz, C. H. Lee and A. Lal, "Ultrasonic separation in microfluidic capillaries," Ultrason 1066 (2003).

48. G. Goddard and G. Kaduchak, "Ultrasonic particle concentration in a line-driven cylindrical tube," J Acoust Soc Am **117**, 3440 (2005).

49. M. Wiklund and H. M. Hertz, "Ultrasonic enhancement of bead-based bioaffinity assays," Lab Chip **6**, 1279 (2006).

50. P. P. A. Suthanthiraraj, M. E. Piyasena, T. A. Woods, M. A. Naivar, G. P. Lopez and S. W. Graves, "One-dimensional acoustic standing waves in rectangular channels for flow cytometry," Methods **57**, 259 (2012).

51. J. E. Prest, B. J. Treves Brown, P. R. Fielden, S. J. Wilkinson and J. J. Hawkes, "Scaling-up ultrasound standing wave enhanced sedimentation filters," Ultrasonics (2014).

52. R. I. Jepras, D. J. Clarke and W. T. Coakley, "Agglutination of Legionella-Pneumophila by Antiserum Is Accelerated in an Ultrasonic Standing Wave," J Immunol Methods **120**, 201 (1989).

53. J. F. Spengler, M. Jekel, K. T. Christensen, R. J. Adrian, J. J. Hawkes and W. T. Coakley, "Observation of yeast cell movement and aggregation in a small-scale MHz-ultrasonic standing wave field," Bioseparation **9**, 329 (2000).

# References

1. Mitchell, P., *Microfluidics - downsizing large-scale biology.* Nature Biotechnology, 2001. **19**(8): p. 717-721.
2. Stone, H.A. and S. Kim, *Microfluidics: Basic issues, applications, and challenges.* Aiche Journal, 2001. **47**(6): p. 1250-1254.
3. Auroux, P.A., et al., *Micro total analysis systems. 2. Analytical standard operations and applications.* Analytical Chemistry, 2002. **74**(12): p. 2637-2652.
4. Beebe, D.J., G.A. Mensing, and G.M. Walker, *Physics and applications of microfluidics in biology.* Annual Review of Biomedical Engineering, 2002. **4**: p. 261-286.
5. Reyes, D.R., et al., *Micro total analysis systems. 1. Introduction, theory, and technology.* Analytical Chemistry, 2002. **74**(12): p. 2623-2636.
6. Andersson, H. and A. van den Berg, *Microfluidic devices for cellomics: a review.* Sensors and Actuators B-Chemical, 2003. **92**(3): p. 315-325.
7. Dittrich, P.S. and A. Manz, *Lab-on-a-chip: microfluidics in drug discovery.* Nature Reviews Drug Discovery, 2006. **5**(3): p. 210-218.
8. Whitesides, G.M., *The origins and the future of microfluidics.* Nature, 2006. **442**(7101): p. 368-373.
9. Bhagat, A.A.S., et al., *Microfluidics for cell separation.* Medical & Biological Engineering & Computing, 2010. **48**(10): p. 999-1014.
10. Xia, B., I.W. Lenggoro, and K. Okuyama, *Nanoparticle separation in salted droplet microreactors.* Chemistry of Materials, 2002. **14**(6): p. 2623-2627.
11. Doucet, F.J., L. Maguire, and J.R. Lead, *Size fractionation of aquatic colloids and particles by cross-flow filtration: analysis by scanning electron and atomic force microscopy.* Analytica Chimica Acta, 2004. **522**(1): p. 59-71.
12. Gascoyne, P., J. Satayavivad, and M. Ruchirawat, *Microfluidic approaches to malaria detection.* Acta Tropica, 2004. **89**(3): p. 357-369.
13. Cheng, X.H., et al., *A microfluidic device for practical label-free CD4+T cell counting of HIV-infected subjects.* Lab on a Chip, 2007. **7**(2): p. 170-178.
14. Wu, Z.G., et al., *Microfluidic high viability neural cell separation using viscoelastically tuned hydrodynamic spreading.* Biomedical Microdevices, 2008. **10**(5): p. 631-638.
15. Abdelgawad, M., M.W.L. Watson, and A.R. Wheeler, *Hybrid microfluidics: A digital-to-channel interface for in-line sample processing and chemical separations.* Lab on a Chip, 2009. **9**(8): p. 1046-1051.
16. Baret, J.C., et al., *Fluorescence-activated droplet sorting (FADS): efficient microfluidic cell sorting based on enzymatic activity.* Lab on a Chip, 2009. **9**(13): p. 1850-1858.
17. Braschler, T., et al., *Continuous separation of cells by balanced dielectrophoretic forces at multiple frequencies.* Lab on a Chip, 2008. **8**(2): p. 280-286.
18. Cui, H.H., et al., *Separation of particles by pulsed dielectrophoresis.* Lab on a Chip, 2009. **9**(16): p. 2306-2312.
19. Jellema, L.C., et al., *Charge-based particle separation in microfluidic devices using combined hydrodynamic and electrokinetic effects.* Lab on a Chip, 2009. **9**(13): p. 1914-1925.
20. Watson, M.W.L., M.J. Jebrail, and A.R. Wheeler, *Multilayer Hybrid Microfluidics: A Digital-to-Channel Interface for Sample Processing and Separations.* Analytical Chemistry, 2010. **82**(15): p. 6680-6686.
21. Lee, H., A.M. Purdon, and R.M. Westervelt, *Manipulation of biological cells using a microelectromagnet matrix.* Applied Physics Letters, 2004. **85**(6): p. 1063-1065.

22. Qu, B.Y., et al., *A glass microfluidic chip for continuous blood cell sorting by a magnetic gradient without labeling.* Analytical and Bioanalytical Chemistry, 2008. **392**(7-8): p. 1317-1324.
23. Yan, J., D. Skoko, and J.F. Marko, *Near-field-magnetic-tweezer manipulation of single DNA molecules.* Physical Review E, 2004. **70**(1).
24. Ashkin, A., et al., *Observation of a Single-Beam Gradient Force Optical Trap for Dielectric Particles.* Optics Letters, 1986. **11**(5): p. 288-290.
25. Grier, D.G., *A revolution in optical manipulation.* Nature, 2003. **424**(6950): p. 810-816.
26. MacDonald, M.P., G.C. Spalding, and K. Dholakia, *Microfluidic sorting in an optical lattice.* Nature, 2003. **426**(6965): p. 421-424.
27. de Castro, M.D.L. and F. Priego-Capote, *Lesser known ultrasound-assisted heterogeneous sample-preparation procedures.* Trac-Trends in Analytical Chemistry, 2007. **26**(2): p. 154-162.
28. Hertz, H.M., *Standing-Wave Acoustic Trap for Nonintrusive Positioning of Microparticles.* Journal of Applied Physics, 1995. **78**(8): p. 4845-4849.
29. Laurell, T., F. Petersson, and A. Nilsson, *Chip integrated strategies for acoustic separation and manipulation of cells and particles.* Chemical Society Reviews, 2007. **36**(3): p. 492-506.
30. Di Carlo, D., et al., *Equilibrium separation and filtration of particles using differential inertial focusing.* Analytical Chemistry, 2008. **80**(6): p. 2204-2211.
31. Sollier, E., et al., *Passive microfluidic devices for plasma extraction from whole human blood.* Sensors and Actuators B-Chemical, 2009. **141**(2): p. 617-624.
32. Xuan, X.C., J.J. Zhu, and C. Church, *Particle focusing in microfluidic devices.* Microfluidics and Nanofluidics, 2010. **9**(1): p. 1-16.
33. Thiel, A., A. Scheffold, and A. Radbruch, *Immunomagnetic cell sorting - pushing the limits.* Immunotechnology, 1998. **4**(2): p. 89-96.
34. Berger, M., et al., *Design of a microfabricated magnetic cell separator.* Electrophoresis, 2001. **22**(18): p. 3883-3892.
35. Voldman, J., *Electrical forces for microscale cell manipulation.* Annual Review of Biomedical Engineering, 2006. **8**: p. 425-454.
36. Shi, J.J., et al., *Acoustic tweezers: patterning cells and microparticles using standing surface acoustic waves (SSAW).* Lab on a Chip, 2009. **9**(20): p. 2890-2895.
37. Wang, Z.C. and J.A. Zhe, *Recent advances in particle and droplet manipulation for lab-on-a-chip devices based on surface acoustic waves.* Lab on a Chip, 2011. **11**(7): p. 1280-1285.
38. Moreau, S., H. Bailliet, and J.C. Valiere, *Measurements of inner and outer streaming vortices in a standing waveguide using laser doppler velocimetry.* Journal of the Acoustical Society of America, 2008. **123**(2): p. 640-647.
39. Kundt, A. and O. Lehmann, *Ueber longitudinale Schwingungen und Klangfiguren in cylindrischen Flüssigkeitssäulen.* Ann. Phys. Chem, 1874. **153**(1).
40. Dual, J., et al., *Acoustofluidics 6: Experimental characterization of ultrasonic particle manipulation devices.* Lab on a Chip, 2012. **12**(5): p. 852-862.
41. King, L.V., *On the Acoustic Radiation Pressure on Spheres.* Proc. R. Soc. London, 1934. **A147**: p. 212-240.
42. Yosioka, K. and Y. Kawasima, *Acoustic radiation pressure on a compressible sphere.* Acustica, 1955. **5**: p. 167.
43. Gorkov, L.P., *On the Forces Acting on a Small Particle in an Acoustical Field in an Ideal Fluid.* Sov. Phys. Dorkl. (Engl. Transl.), 1962. **6**: p. 773.
44. Nyborg, W.L., *Radiation pressure on a small rigid sphere.* J. Acoust. Soc. Am., 1967. **42**: p. 947.
45. Doinikov, A.A., *Acoustic Radiation Pressure on a Compressible Sphere in a Viscous-Fluid.* Journal of Fluid Mechanics, 1994. **267**: p. 1-21.

46. Bruus, H., *Acoustofluidics 7: The acoustic radiation force on small particles.* Lab on a Chip, 2012. **12**(6): p. 1014-1021.
47. Haar, G.T. and S.J. Wyard, *Blood cell banding in ultrasonic standing wave fields: A physical analysis.* Ultrasound in Medicine and Biology, 1978. **4**: p. 111.
48. Barnkob, R., et al., *Acoustic radiation- and streaming-induced microparticle velocities determined by microparticle image velocimetry in an ultrasound symmetry plane.* Physical Review E, 2012. **86**(5).
49. Rayleigh, L., *On the circulation of air observed in Kundt's tube, and on some allied acoustical problems.* Phil. Trans., 1883. **175**: p. 1-21.
50. Schlichting, H., *Berechnung ebener periodischer Grenzschichtstromungen (Calculation of plane periodic boundary layer streaming).* Physikalische Zeitschrift, 1932. **33**(8): p. 327-335.
51. Riley, N., *Acoustic streaming.* Theoretical and Computational Fluid Dynamics, 1998. **10**(1-4): p. 349-356.
52. Loh, B.G., et al., *Acoustic streaming induced by ultrasonic flexural vibrations and associated enhancement of convective heat transfer.* Journal of the Acoustical Society of America, 2002. **111**(2): p. 875-883.
53. Lee, D.R. and B.G. Loh, *Smart cooling technology utilizing acoustic streaming.* Ieee Transactions on Components and Packaging Technologies, 2007. **30**(4): p. 691-699.
54. Mcqueen, D.H., *Frequency-Dependence of Ultrasonic Cleaning.* Ultrasonics, 1986. **24**(5): p. 273-280.
55. Busnaina, A.A. and G.W. Gale, *Removal of silica particles from silicon substrates using megasonic cleaning.* Particulate Science and Technology, 1997. **15**(3-4): p. 361-369.
56. Busnaina, A.A. and T.M. Elsawy, *Post-CMP cleaning using acoustic streaming.* Journal of Electronic Materials, 1998. **27**(10): p. 1095-1098.
57. Gale, G.W. and A.A. Busnaina, *Removal of particulate contaminants using ultrasonics and megasonics: A review.* Particulate Science and Technology, 1995. **13**(3-4): p. 197-211.
58. Suri, C., et al., *Experimental study of a new liquid mixing method using acoustic streaming.* Journal of Chemical Engineering of Japan, 2002. **35**(6): p. 497-502.
59. Ahmed, D., et al., *A millisecond micromixer via single-bubble-based acoustic streaming.* Lab on a Chip, 2009. **9**(18): p. 2738-2741.
60. Kuznetsova, L.A. and W.T. Coakley, *Applications of ultrasound streaming and radiation force in biosensors.* Biosensors & Bioelectronics, 2007. **22**(8): p. 1567-1577.
61. Nilson, R.H. and S.K. Griffiths, *Enhanced transport by acoustic streaming in deep trench-like cavities.* Journal of the Electrochemical Society, 2002. **149**(4): p. G286-G296.
62. Maturos, T., et al., *Enhancement of DNA hybridization under acoustic streaming with three-piezoelectric-transducer system.* Lab on a Chip, 2012. **12**(1): p. 133-138.
63. Edwards, A., et al., *Acoustic streaming: a new technique for assessing adnexal cysts.* Ultrasound in Obstetrics & Gynecology, 2003. **22**(1): p. 74-78.
64. Nightingale, K.R., P.J. Kornguth, and G.E. Trahey, *The use of acoustic streaming in breast lesion diagnosis: A clinical study.* Ultrasound in Medicine and Biology, 1999. **25**(1): p. 75-87.
65. Frampton, K.D., S.E. Martin, and K. Minor, *The scaling of acoustic streaming for application in micro-fluidic devices.* Applied Acoustics, 2003. **64**(7): p. 681-692.
66. Olson, J.R. and G.W. Swift, *Acoustic streaming in pulse tube refrigerators: tapered pulse tubes.* Cryogenics, 1997. **37**(12): p. 769-776.
67. Job, S., et al., *Acoustic streaming measurements in annular thermoacoustic engines.* Journal of the Acoustical Society of America, 2003. **113**(4): p. 1892-1899.
68. Mironov, M., et al., *Acoustic streaming related to minor loss phenomenon in differentially heated elements of thermoacoustic devices.* Journal of the Acoustical Society of America, 2002. **112**(2): p. 441-445.

69. Lighthill, J., *Acoustic Streaming.* Journal of Sound and Vibration, 1978. **61**(3): p. 391-418.

70. Boluriaan, S. and P.J. Morris, *Acoustic streaming: from Rayleigh to today.* Aeroacoustics, 2003. **2 (3&4)**: p. 255-292.

71. Valverde, J.M., *Pattern-formation under acoustic driving forces.* Contemporary Physics, 2015: p. 1-21.

72. Eckart, C., *Vortices and streams caused by sound waves.* Phys. Rev., 1947. **73**(1): p. 68-76.

73. Rudenko, O.V. and A.A. Sukhorukov, *Nonstationary Eckart streaming and pumping of liquid in an ultrasonic field.* Acoustical Physics, 1998. **44**(5): p. 565-570.

74. Faraday, M., *On a Peculiar Class of Acoustical Figures; and on Certain Forms Assumed by Groups of Particles upon Vibrating Elastic Surfaces.* Phil. Trans. R. Soc. Lond, 1831. **121**: p. 299-340.

75. Rayleigh, L., *The theory of sound*. 2nd ed. Vol. 2. 1896, New York: Dover publications.

76. Taylor, S., *Experiments on the Colours Shown by Thin Liquid Films under the Action of Sonorous Vibrations.* Proc. R. Soc. London, 1878: p. 71-76.

77. Westervelt, P.J., *The theory of steady rotational flow generated by a sound field.* J. Acoust. Soc. Am., 1952. **25**(1): p. 60-67.

78. Nyborg, W.L., *Acoustic streaming near a boundary.* J. Acoust. Soc. Am., 1958. **30**(4): p. 329-339.

79. Hamilton, M.F., Y.A. Ilinskii, and E.A. Zabolotskaya, *Acoustic streaming generated by standing waves in two-dimensional channels of arbitrary width.* Journal of the Acoustical Society of America, 2003. **113**(1): p. 153-160.

80. Markham, J.J., *Second-order acoustic field: streaming with viscosity and relaxation.* Phys. Rev., 1951. **86**(4): p. 497-502.

81. Nyborg, W.L., *Acoustic streaming due to attenuated plane waves.* J. Acoust. Soc. Am., 1953. **25**(1): p. 68-75.

82. Andres, J.M. and U. Ingard, *Acoustic streaming at high Reynolds numbers.* J. Acoust. Soc. Am., 1953. **25**: p. 928-932.

83. Andres, J.M. and U. Ingard, *Acoustic streaming at low Reynolds numbers.* J. Acoust. Soc. Am., 1953. **25**: p. 932-938.

84. Andrade, E.N.D.C., *On the circulations caused by the vibration of air in a tube.* Proc. R. Soc. London A, 1931. **134**(824): p. 445-470.

85. Carrière, Z., *Analyse ultramicroscopique des vibrations aeriennes (ultramicroscopic analysis of air vibration).* J. phys. et radium, 1929. **10**: p. 198.

86. Wang, C.Y., *On the separation time of the flow past a circular cylinder which is started from rest.* J. Maths & Phys, 1967. **46**: p. 195-202.

87. Lane, C., *Acoustic Streaming in the Vicinity of a Sphere.* J. Acoust. Soc. Am., 1955. **27**(5): p. 1003.

88. Lee, C.P. and T.G. Wang, *Near-Boundary Streaming around a Small Sphere Due to 2 Orthogonal Standing Waves.* Journal of the Acoustical Society of America, 1989. **85**(3): p. 1081-1088.

89. Wang, C., *The flow field induced by an oscillating sphere.* J. Sound & Vibration, 1965. **2**(3): p. 257-269.

90. Lee, C.P. and T.G. Wang, *Outer Acoustic Streaming.* Journal of the Acoustical Society of America, 1990. **88**(5): p. 2367-2375.

91. Stuart, J.T., *Double boundary layer in oscillatory viscous flow.* J. Fluid Mech, 1965. **24**(4): p. 673-687.

92. Rott, N., *The influence of heat conduction on acoustic streaming.* Z. Angew. Math. Phys, 1974. **25**: p. 417-421.

93. Qi, Q., *The Effect of Compressibility on Acoustic Streaming near a Rigid Boundary for a Plane Traveling-Wave.* Journal of the Acoustical Society of America, 1993. **94**(2): p. 1090-1098.
94. Vainshtein, P., *Rayleigh Streaming at Large Reynolds-Number and Its Effect on Shear-Flow.* Journal of Fluid Mechanics, 1995. **285**: p. 249-264.
95. Menguy, L. and J. Gilbert, *Non-linear acoustic streaming accompanying a plane stationary wave in a guide.* Acta Acust 2000. **86**: p. 249-259.
96. Waxler, R., *Stationary velocity and pressure gradients in a thermoacoustic stack.* Journal of the Acoustical Society of America, 2001. **109**(6): p. 2739-2750.
97. Bailliet, H., et al., *Acoustic streaming in closed thermoacoustic devices.* Journal of the Acoustical Society of America, 2001. **110**(4): p. 1808-1821.
98. Hamilton, M.F., Y.A. Ilinskii, and E.A. Zabolotskaya, *Thermal effects on acoustic streaming in standing waves.* Journal of the Acoustical Society of America, 2003. **114**(6): p. 3092-3101.
99. Carlsson, F., M. Sen, and L. Lofdahl, *Steady streaming due to vibrating walls.* Physics of Fluids, 2004. **16**(5): p. 1822-1825.
100. Rednikov, A.Y. and S.S. Sadhal, *Acoustic/steady streaming from a motionless boundary and related phenomena: generalized treatment of the inner streaming and examples.* Journal of Fluid Mechanics, 2011. **667**: p. 426-462.
101. Nyborg, W.L., *Acoustic streaming*, in *Physical Acoustics*, W.P. Mason, Editor. 1965: Academic, New York. p. 290-295.
102. Zarembo, L.K., *Acoustic streaming*, in *High intensity ultrasound fields*, L.D. Rozenberg, Editor. 1972, Plenum press: New York. p. 137-199.
103. Rudenko, O.V. and S.I. Soluyan, *Theoretical Foundations of Nonlinear Acoustics*. 1977, Consultants Bureau: Plenum, New York.
104. Nyborg, W.L., *Acoustic streaming*, in *Nonlinear Acoustics*, M.F. Hamilton and D.T. Blackstock, Editors. 1998, Academic: San Diego.
105. Sadhal, S.S., *Acoustofluidics 15: streaming with sound waves interacting with solid particles.* Lab on a Chip, 2012. **12**(15): p. 2600-2611.
106. Sadhal, S.S., *Acoustofluidics 13: Analysis of acoustic streaming by perturbation methods Foreword.* Lab on a Chip, 2012. **12**(13): p. 2292-2300.
107. Sadhal, S.S., *Acoustofluidics 16: acoustics streaming near liquid-gas interfaces: drops and bubbles.* Lab on a Chip, 2012. **12**(16): p. 2771-2781.
108. Liebermann, L.N., *The second viscosity of liquids.* Phys. Rev., 1949. **75**(9): p. 1415-1422.
109. Ingard, U. and S. Labate, *Acoustic circulation effects and the nonlinear impedance of orifices.* J. Acoust. Soc. Am., 1950. **22**(2): p. 211-218.
110. West, G.D., *Circulations occurring in acoustic phenomena.* Proc. Phys. Soc. B, 1951. **64**: p. 483-487.
111. Holtsmark, J., et al., *Boundary Layer Flow near a Cylindrical Obstacle in an Oscillating Incompressible Fluid.* J. Acoust. Soc. Am., 1954. **26**: p. 26-39.
112. Raney, W.P., J.C. Corelli, and P.J. Westervelt, *Acoustic Streaming in the Vicinity of a Cylinder.* J. Acoust. Soc. Am., 1954. **26**: p. 1006-1014.
113. Trinh, E.H. and J.L. Robey, *Experimental Study of Streaming Flows Associated with Ultrasonic Levitators.* Physics of Fluids, 1994. **6**: p. 3567-3579.
114. Hartley, C.J., *Doppler measurement of acoustic streaming.* 1995 Ieee Ultrasonics Symposium Proceedings, Vols 1 and 2, 1995: p. 1537-1540.
115. Mitome, H., T. Kozuka, and T. Tuziuti, *Measurement of the establishment process of acoustic streaming using laser Doppler velocimetry.* Ultrasonics, 1996. **34**(2-5): p. 527-530.
116. Nowicki, A., et al., *Estimation of acoustic streaming: theoretical model, Doppler measurement and optical visualisation.* European Journal of Ultrasound, 1998. **7**: p. 73-81.

117. Thompson, M.W. and A.A. Atchley, *Simultaneous measurement of acoustic and streaming velocities in a standing wave using laser Doppler anemometry.* Journal of the Acoustical Society of America, 2005. **117**(4): p. 1828-1838.
118. Thompson, M.W., A.A. Atchley, and M.J. Maccarone, *Influences of a temperature gradient and fluid inertia on acoustic streaming in a standing wave.* Journal of the Acoustical Society of America, 2005. **117**(4): p. 1839-1849.
119. Kumar, A., P.R. Gogate, and A.B. Pandit, *Mapping of acoustic streaming in sonochemical reactors.* Industrial & Engineering Chemistry Research, 2007. **46**(13): p. 4368-4373.
120. Desjouy, C., et al., *LDV measurements of acoustic streaming in a traveling wave, closed-loop resonator*, in *Acoustics*. 2008: Paris. p. 4355-4360.
121. Desjouy, C., et al., *Measurement of acoustic streaming in a closed-loop traveling wave resonator using laser Doppler velocimetry.* Journal of the Acoustical Society of America, 2009. **126**(5): p. 2176-2183.
122. Sharpe, J.P., et al., *The Measurement of Acoustic Streaming Using Particle Image Velocimetry.* Acustica, 1989. **68**(2): p. 168-172.
123. Arroyo, M.P. and C.A. Greated, *Stereoscopic Particle Image Velocimetry.* Measurement Science & Technology, 1991. **2**(12): p. 1181-1186.
124. Hann, D.B. and C.A. Greated, *The measurement of flow velocity and acoustic particle velocity using particle-image velocimetry.* Measurement Science & Technology, 1997. **8**(12): p. 1517-1522.
125. Chouvellon, M., et al., *Velocity study in an ultrasonic reactor.* Ultrasonics Sonochemistry, 2000. **7**(4): p. 207-211.
126. Campbell, M., et al., *Review of LDA and PIV applied to the measurement of sound and acoustic streaming.* Optics and Laser Technology, 2000. **32**(7-8): p. 629-639.
127. Frenkel, V., et al., *Preliminary investigations of ultrasound induced acoustic streaming using particle image velocimetry.* Ultrasonics, 2001. **39**(3): p. 153-156.
128. Loh, B.G., D.R. Lee, and K. Kwon, *Acoustic streaming pattern induced by longitudinal ultrasonic vibration in an open channel using particle imaging velocimetry.* Applied Physics Letters, 2006. **89**(18).
129. Nabavi, M., M.H.K. Siddiqui, and J. Dargahi, *Simultaneous measurement of acoustic and streaming velocities using synchronized PIV technique.* Measurement Science & Technology, 2007. **18**(7): p. 1811-1817.
130. Nabavi, M., K. Siddiqui, and J. Dargahi, *Influence of differentially heated horizontal walls on the streaming shape and velocity in a standing wave resonator.* International Communications in Heat and Mass Transfer, 2008. **35**(9): p. 1061-1064.
131. Nabavi, M., K. Siddiqui, and J. Dargahi, *Effects of transverse temperature gradient on acoustic and streaming velocity fields in a resonant cavity.* Applied Physics Letters, 2008. **93**(5).
132. Nabavi, M., M.H.K. Siddiqui, and J. Dargahi, *Experimental investigation of the formation of acoustic streaming in a rectangular enclosure using a synchronized PIV technique.* Measurement Science & Technology, 2008. **19**(6).
133. Nabavi, M., K. Siddiqui, and J. Dargahi, *Analysis of regular and irregular acoustic streaming patterns in a rectangular enclosure.* Wave Motion, 2009. **46**(5): p. 312-322.
134. Rabenjafimanantsoa, H.A., B.M. Wrobel, and R.W. Time, *PIV visualization of acoustic streaming in non-newtonian fluid.* Ann. Tran. Nor. Rheo. Soc., 2009. **17**.
135. Layman, C.N., et al., *Characterization of acoustic streaming and heating using synchronized infrared thermography and particle image velocimetry.* Ultrasonics Sonochemistry, 2011. **18**(5): p. 1258-1261.
136. Sou, I.M., et al., *A synchronized particle image velocimetry and infrared thermography technique applied to an acoustic streaming flow.* Experiments in Fluids, 2011. **51**(5): p. 1201-1208.

137. Reyt, I., H. Bailliet, and J.C. Valiere, *Experimental investigation of acoustic streaming in a cylindrical wave guide up to high streaming Reynolds numbers.* Journal of the Acoustical Society of America, 2014. **135**(1): p. 27-37.
138. Reyt, I., et al., *Fast acoustic streaming in standing waves: generation of an additional outer streaming cell.* J Acoust Soc Am, 2013. **134**(3): p. 1791-801.
139. Kawahashi, M. and M. Arakawa, *Nonlinear phenomena induced by finite-amplitude oscillation of air column in closed duct (Analysis of acoustic streaming).* Jsme International Journal Series B-Fluids and Thermal Engineering, 1996. **39**(2): p. 280-286.
140. Stansell, P. and C.A. Greated, *Lattice gas automaton simulation of acoustic streaming in a two-dimensional pipe.* Physics of Fluids, 1997. **9**(11): p. 3288-3299.
141. Yano, T., *Turbulent acoustic streaming excited by resonant gas oscillation with periodic shock waves in a closed tube.* Journal of the Acoustical Society of America, 1999. **106**(1): p. L7-L12.
142. Haydock, D. and J.M. Yeomans, *Lattice Boltzmann simulations of acoustic streaming.* Journal of Physics a-Mathematical and General, 2001. **34**(25): p. 5201-5213.
143. Haydock, D. and J.M. Yeomans, *Lattice Boltzmann simulations of attenuation-driven acoustic streaming.* Journal of Physics a-Mathematical and General, 2003. **36**(20): p. 5683-5694.
144. Rednikov, A. and N. Riley, *A simulation of streaming flows associated with acoustic levitators.* Physics of Fluids, 2002. **14**(4): p. 1502-1510.
145. Aktas, M.K. and B. Farouk, *Numerical simulation of acoustic streaming generated by finite-amplitude resonant oscillations in an enclosure.* Journal of the Acoustical Society of America, 2004. **116**(5): p. 2822-2831.
146. Aktas, M.K. and T. Ozgumus, *The effects of acoustic streaming on thermal convection in an enclosure with differentially heated horizontal walls.* International Journal of Heat and Mass Transfer, 2010. **53**(23-24): p. 5289-5297.
147. Sastrapradja, D. and V.W. Sparrow, *Rayleigh streaming simulation in a cylindrical tube using the vorticity transport equation.* Innovations in Nonlinear Acoustics, 2006. **838**: p. 465-468.
148. Feng, H.Y., et al., *Numerical simulation of nonlinear acoustic streaming in a resonator using gas-kinetic scheme.* Journal of Applied Physics, 2012. **112**(8).
149. Daru, V., et al., *Two-dimensional numerical simulations of nonlinear acoustic streaming in standing waves.* Wave Motion, 2013. **50**(5): p. 955-963.
150. *COMSOL Multiphysics 4.3a*. 2014; Available from: http://www.comsol.com/.
151. Kinsler, L.E., et al., *Fundamentals of acoustics*. 4th ed. 2000, New York: Wiley. 548.
152. Lei, J., P. Glynne-Jones, and M. Hill, *Acoustic streaming in the transducer plane in ultrasonic particle manipulation devices.* Lab Chip, 2013. **13**(11): p. 2133-43.
153. Wiklund, M., R. Green, and M. Ohlin, *Acoustofluidics 14: Applications of acoustic streaming in microfluidic devices.* Lab on a Chip, 2012. **12**(14): p. 2438-2451.
154. Hammarstrom, B., T. Laurell, and J. Nilsson, *Seed particle-enabled acoustic trapping of bacteria and nanoparticles in continuous flow systems.* Lab on a Chip, 2012. **12**(21): p. 4296-4304.
155. Spengler, J.F., et al., *Observation of yeast cell movement and aggregation in a small-scale MHz-ultrasonic standing wave field.* Bioseparation, 2000. **9**(6): p. 329-41.
156. Kuznetsova, L.A. and W.T. Coakley, *Microparticle concentration in short path length uftrasonic resonators: Roles of radiation pressure and acoustic streaming.* Journal of the Acoustical Society of America, 2004. **116**(4): p. 1956-1966.
157. Araz, M.K., C.H. Lee, and A. Lal, *Ultrasonic separation in microfluidic capillaries.* 2003 Ieee Ultrasonics Symposium Proceedings, Vols 1 and 2, 2003: p. 1066-1069.
158. Goddard, G. and G. Kaduchak, *Ultrasonic particle concentration in a line-driven cylindrical tube.* Journal of the Acoustical Society of America, 2005. **117**(6): p. 3440-3447.

159. Wiklund, M. and H.M. Hertz, *Ultrasonic enhancement of bead-based bioaffinity assays.* Lab on a Chip, 2006. **6**(10): p. 1279-1292.
160. Suthanthiraraj, P.P.A., et al., *One-dimensional acoustic standing waves in rectangular channels for flow cytometry.* Methods, 2012. **57**(3): p. 259-271.
161. Prest, J.E., et al., *Scaling-up ultrasound standing wave enhanced sedimentation filters.* Ultrasonics, 2014.
162. Jepras, R.I., D.J. Clarke, and W.T. Coakley, *Agglutination of Legionella-Pneumophila by Antiserum Is Accelerated in an Ultrasonic Standing Wave.* Journal of Immunological Methods, 1989. **120**(2): p. 201-205.
163. Glynne-Jones, P., R.J. Boltryk, and M. Hill, *Acoustofluidics 9: Modelling and applications of planar resonant devices for acoustic particle manipulation.* Lab on a Chip, 2012. **12**(8): p. 1417-1426.
164. Glynne-Jones, P., et al., *Array-Controlled Ultrasonic Manipulation of Particles in Planar Acoustic Resonator.* Ieee Transactions on Ultrasonics Ferroelectrics and Frequency Control, 2012. **59**(6): p. 1258-1266.
165. Augustsson, P., et al., *Automated and temperature-controlled micro-PIV measurements enabling long-term-stable microchannel acoustophoresis characterization.* Lab on a Chip, 2011. **11**(24): p. 4152-4164.
166. Mori, N. and C. K-A. *mpiv - MATLAB PIV Toolbox*. Available from: http://www.oceanwave.jp/softwares/mpiv/.
167. *COMSOL Multiphysics 4.4*. 2014; Available from: http://www.comsol.com/.
168. Muller, P.B., et al., *A numerical study of microparticle acoustophoresis driven by acoustic radiation forces and streaming-induced drag forces.* Lab on a chip, 2012. **12**: p. 4617-4627.
169. F.J.Fahy, *Sound intensity*. Second Edition ed. 1995, London: E & FN Spon.
170. Lei, J., M. Hill, and P. Glynne-Jones, *Numerical simulation of 3D boundary-driven acoustic streaming in microfluidic devices.* Lab Chip, 2013. **14**(3): p. 532-41.
171. Muller, P.B., et al., *Ultrasound-induced acoustophoretic motion of microparticles in three dimensions.* Physical Review E, 2013. **88**(2): p. 023006.
172. Hagsater, S.M., et al., *Acoustic resonances in microfluidic chips: full-image micro-PIV experiments and numerical simulations.* Lab on a Chip, 2007. **7**(10): p. 1336-1344.
173. Bernassau, A.L., et al., *Controlling acoustic streaming in an ultrasonic heptagonal tweezers with application to cell manipulation.* Ultrasonics, 2014. **54**(1): p. 268-274.
174. Moller, D., et al., *Acoustic Streaming Used to Move Particles in a Circular Flow in a Plastic Chamber.* International Congress on Ultrasonics (Gdansk 2011), 2012. **1433**: p. 775-778.
175. Yeo, L.Y. and J.R. Friend, *Surface Acoustic Wave Microfluidics.* Annual Review of Fluid Mechanics, Vol 46, 2014. **46**: p. 379-406.
176. Ding, X.Y., et al., *Surface acoustic wave microfluidics.* Lab on a Chip, 2013. **13**(18): p. 3626-3649.
177. Lei, J., P. Glynne-Jones, and M. Hill, *Modal Rayleigh-like streaming in layered acoustofluidic devices.* Physics of Fluids, (under review).
178. Bruus, H., et al., *Forthcoming Lab on a Chip tutorial series on acoustofluidics: Acoustofluidics-exploiting ultrasonic standing wave forces and acoustic streaming in microfluidic systems for cell and particle manipulation.* Lab on a Chip, 2011. **11**(21): p. 3579-3580.
179. Hammarstrom, B., et al., *Acoustic Trapping for Bacteria Identification in Positive Blood Cultures with MALDI-TOF MS.* Anal Chem, 2014. **86**(21): p. 10560-7.
180. Chung, S.K. and S.K. Cho, *On-chip manipulation of objects using mobile oscillating bubbles.* Journal of Micromechanics and Microengineering, 2008. **18**(12).

181. Lutz, B.R., J. Chen, and D.T. Schwartz, *Hydrodynamic tweezers: 1. Noncontact trapping of single cells using steady streaming microeddies.* Analytical Chemistry, 2006. **78**(15): p. 5429-5435.

182. Yazdi, S. and A.M. Ardekani, *Bacterial aggregation and biofilm formation in a vortical flow.* Biomicrofluidics, 2012. **6**(4).

183. Antfolk, M., et al., *Focusing of sub-micrometer particles and bacteria enabled by two-dimensional acoustophoresis.* Lab on a Chip, 2014. **14**(15): p. 2791-2799.

184. Devendran, C., I. Gralinski, and A. Neild, *Separation of particles using acoustic streaming and radiation forces in an open microfluidic channel.* Microfluidics and Nanofluidics, 2014: p. 1-12.

185. Muller, P.B., et al., *Ultrasound-induced acoustophoretic motion of microparticles in three dimensions.* Physical Review E, 2013. **88**(2).

186. Hagsater, S.M., et al., *Acoustic resonances in straight micro channels: Beyond the 1D-approximation.* Lab on a Chip, 2008. **8**(7): p. 1178-1184.

187. Lenshof, A., et al., *Acoustofluidics 5: Building microfluidic acoustic resonators.* Lab on a Chip, 2012. **12**(4): p. 684-695.

188. Hawkes, J.J. and W.T. Coakley, *Force field particle filter, combining ultrasound standing waves and laminar flow.* Sensors and Actuators B-Chemical, 2001. **75**(3): p. 213-222.

189. Hawkes, J.J., et al., *Continuous cell washing and mixing driven by an ultrasound standing wave within a microfluidic channel.* Lab on a Chip, 2004. **4**(5): p. 446-452.

190. Hill, M., R.J. Townsend, and N.R. Harris, *Modelling for the robust design of layered resonators for ultrasonic particle manipulation.* Ultrasonics, 2008. **48**(6-7): p. 521-528.

191. Augustsson, P. and T. Laurell, *Acoustofluidics 11: Affinity specific extraction and sample decomplexing using continuous flow acoustophoresis.* Lab on a Chip, 2012. **12**(10): p. 1742-1752.

192. Evander, M. and J. Nilsson, *Acoustofluidics 20: Applications in acoustic trapping.* Lab on a Chip, 2012. **12**(22): p. 4667-4676.

193. Lenshof, A., C. Magnusson, and T. Laurell, *Acoustofluidics 8: Applications of acoustophoresis in continuous flow microsystems.* Lab on a Chip, 2012. **12**(7): p. 1210-1223.

194. Spengler, J.F., W.T. Coakley, and K.T. Christensen, *Microstreaming effects on particle concentration in an ultrasonic standing wave.* Aiche Journal, 2003. **49**(11): p. 2773-2782.

195. Qiu, Y.Q., et al., *Acoustic Devices for Particle and Cell Manipulation and Sensing.* Sensors, 2014. **14**(8): p. 14806-14838.

196. Lei, J., P. Glynne-Jones, and M. Hill, *Effects of surface profile on a boundary-driven acoustic streaming field*, in *The 21st International Congress on Sound and Vibration*. 2014, iiav: Beijing, China. p. 1-5.

197. Nama, N., et al., *Investigation of acoustic streaming patterns around oscillating sharp edges.* Lab on a Chip, 2014. **14**(15): p. 2824-2836.

198. Ovchinnikov, M., J.B. Zhou, and S. Yalamanchili, *Acoustic streaming of a sharp edge.* Journal of the Acoustical Society of America, 2014. **136**(1): p. 22-29.